



From Quantum Mechanical Restrictions to Everyday Applications: Programmable Tags using Organic Phosphorescence

DISSERTATION
ZUR ERLANGUNG DES AKADEMISCHEN GRADES
DOCTOR RERUM NATURALIUM
(DR. RER. NAT.)

vorgelegt von
Max Gmelch
* 06. März 1990
Neumarkt i.d.OPf.

Dresden Integrated Center for Applied Physics and Photonic Materials (IAPP)
Fakultät Physik
Technische Universität Dresden

GUTACHTER:
Prof. Dr. Sebastian Reineke
Prof. Dr. Tobias Korn

VERTEIDIGT AM 23.10.2020

1. Gutachter Prof. Dr. Sebastian Reineke
2. Gutachter Prof. Dr. Tobias Korn

List of Publications

Research Articles

- [A1] Max Gmelch, Heidi Thomas, Felix Fries, and Sebastian Reineke. *Programmable Transparent Organic Luminescent Tags*. Science Advances **5**, eaau7310, 2019
- [A2] Max Gmelch, Tim Achenbach, Ausra Tomkeviciene, and Sebastian Reineke. *High-Speed and Continuous-Wave Programmable Luminescent Tags*. Submitted, preprint available at arXiv, ID: 2001.11215
- [A3] Anton Kirch, Max Gmelch and Sebastian Reineke. *Simultaneous Singlet - Singlet and Triplet - Singlet Förster Resonance Energy Transfer from a Single Donor Material*. The Journal of Physical Chemistry Letters **10**, 310-315, 2019
- [A4] Marine Louis, Heidi Thomas, Max Gmelch, Anna Haft, Felix Fries, and Sebastian Reineke. *Blue-Light-Absorbing Thin Films Showing Ultralong Room-Temperature Phosphorescence*. Advanced Materials **31**, 1807887, 2019
- [A5] Heidi Thomas, Dominik L. Pastoetter, Max Gmelch, Tim Achenbach, Annika Schlögl, Marine Louis, Xinliang Feng, and Sebastian Reineke. *Aromatic Phosphonates: A Novel Group of Emitters Showing Blue Ultralong Room Temperature Phosphorescence*. Advanced Materials **32**, 2000880, 2020
- [A6] Felix Fries, Marine Louis, Reinhard Scholz, Max Gmelch, Heidi Thomas, Anna Haft, and Sebastian Reineke. *Dissecting Tetra-N-phenylbenzidine: Biphenyl as the Origin of Room Temperature Phosphorescence*. The Journal of Physical Chemistry A **124** (3), 479-485, 2020
- [A7] Marine Louis, Heidi Thomas, Max Gmelch, Felix Fries, Anna Haft, Jakob Lindenthal, and Sebastian Reineke. *Biluminescence Under Ambient Conditions: Water-Soluble Organic Emitter in High-Oxygen-Barrier Polymer*. Advanced Optical Materials, 2000427, 2020

Books

- [B1] Max Gmelch and Sebastian Reineke. *Durchblick in Optik: Mit Phänomenen, Formeln und Fragen zum Verständnis*. Springer Berlin, ISBN 978-3-662-58939-7, 2019

Intellectual Property Applications

- [IP1] Max Gmelch, Heidi Thomas, Felix Fries, and Sebastian Reineke. *Verfahren zur Aktivierung und Deaktivierung der Phosphoreszenz einer Struktur, Verfahren zur Herstellung einer Phosphoreszierenden Struktur und Phosphoreszierende Struktur*. **DE102018214375.7**, 2018
- [IP2] Max Gmelch, Heidi Thomas, Felix Fries, and Sebastian Reineke. *Nachleuchtende Beleuchtungsanordnung für Transportmittel, Verfahren zum Betrieb einer Beleuchtungsanordnung und Transportmittel mit einer Beleuchtungsanordnung*. **DE102018214373.0**, 2018
- [IP3] Max Gmelch, Heidi Thomas, Felix Fries, and Sebastian Reineke. *Phosphoreszierendes Etikett, Verfahren zum Beschreiben, Löschen und Wiederbeschreiben des Etiketts*. **DE102018214374.9**, 2018

Scientific Talks and Presentations

- [T1] Max Gmelch, Heidi Thomas, Felix Fries, Anton Kirch, and Sebastian Reineke. *Programmable Transparent Organic Luminescent Tags*. DPG Spring Conference, Regensburg, Germany, 2019
- [T2] Max Gmelch, Paul-Anton Will, Heidi Thomas, Felix Fries, and Sebastian Reineke. *Printed Light-Storing Foils*. InPrint, Munich, Germany, 2019
- [T3] Max Gmelch, Paul-Anton Will, Heidi Thomas, Felix Fries, Anton Kirch, and Sebastian Reineke. *Schreiben, Lesen und Radieren mit Licht - Neuartige Anwendungen organischer Leuchtstoffe*. Seniors' College, Technische Universität Dresden, Germany, 2019
- [T4] Max Gmelch, Heidi Thomas, Felix Fries, Anton Kirch, Tim Achenbach, and Sebastian Reineke. *Rewritable Luminescent Tags Using Room-Temperature Phosphorescence (RTP)*. SPIE Photonics West, San Francisco, USA, 2020

Abstract

Organic phosphorescence at room temperature is a strongly growing field of research. Together with fluorescence, it describes the radiative transitions of organic molecules after excitation with light of appropriate wavelength. While fluorescence is a process on the nanosecond timescale, organic phosphorescence is known to show afterglow emission in the lifetime range of microseconds to seconds. These long timescales result from quantum-mechanical restrictions in the transition processes underlying the phosphorescence. Namely, the involved electrons of the molecule have to undergo a spin flip, which is forbidden in zeroth-order approximation due to the necessity of conservation of angular momentum. In consequence, this emission feature of organic materials in general is obstructed at ambient temperature by dominating nonradiative deactivation channels. However, by careful design of the system, efficient phosphorescence at room temperature can be realized. In recent years, the number of publications introducing new organic phosphorescent emitters has continuously increased. However, to that date, the high quantity of described materials is not matched by an adequate amount of proposed applications. In fact, most publications present the synthesis of the substances as well as the morphology of the system, but only briefly address possible subsequent developing steps.

In this thesis, as a first step, recent developments in that area are compiled to a broad overview, which includes proposed applications like sensing and optical data storage. Beyond that, a newly detected photophysical effect is introduced and evaluated, which enables the reversible activation of phosphorescence in a thin and transparent film. Since for many emitter materials the presence of adjacent molecular oxygen leads to a complete vanishing of phosphorescence, this emission can locally be tuned by manipulating the respective oxygen concentration. It is shown that a very elegant, non-contact way of achieving that is by using light of different wavelengths only. In detail, radiation in the near UV or blue regime can induce a chemical reaction of the oxygen and its environment, leading to an oxygen depletion at the illuminated

regions. By covering the system with suitable barrier layers, no fresh oxygen can refill the system and phosphorescence becomes visible at the respective areas. By that, any luminescent image can be programmed into the transparent layers and be read out on demand. In addition, subsequent illumination with infrared radiation leads to a rise of the overall temperature, which consequently increases the permeability of the oxygen barrier. Therefore, the system is refilled with molecular oxygen and the pattern is erased. In a next step, new images can be written into the device. When not read out by illumination with appropriate light, the system is completely transparent and does not reveal the programmed information. That enables the fabrication of programmable luminescent tags, which allow multiple cycles of writing, reading and erasing, and thus may be used for temporary labeling in logistics or for invisible document security. Prototypes of the mentioned applications are manufactured and tested in this work, revealing the feasibility of their realization. The overall procedure as well as the device structure are part of patent applications.

As a further part of the thesis, the characterization of multiple organic emitters and additives reveals that the effect of switchable phosphorescence is not limited to a particular material combination, but is rather a very general behavior. In consequence, device features like emission color, pattern contrast, or wavelength sensitivity are successfully optimized using suitable available organic systems. In order to facilitate a targeted development of new phosphorescent emitters in the future, the decisive demands on the materials to enable programmable tags are defined. Conclusively, more application pathways are depicted, of which one already successfully gained funding by the Federal Ministry of Education and Research of Germany. In this follow-up study, the suitability of the discovered results on sensing of UV radiation will be examined. With two more submitted proposals building up on the presented developments, the results of this thesis open up a broad range of further work both from the scientific and the engineering point of view.

Kurzfassung

Organische Phosphoreszenz bei Raumtemperatur ist ein aktuell stark wachsendes Forschungsgebiet. Gemeinsam mit der Fluoreszenz beschreibt sie strahlende Übergänge von organischen Molekülen nach der Anregung mit Licht passender Wellenlänge. Während Fluoreszenz ein Prozess auf einer Zeitskala von Nanosekunden ist, zeigt organische Phosphoreszenz typischerweise ein längeres Nachleuchten im Bereich von Mikrosekunden bis Sekunden. Dieses resultiert daraus, dass die Übergangsprozesse, die zur Phosphoreszenz führen, quantenmechanisch nicht erlaubt sind. Die beteiligten Elektronen müssen sich einem Spin-Flip unterziehen, welcher in nullter Näherung aufgrund der Drehimpulserhaltung verboten ist. Infolgedessen wird die Phosphoreszenz organischer Materialien bei Umgebungstemperatur üblicherweise durch dominierende nichtstrahlende Relaxationswege unterdrückt. Durch gezielte Materialentwicklung lässt sich dennoch effiziente Phosphoreszenz realisieren. In den letzten Jahren ist die Zahl der Publikationen, in denen neue organische phosphoreszierende Emitter vorgestellt wurden, kontinuierlich gestiegen. Dieser hohen Auswahl an Materialien steht aktuell jedoch keine ausreichende Anzahl von Vorschlägen potentieller Anwendungen gegenüber. Tatsächlich stellen die meisten Publikationen die Synthese der Substanzen und die Morphologie des Systems vor, gehen aber nur kurz auf mögliche weitere Entwicklungsschritte ein.

In dieser Arbeit werden nun zunächst die jüngsten Entwicklungen auf diesem Gebiet zu einem breiten Überblick zusammengestellt, der auch einige der vorgeschlagenen Anwendungen wie Sensorik und optische Datenspeicherung umfasst. Darüber hinaus wird ein neu entdeckter photophysikalischer Effekt vorgestellt und bewertet, der die reversible Aktivierung von Phosphoreszenz in einem dünnen und transparenten Film ermöglicht. Da bei vielen organischen Emitttermaterialien die Nähe zu molekularem Sauerstoff zu einem vollständigen Verschwinden der Phosphoreszenz führt, kann diese Emission lokal durch Veränderung der Sauerstoffkonzentration beeinflusst werden. Eine sehr elegante, berührungslose Methode hierfür ist die zielgerichtete Bestrahlung

mit Licht verschiedener Wellenlängen. So kann Strahlung im nahen UV- oder im blauen Bereich eine chemische Reaktion des Sauerstoffs mit seiner Umgebung auslösen, die zu einer Abnahme der Sauerstoffmenge in den beleuchteten Bereichen führt. Durch eine zusätzlich aufgebrachte Barrierschicht kann kein frischer Sauerstoff in das System nachströmen, weshalb an den entsprechenden beleuchteten Stellen nach ausreichender Bestrahlung Phosphoreszenz sichtbar wird. Dadurch kann ein beliebiges lumineszentes Muster in die transparenten Schichten einprogrammiert und bei Bedarf ausgelesen werden. Durch die Beleuchtung mit Infrarotstrahlung hingegen wird die Temperatur und damit auch die Durchlässigkeit der Sauerstoffbarriere erhöht. So wird das System mit molekularem Sauerstoff wieder aufgefüllt und die Phosphoreszenz verschwindet. Daraufhin können erneut Bilder in die Folie geschrieben werden. Wenn nicht durch Bestrahlung mit entsprechendem Licht ausgelesen, ist das System völlig transparent und lässt das eingeschriebene Muster nicht erkennen. Dies ermöglicht die Herstellung von programmierbaren lumineszenten Etiketten, die mehrere Schreib-, Lese- und Löschzyklen ermöglichen und somit zur temporären Beschriftung in der Logistik oder zur unsichtbaren Dokumentensicherung eingesetzt werden können. Die Machbarkeit der genannten Anwendungen wird in der Arbeit durch die Herstellung funktionierender Prototypen aufgezeigt. Sowohl das Gesamtverfahren von Aktivierung und Deaktivierung als auch der Aufbau des Systems sind Teil von Patentanmeldungen.

Die im Rahmen dieser Arbeit erfolgte Charakterisierung weiterer organischer Emitter und Additive zeigt, dass der Effekt der schaltbaren Phosphoreszenz nicht auf eine bestimmte Materialkombination beschränkt ist, sondern ein sehr allgemeingültiges Verhalten darstellt. Deshalb werden Eigenschaften der Materialsysteme wie die Emissionsfarbe, der Kontrast der Muster oder die Empfindlichkeit gegenüber verschiedenen Lichtwellenlängen mit geeigneten Kombinationen optimiert. Um in Zukunft eine gezielte Entwicklung von organischen phosphoreszierenden Emitttern zu ermöglichen, werden die entscheidenden Anforderungen an die Materialien bezüglich ihres Einsatzes in programmierbaren Etiketten dargestellt. Abschließend werden potentielle weitere Entwicklungsrichtungen hin zu weiteren Anwendungen beschrieben, von denen eine bereits Gegenstand von erfolgreich eingeworbener Förderung durch das Bundesministerium für Bildung und Forschung ist. In dieser Folgestudie wird die Eignung der gefundenen Ergebnisse zur Messung von UV-Strahlung untersucht. Mit zwei weiteren eingereichten Anträgen, die auf den vorgestellten Entwicklungen auf-

bauen, eröffnen die Ergebnisse dieser Arbeit sowohl aus wissenschaftlicher als auch aus technischer Sicht ein breites Spektrum weiterer Forschungsarbeiten.

Contents

| | |
|--|------------|
| List of Publications | iii |
| Abstract | v |
| 1. Introduction | 1 |
| 2. Theory | 5 |
| 2.1. Fundamentals of Organic Materials | 5 |
| 2.1.1. Chemical Structure of Organic Materials | 5 |
| 2.1.2. Atomic Orbitals | 6 |
| 2.1.3. Hybridization | 8 |
| 2.1.4. Conjugation | 9 |
| 2.1.5. Energetics of Molecular Orbitals | 10 |
| 2.1.6. Singlet and Triplet Configuration | 11 |
| 2.1.7. Excitons | 13 |
| 2.1.8. Excitonic Energy Levels and States | 13 |
| 2.1.9. Donor and Acceptor Materials | 16 |
| 2.1.10. Charge-Transfer States | 16 |
| 2.1.11. Organic Polymers | 17 |
| 2.2. Interplay of Excited States and Photons | 21 |
| 2.2.1. The Franck-Condon Principle | 21 |
| 2.2.2. The Jablonski Diagram | 21 |
| 2.2.3. Absorption | 22 |
| 2.2.4. Fluorescence | 23 |
| 2.2.5. Intersystem Crossing | 26 |
| 2.2.6. Phosphorescence | 31 |
| 2.2.7. Charge-Transfer State Emission | 33 |
| 2.2.8. Energy Transfer Mechanisms | 34 |

—— Contents ——

| | | |
|-----------|--|-----------|
| 2.2.9. | Interaction of Multiple Excited States | 36 |
| 2.3. | Properties of Molecular Oxygen | 42 |
| 2.3.1. | Molecular Electronic Configuration of Oxygen | 42 |
| 2.3.2. | Oxygen-Induced Exciton Quenching | 44 |
| 2.3.3. | Decay Channels of Singlet Oxygen | 47 |
| 2.4. | Recent Progresses in Research on Organic Phosphorescence | 51 |
| 2.4.1. | Crystallization- and Aggregation-Based Emitters | 52 |
| 2.4.2. | Polymer-Based Emitters | 53 |
| 2.4.3. | Host-Guest Systems | 55 |
| 2.4.4. | Protection Against Oxygen Quenching | 58 |
| 2.4.5. | Stimuli-Responsive RTP Systems | 59 |
| 3. | Methods | 63 |
| 3.1. | Sample Preparation | 63 |
| 3.1.1. | Solution Preparation | 63 |
| 3.1.2. | Coating Techniques | 63 |
| 3.2. | Photoluminescence Spectroscopy | 64 |
| 3.2.1. | Time-Gated Spectra | 65 |
| 3.3. | Time-Resolved Measurements | 65 |
| 3.3.1. | Lifetime-Determination in the Millisecond Regime | 66 |
| 3.3.2. | Lifetime-Determination in the Micro- and Nanosecond Regime | 66 |
| 3.3.3. | Further Time-Resolved Techniques | 68 |
| 3.4. | Quantum-Yield Determination | 69 |
| 3.4.1. | Measurement Technique | 69 |
| 3.4.2. | Data Evaluation | 69 |
| 3.5. | Evaluation of Absorption | 70 |
| 3.5.1. | Absorbance and Transmission Measurements | 70 |
| 3.5.2. | Excitation-Scan Technique | 70 |
| 3.6. | Further Measurement Techniques | 71 |
| 3.6.1. | Determination of Film Thickness | 71 |
| 3.6.2. | Measurements at Low Temperature | 71 |
| 3.6.3. | Resolution Determination | 71 |
| 3.6.4. | Photograph Acquisition | 71 |

| | |
|--|------------|
| 4. Basic Principles of Programmable Luminescent Tags (PLTs) | 73 |
| 4.1. Activation - Removing of Molecular Oxygen | 75 |
| 4.1.1. Dynamics of Activation | 75 |
| 4.1.2. Writing Patterns | 80 |
| 4.2. Preservation - Keeping the Disequilibrium Stable | 83 |
| 4.2.1. Unintended Activation | 83 |
| 4.2.2. Storage Stability | 84 |
| 4.2.3. Moisture Protection | 87 |
| 4.3. Deactivation - Refilling with Molecular Oxygen | 88 |
| 4.4. Reactivation - Restarting the Cycle | 90 |
| 4.5. Discussion | 92 |
| 5. Characterization of Guest Materials | 97 |
| 5.1. Single-Guest Systems | 97 |
| 5.1.1. NPB - The Starting Material | 98 |
| 5.1.2. PhenDpa - Shifting to Visible Absorption | 102 |
| 5.1.3. HPhN and BF ₂ (HPhN) - A Different Approach | 105 |
| 5.1.4. 2-Hydroxycarbazole - Blue Phosphorescence | 107 |
| 5.1.5. Ir(MDQ) ₂ (acac) and PtOEP - The Old Hands | 108 |
| 5.1.6. BP and TA - The Components | 110 |
| 5.1.7. BP-2TA - The Workhorse | 111 |
| 5.2. Multi-Guest Systems | 118 |
| 5.2.1. NPB:DCJTB and BP-2TA:DBP - Towards Red PLTs | 118 |
| 5.2.2. PhenDpa:DBP - Delayed Emission Spanning the Full Visible Range | 120 |
| 5.2.3. NPB:DBBP - Improving P2F with Additives | 121 |
| 5.3. Overview and Summary | 125 |
| 6. Optimization via Diversification: PLTs with Various Material Systems | 127 |
| 6.1. Tuning the Important Parameters | 127 |
| 6.1.1. P2F: Simplifying the Readout Process | 127 |
| 6.1.2. τ_p : Ensuring Oxygen Quenching | 130 |
| 6.1.3. λ_{ex} : Extension of the Excitation Window | 132 |
| 6.1.4. D_{act} : Extending the Readout Timeframe | 134 |

—— Contents ——

| | |
|--|------------|
| 6.2. Substrates and Processing Techniques | 137 |
| 6.2.1. Substrate Diversity | 137 |
| 6.2.2. Additional Processing Techniques | 139 |
| 7. Conclusions and Outlook | 141 |
| 7.1. Conclusion | 141 |
| 7.2. Outlook | 143 |
| 7.2.1. SwiP and PLTs | 143 |
| 7.2.2. Further Application Pathways | 145 |
| 7.2.3. Widening the Scope | 146 |
| Appendix A. List of Abbreviations and Symbols | 149 |
| Appendix B. Beyond Science | 153 |
| Appendix C. Additional Data | 155 |
| Appendix D. Details on Setups | 159 |
| Bibliography | 161 |
| Acknowledgements | 195 |

1. Introduction

Although it may seem reasonable at first glance, the organic materials investigated in this thesis are not related to ecological food products in grocery stores. However, this does not prevent them from undergoing a similar accelerating growth of public interest in recent years. From a scientific point of view, the term *organic* refers to any materials which consist mainly of carbon and hydrogen atoms¹. Organic light-emitting diodes (OLEDs) are found in many smartphone displays², organic solar cells promise to harvest the sun's energy with flexible and semitransparent foils³, and organic electronics are said to enable clothes with integrated sensors and other appliances in a few years^{4;5}.

A further direction of research covers organic photoluminescent devices. These make use of fluorescence or phosphorescence, i.e. certain materials' emission of light after excitation with appropriate radiation. While fluorescence is a very fast process in the range of nanoseconds, inorganic phosphorescent emission ranges from microseconds⁶ to several hours⁷ and is known for its afterglow, which is widely used in watches or emergency exit signs⁸. The growing interest in its organic counterpart is visible in the increased number of publications in recent years. Here, the research field of *Room Temperature Phosphorescence* (RTP) showed a growth of more than 50% from 2018 to 2019.⁹ The growth for 2020 in comparison to 2019 was expected to exceed 70% before the COVID-19 pandemic has hit.

The term 'RTP' comprising the temperature evolved from the fact that, for many years, organic phosphorescence was known to occur at low temperature only^{10;11}. The reason for that is a very low radiative rate of the quantum-mechanically forbidden transitions involved in phosphorescence¹². In consequence, nonradiative quenching channels like molecular vibration or interaction with adjacent molecules deactivate the excited triplet state and phosphorescence is suppressed. However, by embedding heavy atoms into an organic molecule, it is possible to boost the efficiency of phosphorescence, and yields up to unity were reported¹³. The reason for this high efficiency

is the large spin-orbit coupling between the heavy nuclei and the charge carriers of the emitting units. Therefore, the electrons’ spin flip, which is required for the electronic transitions leading to phosphorescence, is promoted. For the same reason, the respective excited state lifetime is typically limited to the range of microseconds.

In line with the overarching aims of reducing the overall material costs, enabling organic phosphorescence at longer timescales, and driving the development of new applications, the main focus of RTP research today is the design of emitters for which no heavy metals are needed¹⁴. Due to the very low radiative rates of these compounds, a crucial requirement is the suppression of nonradiative decay channels by rigidification of the emitting systems. Here, a multitude of approaches can be found in literature, including crystallization^{15–18}, self-assembly^{19;20} or aggregation^{21–25}. However, a common drawback of these approaches is a high sensitivity on the morphology of the emitting material and the respective powdery shape, owning low applicability^{26;27}.

An approach which may overcome these limitations is the doping of single emitter molecules into an inert polymeric host as guest materials^{28–45}. In this case, the emitter must possess intrinsic RTP properties and the required rigidity has to be provided by the host material. Due to their straightforward morphologies, such material systems are reported to show good processability and allow the fabrication of thin transparent films, which can be applied to a multitude of different surfaces. Further, phosphorescent lifetimes in the range of milliseconds^{44;46} to a few seconds are reported^{30;47}.

Nevertheless, it still remains unclear where the RTP journey will go. On the one side, there are many proposals for applications, including imaging^{34;48–51}, sensing^{35;42;52}, anti-counterfeiting^{22;23;40;53} or data storage^{54;55}. On the other side, the majority of these publications focuses on the synthesis and characterization of new material systems, but does not go into detail on specific development pathways for the applications listed above.

This discrepancy contributes strongly to the central motivation for this thesis. Its main focus is not set on the design of further RTP molecules, but is mostly oriented on the exploitation of existing material. Here, a newly discovered photophysical effect plays the major role, whose discovery was the starting point of the work presented. In short, organic phosphorescent emission is strongly dependent on the presence and absence of oxygen surrounding the emitting molecules. By using targeted illumination, we were able to remotely control the concentration of oxygen inside of an organic layer. Therefore, we were able to selectively activate and deactivate phospho-



Figure 1.1.: A large-scale programmable luminescent tag, as developed in this thesis, showing a phosphorescent imprint in delayed afterglow emission.

rescence, and achieved spatially resolved phosphorescent patterns in fully transparent films. We call this effect *Switchable Phosphorescence* (SwiP) and name our material systems, due to the feasibility of multiple writing and erasing cycles, *Programmable Luminescent Tags* (PLTs). Figure 1.1 shows such a PLT during the readout process. The structure of this thesis will be as followed. In Chapter 2, basic principles and properties of organic materials will be introduced. Further, a detailed introduction into electronic states and interaction ways of molecular oxygen is given. After that, recent developments in the research field of RTP are summed up. Chapter 3 focuses on sample processing and measurement techniques. The basic principles of PLTs, including activation, preservation, and deactivation of phosphorescent patterns are described in Chapter 4. In order to broaden the variety of SwiP material systems, a detailed look into possible additional guest materials is given in Chapter 5. The optimization of PLTs regarding multiple properties is addressed in Chapter 6. Chapter 7 sums up the major results, draws a conclusion, and lists past and future development steps leading to photonic applications using PLTs. These include patent registrations, the acquisition of new funding, as well as projected commercialization pathways. In addition, further possible application scenarios of RTP and SwiP are introduced.

2. Theory

In this chapter, the basic theoretical background is set. After an introduction to organic materials and their electronic properties in Section 2.1, a deep insight into their different photophysical characteristics is given in Section 2.2. Molecular oxygen is introduced in detail in Section 2.3, since its interaction with excited states plays a major role in this thesis. In Section 2.4, recent developments in the field of organic room temperature phosphorescence are presented.

2.1. Fundamentals of Organic Materials

The widespread diversity of organic compounds is the reason for our existence as well as our prosperity. Any living being consists of these materials, including proteins, cellular components and hormones. Further, organic materials are present in any food, plastics, clothes, rubbers, and innovative electronic devices like organic light-emitting diodes or solar cells. The properties and structures of these materials are described in the field of organic chemistry, which will be more closely portrayed in the following paragraphs. These are mainly based on the given references^{1;56–59}.

2.1.1. Chemical Structure of Organic Materials

The basis of organic chemistry is the carbon atom. Due to its four valence electrons, it is able to form multiple covalent bonds with further carbon atoms. By that, a high number of different materials can be manufactured with high modularity, containing long carbon chains, rings or other shapes. The implementation of mainly oxygen, nitrogen or sulfur to the carbon backbone further increases the variety of possible combinations. Additionally, heavy atoms as platinum or bromine can also be involved in organic structures⁶⁰. Remaining free electrons form bonds to hydrogen atoms.

The most basic organic compound, consisting of one carbon atom surrounded by four hydrogen atoms, is methane (Figure 2.1 a) and well known as natural gas. Its chem-

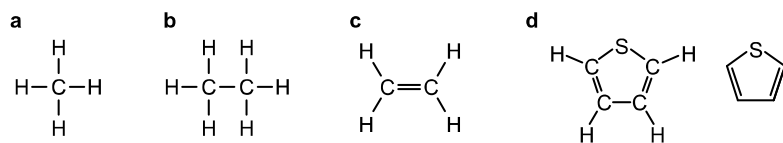


Figure 2.1.: **a** Methane. **b** Ethane. **c** Ethylene. **d** Different ways of presentation for tiophene.

ical formula is CH₄ and the inter-atomic bonds involve two valence electrons each, resulting in four so-called *single bonds*. This is visualized by single connection lines. Adding one carbon and two hydrogen atoms leads to ethane, or C₂H₆ (Figure 2.1 b). Here the connection of the two carbon units is also of single-bond nature. In contrast, the compound C₂H₄, ethylene (Figure 2.1 c), shows a *double bond* with two connection lines between the carbon atoms, representing the involvement of four valence electrons. In order to simplify the depiction of complex organic structures, the letters C and H are usually removed, and the carbon atoms are located at the vertices and ends of the drawn lines. Other letters are still shown, as for sulfur-containing tiophene, C₄H₄S (Figure 2.1 d). The latter is called a *heterocyclic* compound, containing non-carbon atoms, namely heteroatoms, in the ring structure.

The molecular mass is given in *dalton* (symbol u), with⁶¹

$$u = 1.66 \times 10^{-27} \text{ kg}. \quad (2.1)$$

For carbon, the atomic mass is $m_C \approx 12 u$, and typical small molecule weights are in the range of several hundred daltons.

2.1.2. Atomic Orbitals

For a better understanding of the organic materials' electronic properties, a deeper look into quantum mechanics is necessary. In order to gather information about the configuration of the carbon's four valence electrons, one has to solve their Schrödinger wave equation⁶²

$$H\psi = E\psi, \quad (2.2)$$

where ψ resembles the electrons' wave function. This solves the differential equation, with energetic eigenvalues E and the Hamiltonian H . If H contains a central sym-

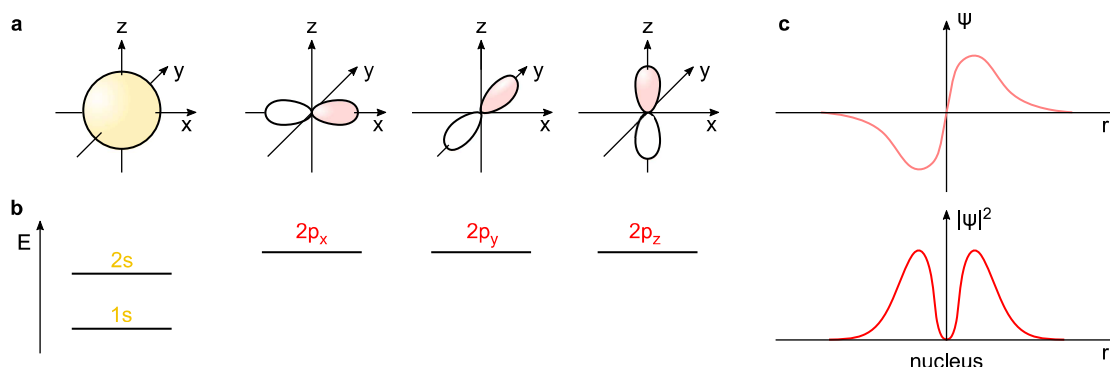


Figure 2.2.: **a** Shapes of the orbitals 1s and 2s (yellow), 2p_x, 2p_y and 2p_z (red). **b** Energies of the corresponding orbitals. **c** Wave function ψ and $|\psi|^2$, namely the probability density of 2p as a function of distance r to the nucleus. Figure is adapted from^{1;63} and slightly modified.

metric potential, the shape of ψ can be described by a radial component $R_{nl}(r)$ and an angular part $Y_{lm}(\Omega)$:

$$\psi(r, \Omega) = R_{nl}(r)Y_{lm}(\Omega). \quad (2.3)$$

$|\psi|^2$, the absolute square of this orbital wave function depicts the probability density of the electrons' positions influenced by a central Coulomb potential of a nucleus. The lowest energy orbital is called 1s, corresponding to the principal, azimuthal and magnetic quantum numbers $n = 0$, $l = 0$ and $m = 0$, followed by 2s with $n = 1$ and the rest unchanged. The subsequent 2p with $n = 1$, $l = 1$ and $m \in \{-1, 0, 1\}$ appear in three dumbbell-shaped orbitals pointing into different directions, leading to 2p_x, 2p_y and 2p_z. An illustration of these orbitals, their radial part and energies are shown in Figure 2.2. Note that the shown surfaces are no rigid borders but isosurfaces, within which the electrons' presence is equally likely. Here, positive sections of the wave functions are shaded, while for negative values the orbitals are sketched in white.

Any of these orbitals can be occupied by two electrons at maximum, which have to follow the Pauli exclusion principle and therefore differ in at least one quantum number. That means that since they share the same n , l and m , they have to differ in the fourth number, the spin quantum number $s = \pm\frac{1}{2}$. Its values are also referred to as *spin up* and *spin down*. The spin resembles an intrinsic quantum-mechanically angular momentum of the electron. Flipping the spin value therefore always requires an interplay with external parameters to ensure conservation of total angular momentum. Electrons with the same spin quantum numbers possess *parallel*

—— 2. Theory ——

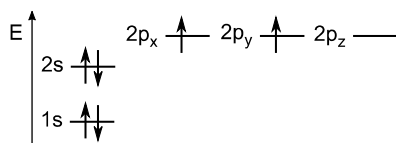


Figure 2.3.: Electronic configuration of a carbon atom. Note the electrons in $2p_x$ and $2p_y$ both possessing spin up. Figure is adapted from¹ and slightly modified.

spin, while different s values are described as *antiparallel*. When virtually filling electrons into the orbitals, one has to follow Hund's rule of maximum multiplicity, which states that before adding a second electron with antiparallel spin to an orbital, all other orbitals equivalent in energy have to be filled with one electron first, all of them with parallel spin.

Thus, the electron configuration of the carbon atom in the ground state can be written as $1s^2 2s^2 2p^2$ and be depicted as in Figure 2.3.

2.1.3. Hybridization

sp^3 -Hybridization

To explain the four equivalent covalent bonds in methane (cf. Figure 2.1 a), the simple picture of independent orbitals is not sufficient, since there are only three equivalent orbitals in the carbon atom. Here, the Valence Bond (VB) theory comes into play, suggesting the mixing of s - and p -orbitals. In methane and ethane, this *hybridization* involves one $2s$ and three $2p$ orbitals and results in four equivalent sp^3 *hybrid orbitals*, each pointing to one edge of a tetrahedron (Figure 2.4 a). These orbitals are also identical in energy, which leads to a balanced population with electrons all possessing parallel spin. In methane, the covalent bond to the hydrogen is formed by the overlap of the carbon's sp^3 orbitals and the hydrogen's $1s$ orbital. The C–C single bond in ethane arises from an overlap of two sp^3 orbitals, is called σ *bond* and is rotationally symmetric, enabling molecular twisting at this position.

sp^2 -Hybridization

Going to ethylene with only two hydrogens per carbon atom, the hybridization changes to an sp^2 *hybridization*, with three equivalent sp^2 orbitals flatly aligned and one unchanged p_z orbital perpendicular to this plane (Figure 2.4 b). Since all the

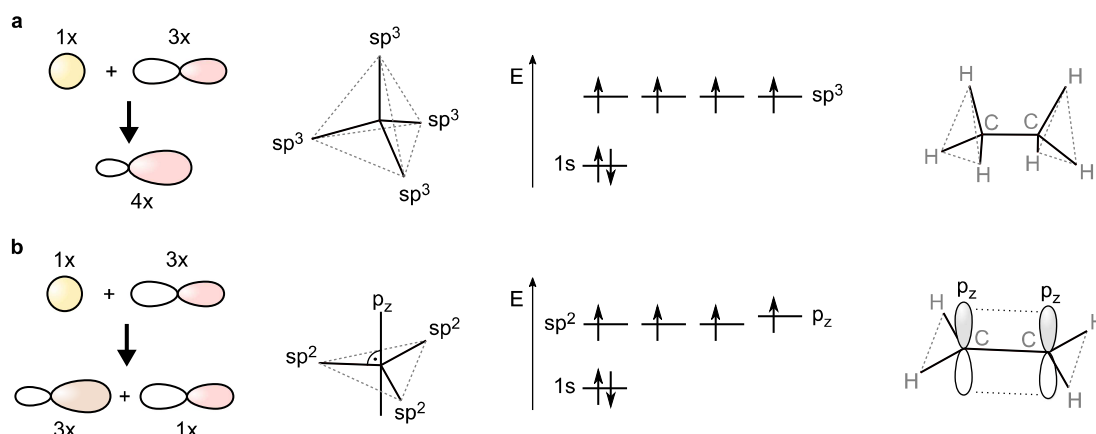


Figure 2.4.: **a** Orbital mixing, geometry and electronic configuration of the carbon's sp^3 hybridization in ethane. **b** Orbital mixing, geometry and electronic configuration of the carbon's sp^2 hybridization in ethylene. Figure is partly adapted from¹.

hydrogen atoms get bound via sp^2 orbitals, the parallel oriented p_z orbitals of both carbons, occupied by one electron each, are available for further C–C bonding. This bond is named a π bond, which completes the existing σ bond to a C=C double bond. Molecular twisting at this position is therefore prevented. Compared to the σ bonds, the π electrons' bonding is rather weak, leading to electronic excitation energies matching to photon energies of infrared (IR), visible or ultraviolet (UV) light. This enables efficient light-matter interaction and is the key property of organic photoactive materials.

2.1.4. Conjugation

An organic structure forming alternating sequences of single and double bonds next to each other is named *conjugated*. That is due to the fact that the parallel p_z orbitals of the atoms overlap with both neighbors. This leads to one extended conjugated electronic orbital, showing a uniformly distributed spatial probability density over the whole system. Here, a well known example is benzene, constituted of six hydrogen and six carbon atoms, where the latter are fully conjugated (Figure 2.5). If not interrupted by electronic or geometric influences like rotation, such conjugated systems may spread over more than 100 single atoms⁶⁴. A distinct conjugated section is referred to as a *chromophore*. Small organic molecules may hold one or several chromophores, depending on their molecular shape.

—— 2. Theory ——

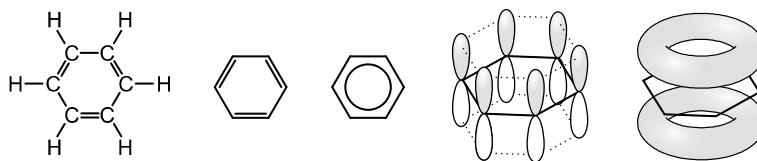


Figure 2.5.: Benzene as an example of a conjugated molecular system, possessing a ring-shaped delocalized electron system. All depictions are equivalent.

Like in the particle-in-a-box model, the energy eigenvalues of the electron wave functions are reciprocal to the extent of the system. It is possible to tune the material's optical properties via altering their conjugation length (Figure 2.6). While benzene, as a single cyclic unit, shows absorption at 254 nm (4.9 eV), anthracene with three cyclic units is redshifted to 375 nm (3.3 eV) and pentacene with five cycles to 582 nm (2.1 eV).

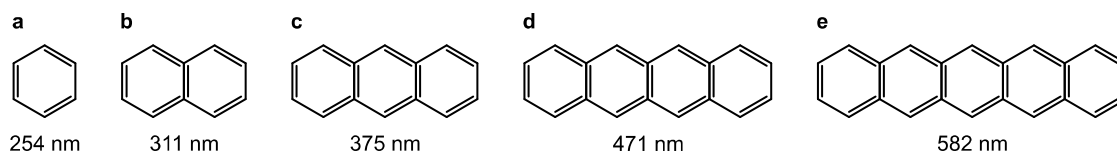


Figure 2.6.: Conjugated molecules with respective peak absorption wavelengths. **a** Benzene. **b** Naphthalene. **c** Anthracene. **d** Tetracene. **e** Pentacene.

2.1.5. Energetics of Molecular Orbitals

Going back to a single benzene molecule, one can find six different atomic p_z orbital configurations respective to their individual signs, all of them forming different conjugated molecular orbitals ψ with varying electron-binding-energy configurations (Figure 2.7). The six p_z electrons of benzene fill these orbitals in an ascending order in energy, resulting in three orbitals filled with two electrons each, namely the so-called *bonding* orbitals ψ . The remaining orbitals are not occupied by electrons and are therefore referred to as *antibonding* orbitals ψ^* . The highest occupied molecular orbital (HOMO) and the lowest unoccupied molecular orbital (LUMO) represent the organic counterparts to the valence and conduction bands in inorganic semiconductors and are mainly responsible for the optical properties of the material.

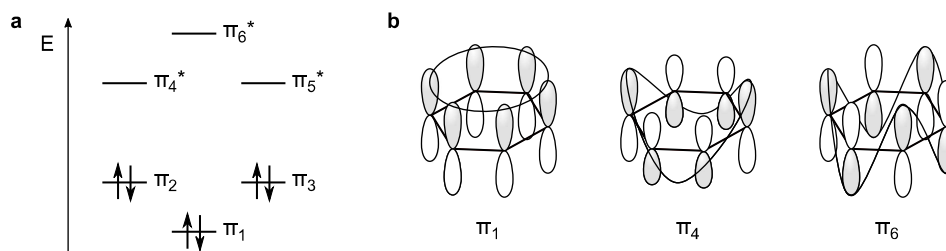


Figure 2.7.: **a** Electronic configuration of the molecular ψ orbitals of benzene. **b** Molecular orbitals ψ_1 , ψ_4 and ψ_6 as results from an overlap of p_z orbital with varying orientation. Figure is partly adapted from⁶³.

Again, the Schrödinger wave equation is set up to

$$H\psi_M = E\psi_M, \quad (2.4)$$

where ψ_M is the molecular wave function. A mathematical description of molecular orbitals can be realized by using the Born-Oppenheimer approximation. It states that any electronic motion in orbitals is much faster than vibrational motions of the molecule's nuclei. In consequence, the molecular wave function can be split into three parts: vibrational χ and electronic motions ψ as well as spin \mathbf{S} , each treated independently⁶²:

$$\psi_M = \chi\psi\mathbf{S}. \quad (2.5)$$

This zero-order approximation does not involve interactions like vibronic coupling or spin-orbit coupling, which will be discussed later.

In heterocyclic structures, as in thiophene (cf. Figure 2.1 d), an additional non-bonding n orbital may arise resulting from the heteroatom's electronic configuration.

2.1.6. Singlet and Triplet Configuration

Considering two coupled electrons, labeled α and β , with both having spin

$$s_{\alpha,\beta} = \frac{1}{2}, \quad (2.6)$$

as present in organic photochemistry, their respective total spin S is either

$$S = s_\alpha - s_\beta = 0 \quad (2.7)$$

—— 2. Theory ——

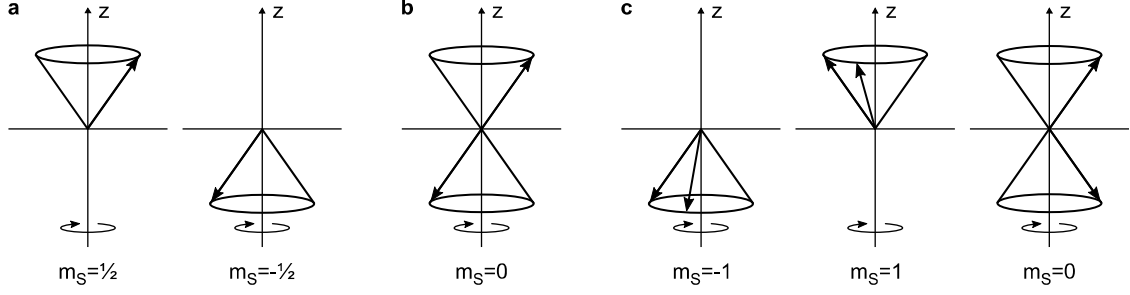


Figure 2.8.: **a** Cones of orientation for single electrons with $S = s_\alpha = \frac{1}{2}$, $M = 2$ and $m_S \in \{-\frac{1}{2} \dots \frac{1}{2}\}$. **b** Cone of orientation for two coupled electrons in the singlet state with $S = 0$, $M = 1$ and $m_S = 0$. **c** Cones of orientation for two coupled electrons in the triplet state with $S = 1$, $M = 3$ and $m_S \in \{-1, 0, 1\}$. Figure is adapted from⁶².

or

$$S = s_\alpha + s_\beta = 1. \quad (2.8)$$

This leads to a spin multiplicity M of either

$$M = (2S + 1) = 1 \quad (2.9)$$

or

$$M = (2S + 1) = 3, \quad (2.10)$$

which therefore can be assigned to a *singlet state* ($M = 1$) or a *triplet state* ($M = 3$)⁶². In order to visualize these spin configurations, a vector model can be introduced (Figure 2.8), where the spin multiplicity is the total number of possible projections of the rotating total spin vector S onto the rotational z axis, namely the magnetic spin quantum numbers $m_S \in \{-S \dots S\}$. In the case of triplets, it includes $m_S = -1$ ($\downarrow\downarrow$), $m_S = 0$ ($\uparrow\downarrow$) and $m_S = 1$ ($\uparrow\uparrow$).

For clarity, the notation will be simplified to $\uparrow\downarrow$ for singlet and $\uparrow\uparrow$ for triplet states, as shown in Figure 2.9. In the absence of external magnetic or electric fields, the three triplet configurations are degenerate and on the same energy level.

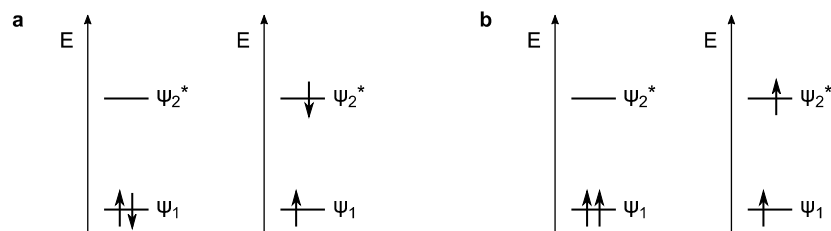


Figure 2.9.: **a** Simplified notation for ground and excited singlet states and **b** for ground and excited triplet states.

2.1.7. Excitons

An *exciton* is a quasiparticle consisting of a negatively charged electron and a positively charged hole that are bound via Coulomb interaction. In organic materials, this electron-hole pair consists of an electron in the HOMO or LUMO and a hole in the HOMO. The latter represents the absence of an electron. Due to the typically low dielectric constant of $\epsilon_r = 3\ldots 4$ and the small molecular dimensions of organics, here the Coulomb binding energy can reach values up to $E_B = 1.5\text{ eV}$, which causes a strong bonding of the exciton to the molecule^{65;66}. These so called *Frenkel excitons* are in contrast to *Wannier-Mott excitons*, which show weak electrostatic binding and large charge separation and can be found mostly in inorganic semiconductors with high $\epsilon_r > 10$.⁶⁷

2.1.8. Excitonic Energy Levels and States

Ground State

The basic state of an exciton is the *ground state*. In ordinary organic molecules, this depicts the electron and hole both in the HOMO and no electron in the LUMO⁶². Following the Pauli exclusion principle, two coupled HOMO electrons thus differ in the spin quantum number, resulting in antiparallel spins with $S_S = 0$, leading to a *singlet ground state* S_0 . The energy of the ground states is by definition⁶²

$$E_0 = 0. \quad (2.11)$$

Excited States

An excited exciton consists of an electron in the LUMO or higher and a hole in the HOMO. Despite being located in a different orbital, the LUMO electron still is coupled to the residual HOMO electron, leading to either an *excited singlet state* S_n (for $M = 1$) or an *excited triplet state* T_n (for $M = 3$)⁶². The subscript n indexes different energetic levels of the excited states, starting at $n = 1$. In photophysics, S_0 , S_1 and T_1 are the most relevant excitonic states (cf. Section 2.2). The geometry of the molecule in the excited state can differ from its ground state conformation.

The involvement of π - or non-bonding orbitals can also be implemented into the notation of excited states. In ethylene (cf. Figure 2.1 c), the S_0 state is denoted as (π^2) , while the first excited states are $^1(\pi, \pi^*)$ for S_1 and $^3(\pi, \pi^*)$ for T_1 , where the LUMO is asterisked. In contrast, in formaldehyde ($\text{CH}_2=\text{O}$), the oxygen's non-bonding orbital is involved, leading to $^1(n, \pi^*)$ for S_1 and $^3(n, \pi^*)$ for T_1 . Exemplary, these orbital configurations are sketched for S_1 states in Figure 2.10 a.

The strict separation of (n, π^*) and (π, π^*) states, however, is perturbed when going to first order approximation. Due to electron-electron interactions and molecular vibrations, these states may be mixed. The *vibronic mixing* is caused by non-planar vibrations, since they can enhance the overlap integral of the molecule's orbitals⁶². Such mixing enables electrons to switch between the n and π orbitals permanently. The change in electronic configuration may lead to an energetic rearrangement of the orbitals, as depicted in Figure 2.10 b, and a mixing of (n, π^*) and (π, π^*) states.

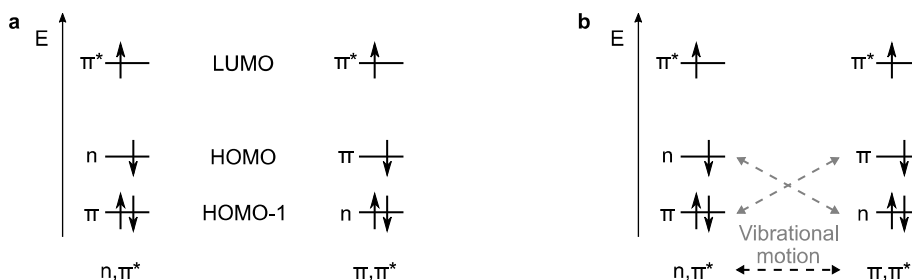


Figure 2.10.: **a** Exemplary occupation of orbitals in $^1(n, \pi^*)$ and $^1(\pi, \pi^*)$ S_1 states. **b** Vibronic mixing and switching of $^1(n, \pi^*)$ and $^1(\pi, \pi^*)$ S_1 states. Figures are partly adapted from⁶².

Singlet-Triplet Splitting

The energy of an excited state, e.g. (n, π^*) , can be approximated as a combination of three parts. The first one is the zero-order energy $E_{\text{zo}}(n, \pi^*) > 0$ of one single electron moving in a fixed nuclear framework. The second part $K(n, \pi^*) > 0$ is a first order Coulombic correction resulting from electron-electron interaction in the molecule. The third one $J(n, \pi^*) > 0$ results from a first order quantum mechanical correction involving different spin configurations. According to the Pauli principle, the convergence of two electrons with identical spin numbers is prevented in comparison to electrons with opposite spin orientation. This leads to an increased average distance between electrons with parallel spin $\uparrow\uparrow$ (as present in the triplet configuration), and therefore to an effective negative coulombic repulsion $-J(n, \pi^*)$. Opposite spin orientation $\uparrow\downarrow$ (as found in singlet states) decreases the average distance and therefore increases the repulsion $J(n, \pi^*)$. In total, one can deduce⁶²

$$E_S = E_{\text{zo}}(n, \pi^*) + K(n, \pi^*) + J(n, \pi^*) \quad (2.12)$$

$$E_T = E_{\text{zo}}(n, \pi^*) + K(n, \pi^*) - J(n, \pi^*) \quad (2.13)$$

for the S_1 and T_1 energies (Figure 2.11). Here it is noteworthy that for the same electronic configuration in an organic molecule, E_T is always lower than E_S , since the *singlet-triplet splitting*

$$\Delta E_{\text{ST}} = E_S - E_T = 2J(n, \pi^*) > 0 \quad (2.14)$$

is always positive. This accounts for (n, π^*) as well as (π, π^*) states. Since the overlap of two π orbitals is generally larger than an n - π -overlap, the Pauli repulsion represented in $J(\pi, \pi^*)$ is also stronger than in $J(n, \pi^*)$ configuration. As a consequence,

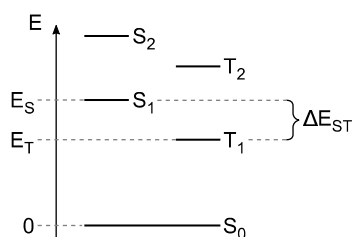


Figure 2.11.: Energetically lowest singlet and triplet states in organic molecules. Figure is partly adapted from⁶⁸.

the singlet-triplet splitting can be reduced in heterocyclic compounds possessing an n orbital⁶²:

$$\Delta E_{\text{ST}}(n, \pi^*) < \Delta E_{\text{ST}}(\pi, \pi^*) \quad (2.15)$$

2.1.9. Donor and Acceptor Materials

The energy, which is released while attaching an additional electron to a neutral molecule, is called *electron affinity* E_{A} ⁶⁹. Organic molecules possessing a high electron affinity therefore favor the uptake of an electron and are called *electron acceptors*, while low E_{A} materials are named *electron donors*⁶⁶. In Figure 2.12, different organic donor and acceptor materials are depicted.

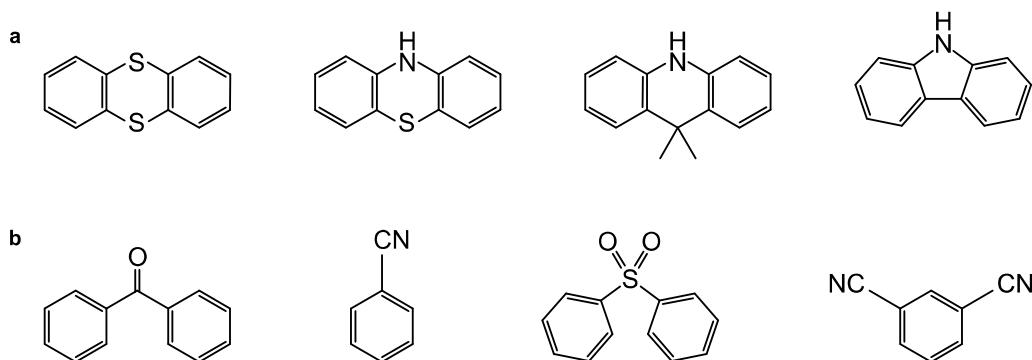


Figure 2.12.: **a** Different donor materials (from left to right): thianthrene, phenothiazine, 9,9-dimethyl-9,10-dihydroacridine and carbazole. **b** Different acceptor materials (from left to right): benzophenone, benzonitrile, diphenylsulfone and 1,3-dicyanobenzene. Structures are adapted from^{70;71}.

2.1.10. Charge-Transfer States

Neighboring chromophores, located on two adjacent molecules or implemented in one single molecular species, may show overlap of their respective orbitals. In the presence of both donor D and acceptor A compounds, an excited state, D^* or A^* , may lead to a *charge-transfer* (CT) from the donor's LUMO (for D^*) or HOMO (for A^*) to the acceptor's LUMO or HOMO, respectively (Figure 2.13)⁶².

A CT state within a single molecule is referred to as intramolecular charge-transfer (ICT) state. Resulting from this electron exchange, the exciton's dipole moment increases and the conformation of the involved molecules or molecular moieties can significantly change⁷². For twisted intramolecular charge-transfer (TICT) states, the

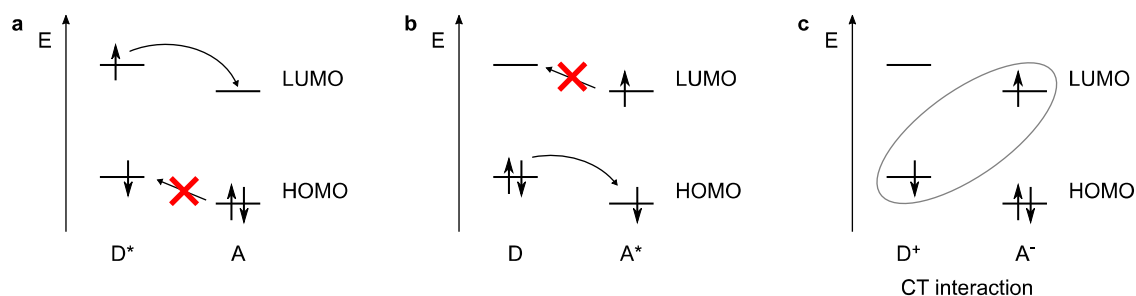


Figure 2.13.: **a** Energetically favored electron transfer from the LUMO of the excited donor D^* to the LUMO of the ground state acceptor A . **b** Energetically favoured electron transfer from the HOMO of the ground state donor D to the HOMO of the excited state acceptor A^* . **c** Resulting charge-transfer (CT) state. Figure is partly adapted from⁶².

D and A moieties can show a twist of 90° in respect to each other at the connecting single bond (Figure 2.14)^{73;74}. Further, the CT state's excited state energy can be sensitive to environmental parameters like the local dielectric constants, known as *solvatochromism* (cf. Section 2.2.7)⁷⁵.

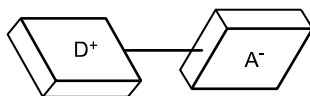


Figure 2.14.: Twisted conformation between a positively charged donor and a negatively charged acceptor moiety of a molecule in the TICT excited state. Figure is partly adapted from⁷².

2.1.11. Organic Polymers

In this work, polymers serve either as *host polymers*, in which guest materials are doped at low concentration, or as *oxygen barrier polymers*, which are realized as an additional protection layer to prevent the diffusion of ambient oxygen into the emitting host-guest structure. The requirements to the first are solubility in suitable solvents (cf. Section 3.1) and rigidification of the emitter to suppress nonradiative decay channels (cf. Section 2.2.6). The most important feature of the second is a highly reduced oxygen transmission rate (OTR), which will be discussed in the following.

Chemical Structure

Organic polymers consist of similar materials as small organic luminophores, e.g. carbon, hydrogen or oxygen. The difference to them is the much higher number of atoms forming one unit, why polymers are also referred to as macro molecules¹. In homopolymers, every of these units consists of a number of n repetitions of the same monomer structure. For example, poly(methyl methacrylate) (PMMA), Figure 2.15 b) is a repetitive concatenation of methyl methacrylate⁷⁶. The same accounts for polystyrene (PS, Figure 2.15 d) and styrene.

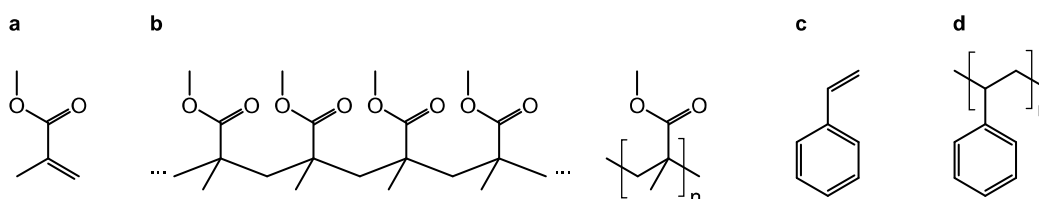


Figure 2.15.: **a** Methyl methacrylate. **b** Two different illustrations of poly(methyl methacrylate). **c** Styrene. **d** Polystyrene.

The number n , and therefore the molecular weight M_W , may be highly diverse for the same polymer. For example, PMMA is available ranging from $M_W = 10^3$ u to $M_W \geq 10^6$ u.⁷⁷ Note that even in a singular batch there usually is a statistical distribution (Figure 2.16) in M_W due to random stopping of chain forming during polymerization⁷⁶. Narrow distributions are available, but difficult to fabricate and therefore more expensive⁷⁸.

A common notation is the abbreviation of the polymer followed by the average molecular weight \overline{M}_W , e.g. PMMA550k for PMMA with $\overline{M}_W = 5.5 \times 10^5$ u. However, the exact distribution is not visible that way.

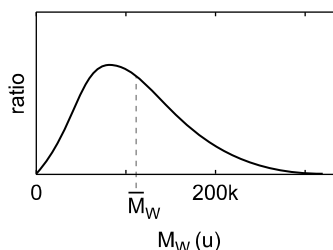


Figure 2.16.: A typical distribution of molecular weight in a polymer batch, including an average weight \overline{M}_W . Figure adapted from¹.

Optical Properties

Non-conjugated polymers like PS or PMMA are transparent and do not show absorption of light above $\lambda = 300$ nm.⁷⁹ Their refractive index typically ranges from $n = 1.4$ to $n = 1.6$.⁸⁰ Detailed values for some polymers are given in Table 2.1.

Table 2.1.: Refractive indices n for different polymers for different wavelengths. Adapted from^{80;81}.

| Polymer | Abbreviation | n (437 nm) | n (633 nm) |
|---------------------------|--------------|--------------|--------------|
| Poly(vinyl alcohol) | PVA | — | 1.47 |
| Polystyrene | PS | 1.61 | 1.59 |
| Poly(methyl methacrylate) | PMMA | 1.50 | 1.49 |

Oxygen Permeability

Since oxygen can have a large impact on photophysical processes of organic emitters (cf. Section 2.3.2), its mobility in organic host and barrier polymers is an important parameter. As already stated, the *oxygen permeability* of a polymer can be addressed using the OTR, which describes the amount of oxygen and its penetration depth for a certain area, time and pressure gradient. One of its common units is⁸²:

$$[\text{OTR}] = \frac{\text{cm}^3 \cdot \text{mm}}{\text{m}^2 \cdot 24 \text{ h} \cdot \text{atm}} \quad (2.16)$$

$$(2.17)$$

In Table 2.2, some values for different polymers are shown.

Table 2.2.: Oxygen transmission rates (OTR) of different polymers. EVOH and Exceval are measured at a relative humidity of 60% RH. For the rest, no information is given.

| Polymer | Abbreviation | OTR $\left(\frac{\text{cm}^3 \cdot \text{mm}}{\text{m}^2 \cdot 24 \text{ h} \cdot \text{atm}} \right)$ |
|---|--------------|---|
| Polystyrene | PS | 100 . . . 160 ^{83–85} |
| Poly(lactic acid) | PLA | 3.5 . . . 60 ^{84;86} |
| Poly(methyl methacrylate) | PMMA | 4.8 ⁸⁵ |
| Poly(ethylene terephthalate) | PET | 1 . . . 5 ^{83–87} |
| Ethylene vinyl alcohol (44 mol% ethylene) | EVOH-44 | 0.04 ⁸⁷ |
| Ethylene vinyl alcohol (32 mol% ethylene) | EVOH-32 | 0.01 ⁸⁷ |
| Poly(vinyl alcohol) | PVOH, PVA | 0.02 ⁸⁴ |
| Polyacrylonitrile | PAN | 0.013 ⁸³ |
| Exceval AQ-4104 | Exceval | < 0.002 ⁸⁸ |

2.2. Interplay of Excited States and Photons

This section depicts the interaction of photons and excited states in organic molecules.

2.2.1. The Franck-Condon Principle

The observable transition rate k_{obs} from an initial $\psi_{\text{M},1}$ to a final excited state $\psi_{\text{M},2}$ is described via⁶²

$$k_{\text{obs}} \propto \frac{\langle \psi_1 | H_{\text{e}} | \psi_2 \rangle^2}{\Delta E^2} \times \frac{\langle \psi_{\text{M},1} | H_{\text{so}} | \psi_{\text{M},2} \rangle^2}{\Delta E^2} \times \langle \chi_1 | \chi_2 \rangle^2, \quad (2.18)$$

with the transition matrix elements for orbital H_{e} and spin-orbit interactions H_{so} , the energy gap ΔE between $\psi_{\text{M},1}$ and $\psi_{\text{M},2}$ and the *Franck-Condon-Factor* $\langle \chi_1 | \chi_2 \rangle^2$. As already stated in Section 2.1.5, the vibrational χ and electronic ψ motion parts of the molecular wave function ψ_{M} can be treated independently due to their different time scales. The fast electronic motions in the orbital outcompete the vibrational ones by several orders of magnitude. Therefore, during an electronic transition from χ_1 to χ_2 , the molecule cannot rearrange its shape. According to the *Franck-Condon principle*, the most favored transitions of the electrons from state χ_1 to χ_2 therefore are comprised by configurations with similar vibrational wave functions. This bears maximal overlap between the initial $\psi_{\text{M},1}$ and the final $\psi_{\text{M},2}$ state.

Differences in the molecular geometry for ψ_{M} and ψ_{M}^* , as depicted in Section 2.1.8, lead to a relative displacement of the orbitals' potential energy curves (Figure 2.17 a). In consequence, the electronic transitions from different vibronic sublevels of S_0 to levels of S_1 show diverse probabilities. Particularly, the transition between the vibronic ground states ($v = 0 \rightarrow v^* = 0$) is usually suppressed in comparison to other transitions ($\Delta v \neq 0$, like $v = 0 \rightarrow v^* = 1$ or $v = 0 \rightarrow v^* = 2$)⁶².

2.2.2. The Jablonski Diagram

Reducing the sketches of the potential energy curves from Figure 2.17 a to only the energy dimension enables the illustration of a complex energetic scheme of multiple states, namely the Jablonski diagram (Figure 2.17 b). Here, absorption, fluorescence, intersystem crossing, phosphorescence, and additional nonradiative pathways between vibronic sublevels of excited states of different spin multiplicities are depicted in detail. In the following sections, a closer look into these transitions is provided.

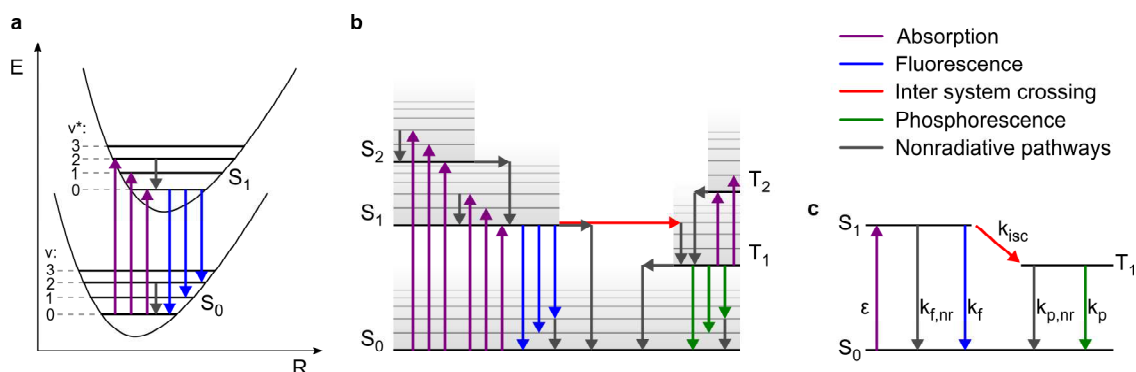


Figure 2.17.: **a** Potential energy curves of S_0 and S_1 with respect to the molecular coordinate R , including radiative (color) and nonradiative (grey) transitions between different vibrational sublevels of S_0 and S_1 . **b** Jablonski diagram including different S and T states and their vibronic sublevels, as well as transitions inbetween. **c** Reduced Jablonski diagram showing all relevant transitions in a single organic luminophore, including absorption to S_1 , fluorescence, intersystem crossing, phosphorescence and nonradiative pathways. Figure is partly adapted from^{62;67;75}.

2.2.3. Absorption

Macroscopically, the absorption spectrum of organic materials is defined by Lambert's and Beer's laws. Lambert's law describes the independence of absorption from the initial light intensity I_0 , Beer's law the linear relation of the number of absorbing molecules and the absorbed light. For very intense irradiation or high luminophore concentrations, however, the laws are no longer valid.

A measure for the absorption is the *optical density* OD, given by⁶²

$$\text{OD} = \log \frac{I_0}{I_t}, \quad (2.19)$$

where $\frac{I_0}{I_t}$ is the ratio of incident to transmitted light.

On a molecular scale, absorption resembles the excitation of the exciton from the lowest vibrational level of the ground state S_0 to a vibronic sublevel of an excited state (S_1 or higher), as shown in Figure 2.18. Here, the molecular extinction coefficient ϵ plays a major role, defined as⁶²

$$\epsilon = \left(\log \frac{I_0}{I_t} \right) lC, \quad (2.20)$$

with the optical path length l and the absorbing material's concentration C . This value is an intrinsic material property, ranging up to⁷⁵ $\epsilon = 10^5 \dots 10^6 \text{ mol}^{-1}\text{cm}^{-1}$ and

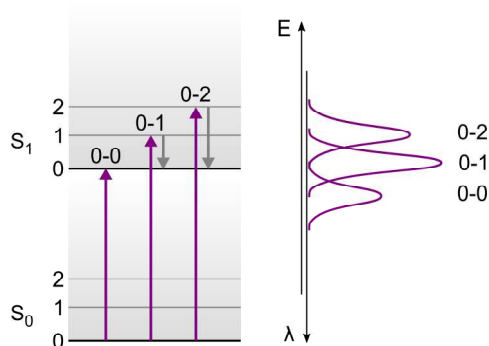


Figure 2.18.: Absorption of light from the lowest vibrational level of S_0 to different vibronic levels of S_1 , and respective absorption peaks in light energy E and wavelength λ .

is related to the theoretical oscillator strength f via the integration of ε over the photon's energy E ⁶²

$$f \propto \int \varepsilon dE. \quad (2.21)$$

If the latter fits to an absorption peak of the chromophore, incident light can be absorbed. The light's energy is calculated via⁸⁹

$$E = \frac{hc}{\lambda}, \quad (2.22)$$

with the speed of light c , the Planck constant h and the light's wavelength λ .

A further possible but weak absorption channel is the spin-allowed transition from the excited T_1 to a higher lying T_n state, namely *triplet absorption*⁹⁰.

2.2.4. Fluorescence

After excitation, the luminophore quickly ($t_{\text{relaxation}} \approx 10^{-12}$ s) relaxes to the lowest vibrational state of the excited state S_1 due to nonradiative energy losses. Therefore, the fluorescent emission usually is independent of the excitation wavelength and always originates from this lowest vibrational state⁷⁵, referred to as *Kasha's rule*. However, due to the radiative relaxation down to different vibronic levels of the ground state S_0 , several fluorescent peaks are present (Figure 2.19). As a consequence, the fluorescent emission is always lower in energy and therefore redshifted compared to the absorption, which is known as *Stokes shift*. It is noteworthy that the $0 - 0$ transition usually is, according to the Franck-Condon principle (cf. Sec-

2. Theory

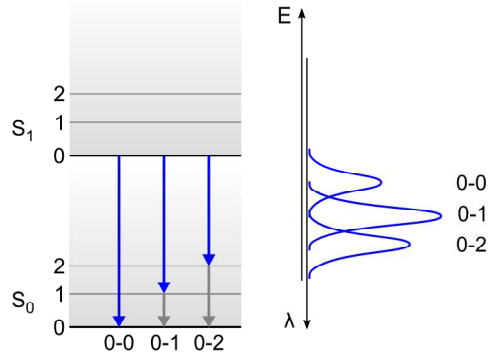


Figure 2.19.: Fluorescence resulting from the chromophore's energetic relaxation from the lowest vibrational level of S_1 to different vibronic levels of S_0 , and respective fluorescence peaks in energy E and wavelength λ of light.

tion 2.2.1), not the dominating one. Further, due to spectral broadening caused by the environment, the emission peaks may be smeared out and therefore form one broad emission spectrum⁶².

The radiative rate k_f of the fluorescence is connected to the oscillator strength f via⁶².

$$k_f \propto \bar{\nu}_0^2 f \quad (2.23)$$

where $\bar{\nu}_0$ is the wavenumber corresponding to the maximum wavelength of absorption.

With this rate, two important characteristics of fluorescent emission can be defined. The first one is the *fluorescence lifetime*: τ_f ⁷⁵

$$\tau_f = \frac{1}{k_f + \sum k_{nr,f}}, \quad (2.24)$$

where $\sum k_{nr,f}$ is the sum of all nonradiative decay rates, which may be intrinsic or externally originated. The intrinsic nonradiative decay rates of the S_1 singlet state consist of the internal conversion channels described by $k_{nr,f}$ and the intersystem crossing to the triplet state, described by the rate k_{isc} , which will be discussed in Section 2.2.5. This results in an intrinsic lifetime $\tau_{f,0}$ of

$$\tau_{f,0} = \frac{1}{k_f + k_{nr,f} + k_{isc}}. \quad (2.25)$$

The lifetime of an excited state is a measure for the average duration until the exciton decays to the ground state. It is implemented in an exponential decay law⁷⁵

$$I(t) = I_0 \exp\left(-\frac{t}{\tau_f}\right), \quad (2.26)$$

where $I(t)$ is the emission intensity after a certain time t , and I_0 is the initial intensity. Note that this law only accounts for an ensemble of multiple identical chromophores. For single emitting units, a decay of intensity cannot be given, since there is only one possible photon emission. Here, the lifetime describes the expected duration of the exciton remaining excited.

For multiple chromophores with slightly different ambiances, the single chromophore's lifetimes can alter, leading to a multi-exponential intensity decay

$$I(t) = I_0 \sum_i a_i \exp\left(-\frac{t}{\tau_{f,i}}\right), \quad (2.27)$$

with different shares a_i . Typical values for τ_f range from below 1 ns to > 10 ns.⁶²

The second important property is the fluorescence quantum yield Φ_f , which is defined as the ratio of the fluorescent photons $N_{\text{em},f}$ to the absorbed photons N_{abs} and can also be written as⁷⁵

$$\Phi_f = \frac{N_{\text{em},f}}{N_{\text{abs}}} = \frac{k_f}{k_f + \sum k_{\text{nr},f}}, \quad (2.28)$$

where again k_f is the radiative rate of the fluorescence and $\sum k_{\text{nr},f}$ is the sum of all nonradiative decay rates. This value ranges from 0 to close to 1.

The rate equation describes the change of the occupation of singlet states $[S_1]$ of multiple emitters^{91;92}:

$$\frac{d[S_1]}{dt} = G - (k_f + k_{\text{nr},f} + k_{\text{isc}}) [S_1], \quad (2.29)$$

with an absorption-dependent generation term G . The solution of this differential equation results in the exponential decay as noted above.

2.2.5. Intersystem Crossing

Intersystem crossing (ISC) describes the spin flip of an electron in an exciton during the transition e.g. from an excited singlet state S_1 to the excited triplet state T_1 (cf. Figure 2.17 b and c)⁷⁵. Due to the conservation of angular and spin momentum, this transition is quantum-mechanically forbidden in zero-order approximation⁹³.

Nevertheless, there are ways to overcome this limitation, of which *spin-orbit coupling* (SOC) is the most significant mechanism⁶². Here, the spin flip of the electron is made possible by a momentum conserving exchange interaction involving a change in the orbital occupation, described by the spin-orbit coupling operator H_{SOC} ⁶²

$$H_{\text{SOC}} \propto \xi_{\text{SOC}} \mu_{\text{S}} \mu_{\text{L}}, \quad (2.30)$$

with the spin-orbit coupling constant ξ_{SOC} and the magnetic moments due to the electron's spin (μ_{S}) and orbital (μ_{L}) momentum.

As already mentioned in Chapter 2.2.4, one can define the intersystem crossing rate k_{isc} as part of $\sum k_{\text{nr},}$, and the yield Φ_{isc} . The latter is

$$\Phi_{\text{isc}} = \frac{k_{\text{isc}}}{k_{\text{f}} + \sum k_{\text{nr},f}}, \quad (2.31)$$

or without external quenchers

$$\Phi_{\text{isc}} = \frac{k_{\text{isc}}}{k_{\text{f}} + k_{\text{nr},f} + k_{\text{isc}}}, \quad (2.32)$$

and is a measure for the amount of generated triplet T_1 excitons.

Spin-Orbit Coupling via the Heavy-Atom Effect

In molecules containing *heavy atoms* like bromine ($Z = 35$), iridium ($Z = 77$), or platinum ($Z = 78$) (Figure 2.20), the orbital magnetic moment μ_{L} of an electron, and therefore the spin-orbit coupling H_{SOC} is increased. This is due to the electron's intense acceleration caused by the electrostatic attraction of the strongly positively charged nucleus⁶².

The strength of heavy-atom induced spin-orbit coupling is proportional to Z^4 . The increase in k_{isc} and Φ_{isc} can outcompete k_{f} and Φ_{f} , leading to a total vanishing of fluorescence in favor of phosphorescence, which will be discussed in Section 2.2.6. The heavy-atom effect is utilized in phosphorescent organic light emitting diodes

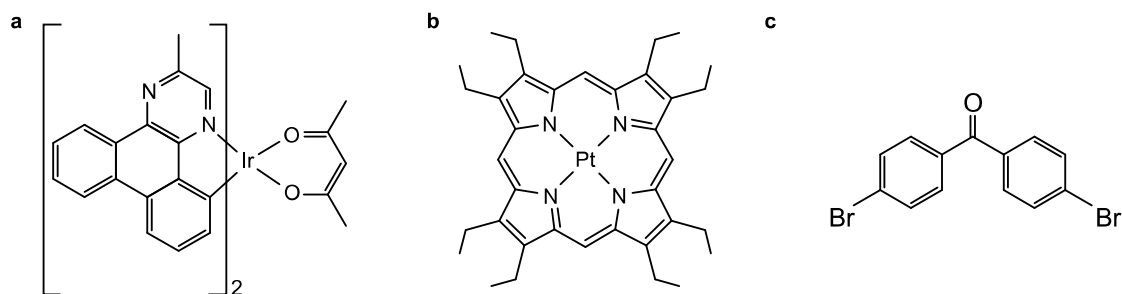


Figure 2.20.: Different organic heavy atom compounds. **a** Bis(2-methyldibenzo[f,h] quinoxaline)(acetylacetonate)iridium(III) ($\text{Ir}(\text{MDQ})_2(\text{acac})$). **b** Platinum octaethylporphyrin (PtOEP). **c** 4,4'-Dibromobenzophenone (DBBP).

(OLEDs) to gain electron-to-photon conversion with greatly enhanced efficiency up to unity^{94–96}.

One can distinguish between the *internal* heavy atom effect, with high- Z atoms embedded in the emitter's structure, and the *external* heavy atom effect, where emitting molecules are in close proximity to a heavy-atom-containing material^{28;62}.

Spin-Orbit Coupling via El-Sayed's Rules

A different, heavy-atom free approach to enhance intersystem crossing is the careful design of emitting molecules in order to follow the principles of *El-Sayed's rules*^{48;97}. They state that ISC is favored if the spin-flipping electron undergoes a change of orbital configuration, resulting in the following transition permissions⁶²:

$$S_1(\pi, \pi^*) \rightarrow T_1(\pi, \pi^*) \quad \text{Forbidden} \quad (2.33)$$

$$S_1(n, \pi^*) \rightarrow T_1(\pi, \pi^*) \quad \text{Allowed} \quad (2.34)$$

$$S_1(\pi, \pi^*) \rightarrow T_1(n, \pi^*) \quad \text{Allowed} \quad (2.35)$$

$$S_1(n, \pi^*) \rightarrow T_1(n, \pi^*) \quad \text{Forbidden} \quad (2.36)$$

This particularly implies the necessity of the presence of a non-bonding orbital n perpendicular to the π orbitals, as it can occur in heterocyclic compounds (cf. Section 2.1.5). A closer look into Equations 2.33 and 2.34 will be given for the electronic configuration in a carbonyl group ($\text{C}=\text{O}$), as it is present in benzophenone (cf. Figure 2.12 b).

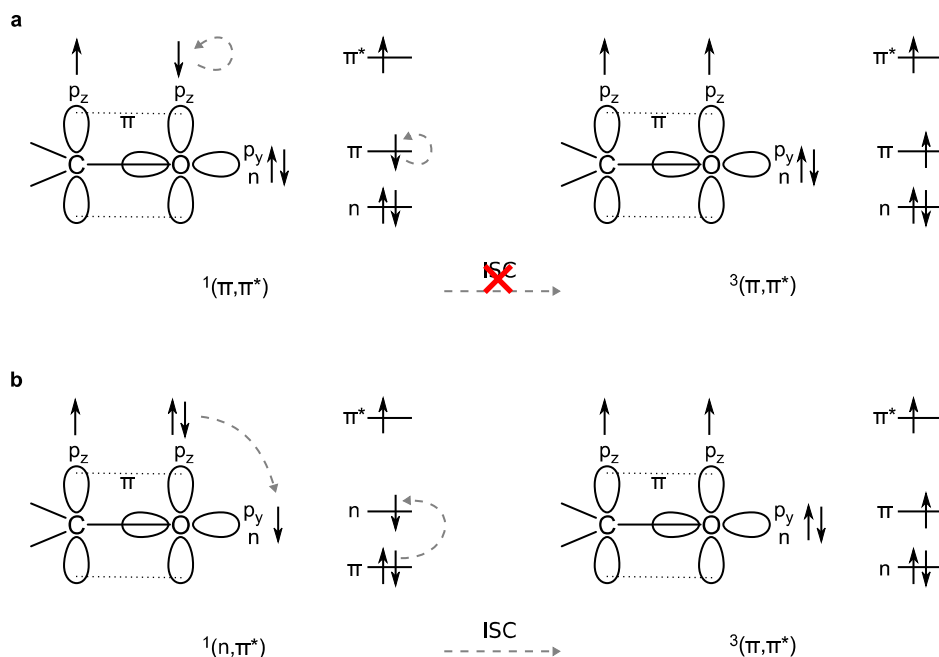


Figure 2.21.: **a** Forbidden $S_1(\pi, \pi^*) \rightarrow T_1(\pi, \pi^*)$ transition. **b** Allowed $S_1(n, \pi^*) \rightarrow T_1(\pi, \pi^*)$ transition due to total momentum conservation. Figure is partly adapted from⁶².

The transition from Equation 2.33 is shown in Figure 2.21 a. Here, for intersystem crossing, a spin flip of an electron in the p_z orbital would be required. Since there is no possibility for momentum conservation, this transition is unlikely. In contrast, the ISC transition in Equation 2.34 is coupled with an alteration of the electron's configuration from the π bonding p_z to the perpendicular non-bonding p_y orbital of the oxygen (Figure 2.21). This switching is accompanied by a change in angular momentum, which can compensate the electron's spin flip. Further, the transition is enforced by the electrophilic character of the half-filled n orbital, which is then fully occupied, rendering the π orbital the new HOMO. This newly formed electronic configuration is denoted in the transition from a (n, π^*) to a (π, π^*) state. Analogously, the residual transitions in Equation 2.35 and 2.36 can be explained.

Additionally to El-Sayed's rules, ISC is most favorable⁴⁸ for transitions from singlet to triplet states with small energy splitting ΔE_{STn} ^a. In consequence, originating from S_1 , it usually involves vibronic states of T_1 or energetically higher electronic triplet

^aThe letter n in the subscript of ΔE_{STn} indicates, that this parameter may describe the energy difference between S_1 and a higher lying triplet state T_n . This is in contrast to ΔE_{ST} , which describes the gap between S_1 to T_1 only.

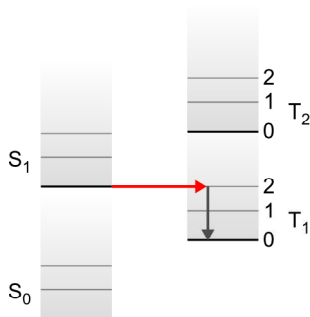


Figure 2.22.: Intersystem crossing from S_1 to a higher lying triplet state with subsequent vibrational relaxation to the lowest vibrational state of T_1 .

states T_n . From there, fast vibrational relaxation to the lowest vibrational state of T_1 takes place (Figure 2.22).

The magnitude of k_{isc} induced by orbital transitions in heavy-atom free molecules is dependent on the molecular geometry and can range from very fast as in benzophenone ($k_{\text{isc}} \approx 10^{11} \dots 10^{10} \text{ s}^{-1}$), where it outcompetes the fluorescence, to very slow as in pyrenealdehyde ($k_{\text{isc}} \approx 10^7 \dots 10^6 \text{ s}^{-1}$).⁶²

Twisting-Induced Spin-Orbit Coupling

In the absence of heavy atoms or n -type orbitals, molecular twisting can be the main reason for ISC⁹⁸. In comparison to similar but flat molecular analogons, some twisted materials show an increase in SOC of up to two orders of magnitude. Again, the underlying mechanism is a compensation of the electron's spin flip by a change of angular momentum⁹⁹ and a twisting-induced mixing of σ and π orbitals resulting in rehybridized orbitals Ψ (Figure 2.23)¹⁰⁰.

2. Theory

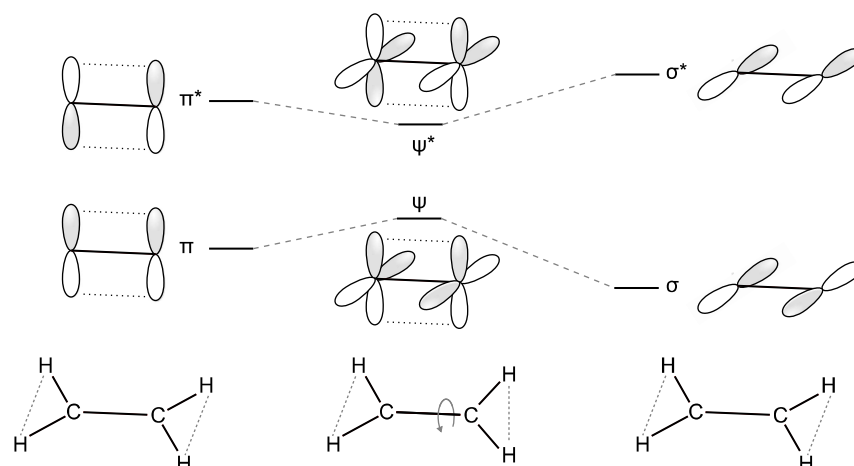


Figure 2.23.: Twisting-induced rehybridization leading to mixed Ψ orbitals in ethylene (middle) compared to flat electronic configuration with σ and π orbitals (left and right). Figure adapted from¹⁰⁰.

Charge-Transfer-Enhanced Intersystem Crossing

An additional pathway for efficient population of the triplet state is the intermediation via a CT or ICT state (cf. Section 2.1.10). In highly twisted D - A systems, the absence of electron-exchange interactions results in a minimized singlet-triplet splitting energy ΔE_{ST} and an efficient ISC from the 1CT singlet to the 3CT triplet state^{101;102}. While radiative emission from 3CT is hardly observed⁷², this state can be used as an intermediate state for population of the local excited triplet state T_1 , also named 3LE , of D or A (Figure 2.24)^{103;104}. For efficient energy transfer, 3LE should be energetically lower compared to 3CT .¹⁰⁵

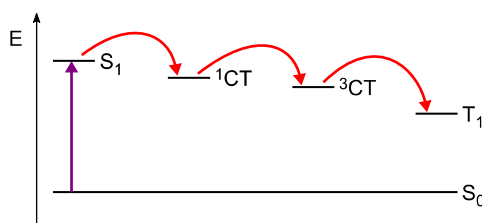


Figure 2.24.: CT-state-mediated ISC pathway (red) from S_1 to T_1 .

Reverse Intersystem Crossing

ISC from the triplet regime back to a singlet state is referred to as *reverse intersystem crossing* (RISC). It is weaker than ISC and occurs for small singlet-triplet energy splitting, when thermal energy can lift the exciton to overcome ΔE_{ST} . It enables the increase of electroluminescent efficiency in OLEDs by turning weakly radiative triplets into efficient singlet emission. Named *thermally activated delayed fluorescence* (TADF) or *E-type fluorescence*, this effect had a fundamental impact in OLED research in recent years^{70;105–108}. A RISC population rate k_{risc} can be added to the singlet states' rate equation:

$$\frac{d[S_1]}{dt} = G + k_{\text{risc}}[T_1] - (k_f + k_{\text{nr},f} + k_{\text{isc}})[S_1]. \quad (2.37)$$

2.2.6. Phosphorescence

In opposite to fluorescence, as a radiative ISC transition from T_1 to S_0 , phosphorescence requires the spin flip of a participating electron. Therefore, the radiative rate

$$k_p \approx 10^6 \dots 10^{-3} \text{ s}^{-1} \quad (2.38)$$

is drastically lower compared to k_f , with phosphorescent lifetimes

$$\tau_p \approx 10^{-6} \dots 10^0 \text{ s} \quad (2.39)$$

spanning from microseconds to seconds¹². Similar to fluorescence, the lifetime is defined via

$$\tau_p = \frac{1}{k_p + \sum k_{\text{nr},p}}, \quad (2.40)$$

where $\sum k_{\text{nr},p}$ is the sum of all nonradiative decay rates, which may be intrinsic or externally originated. Internal pathways can be vibrational relaxation or RISC, external quenching may arise from interaction with other excited states (cf. Section 2.2.9) or molecular oxygen (cf. Section 2.3).

2. Theory

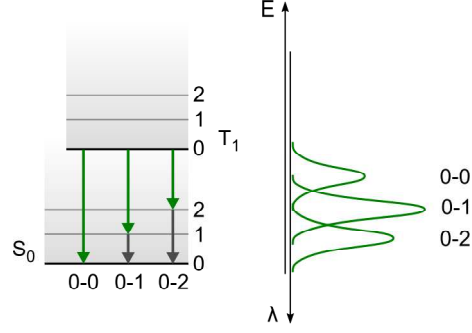


Figure 2.25.: Phosphorescence from T_1 to different vibrational states of S_0 .

Resulting from the positive singlet-triplet splitting $\Delta E_{ST} > 0$ (cf. Section 2.1.8), a material's phosphorescence is always lower in energy, i.e. redshifted compared to its fluorescent emission. The phosphorescence quantum yield is given by¹¹

$$\Phi_p = \Phi_{isc} \times k_p \tau_p = \frac{k_{isc}}{k_f + \sum k_{nr,f}} \times \frac{k_p}{k_p + \sum k_{nr,p}} \quad (2.41)$$

and is limited both by the S_1 to T_1 ISC yield Φ_{isc} and the T_1 state yield $k_p \tau_p$.

The triplet state's rate equation is^{91;92}

$$\frac{d[T_1]}{dt} = k_{isc}[S_1] - \left(k_p + \sum k_{nr,p}\right) [T_1], \quad (2.42)$$

with the triplet state's population $[T_1]$.

Tuning k_p again is possible by introducing heavy atoms into the organic emitter. Since the large spin-orbit coupling reduces the phosphorescence lifetime down to several microseconds by increasing k_p , slower nonradiative decay channels are suppressed^{109;110}. This allows efficient room temperature phosphorescence (RTP) and is widely used in triplet-emitting OLEDs^{94;95}.

Achieving purely organic heavy-atom-free RTP on the other side is challenging, since the ISC is solely based on El-Sayed's molecular orbital change rules (cf. Section 2.2.5) or molecular twisting (cf. Section 2.2.5), rendering only weak k_{isc} and k_p . The first is in competition to k_f , and the second, even more importantly, is easily outcompeted by nonradiative transitions $\sum k_{nr,p}$ from T_1 .¹¹¹

Nevertheless, purely organic RTP is subject of intense research due not requiring possibly hazardous and expensive heavy-atom materials and having a long triplet lifetime ranging from milliseconds to seconds. The latter may enable novel applications in

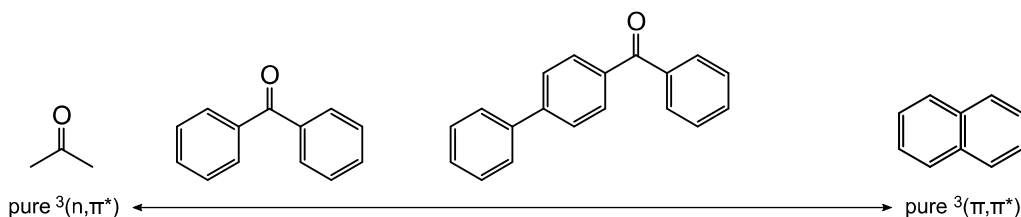


Figure 2.26.: From left to right: acetone with a pure $^3(n, \pi^*)$ state. Benzophenone, possessing a nearly pure $^3(n, \pi^*)$ state. 4-benzoylbiphenyl, with a mixed $^3(n, \pi^*) \leftrightarrow ^3(\pi, \pi^*)$ configuration. Naphthalene, possessing a pure $^3(\pi, \pi^*)$ state.

health technology^{112;113}, bioimaging^{50;114}, sensing^{52;115} and data security^{22;23;40} (cf. Section 2.4 for details).

Excited triplet states of pure organic chromophores can be of $^3(n, \pi^*)$ or $^3(\pi, \pi^*)$ nature, or a mixture of both (cf. Figure 2.10 b), resulting in different k_p . Examples for the pure states are acetone for $^3(n, \pi^*)$ with $k_p = 60 \text{ s}^{-1}$ and naphthalene for $^3(\pi, \pi^*)$ with $k_p = 0.1 \text{ s}^{-1}$ (Figure 2.26).⁶² Hybrid configurations, as in benzophenone or 4-benzoylbiphenyl result in intermediate phosphorescent rates $k_p = 20 \text{ s}^{-1}$ or $k_p = 1 \text{ s}^{-1}$, respectively. Careful design of emitters complying with this approach enables the tuning of radiative parameters of purely organic RTP emitters^{48;97}.

In a biluminescent dual emitter, the ratio of phosphorescence to fluorescence P2F is defined using the ratio of the quantum yields or of the total number of photons N_{em} :

$$\text{P2F} = \frac{\Phi_p}{\Phi_f} = \frac{\int_{\lambda} N_{\text{em},p}(\lambda)}{\int_{\lambda} N_{\text{em},f}(\lambda)}. \quad (2.43)$$

2.2.7. Charge-Transfer State Emission

Similar to LE state emission, ICT states, as formed between a molecule's donor and acceptor moiety (cf. Section 2.1.10), may also possess a significant radiative rate. This is manifested in, compared to the local emission, redshifted fluorescence from the ^1CT state to the ground state GS. Due to the high dipole moment resulting from separated charges, this redshift depends on the environment and increases with solvent polarity⁷². The ISC-populated ^3CT triplet state barely shows phosphorescence, but may act as an intermediate step for the population of local excited triplet states ^3LE (Figure 2.27, cf. Section 2.2.5)^{103;104}.

—— 2. Theory ——

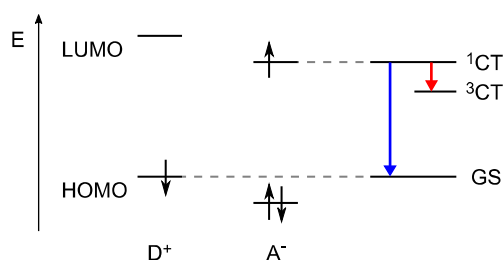


Figure 2.27.: Fluorescence to the ground state GS (blue) and intersystem crossing to the ^3CT state (red) from an excited ^1CT state.

2.2.8. Energy Transfer Mechanisms

Alongside the radiative and intrinsic nonradiative transitions, a further excited state depletion channel is energy transfer to adjacent molecules. Here, the literature generally distinguishes between Förster resonance energy transfer and Dexter energy transfer, both involving a donor D and an acceptor A molecule and reducing the donor state's excited state lifetime.

Förster Resonance Energy Transfer

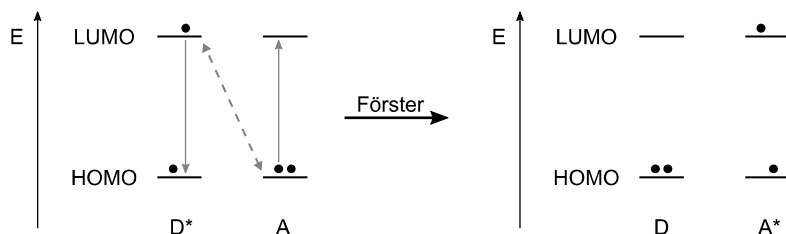


Figure 2.28.: FRET via D - A dipole-dipole interaction. Note that total spin conservation is not mandatory. Figure adapted from⁶².

Named after Theodor Förster, who first described this mechanism in 1949¹¹⁶, *Förster resonance energy transfer* (FRET) quantifies a nonradiative exciton pathway in the distance range of $r < 10$ nm induced by dipole-dipole coupling (Figure 2.28). The transfer rate k_{FRET} is defined as⁷⁵

$$k_{\text{FRET}} = \frac{1}{\tau_{\text{D}}} \left(\frac{R_{\text{F}}}{r} \right)^6, \quad (2.44)$$

— 2.2. Interplay of Excited States and Photons —

where τ_D is the donor's excited state lifetime without FRET, r is the distance between the involved chromophores, and R_F is the Förster radius⁷⁵

$$R_F[\text{nm}] = 0.0211 [\kappa^2 n^{-4} \Phi_D J(\lambda)]^{1/6}, \quad (2.45)$$

with an orientation factor $\kappa^2 = 0.476$ (for randomly oriented fixed molecules¹¹⁷), the refractive index n , the donor state's quantum yield Φ_D , and an overlap integral $J(\lambda)$. The latter represents the overlap of the donor's emission and the acceptor's absorption spectrum⁷⁵:

$$J(\lambda)[\text{mol}^{-1}\text{dm}^3\text{cm}^{-1}\text{nm}^4] = \int_0^\infty F_D(\lambda)\varepsilon_A(\lambda)\lambda^4 d\lambda, \quad (2.46)$$

with the donor's area-normalized emission spectrum $F_D(\lambda)$, the acceptor's extinction coefficient $\varepsilon_A(\lambda)[\text{mol}^{-1}\text{dm}^3\text{cm}^{-1}]$ and the light's wavelength $\lambda[\text{nm}]$.

The donor's excited state lifetime is reduced in the presence of FRET to

$$\tau_{D,\text{FRET}} = \frac{\tau_D}{1 + k_{\text{FRET}}\tau_D}. \quad (2.47)$$

The transfer efficiency ϕ_{FRET} is also highly dependent on the D - A -distance (Figure 2.29)⁷⁵:

$$\Phi_{\text{FRET}} = \frac{R_F^6}{R_F^6 + r^6}. \quad (2.48)$$

That also explains the definition of R_F : if $r = R_F$, the transfer efficiency is $\phi_{\text{FRET}} = 0.5$.

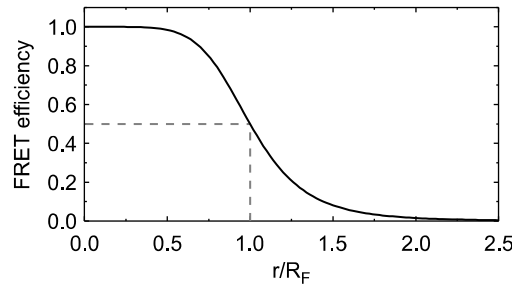


Figure 2.29.: FRET efficiency ϕ_{FRET} as a function of D - A -distance r .

In conclusion, the main requirements for FRET are closely spaced molecules with overlapping emission and absorption spectra. This accounts not only for fluorescent, but also for phosphorescent donor materials¹¹⁸.

Dexter Energy Transfer

In contrast to FRET, *Dexter energy transfer* is not mediated by dipole-dipole interaction, but is based on an electron exchange between a donor D and an acceptor A ¹¹⁹. Thus, an overlap of the involved molecular orbitals is required and the transfer efficiency Φ_{Dex} follows a distance-dependent exponential law¹²⁰:

$$\Phi_{\text{Dex}} = \exp(-4\alpha r) \quad (2.49)$$

with a decay coefficient α of the electronic wavefunctions and the D - A distance r . As a broad rule, interaction is limited to an intermolecular distance of $r < 1$ nm. Typically, Dexter energy transfer refers to triplet-triplet interaction, because it does not require a radiative dipole moment and the involved electrons' total spin has to be conserved. Thus, it plays a major role in triplet-triplet annihilation (cf. Section 2.2.9) and generation of singlet oxygen (cf. Section 2.3.2)¹²¹.

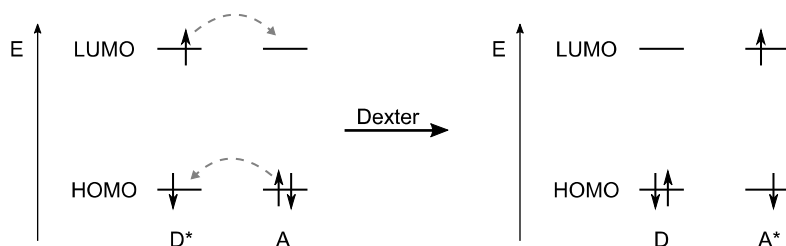


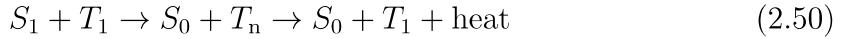
Figure 2.30.: Dexter energy transfer via electron exchange. Here, total spin conservation is mandatory. Figure adapted from⁶².

2.2.9. Interaction of Multiple Excited States

The interaction of two excited states is usually connected to the quenching of one or both of the states. In this work, the focus will be on single-triplet and triplet-triplet annihilation, since these are the dominant multi-exciton quenching processes when long-lived triplet states are involved^{122–124}.

Singlet-Triplet Annihilation

Singlet-triplet annihilation (STA) is usually based on FRET and, starting from an excited singlet S_1 and triplet T_1 state, leads to a quenching of the singlet state, while the triplet state remains unchanged. In more detail, S_1 populates a higher-lying triplet state T_n via dipole-dipole interaction, with a subsequent thermal relaxation of the latter back to T_1 ¹²⁵:



The STA quenching rate k_{STA} therefore influences the singlet state population

$$\frac{d[S_1]}{dt} = G - (k_f + k_{\text{nr},f} + k_{\text{isc}})[S_1] - k_{\text{STA}}[S_1][T_1], \quad (2.51)$$

and reduces the fluorescence lifetime τ_f (cf. Section 2.2.4) via

$$\tau_{f,\text{STA}} = \frac{1}{k_f + k_{\text{nr},f} + k_{\text{isc}} + k_{\text{STA}}[T_1]}. \quad (2.52)$$

The dependence of STA on the excited triplet concentration $[T_1]$ results from the underlying bimolecular interaction⁹². Due to the involvement of two interaction partners ($[S_1]$ and $[T_1]$), k_{STA} is named a second-order rate constant, and high density of excited triplets leads to a reduction of the fluorescence emission and lifetime.

A substantial approach to quantify the different parameters STA, TTA and saturation in an RTP system was realized by Martin Kroll in his master's thesis¹²⁶. From the comparison of millisecond-time-resolved measurements and numerical simulations, he deduced that with both the increase of excitation intensity and the decrease of inter-emitter distance, the STA influence increases.

Triplet-Triplet Annihilation

The origin of *triplet-triplet annihilation* (TTA) may lay both in Förster or Dexter energy transfer (Figure 2.31)^{127;128}. Since it can have huge impact on the efficiency of phosphorescent OLEDs, it has been the subject of a plethora of studies^{129–134}.

The triplet's rate equation involving TTA as a constant second-order quenching rate k_{TTA} is¹²⁸

$$\frac{d[T_1]}{dt} = k_{\text{isc}}[S_1] - \frac{[T_1]}{\tau_p} - f k_{\text{TTA}}[T_1]^2, \quad (2.53)$$

—— 2. Theory ——

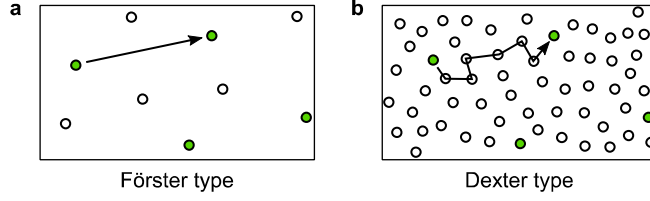


Figure 2.31.: **a** Förster-dominated TTA at low emitter concentrations. **b** Dexter-type triplet diffusion at high emitter concentrations.

with the intrinsic triplet lifetime τ_p and a fraction $f = 0.5$ if one and $f = 1$ if both triplets are quenched. The quadratic dependence on $[T_1]$ results from two molecules being involved in the interaction.

The solution of this differential equation leads to the population over time ($[T_1](t)$). With $[S_1] = 0$, the phosphorescence decay $I(t) = k_p[T_1](t)$ after turning off the excitation results in¹²⁸

$$I(t) = I_0 \frac{1}{(1 + fT_0k_{\text{TTA}}\tau_{p0}) \exp(t/\tau_{p0}) - fT_0k_{\text{TTA}}\tau_{p0}}, \quad (2.54)$$

with the intrinsic lifetime τ_{p0} in the absence of TTA.

For low emitter concentrations with distances of several nanometers, single-step FRET is the dominating TTA mechanism. Therefore, the interaction rate k_{TTA} is not constant, but significantly depending on the triplet density $[T_1]$ ¹²⁷:

$$k_{\text{TTA}}([T_1]) = \pi \frac{V_F}{\tau_p} \left[1 + \left(\frac{\pi}{2} - 1 \right) V_F[T_1] + O((V_F[T_1])^2) \right], \quad (2.55)$$

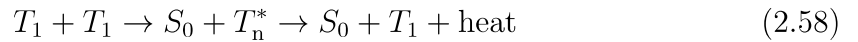
where

$$V_F = \frac{4}{3} \pi R_F^3 \quad (2.56)$$

is the volume of a sphere with Förster radius R_F . In zeroth approximation, which accounts for low concentrations and $V_F[T_1] \ll 1$, however, the quenching rate can be treated as constant with $[T_1]$:

$$k_{\text{TTA}} = \pi \frac{V_F}{\tau_p}. \quad (2.57)$$

Similar to STA, the Förster-mediated TTA results in one residual excited T_1 state and a relaxed ground state S_0 :



2.2. Interplay of Excited States and Photons

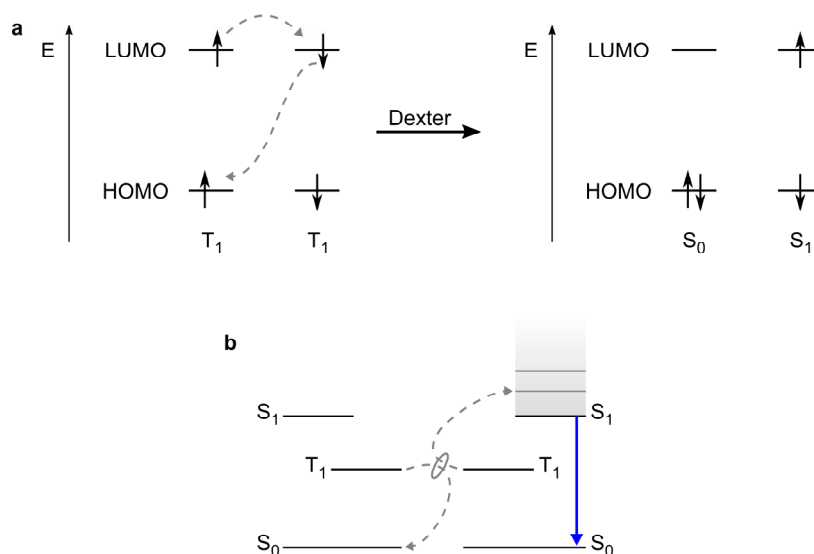


Figure 2.32.: **a** Dexter transfer from $T_1(\uparrow\uparrow)$, $T_1(\downarrow\downarrow)$ to $S_0(\uparrow\downarrow)$, $S_1(\uparrow\downarrow)$. **b** Resulting TTA, which generates an excited S_1 state, from where delayed fluorescence may occur.

For high molecular concentrations, the Dexter-based diffusion model is applicable. Via electron exchange, the triplet excitons can hop from one chromophore to another. In this case, k_{TTA} again can be assumed as a constant value¹²⁷

$$k_{\text{TTA}} = 8\pi R_C D, \quad (2.59)$$

with the triplet diffusivity D and a capture radius R_C . Originating from Dexter's theory (cf. Section 2.30), this radius is an approximation for infinite energy transfer rate for a D - A distance $r < R_C$ and zero for $r > R_C$ ¹³².

Since in Dexter electron exchange the total spin is conserved, a closer look to the triplet's spin statistics is necessary. A combination of two triplet states, each possessing $T(\downarrow\downarrow)$, $T(\downarrow\uparrow)$ or $T(\uparrow\uparrow)$ (cf. Section 2.1.6), can result in three different total spin numbers $S \in \{0, 1, 2\}$ (Table 2.3).

The multiplicity of the final state is either $M = 1$ (singlet type), $M = 3$ (triplet type) or $M = 5$ (quintet type). This leads to a total number of nine possible states, of which one is of singlet nature owning a total spin of $S = 0$.⁶² Therefore, only via the latter, the generation of two singlet states (with again total spin $S = 0$) is allowed. If the T_1 's energy E_T exceeds the singlet-triplet splitting ΔE_{ST} (Figure 2.32), this may result in one singlet ground state S_0 and one excited singlet state S_1 . The

— 2. Theory —

Table 2.3.: Spin statistics for two-triplet interaction. Adapted from⁶².

| T_A | T_B | $T_A + T_B$ | Total spin S | Multiplicity M | Final state |
|-----------------------|---------------------------|--|----------------|------------------|-------------|
| $T(\uparrow\uparrow)$ | $T(\downarrow\downarrow)$ | $\uparrow\downarrow\uparrow\downarrow$ | 0 | 1 | Singlet S |
| $T(\uparrow\uparrow)$ | $T(\downarrow\uparrow)$ | $\uparrow\uparrow\downarrow\uparrow$ | 1 | 3 | Triplet T |
| $T(\uparrow\uparrow)$ | $T(\uparrow\uparrow)$ | $\uparrow\uparrow\uparrow\uparrow$ | 2 | 5 | Quintet Q |

subsequent emission from this state is named delayed fluorescence, sometimes referred to as *P-type fluorescence*.

Saturation

Saturation is not an actual interaction of multiple excited states. Nevertheless it is mentioned here, since it shows similar behavior as STA. For emitters possessing a long triplet state lifetime τ_p , continuous illumination may lead to an ongoing increase of the number of triplets $[T_1]$, since the population rate outcompetes the slow deactivation processes of this state (Figure 2.33).

The number of excitons in the ground state $[S_0]$, which are able to absorb a photon of a pump term $P(t)$, is therefore reduced:

$$[S_0] = [N] - [S_1] - [T_1], \quad (2.60)$$

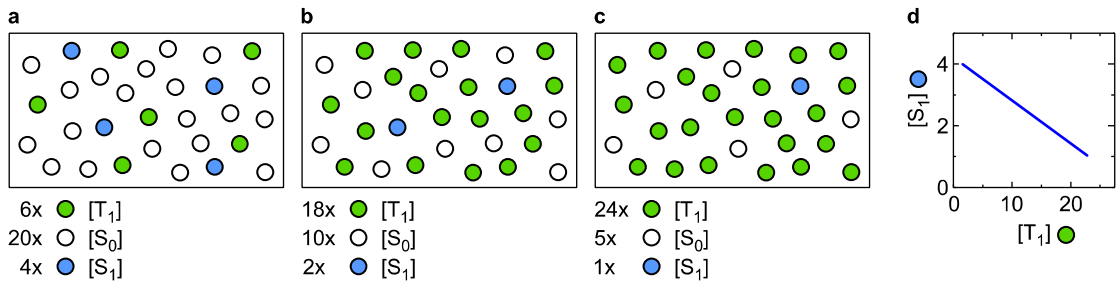


Figure 2.33.: Model system of saturation for $[N] = 30$ emitters. **a** At low triplet $[T_1]$ (green) concentrations, saturation is negligible, since most of the emitters are in $[S_0]$. A certain ratio (here 1/5) is excited to $[S_1]$ (blue). **b** $[S_0]$ decreases with increasing $[T_1]$ density. From the reduced number of $[S_0]$, still the ratio 1/5 is excited to $[S_1]$. **c** For high triplet saturation, fluorescence is drastically reduced. **d** The linear dependence of $[S_1]$ from $[T_1]$ for saturation.

—— 2.2. Interplay of Excited States and Photons ——

with the total number of molecules $[N]$. Thus, equation 2.29 needs to be modified⁹²:

$$\frac{d[S_1]}{dt} = P(t) \times ([N] - [S_1] - [T_1]) - (k_f + k_{nr,f} + k_{isc}) [S_1]. \quad (2.61)$$

Due to this decrease of the exciton generation rate with increasing $[T_1]$, at some point a steady state is reached, where the numbers of generated and decayed triplets match⁹². For a high excitation density, a large share of the emitters is then in the excited triplet state. Therefore, a significant decrease of the number of $[S_1]$ states is observed, which leads to reduced fluorescent emission.

2.3. Properties of Molecular Oxygen

Molecular oxygen ($\text{O}=\text{O}$ or O_2), consisting of two oxygen atoms, plays a major role in organic photophysics, since it is able to quench RTP very efficiently^{12;135}. The reason for that is its triplet ground state $^3\text{O}_2$, which annihilates the emitters' excited T_1 in a spin-allowed and thus very efficient triplet-triplet interaction (cf. Section 2.2.9). The resulting excited singlet oxygen $^1\text{O}_2$ is highly reactive¹³⁶ and plays a major role in several biological^{137–139}, medical^{140;141} and chemical¹⁴² processes. Since most of the RTP applications presented in this thesis also base on this interaction, a closer look is given into its photochemistry.

2.3.1. Molecular Electronic Configuration of Oxygen

As a combination of two oxygen atoms, molecular oxygen possesses 16 electrons, which are distributed in σ - and π -orbitals as sketched in Figure 2.34.

The full electronic configuration of O_2 is⁶²

$$(\sigma_{1s})^2(\sigma_{1s}^*)^2(\sigma_{2s})^2(\sigma_{2s}^*)^2(\sigma_z)^2(\pi_x)^2(\pi_y)^2(\pi_x^*)^1(\pi_y^*)^1. \quad (2.62)$$

In the molecule's ground state (Figure 2.34 and Figure 2.35 a), the two energetically highest electrons are located in the degenerate π_x^* and π_y^* orbitals, respectively, and show the same spin configuration, according to Hund's rules. This leads to a total spin of $S = 1$ and reveals the triplet configuration of this state $^3\text{O}_2$ (cf. Section 2.1.6), which often is also noted as $^3\Sigma$, as Σ is an indicator for a vanishing total electronic angular momentum L about the intermolecular axis⁶².

Further, these two half-filled antibonding $(\pi_x^* \uparrow)(\pi_y^* \uparrow)$ orbitals are both referred to as HOMO and LUMO at the same time. In consequence, the first excited states involve transitions of electrons within these orbitals only⁶². The lowest excited state (Figure 2.35 b) is realized by a spin-flipped and orbital-hopped electron resulting in $(\pi_x^*)^0(\pi_y^* \uparrow\downarrow)^2$ (or $(\pi_x^* \uparrow\downarrow)^2(\pi_y^*)^0$ or a linear combination of both). Due to $S = 0$, this state is of singlet nature $^1\text{O}_2$. Corresponding to its angular momentum L , it is also addressed as $^1\Delta$, where Δ indicates two units of electronic angular momentum about the intermolecular axis. An additional excited oxygen singlet state, namely $^1\Sigma$, is shown in Figure 2.35 c. With $E_{1\Sigma} = 1.63 \text{ eV}$, this state is energetically higher than $^1\Delta$ with $E_{1\Delta} = 0.98 \text{ eV}$. This again is in accordance with Hund's rules, since

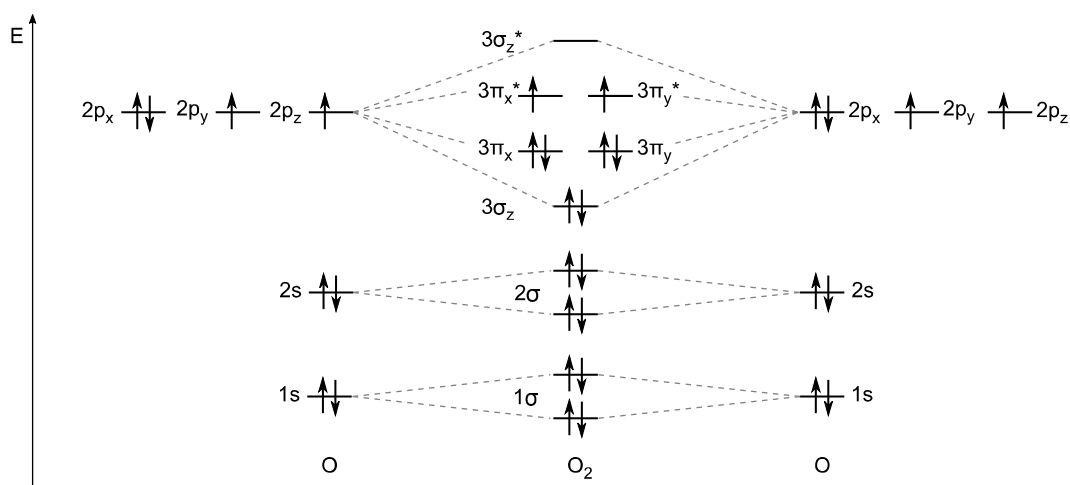


Figure 2.34.: Atomic (left and right) and molecular orbitals (in the middle) of single oxygen atoms and an O_2 molecule in the ground state. Figure partly adapted from ¹⁴³.

for identical S , states with higher angular momentum $L(^1\Delta) > L(^1\Sigma)$ are of lower energy¹⁴⁴. $^1\Sigma$ usually undergoes a fast spin-allowed transition to $^1\Delta$ in the range of a few to several hundred nanoseconds¹⁴⁵.

In Table 2.4, calculated excited state lifetimes of singlet oxygen in different host polymers are shown. A theoretical approach was used to quantify the energy transfer from $^1\text{O}_2$ to vibrational modes of the polymers¹⁴⁶. An experimental study using a triplet emitter embedded into the polymers revealed similar results for PS and PMMA (Table 2.4, brackets). Via deconvolution of the additives' T_1 emission from the $^1\text{O}_2$ decay, an intrinsic $^1\text{O}_2$ lifetime was deduced¹⁴⁷.

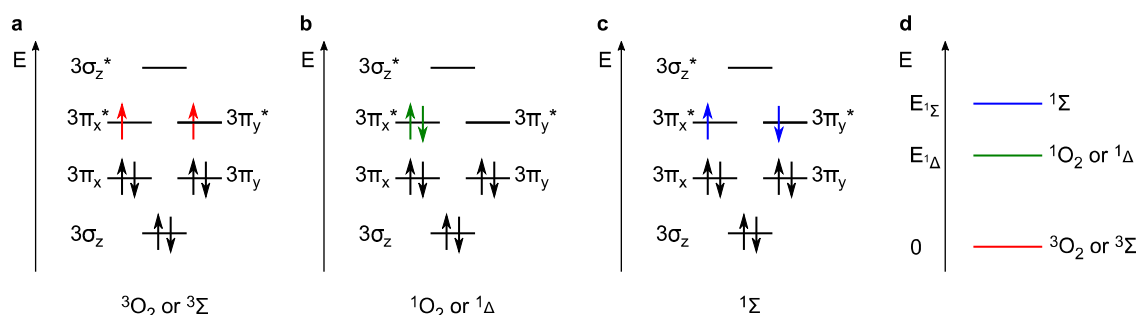


Figure 2.35.: Electronic states of molecular oxygen. **a** Triplet ground state $^3\text{O}_2$ or $^3\Sigma$. **b** First excited singlet state $^1\text{O}_2$ or $^1\Delta$. **c** Second excited singlet state $^1\Sigma$. **d** Energetic order of the different electronic states. Figure is partly adapted from ⁶².

Table 2.4.: Excited singlet oxygen lifetimes in different polymers. Values from^{146;147}.

| Polymer | Abbreviation | τ_{1O_2} (μ s) |
|---------------------------|--------------|--------------------------|
| Poly(vinyl alcohol) | PVA | 10.3 |
| Polystyrene | PS | 18.9 (17...21) |
| Poly(methyl methacrylate) | PMMA | 25.8 (20...25) |

The first spin-allowed transition involving the ground state $^3\Sigma$ is absorption of light at a wavelength of $\lambda \approx 200$ nm to a high-energy triplet state⁶². However, this is not the main excitation route for excited state oxygen, as will be discussed in the following.

2.3.2. Oxygen-Induced Exciton Quenching

In the presence of molecular oxygen, there are several quenching routes affecting excited chromophores with different resulting products, upon which a detailed look is given in this section. The emitters sensitive to oxygen quenching are referred to as photosensitizers, and there is a great diversity of available materials^{148;149}.

Triplet-State Quenching

Triplet-state quenching induced by oxygen is a common nonradiative energy pathway for emitters in gas phase¹⁴⁵, solutions¹⁵⁰, and rigid polymer environments^{147;151;152}. Therefore, realizing RTP in ambient atmosphere is challenging, and different approaches exist to minimize the interaction with oxygen (cf. Section 2.4.4).

An emitter's excited triplet state T_1 and the oxygen's ground state $^3\Sigma$ can undergo a reversible formation of an excited complex with total spin $S = 0$ ($^1(T_1\ ^3\Sigma)$, $M = 1$), $S = 1$ ($^3(T_1\ ^3\Sigma)$, $M = 3$), or $S = 2$ ($^5(T_1\ ^3\Sigma)$, $M = 5$), equal as for TTA (cf. Table 2.3 in Section 2.2.9)^{150;153}. Since solely for a total spin $S = 0$ two singlets may result from this interaction, only $^1(T_1\ ^3\Sigma)$ can lead to energy transfer k_{et} and consequently to generation of $^1\Sigma$ or $^1\Delta$ singlet oxygen. The eight residual complexes, of which the three $^3(T_1\ ^3\Sigma)$ are dominating, are able to quench T_1 via internal conversion k_{ic} , but do not yield excited oxygen due to spin forbiddenness¹⁵³.

With the diffusion-based excited-complex formation rate k_{diff} , and its separation counterpart k_{-diff} , one can formulate a second-order rate constant k_{qT} for the oxygen-induced triplet quenching as¹⁵³

$$k_{qT} = \frac{1}{9} \frac{k_{\text{diff}} k_{\text{et}}}{k_{-\text{diff}} + k_{\text{et}}} + \frac{1}{3} \frac{k_{\text{diff}} k_{\text{ic}}}{k_{-\text{diff}} + k_{\text{ic}}}. \quad (2.63)$$

Note that while the first term represents the formation of excited singlet oxygen, the second one describes the internal conversion with a resulting triplet ground state.

This rate is in competition to the intrinsic decay rates of the emitters' T_1 state:

$$\frac{d[T_1]}{dt} = k_{\text{isc}}[S_1] - \frac{[T_1]}{\tau_p} - k_{qT}[\text{O}_2][T_1], \quad (2.64)$$

where $[\text{O}_2]$ is the oxygen concentration in the film.

To sum up, there are three possible interactions of excited triplet states T_1 and ground-state oxygen $^3\Sigma^{153}$:



where the first case (Equation 2.65, rate $k_{1\Sigma}$) leads to an emitter's singlet ground state S_0 and an excited oxygen singlet $^1\Sigma$ state, the second case (Equation 2.66, rate $k_{1\Delta}$) yields also S_0 , but an excited O_2 singlet $^1\Delta$ state, and the third case (Equation 2.67, rate $k_{3\Sigma}$) results in both a singlet S_0 and an oxygen ground state $^3\Sigma$.

The ratio of generated excited singlet states ($^1\Sigma$ or $^1\Delta$) compared to the number of quenched triplet states T_1 is denoted as singlet generation rate S_Δ ⁶², and described via¹⁴⁵

$$S_\Delta = \frac{k_{1\Sigma} + k_{1\Delta}}{k_{1\Sigma} + k_{1\Delta} + k_{3\Sigma}}, \quad (2.68)$$

which is correlated to Equation 2.63 via the excited-singlet-oxygen generation rates

$$k_{1\Sigma} + k_{1\Delta} = \frac{1}{9} \frac{k_{\text{diff}} k_{\text{et}}}{k_{-\text{diff}} + k_{\text{et}}}, \quad (2.69)$$

—— 2. Theory ——

the ground-state-oxygen generation rate

$$k_{3\Sigma} = \frac{1}{3} \frac{k_{\text{diff}} k_{\text{ic}}}{k_{-\text{diff}} + k_{\text{ic}}} \quad (2.70)$$

and the triplet state T_1 quenching rate

$$k_{\text{qT}} = k_{1\Sigma} + k_{1\Delta} + k_{3\Sigma}. \quad (2.71)$$

For $k_{\text{ic}} \ll k_{-\text{diff}}$, high values up to unity for S_Δ are possible¹⁵³, with $S_\Delta \geq 0.8$ for $^3(\pi, \pi^*)$ states of polynuclear aromatics like naphthalene, while the $^3(n, \pi^*)$ emitter benzophenone shows $S_\Delta = 0.3 \dots 0.4$.^{62;154} The origin of the deviation of S_Δ between $^3(\pi, \pi^*)$ and $^3(n, \pi^*)$ states is widely discussed and may be found in higher reorganization energies for $^3(n, \pi^*)$ while forming the excited complex¹⁵⁵.

Further, it is reported that for $^3(\pi, \pi^*)$ triplets, S_Δ shows a dependence of the T_1 triplet energy E_T , as it is maximized for values between $E_T = 1.92 \text{ eV}$ (650 nm) and $E_T = 2.33 \text{ eV}$ (530 nm). For $E_T > 2.49 \text{ eV}$ ($< 500 \text{ nm}$), it drastically drops due to the formation of an additional emitter- O_2 -CT mediated energy pathway favoring $k_{3\Sigma}$ ¹⁴⁵. At the same time, all rates $k_{1\Sigma}$, $k_{1\Delta}$ and $k_{3\Sigma}$, increase with decreasing oxidation potential E_{ox} (and therefore increasing donor nature) of the triplet emitter. Since $k_{3\Sigma}$ shows the greatest dependence on E_{ox} , the singlet formation rate S_Δ drops with E_{ox} .¹⁵⁰ For $^3(n, \pi^*)$ triplets, the dependence on E_T and E_{ox} is much weaker due to a different electronic and steric structure of the excited complexes^{153;154}.

Singlet-State Quenching

Even if the usual excitation pathway to oxygen is via an excited triplet T_1 state^{143;156;157}, there are further pathways of singlet oxygen generation involving the emitter's excited singlet state S_1 ^{62;158}:



The first transition (Equation 2.72) is a spin-allowed electron exchange leading to ISC in the excited molecule, and is energetically limited to emitters with $\Delta E_{\text{ST}} > 0.98 \text{ eV}$, which is needed to excite the oxygen. For molecules with lower ΔE_{ST} , the allowed interactions are oxygen spin-catalyzed ISC (Equation 2.73) and a formation of two ground states (Equation 2.74). Both processes are mediated through the formation of an excited complex⁶².

In solution, the singlet-oxygen formation rate ranges from $S_{\Delta}^S \approx 0$ for phenanthrene, anthracene or triphenylene to unity for 9,10-dicyanoanthracene¹⁵⁸. With increasing solvent viscosity, the generation rate was shown to be reduced¹⁵³. The S_1 quenching rate k_{qS} can exceed k_{qT} by one order of magnitude⁶². Still, the overall S_1 singlet-quenching efficiency may be drastically lower than it is the case for T_1 triplet quenching, since it competes with much faster radiative and intrinsic nonradiative decay channels:

$$\frac{d[S_1]}{dt} = G - (k_{\text{f}} + k_{\text{nr,f}} + k_{\text{isc}}) [S_1] - k_{\text{qS}}[\text{O}_2][S_1]. \quad (2.75)$$

2.3.3. Decay Channels of Singlet Oxygen

Once it is formed, excited singlet oxygen can undergo three different pathways, namely physical quenching, chemical quenching or radiative decay.

Physical Quenching

Physical quenching describes a deactivation of $^1\text{O}_2$ via an energy transfer to a lower lying state of an adjacent molecule or via CT- and vibrational interactions. For example, the T_1 state of the well known antioxidant β -carotene (β -C) with $E_{\text{T}} \approx 0.84 \text{ eV}$ ¹⁵⁹ is able to act as an energy acceptor via⁶²



The corresponding second-order quenching rate constant was determined to $k_{\text{q1O}_2} = 11 \times 10^9 \text{ M}^{-1}\text{s}^{-1}$ in toluene¹⁶⁰. This quenching route does not reduce the overall concentration of molecular oxygen, since it just decays back to its ground state without a chemical reaction. This is in contrast to chemical quenching processes (cf. next Section) and can be in competition with the latter. In detail, adding the physical $^1\text{O}_2$

quencher 1,4-diazabicyclo(2.2.2)octane (DABCO or TED for Triethylenediamine) to polymers like PS can drastically reduce the rate of chemical $^1\text{O}_2$ quenching by depopulating it before a reaction occurs (cf. Figure 2.38)¹⁶¹.

Chemical Quenching

In contrast to its triplet ground state, excited singlet oxygen is a highly reactive species due to its low activation energy¹⁶². The chemical reaction between $^1\text{O}_2$ and a reactant leads to the depletion of molecular oxygen and is named *chemical quenching*, *photoconsumption* or *oxygen uptake*. It plays a major role in photodegradation of polymers¹⁶¹, DNA¹⁶³ and cell damaging¹⁵³ as well as food degradation¹⁶². Besides that, $^1\text{O}_2$ reactions also enable photodynamic therapy of cancer cells^{140;141} and antimicrobial treatments¹⁶⁴.

Photoconsumption can efficiently reduce the concentration of molecular oxygen in polymeric films¹⁶⁵ and its impact is strongly depending on the polymer species. Big differences can be found in PS250k compared to PMMA35k¹⁶¹. Here, photosensitized chemical quenching of $^1\text{O}_2$ is roughly one to two orders of magnitude faster for PMMA35k as it is for PS250k. Photooxidation experiments of PMMA and PS without triplet sensitizers show the formation of carbonyl and carboxyl groups in both polymers when illuminated with UV light of $\lambda = 254$ nm (Figure 2.36)^{166;167}. This was validated by X-ray photoelectron spectroscopy (XPS). In methyl methacrylate, also the generation of hydroperoxides is discussed¹⁶⁸.

Besides polymers, small molecules can also be subject of $^1\text{O}_2$ photoconsumption. In β -carotene, alongside to physical oxygen quenching, minor channels are chemical reactions resulting in modified products (Figure 2.37)¹³⁷.

Adding the chemical quencher 1,2,2,6,6-pentamethyl-4-piperidinol (HAL or HOPEMP) to a polymer like PS increases the overall oxygen uptake under illumination and reduces the needed time until oxygen is depleted (Figure 2.38)¹⁶¹. Therefore, by adding

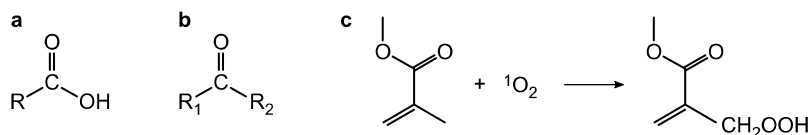


Figure 2.36.: **a** and **b** Products of photooxidation of PS and PMMA, carboxyl and carbonyl. R represents the residual polymer or other rests. **c** $^1\text{O}_2$ uptake in methyl methacrylate. Figure partly adapted from¹⁶⁸.

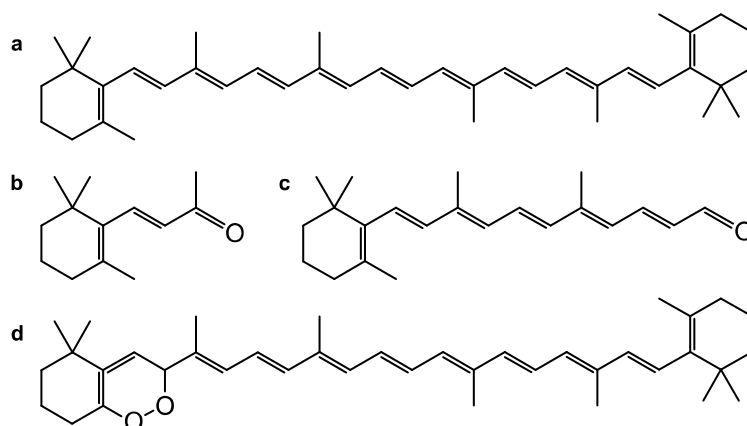


Figure 2.37.: **a** β -carotene, a physical and chemical oxygen quencher. **b** to **d** Some experimentally proven $^1\text{O}_2$ -degradation products of β -carotene. Figure adapted from¹³⁷.

physical or chemical quenchers to a material system, the photoconsumption can be either slowed down or accelerated.

Aromatic compounds like naphthalene derivatives¹⁶⁹, 2-pyridone¹⁷⁰ or rubrene¹⁷¹ also show chemical quenching. A comparison of anthracene, tetracene and pentacene (cf. Figure 2.6) shows an increase of reactivity by around two orders of magnitude for each additional conjugated ring¹⁴³. This is explained by the electrophilic nature of singlet oxygen. The oxygen uptake is realized via the formation of a singlet charge-transfer state in between the reactants. Subsequently, this state either converts into a triplet state via ISC, from where the initial structures evolve, or it undergoes cycloaddition, leading to an endoperoxide and the vanishing of molecular oxygen (Figure 2.39 a).

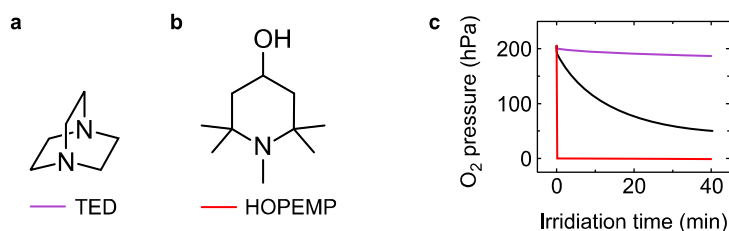


Figure 2.38.: **a** The physical quencher DABCO or TED. **b** The chemical quencher HAL or HOPEMP. **c** Oxygen consumption in PS without (black) and with the physical quencher TED (purple) and the chemical quencher HOPEMP (red). Figure partly adapted from¹⁶¹.

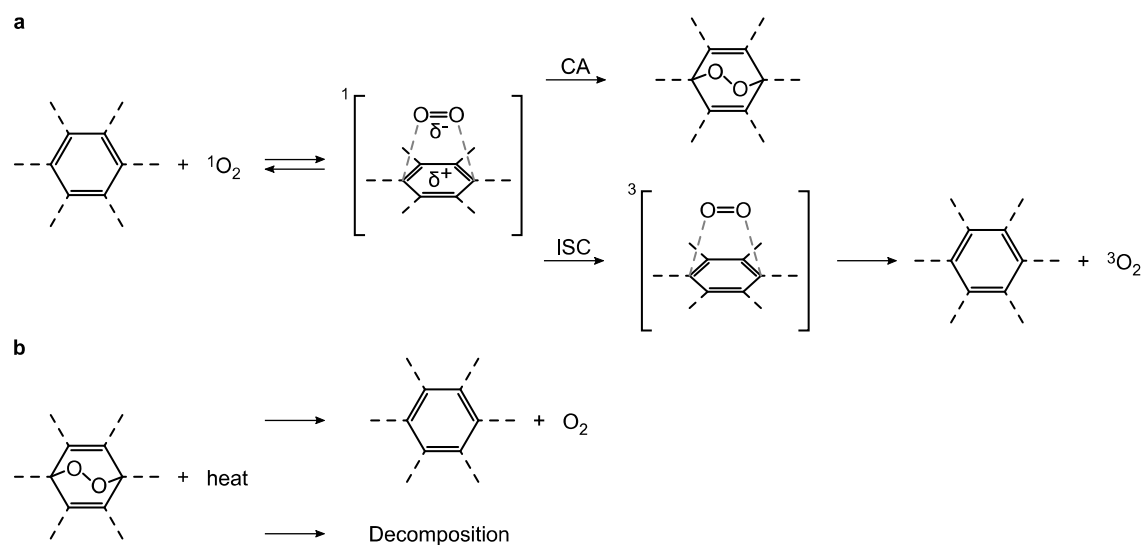


Figure 2.39.: **a** Mechanism of cycloaddition (CA) or physical quenching via ISC on aromatic hydrocarbons. **b** Transformation of endoperoxides during thermal treatment. Figures adapted from¹⁷⁶.

Interestingly, the photoconsumption can be reversible for some uptake materials^{172–175} and thermal treatment may lead to a dissociation into the original material and singlet or triplet oxygen (Figure 2.39 b)¹⁷⁶.

Radiative Decay

Due to the necessity of a spin flip, the radiative rate of these states to the triplet ground state $^3\Sigma$ is extremely low ($k_{1\Sigma} \approx 10^{-1} \text{ s}^{-1}$, $k_{1\Delta} \approx 4 \times 10^{-4} \text{ s}^{-1}$ ⁶²). Since it competes with high rates of nonradiative deactivation, it also shows very low phosphorescence yield. Still, phosphorescence from $^1\Delta \rightarrow ^3\Sigma$ at $\lambda = 1270 \text{ nm}$ can be detected in solution measurements¹⁷⁷ as well as in polymeric matrices¹⁷⁸ including PMMA¹⁵².

2.4. Recent Progresses in Research on Organic Phosphorescence

As already stated in Section 2.2.6, room temperature phosphorescence (RTP) from heavy-atom-free organic materials, also known as organic ultralong room temperature phosphorescence (OURTP)¹⁷⁹, ultralong organic phosphorescence (UOP)²² or room temperature ultralong phosphorescence (RTUP)¹³⁵, has recently gained increasing attention for applications ranging from imaging^{34;48–51} and sensing^{35;42;52} to anti-counterfeiting^{22;23;40;53} and data storage^{54;55}. Benefits of this technology are assigned to its low toxicity¹³⁵, its biocompatibility¹⁸⁰, its wide variety of materials^{12;181} and, for some of these, their easy processability^{35;42}.

Phosphorescence in organic materials usually is observed at liquid nitrogen conditions, and completely disappears when measuring at room temperature (RT). This is mainly due to the increased nonradiative vibrational loss channels from the triplet state. Thus, to achieve purely organic RTP, several challenges have to be overcome. The main goal is a high phosphorescence quantum yield, given by equation 2.41:

$$\Phi_p = \frac{k_{isc}}{k_f + \sum k_{nr,f}} \times \frac{k_p}{k_p + \sum k_{nr,p}}$$

This leads to the following demands for efficient RTP emitters:

- Very high intersystem crossing k_{isc}
- Very small nonradiative triplet decay channels $\sum k_{nr,p} \lesssim k_p$
- Efficient protection from molecular oxygen quenching k_{qT} , which is part of $\sum k_{nr,p}$

Further, for some applications, a long phosphorescent lifetime τ_p is desired, requiring:

- Competitive, but low radiative triplet rate k_p

Realizing especially the first three points in purely organic materials is complicated, on the one hand due to the lack of heavy atoms (cf. Section 2.2.5). On the other hand, a rigidification of the emitters has to be implemented to level down the vibrational nonradiative decay channels. In order to overcome these hindrances, different approaches have already been experimentally tested, which will be discussed in the following.

2.4.1. Crystallization- and Aggregation-Based Emitters

In 2017, Yu et. al. realized an ISC yield of $\Phi_{\text{isc}} = 100\%$ in heavy-atom-free crystalline nano wires by introducing sulfur into a difluoroboron compound (Figure 2.40 a), measured in solution¹⁸². Due to the small molecular weight of the powdery nano wires, the authors were not able to obtain smooth films. The phosphorescence spectrum peaks at $\lambda = 610\text{ nm}$, its yield $\Phi_{\text{p}} = 10\%$ is moderate and the absorption reaches far into the visible, up to $\lambda = 550\text{ nm}$. The respective phosphorescence lifetime $\tau_{\text{p}} = 8.3\text{ }\mu\text{s}$ is rather short, again resulting from the high ISC.

Higher RTP lifetimes, reaching up to $\tau_{\text{p}} = 518\text{ ms}$ for Cz-BP (Figure 2.40 b)¹⁸³ and $\tau_{\text{p}} = 748\text{ ms}$ for CPM (Figure 2.40 c)¹⁸⁴, are reached by incorporating oxygen as carbonyl or carboxyl groups. The corresponding RTP yield is $\Phi_{\text{p}} = 1\%$ for Cz-BP, the overall yield for CPM is $\Phi_{\text{f+p}} = 3\%$. It is stated that ISC here is induced by the intermolecular electronic coupling between the carbonyl C=O and the carbazole units (cf. Figure 2.12 a)¹⁸⁴. Therefore, a close spacing ($\approx 0.3\text{ nm}$) of these moieties via crystallization is necessary. Through this rigidification, nonradiative vibrational losses are reduced¹⁴.

These multi-emitter-involving approaches, further including (H-)aggregation^{21–25}, self-assembly^{19;20}, and (co-)crystallization^{15–18} are the by far most common ways to achieve RTP and are pursued by a great diversity of research groups. However, due to the emitters' powdery shapes, they always come along with difficult processing and limited fields of use^{27;185}. As an example, in Figure 2.41, a compilation of several proposed applications of recent publications is shown, which all use organic afterglow phosphorescence for labeling and data security, but at the same time share the inconvenient powdery structure.

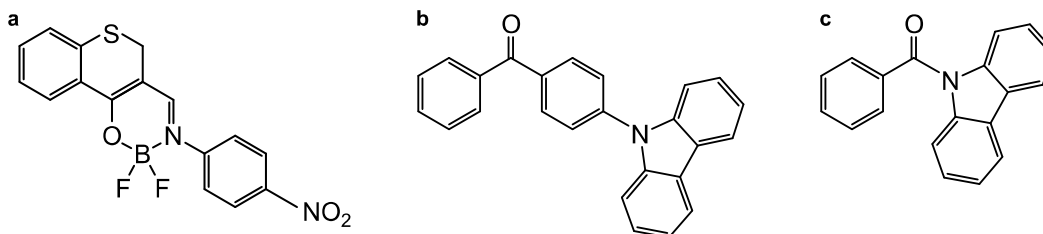


Figure 2.40.: **a** (E)-3-(((4-nitrophenyl)imino)methyl)-2H-thiochroman-4-olate-BF₂ (S-BF₂) with $\Phi_{\text{isc}} = 100\%$. Figure adapted from¹⁸². **b** 4-(9H-carbazol-9-yl)benzophenone (Cz-BP). Figure adapted from¹⁸³. **c** (9H-carbazol-9-yl)(phenyl)methanone (CPM). Figure adapted from¹⁸⁴.

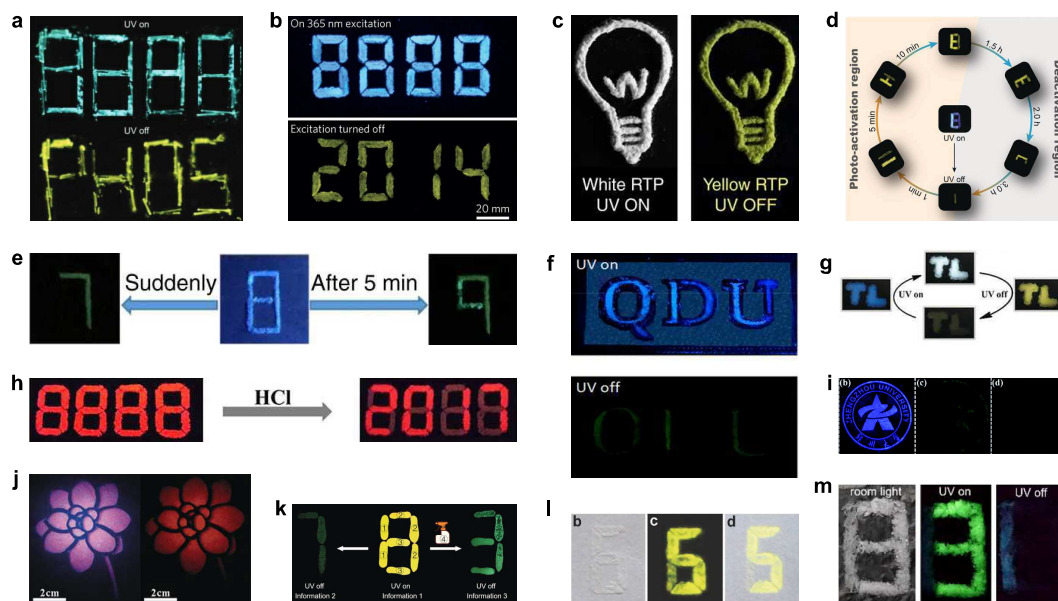


Figure 2.41.: Proposed labeling and security applications of recent crystalline-RTP publications. **a** *o*-PBCM¹⁸⁶. **b** DPhCzT²³. **c** ClBDBT¹⁸⁷. **d** MCzT, PCzT, BCzT, and FCzT¹⁸⁸. **e** CS-CF3 and CS-F⁵¹. **f** QDU-10Cl¹⁸⁹. **g** ImBr¹⁹⁰. **h** S-2CN/I-Ph-NH2 and S-2I/I-Ph-NH2¹⁹¹. **i** Htynca-linked aggregated coordination polymers¹⁹². **j** CDs-MnAPO-CJ50¹⁹³. **k** B15C5¹⁹⁴. **l** *o*-BrTCz¹⁹⁵. **m** Urea and Thiourea¹⁹⁶.

2.4.2. Polymer-Based Emitters

Polymeric materials, which are able to form smooth films, promise better processability³⁵ and are discussed in this section.

One way to reduce nonradiative deactivation pathways is the functionalization of common polymers like PLA with phosphorescent emitters or the careful design of emitting polymers²⁶. Chen et al. successfully combined the rigidity of PLA and the CT-state-enhanced ISC of a donor-acceptor (*D-A*) material (cf. Section 2.2.7). They reached RTP from 1,2-OPh-PLA (Figure 2.42) peaking at $\lambda_p = 510$ nm with a lifetime of $\tau_p = 1.2$ s and a yield of $\Phi_p = 4\%$ ³⁴ when excited with $\lambda_{ex} = 365$ nm in vacuum. As a proof of concept, they show the use as a bioimaging agent in microscopy. Another PLA-based heavy-atom-free RTP polymer is BF₂dbmPLA¹⁹⁷. As thin film it shows fluorescence at $\lambda_f = 442$ nm and very weak phosphorescence at $\lambda_p = 509$ nm. The P2F ratio of this polymer and similar ones could significantly be improved by introducing the heavy atoms bromine and iodine into the molecular structure^{198;199}.

A very high phosphorescence yield was reached by Ma et al.²⁰⁰ by copolymerization of acrylamide and oxygen-containing emitters, enabling enhanced ISC via *n*- π^* tran-

— 2. Theory —

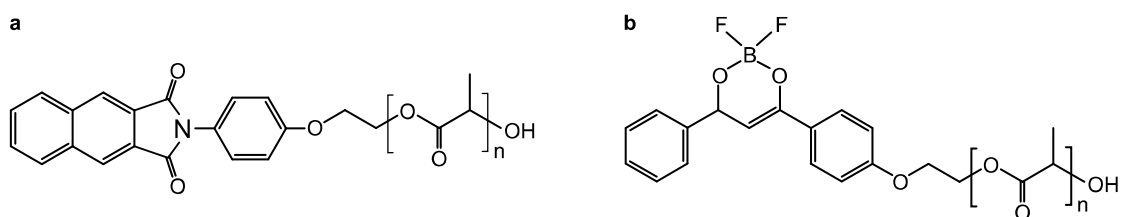


Figure 2.42.: **a** 1,2-OPh-PLA. Figure adapted from²⁰⁰. **b** BF₂dbmPLA. Figure adapted from¹⁹⁷

sitions (cf. Section 2.2.5). When illuminated at $\lambda_{\text{ex}} = 254 \text{ nm}$, a phosphorescence yield $\Phi_p = 31\%$ combined with a lifetime $\tau_p = 195 \text{ ms}$ and emission at $\lambda = 433 \text{ nm}$ was reached for compound P9 (Figure 2.43 b). Further, P3 (Figure 2.43 c) shows notable values of $\Phi_p = 15\%$ and $\tau_p = 537 \text{ ms}$ and was used for the demonstration of water-induced switchable phosphorescence. By wetting the material applied onto paper, the intermolecular hydrogen bonds break, and phosphorescence disappears due to increased nonradiative channels (Figure 2.43 d). This process is reversed by drying the sample.

In 2017, Ogoshi et al. demonstrated RTP in the commercially available polymer Poly(styrene sulfonic acid) (PSS)⁴⁷. For PSS350k, they showed a RTP lifetime $\tau_p = 1.5 \text{ s}$ in the absence of molecular oxygen, and $\tau_p = 1010 \text{ ms}$ in ambient conditions. However, the overall quantum yield $\Phi_{f+p} = 8\%$, including fluorescence and phosphorescence, was rather low. Again dependence on humidity was shown, enabling patterning of emitting layers (Figure 2.44 a).

Polyacrylonitrile (PAN, Figure 2.44 b), an oxygen-barrier polymer, also is able to show RTP resulting from aggregation and $n-\pi$ overlapping²⁰¹. Further routes to

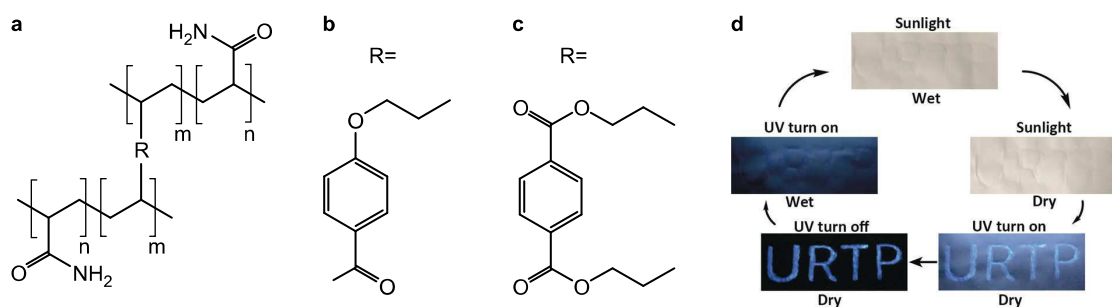


Figure 2.43.: **a** The acrylamide backbone of the polymers P9 and P3, where R is different for P9 (**b**) and P3 (**c**). **d** Reversible phosphorescence of P3, applied on a paper and subsequently wetted and dried. Figures adapted from²⁰⁰.

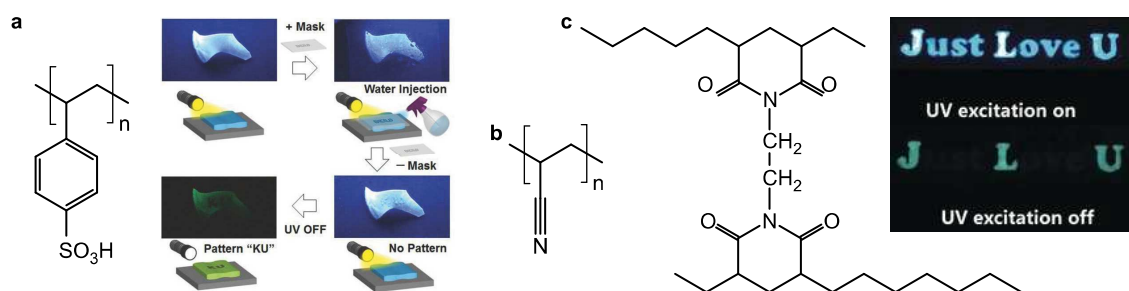


Figure 2.44.: **a** Poly(styrene sulfonic acid) showing humidity-dependent emission. Figure adapted from⁴⁷. **b** Polyacrylonitrile. Figure adapted from²⁰¹. **c** Crosslinked PCDs_{I-1} enabling information encryption. Figure adapted from²⁰².

polymer-based RTP are crosslink-enhanced emission of polymer carbon dots (PCDs, Figure 2.44 c)²⁰² or intermolecular interlocking²⁰³.

Polymer-based RTP materials show enhanced processability compared to crystalline RTP. On the other side, the chemical coupling reactions are often difficult and of high cost²⁶. A less challenging way is the doping of RTP emitters as guests into host material, as described in the following section.

2.4.3. Host-Guest Systems

In host-guest systems, the host material, most commonly a high-band-gap polymer, only acts as a rigid host matrix to space the emitter materials and suppress nonradiative vibrational relaxations of the excited states²⁸. The photophysical processes usually involve the guests only²⁶. From the multitude of publications including PMMA^{28–35}, PS²⁸, PLA^{36–39}, PVA^{40–43} and Zeonex^{44;45} as host materials, several highlights will be discussed in this section.

Very high phosphorescent lifetime $\tau_p = 5.6$ s was realized by Mieno et al. via doping coronene (Figure 2.45 a) into PMMA at low concentration³⁰. Due to the high rigidity of PMMA, nonradiative decay channels were efficiently reduced. The excitation was at $\lambda_{ex} = 380$ nm, and the phosphorescence yield $\Phi_p = 2\%$ was rather low. The rigidity of PMMA films can be dependent on the sample preparation. By using anisole instead of chloroform as solvent, RTP of a host-guest system was drastically raised by Reineke et al²⁸. The anisole's higher boiling point here leads to its slower evaporation, which increases the molecular packing density and reduces nonradiative decay rates.

A phosphor-containing emitter CTP-COOH doped into a PVA host showed a lifetime $\tau_p = 710$ ms with a yield $\Phi_p = 11\%$.⁴⁰ In addition, long lifetimes are also reported for

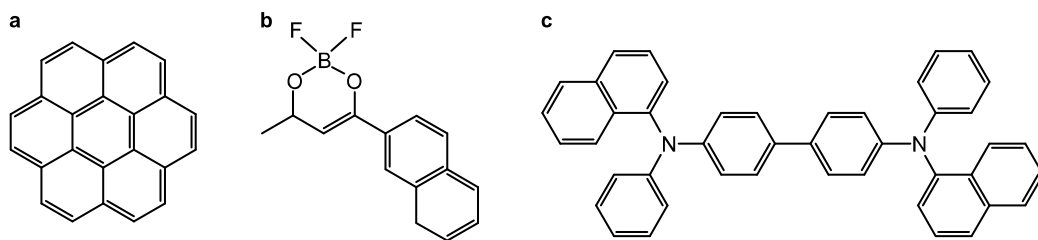


Figure 2.45.: Different guest materials for RTP systems. **a** Coronene. Figure adapted from³⁰. **b** Me-Np-difluoroboron diketonate (BF₂mnm). Figure adapted from³⁷. **c** N,N'-di(naphtha-1-yl)-N,N'-diphenyl-benzidine (NPB). Figure adapted from²⁸.

BF₂mnm (Figure 2.45 b) in PLA ($\tau_p = 612$ ms)³⁷ and for NPB (Figure 2.45 c) in PS ($\tau_p = 400$ ms)²⁸.

D-A materials were also shown to work as RTP guest materials⁴⁵. Chen et al. show, additionally to their polymer 1,2-OPh-PLA (cf. Section 2.4.2), an enhanced RTP emission from the ICT donor-acceptor emitter MeO₃Ph (Figure 2.46 a) embedded in PMMA with $\Phi_p = 4\%$ and $\tau_p = 230$ ms³⁴. They propose a stepwise exciton transition from a local excited singlet state S_1 via ¹CT and ³CT to a local excited T_1 , from where RTP then emerges (cf. Section 2.2.7).

Pander et al. fabricated RTP emitters (Figure 2.46 b and c) by linking different side groups to thianthrene (TA)^{44;204}. Interestingly, pure TA (cf. Figure 2.12 a) doped into PMMA already shows notable RTP due to a folding-induced increase of SOC, peaking at $\lambda = 520$ nm⁴⁶. In some of the TA derivatives synthesized by Pander et al., namely 1b, 1c and 2a, phosphorescence makes 94% of the total emission, indicating a high P2F value. The respective lifetimes range from $\tau_p = 6$ ms for 1b and $\tau_p = 11$ ms for 2a to $\tau_p = 88$ ms for 1c, and the overall quantum yields ($\lambda_{ex} = 355$ nm) are given as $\Phi_{f+p} = 22\%$ (1b), $\Phi_{f+p} = 42\%$ (2a) and $\Phi_{f+p} = 12\%$ (1c). The phosphorescence spectra of 1b and 1c resemble, apart from a tiny redshift, the triplet emission of pure TA, indicating the lack of conjugation between TA and the side groups. This is in contrast to 2a, where the spectrum is of lower energy and changed in shape, hinting at enlarged conjugation. As reason for this intense phosphorescence, the influence of the heteroatom sulfur is given. In all three emitters, the triplet emission was fully quenched in the presence of oxygen.

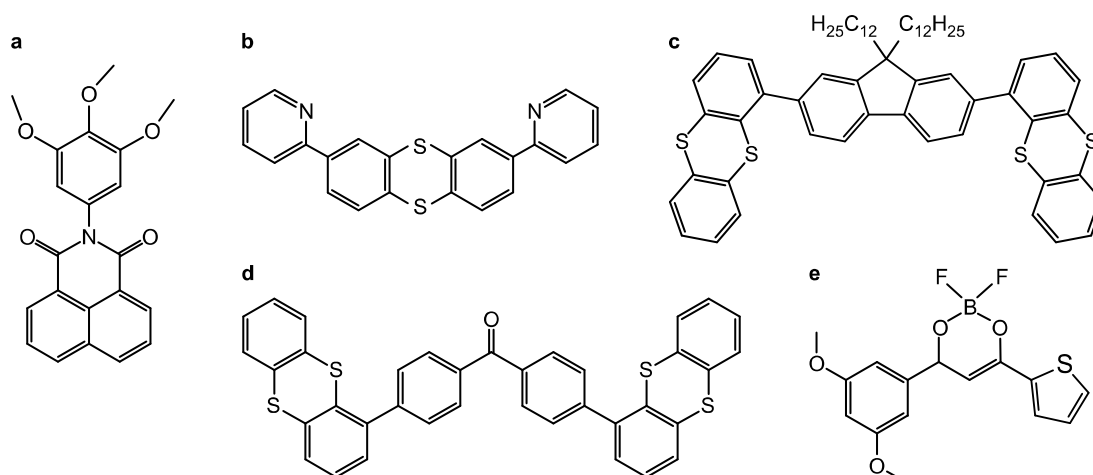


Figure 2.46.: Donor-acceptor and thianthrene based materials. **a** MeO₃Ph. Figure adapted from³⁴. **b** Compound 2a. **c** Compound 1c. Figures adapted from⁴⁴. **d** 4,4'-dithianthrene-1-yl-benzophenone (BP-2TA). Figure adapted from⁷¹. **e** Difluoroboron β -diketonate (BF₂dk). Figure adapted from²⁰⁵.

Similar results, involving a *D-A* RTP emitter consisting of two TA units as donors and the triplet emitter benzophenone (BP) as acceptor, were recently presented by Tomkeviciene et al⁷¹. Their BP-2TA (Figure 2.46 d) shows weak prompt solvatochromic CT state emission and phosphorescence with high P2F. This hints at CT-state-enhanced ISC being the reason for the high triplet emission, as described in Section 2.2.5. They note a phosphorescence lifetime $\tau_p = 14$ ms and a fluorescence yield in air $\Phi_f = 1\%$. Very recently, DeRosa et al. introduced a difluoroboron β -diketonate (BF₂dk, Figure 2.46 e) embedded in PLA with a P2F value > 2 and visible absorption up to $\lambda = 440$ nm²⁰⁵. Phosphorescence peaked at $\lambda_p = 560$ nm and showed a lifetime of $\tau_p = 154$ ms. They once more claim enhanced ISC via the formation of a intramolecular CT state as the origin of RTP.

An overview of the different presented RTP materials is given in Table 2.5.

— 2. Theory —

Table 2.5.: Crystalline and aggregated (Cry), polymeric (Pol), and host:guest (H:G) heavy atom free RTP materials and their properties.

| RTP material | Shape | λ_{abs} | λ_{p} | Φ_{p} | τ_{p} | P2F |
|--|-------|-----------------------------|----------------------|-------------------|------------------------------|----------------------|
| S-BF ₂ ¹⁸² | Cry | up to 500 nm | 610 nm | 10% | 8.3 μ s | $\sim 10^{\text{i}}$ |
| Cz-BP ¹⁸³ | Cry | up to 390 nm | 552 nm | 1% | 518 ms | < 1 |
| CPM ¹⁸⁴ | Cry | up to 370 nm | 530 nm | $< 3\%$ | 748 ms | < 1 |
| 1,2-OPh-PLA ³⁴ | Pol | around 365 nm ⁱⁱ | 510 nm | 4% | 1.2 s | 11 |
| BF ₂ dbmPLA ¹⁹⁷ | Pol | around 365 nm ⁱⁱ | 510 nm | - | 170 ms | < 1 |
| P9 ²⁰⁰ | Pol | up to 340 nm | 433 nm | 31% | 195 ms | - |
| P3 ²⁰⁰ | Pol | up to 310 nm | 427 nm | 15% | 537 ms | - |
| PSS ⁴⁷ | Pol | up to 420 nm | 496 nm | $< 8\%$ | 1.5 s | < 1 |
| PAN ²⁰¹ | Pol | up to 400 nm | 440 nm | very low | ~ 100 ms ⁱⁱⁱ | < 1 |
| PMMA:Coronene ³⁰ | H:G | up to 355 nm | 550 nm | 2% | 5.6 s | 0.2 |
| PVA:CTP-COOH ⁴⁰ | H:G | around 280 nm ⁱⁱ | 480 nm | 11% | 710 ms | - |
| PLA:BF ₂ mm ³⁷ | H:G | up to 410 nm | 526 nm | - | 612 ms | < 1 |
| PS:NPB ²⁸ | H:G | around 365 nm ⁱⁱ | 530 nm | - | 400 ms | < 1 |
| PMMA:MeO ₃ Ph ³⁴ | H:G | around 365 nm ⁱⁱ | 541 nm | 4% | 230 ms | > 39 |
| PMMA:TA ⁴⁶ | H:G | up to 280 nm | 520 nm | - | 2.4 ms | 2...4 |
| PMMA:1b ⁴⁴ | H:G | up to 320 nm | 525 nm | 22% | 6 ms | ~ 16 |
| PMMA:1c ⁴⁴ | H:G | up to 360 nm | 525 nm | 12% | 88 ms | ~ 16 |
| PMMA:2a ⁴⁴ | H:G | up to 360 nm | 560 nm | 42% | 11 ms | ~ 16 |
| Zeonex:BP-2TA ⁷¹ | H:G | up to 360 nm | 530 nm | - | 14 ms | ~ 8 |
| PLA:BF ₂ dk ²⁰⁵ | H:G | up to 440 nm | 560 nm | - | 154 ms | > 2 |

ⁱ Estimated from spectrum. ⁱⁱ Excitation wavelength used. ⁱⁱⁱ Estimated from delayed spectrum.

2.4.4. Protection Against Oxygen Quenching

As discussed in Section 2.3.2, oxygen-induced quenching k_{qT} is a very efficient non-radiative pathway, which depopulates the emitter's triplet state:

$$\frac{d[T_1]}{dt} = k_{\text{isc}}[S_1] - \frac{[T_1]}{\tau_{\text{p}}} - k_{\text{qT}}[\text{O}_2][T_1].$$

To reduce this loss channel, the interaction of $[T_1]$ and $[\text{O}_2]$ has to be minimized. This is realized by several different approaches²⁰⁶. One way is to functionalize the

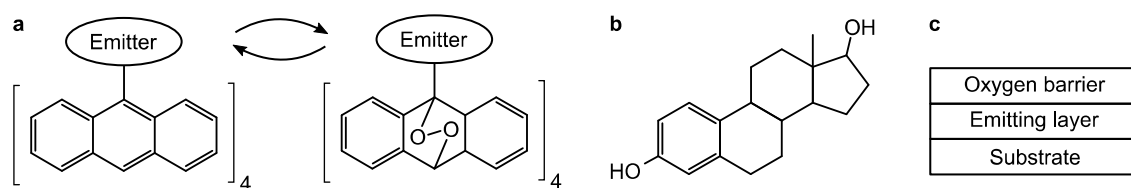


Figure 2.47.: **a** Reversible photosensitized oxygen addition. Figure adapted from¹⁷⁴. **b** β -estradiol, a steroidal oxygen barrier host material. Figure adapted from²⁰⁷. **c** Oxygen shielding via an additional barrier layer.

emitters with protective groups like dendrimers, cyclodextrins or $^1\text{O}_2$ -binding moieties. The latter was successfully realized by upgrading a phosphorescent material with diphenylanthracene subunits, which are able to reversibly form endoperoxides via chemical quenching of oxygen (Figure 2.47 a)¹⁷⁴. Thus, local oxygen around the emitter was removed upon excitation. However, the O_2 -shielding is limited in time and total uptake, since every subunit interacts with one oxygen molecule at a time only.

Since their OTR is too high (cf. Section 2.1.11), in common polymers like PMMA, PS, PLA or Zeonex, RTP usually is fully quenched by ambient molecular O_2 . Hirata et al. realized RTP from a host-guest system in ambient conditions, where different emitters were doped into a host matrix consisting of β -estradiol (Figure 2.47 b)²⁰⁷. This steroidal material showed very low oxygen diffusion, leading to stable RTP emission even after sample storage in air for more than 11 days.

There are some further examples of organic RTP in air^{47;208;209}, but none of these solutions is of general nature.

A feasible and effective strategy to protect RTP materials from ambient oxygen is coating the emitting layer with an oxygen-barrier layer with low OTR (Figure 2.47 c), for example EVOH, Exceval or PAN (cf. Section 2.1.11). In addition to these conventional polymers, nanofibrillated cellulose (NFC) as a biodegradable material was also shown to act as an oxygen barrier layer for organic phosphorescent emitters²¹⁰. When applied to a PLA layer, a thin ($\sim 400\text{ nm}$) film of NFC reduced the overall oxygen permeability to $\sim 0.13\%$ of the uncoated value²¹¹.

2.4.5. Stimuli-Responsive RTP Systems

In this section, recent applications utilizing the interplay of RTP emitters and external stimuli like temperature, oxygen, water or light are presented. Especially for

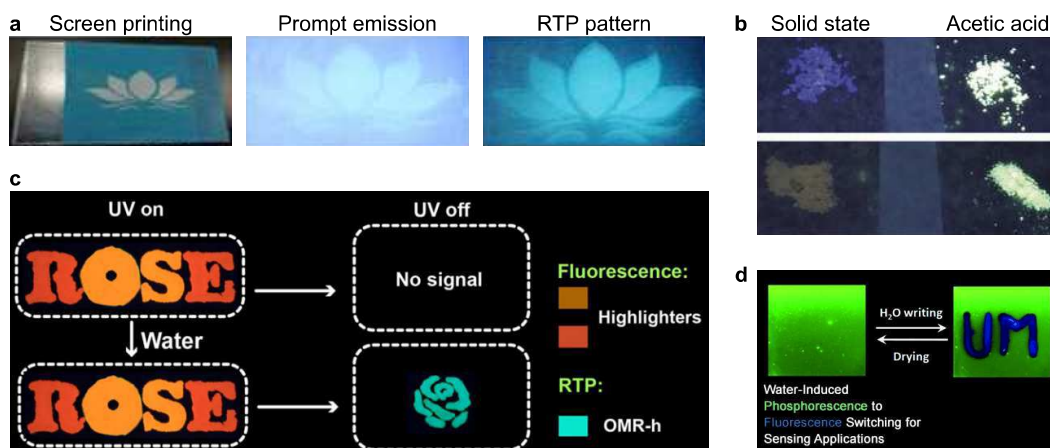


Figure 2.48.: **a** From left to right: Mask on top of the PVA:CTP-COOH film used to photoprint the RTP-pattern; Prompt emission under UV light; Delayed RTP emission showing the imprint. Figure adapted from⁴⁰. **b** RTP crystals DSQ and DSP before and after exposure to acetic acid vapor. **c** Security application using water-induced RTP emission from OMR-h. Figure adapted from²¹⁵. **d** Sensing application using water-induced RTP quenching in PVA:Br6a. Figure adapted from⁴².

the latter, the focus is on interactions beyond simple absorption and emission of photons, but rather on light-induced conformational or chemical modifications. A larger field of interest, yet not in the main scope of this thesis, is RTP-based oxygen sensing^{115;212–214}. Here, the ratio of RTP intensities or lifetimes with and without oxygen is used to calculate the ambient oxygen concentration.

Crystalline RTP materials showing an increase of emission via UV illumination were already sketched in Figure 2.41 d, e and g. As origin of the RTP, a UV-induced conformational change of the crystals is proposed^{51;190}, which can also be reversible¹⁸⁸. Su et al. showed UV-activated RTP in a PVA based host-guest system⁴⁰. They illuminated a non-phosphorescing sample with a wavelength of $\lambda = 254$ nm for 65 minutes, and achieved RTP via cross-linking H-bonds between PVA and the guest CTP-COOH. By applying masked illumination, RTP patterns were photoprinted into the layer (Figure 2.48 a). A printed image then could be deleted and restored again via water injection and heating, respectively.

Further RTP-enhancing morphological changes of crystals were shown resulting from post-hoc treatment with potassium ions (cf. Figure 2.41 k)¹⁹⁴ or acetic acid (Figure 2.48 b)²¹⁶. Interestingly, acidizing can also lead to the suppression of RTP, as shown for S-2I/I-Ph-NH₂ crystals and hydrochloric acid (Figure 2.41 h)¹⁹¹. Similar, the presence of water or moisture can both lead to intensification or weakening

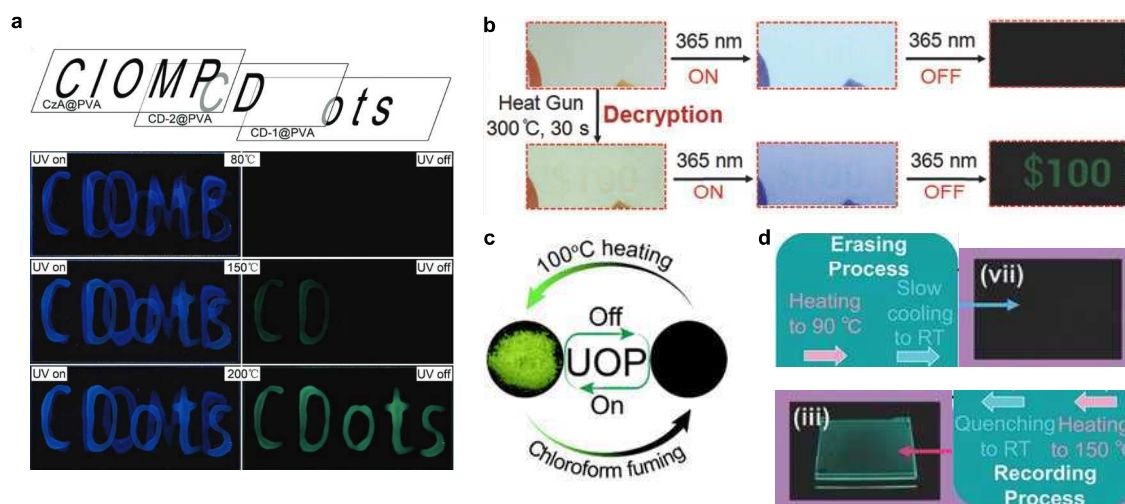


Figure 2.49.: Heating induced RTP modifications. **a** The carbon dots CD-1 (bottom, "ots") and CD-2 (middle, "CD") show RTP emission after different annealing temperatures. Figure adapted from²¹⁷. **b** Heat decrypted RTP tag. Figure adapted from⁵³. **c** Reversible activation from crystalline RTP by heating and solvent fuming. Figure adapted from²¹⁸. **d** RTP erasing and recording processes via different heating and cooling parameters. Figure adapted from⁵⁴.

of RTP. Liang et al. presented water-induced RTP emission resulting from the formation of a network of hydrogen bonds between H_2O and the crystalline emitter²¹⁵ (Figure 2.48 c). On the other hand, water destroyed the halogen and hydrogen bonds in polymeric⁴⁷ (cf. Figure 2.44 a) and host-guest⁴² systems (Figure 2.48 d), here leading to a reversible switching of RTP emission.

Besides a straightforward use of the temperature dependence of RTP as sensing material³⁵, there are further different approaches to manipulate the phosphorescence by heating. Tian et al. improved RTP from carbon dots by a heat induced bonding of the emitters to the host material PVA²¹⁷. Through annealing at 150°C and 200°C, they realized a stepwise appearance of RTP by two differently prepared emitters CD-1 and CD-2 (Figure 2.49 a). Another approach involving thermal treatments of quantum dots led to an invisible anti-counterfeiting tag, which could be decrypted by applying heat and therefore activating RTP (Figure 2.49 b)⁵³. In combination with chloroform fuming, high temperature treatment facilitated reversible activation of the crystalline RTP emitter TDP-CF (Figure 2.49 c)²¹⁸. A RTP system, which mainly was sensitive to the cooling time after heating, was realized by Hirata et al.⁵⁴. At fast cooling from 150°C to room temperature, the guest emitters were distributed homogeneously into

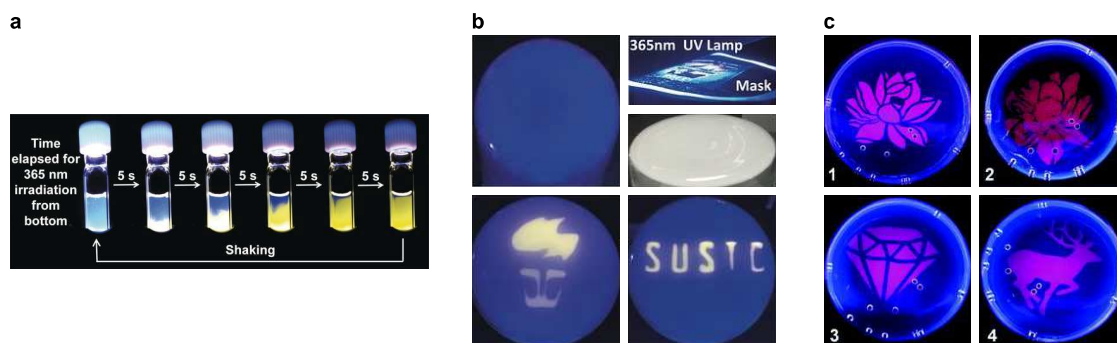


Figure 2.50.: **a** Activation and deactivation of phosphorescence via illumination and shaking of Au-2 in solution. **b** DMSO gel in UV and daylight and a printing mask (top). Different RTP patterns photoprinted into the gel subsequently (bottom). Figures adapted from⁵⁵. **c** Multiple patterns printed into the same RTP sample. Figure adapted from²¹⁹.

the host materials α, α, α' -tris(4-hydroxyphenyl)-1-ethyl-4-isopropylbenzene (THEB) mixed with the steroid cholesterol, resulting in efficient RTP. At slow cooling from 90°C to RT, the guest formed aggregates, which showed drastically reduced emission. This behavior was used in a simple reversible recording medium (Figure 2.49 d).

A completely different approach was realized by Wan et al.⁵⁵. They showed the emergence of phosphorescence via UV illumination, but in contrast to the previously shown techniques, the RTP increase is not resulting from a morphological change. Instead, surrounding molecular oxygen is chemically quenched by the DMSO solution molecules (cf. Section 2.3.3). Due to the concomitant decrease of molecular O₂ concentration, this nonradiative triplet decay channel k_{qT} gets insignificant and RTP can occur (Figure 2.50 a). By shaking the solution, the oxygen redistributes and the phosphorescence is quenched again. They further realized a liquid gel-like shape of this system, and were able to reversibly photoprint different RTP patterns, which could be erased by heating the gel (Figure 2.50 b). Also without heating, the schemes disappeared after a few hours due to oxygen diffusion. Lin et al. showed multiple rewriting up to ten times in similar gel structures (Figure 2.50 c)²¹⁹.

3. Methods

A short overview over the experimental methods is given in this chapter, including sample preparation, measurement techniques, and data evaluation.

3.1. Sample Preparation

The general procedure of sample preparation is described in the following. All prepared samples were stored in darkness in ambient atmosphere. A detailed description of all materials investigated in this thesis can be found in Section 5.

3.1.1. Solution Preparation

If not stated differently, the powdery or pellet-shaped materials were dissolved in anisole (methoxybenzene). The guest compounds' concentration was 10 mg ml^{-1} , and the solution was stirred at 70°C for several hours. For $\text{BF}_2(\text{HPhN})$ (cf. Section 5.1.3), 2 mg ml^{-1} was chosen to reach its full dissolution. For the host materials, the concentration was 80 mg ml^{-1} , and the solution was stirred at 70°C for several hours. In order to reach the desired host:guest weight ratio, the two solutions were mixed appropriately. Exceval, which was used as oxygen-barrier material was dissolved in pure water at 50 mg ml^{-1} and stirred in a sealed vial at 130°C to 160°C for one hour.

3.1.2. Coating Techniques

The final solutions were applied to a cleaned quartz substrate of 25 mm edge length (Figure 3.1). Some substrates were of bigger size or flexible nature, in which case it will be denoted. The different coating techniques will be presented briefly in the following.

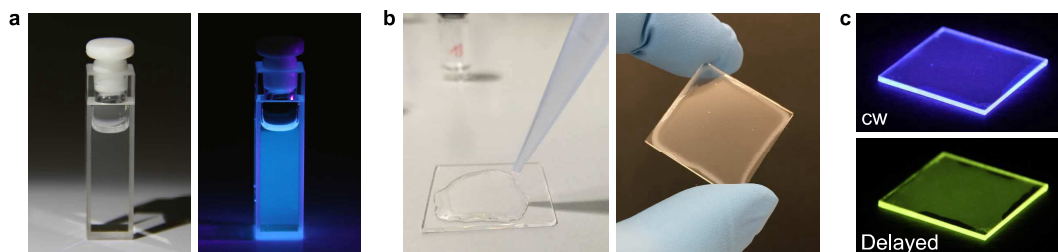


Figure 3.1.: **a** A host:guest solution in ambient and UV light. **b** The process and the result of drop casting. **c** A two-layered spin-coated sample showing prompt and delayed emission, respectively.

Spin Coating

The first of the two main preparation techniques was spin coating. Here, the quartz substrate was vacuum-fixed onto a rotating plate. After dropping 150 μl of the host:guest-solution onto the quartz, it was spinned for 60 s at a speed of 2000 rpm. Therefore, smooth emitting layers of a height of around 900 nm were obtained. If necessary, the oxygen barrier layer was coated on top by using 500 μl of the watery solution in the same process. Due to the orthogonality of anisole and water, this second solution did not dissolve the underlying film and thus could easily applied. Depending on the necessity of molecular oxygen inside the emitting layer, spin coating was either performed in ambient air or in an inert nitrogen glovebox.

Drop Casting

The second import coating technique was drop casting, which was used to obtain thick films and therefore higher emission intensities compared to the spin-coated samples. By dropping 500 μl of the host:guest-solution onto the substrate, a film thickness of around 40 μm could be reached after drying for one day. Drop casting of the optional Exceval layer was also performed by using 500 μl of solution and again letting the sample dry for one day. For some two-layer samples, both spin coating and drop casting were used for one layer, respectively.

3.2. Photoluminescence Spectroscopy

If not stated differently, the samples were illuminated normal to the substrate plane with a collimated 365 nm UV LED M365L1 by Thorlabs. The full setup was light-

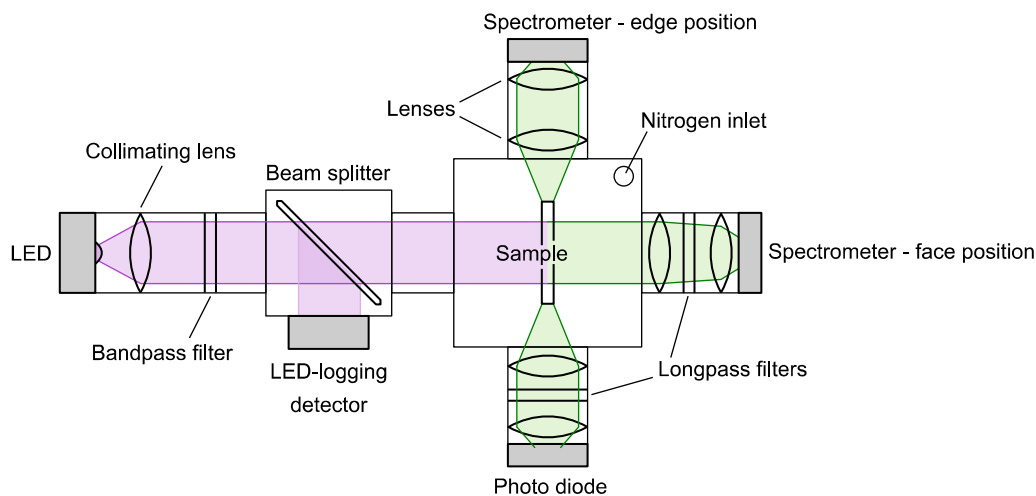


Figure 3.2.: Setup for spectral and millisecond-regime measurements.

and air-tight and could be purged with gaseous nitrogen N₅ or used in ambient conditions. For photoluminescence spectra, a CAS 140CTS spectrometer from Instrument Systems was used. The spectra were either taken in edge-emission or face-emission position (Figure 3.2). Both channels were upgraded with focusing lenses to enhance the intensity of the signal. Edge emission shows a better signal-to-LED ratio, but may be affected by spectral distortions due to reabsorption and waveguide effects. On the other hand, for face emission, a 400 nm longpass wavelength filter had to be inserted to block the excitation light. Integration time usually ranged from $t_{\text{int}} = 0.2$ s to $t_{\text{int}} = 2$ s, and the LED was running in continuous wave (cw) mode.

3.2.1. Time-Gated Spectra

Time-gated spectra for delayed emission were obtained by triggering the LED, and subsequently the spectrometer by using a pulse generator TGP3122 by AIM-TTI Instruments. Shortly after turning off the LED, a spectrum was recorded with an integration time of $t_{\text{int}} = 0.45$ s. If necessary, this measurement was cyclically repeated and the spectra were averaged.

3.3. Time-Resolved Measurements

The spectrometer is not suitable to achieve high time resolution in the nano- or millisecond regime, which is necessary to obtain the state lifetimes of the excited

triplet and singlet states, respectively. Therefore, below, further detection methods are introduced.

3.3.1. Lifetime-Determination in the Millisecond Regime

Measurement Technique

For the millisecond regime, a PDA100A photo diode by Thorlabs was used to detect the emission signal in edge emission. The data were recorded using an oscilloscope Infinium 500 MHz by Hewlett Packard (cf. Figure 3.2). In order to increase the signal-to-noise ratio, a focusing lens system was installed in front of the photo diode. Excited state lifetimes were determined by acquiring the exponential decay of the emission after turning off the excitation LED.

Data Evaluation

The standard processing routine of the resulting data was fitting with a biexponential decay curve and subsequently calculating the intensity-weighted average lifetime $\bar{\tau}$ of the two exponents via⁷⁵

$$\bar{\tau} = \frac{a_1\tau_1^2 + a_2\tau_2^2}{a_1\tau_1 + a_2\tau_2}. \quad (3.1)$$

The intensity-averaged lifetime $\bar{\tau}$ is a reliable measure of the afterglow time and should be preferred over the amplitude-weighted lifetime⁷⁵.

3.3.2. Lifetime-Determination in the Micro- and Nanosecond Regime

Measurement Technique

In contrast to emission on the millisecond timescale, fluorescent and fast phosphorescent decays in the nano- and microsecond regime require a more advanced approach, namely a time-correlated single photon counting (TCSPC) setup. Here, a 375 nm UV picosecond-pulsed laser LDHDC375 from PicoQuant excited the sample repeatedly with a frequency of around 500 kHz. The laser intensity had to be set to a value which resulted in one single emitted photon reaching the detector for every hundredth excitation pulse. The highly sensitive detector, a PMA Hybrid 40 from PicoQuant,

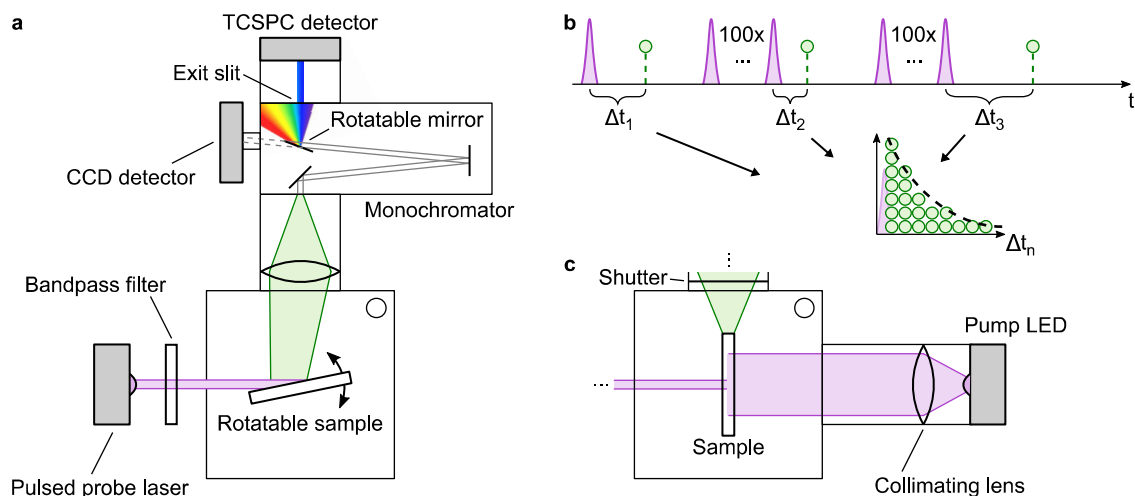


Figure 3.3.: **a** Setup for wavelength resolved TCSPC measurements. **b** Measurement principle of TCSPC. **c** Setup modification for pump probe experiments.

associated every single arriving photon with a time stamp at a resolution of down to 25 ps. A continuously running measurement therefore created a histogram of photon arrival times, from which the decay of the excited state could be obtained (Figure 3.3 b). As part of this thesis, this setup was upgraded with a monochromator unit SpectraPro HRS-300, which enabled wavelength-resolved TCSPC detection in the complete visible range of the spectrum (Figure 3.3 a). Further, an optional high-intensity cw UV LED source was temporarily attached for generating high triplet densities in order to detect STA effects using the pump-probe method (Figure 3.3 c). Here, the precise timing of the shutter in front of the TCSPC detector was necessary to ensure the detection immediately after the LED turnoff. Therefore, measurements at high triplet density, but without steady-state emission were realized. This was necessary as the latter would have saturated or destroyed the detector unit. In addition, the charge-coupled device (CCD) detector, which was additionally attached to the monochromator, allowed to record spectra at the TCSPC setup, which were used to verify the wavelength resolved TCSPC data.

Data Evaluation

The resulting raw decay measured at the detector is a convolution of the actual signal and the laser-correlated instrument response function (IRF). The IRF mainly originates from the exciting laser pulse, which is not infinitely short, but has a certain

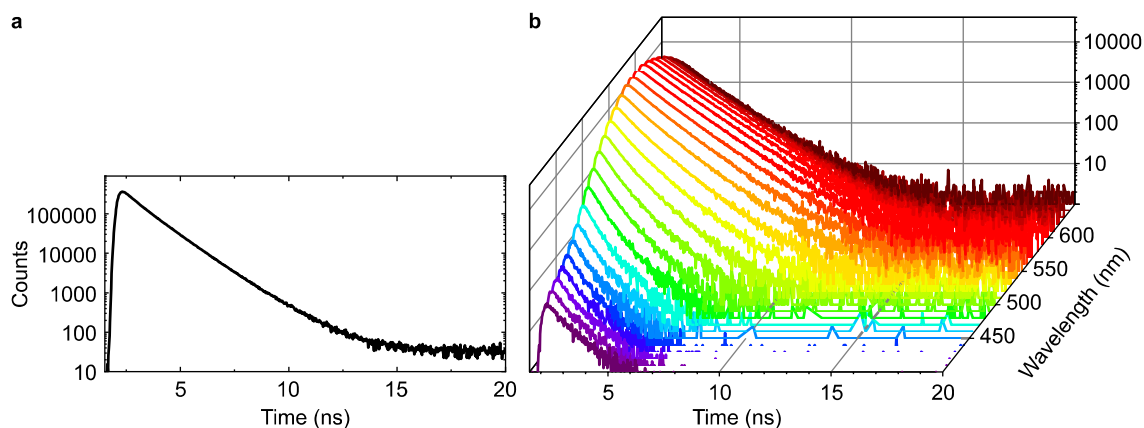


Figure 3.4.: Measurements before and after the upgrade of the TCSPC setup. **a** Data as obtained using the old setup without wavelength resolution. **b** Wavelength dependent measurements on the upgraded setup. The data show the nanosecond decays of PMMA:NPB:DCJTb (cf. Section 5.2.1).

extent in time. In order to obtain the true signal of the sample, the software FluoFit from PicoQuant was used. It approximates the raw decay by an exponential function and thereafter convolutes the IRF to the resulting fit. The outcome then is optimized to resemble the raw data until they match. Using this reconvolution, the excited states' lifetime is determined. This procedure is essential for lifetimes below $\tau \approx 100$ ns. For microsecond lifetimes, a simple exponential fit is sufficient.

3.3.3. Further Time-Resolved Techniques

Phosphorescence-Activation Monitoring

For the acquisition of the chemical-quenching-induced activation curve of the phosphorescence, different techniques were applied. The detailed procedures will be discussed in the respective sections.

Long-Time-Performance Measurements

In order to test the stability of the activated phosphorescence, a long-time measurement routine was established, using a LabView software by Martin Kroll and a VirtualBench VB-8012 by National Instruments. By that, it was possible to precisely trigger all relevant measurement devices on a timescale of many hours up to days.

3.4. Quantum-Yield Determination

In order to obtain the photoluminescent quantum yield (PLQY), the ratio of emitted to absorbed photons had to be determined (cf. Section 2.28).

3.4.1. Measurement Technique

For the determination of the PLQY of a sample, it is placed into an integrating sphere, which collects its emission in every direction. Illumination is realized using a collimated 340 nm UV LED. According to de Mello²²⁰, in addition to one measurement of the empty sphere (A) and one of the sample (C), an additional measurement (B) is necessary, where the sample is only indirectly illuminated by the reflections of the light on the inner sphere (Figure 3.5).

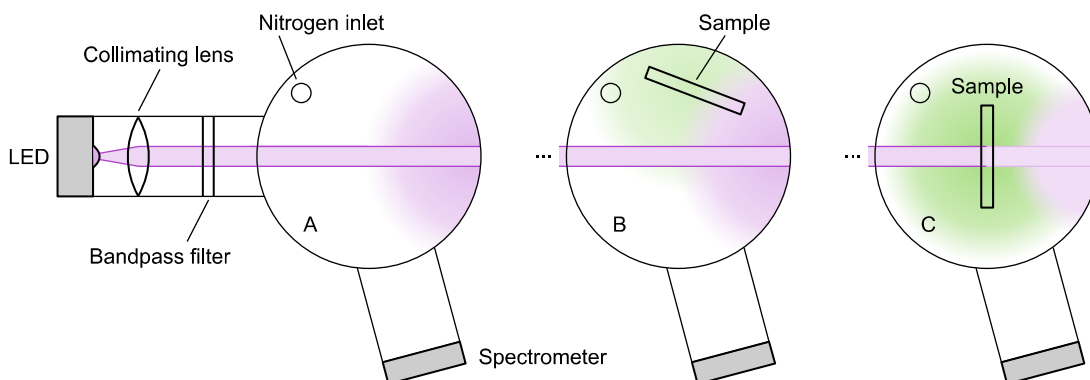


Figure 3.5.: Setup for PLQY measurements, showing measurements A, B and C.

3.4.2. Data Evaluation

In each data set, the spectrum has to be converted to the number of photons, and the excitation $X_{A,B,C}$ is then spectrally separated from the emission $E_{B,C}$. The absorption A can be calculated via²²¹

$$A = 1 - \frac{X_C}{X_B} \quad (3.2)$$

and the PLQY results in

$$\Phi = \frac{E_C - (1 - A)E_B}{AX_A}. \quad (3.3)$$

The reliability of these measurements could be increased by measuring A, B and C multiple times and cross-correlating all measurements to get a Gaussian distribution of PLQY values²²¹. The center of this peak was used to denote the respective PLQY value.

For PLQY of the fluorescence, Φ_f , the samples were measured in ambient atmosphere. For phosphorescence PLQY, Φ_p , if not marked otherwise, nitrogen atmosphere was used. This measurement resulted in the total PLQY of both emissions. In the simplest case, Φ_p was just the difference of the nitrogen-atmosphere value to the ambient value. However, in the presence of triplet-related reduction effects of fluorescence like STA, this approach leads to wrong values. Therefore, the phosphorescence PLQY had to be measured at a very low excitation density, where these effects were reduced as much as possible. For very low relative fluorescence signals, Φ_f was evaluated using a spectral analysis of a spectrum containing both fluorescence and phosphorescence. This spectrum was converted in photon numbers and divided in fluorescent and phosphorescent emission. The overall PLQY value was therefore distributed into Φ_p and Φ_f in the respective ratio. In this case, also the P2F value was gained via spectral calculations and not by comparing Φ_p and Φ_f .

3.5. Evaluation of Absorption

3.5.1. Absorbance and Transmission Measurements

To measure the wavelength-dependent absorbance or transmission, a Multi-Purpose Large-Sample Compartment MPC-3100 from Shimadzu was used. Here, two identical light beams pass through the sample and a reference substrate. Using two synchronous monochromators, the wavelength of these beams can be scanned from UV-B to infrared and their intensity change is measured and converted into transmission and absorbance values.

3.5.2. Excitation-Scan Technique

Another technique for the investigation of the absorption properties of a sample is performing an excitation scan using the SPEX FluoroMax from Horiba. Here, the excitation sweeps through defined wavelengths, and the sample's emission is detected at a certain spectral position, mostly the peak emission position. Via the inten-

sity change in emission, information about the absorption channels leading to these photons is given.

3.6. Further Measurement Techniques

3.6.1. Determination of Film Thickness

The thickness of the coated films was determined by scratching thin furrows into the organic film and then scanning this area using a Veeco Dektak 150 Profilometer.

3.6.2. Measurements at Low Temperature

Liquid Nitrogen Bathing

To realize measurements at 77 K, the sample was put into a liquid nitrogen bath, from which spectra and decays were acquired.

Peltier Cooling

For experiments where cooling of the samples to around 0°C was necessary, a peltier element was used.

3.6.3. Resolution Determination

The resolution of the luminescent tags was determined using a USAF1951 test target and a self-assembled microscope. The latter consisted of two properly aligned convex lenses and a simplistic sample stage.

3.6.4. Photograph Acquisition

If not denoted differently, all photos were taken using a digital single-lens reflex camera EOS60D from Canon.

4. Basic Principles of Programmable Luminescent Tags

This chapter covers the basic working principles of programmable luminescent tags (PLTs), which were developed in this thesis. A PLT consists of an emitting layer, which is covered with an oxygen-barrier layer (Figure 4.1). The thickness of the two layers ranges from around one to tens of micrometers in total. The emitting layer is a host-guest RTP system. Both layers are processed in ambient conditions. Therefore, the emitting layer still contains molecular oxygen (Figure 4.2 a). In this state, excited triplet states are fully quenched by O_2 , which is why it is termed the *deactivated* or *non-activated* state. In the *activated* state, the oxygen concentration is below a certain threshold value ϑ_{O_2} , and the triplets are radiative. The possibility of partly and spatially resolved activation of the sample enables the printing of a phosphorescent pattern which contrasts to the non-activated areas (Figure 4.2 b). Via a repopulation with oxygen, the luminescent images can be erased and the PLT

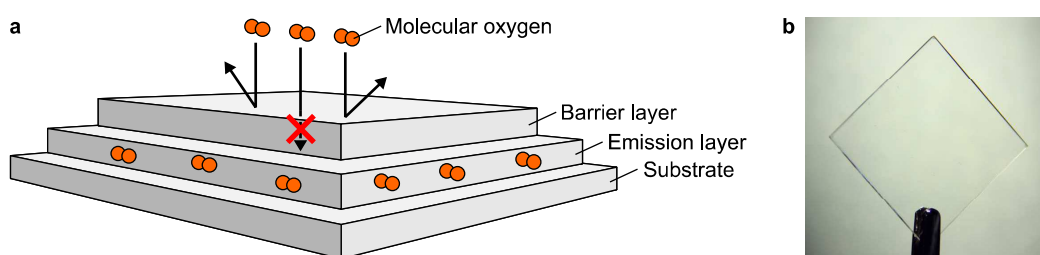


Figure 4.1.: **a** The general structure of a programmable luminescent tag (PLT). The RTP-emission layer is embedded between the substrate and the oxygen-barrier layer, which prevents the diffusion of ambient gas molecules into the sample. Still, due to the preparation in ambient conditions, some residual molecular oxygen is still present in the emission layer. Note that the layer thicknesses are not in scale. **b** A PLT in ambient light.

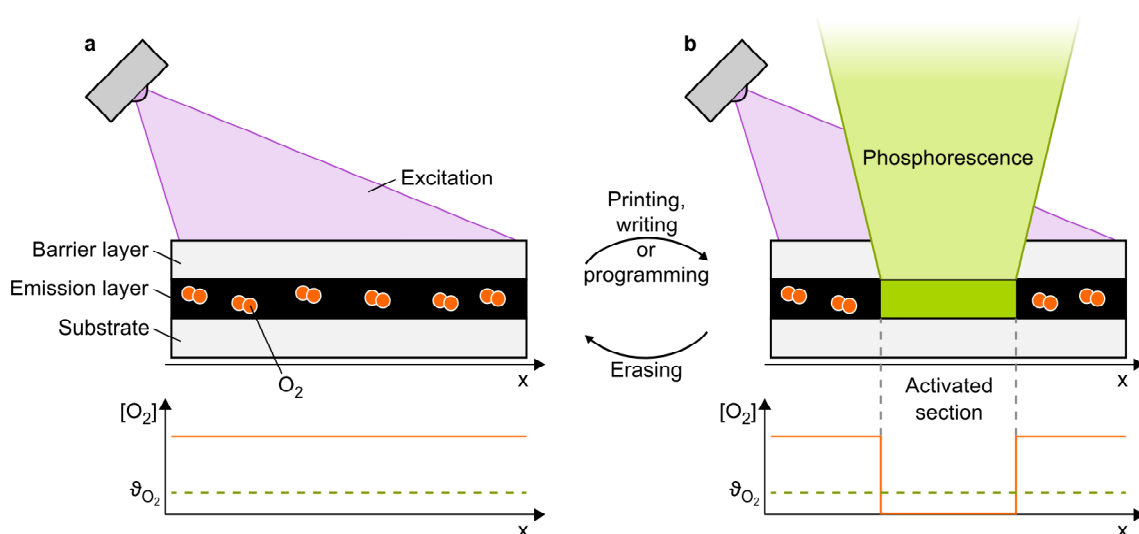


Figure 4.2.: Schematic illustrations of the different states of PLTs. **a** Top: a PLT in the fully non-activated state under excitation, showing no phosphorescence. Bottom: the oxygen concentration (orange) is above the threshold ϑ_{O_2} (dashed green), below which the triplets become radiative. **b** Top: a PLT, which is partly in the activated state, from where it emits phosphorescence when excited. Bottom: the oxygen concentration in the activated region is below ϑ_{O_2} .

is set to its original deactivated state. The physical and technical background of this cycle is described in detail in this chapter, where the schematics presented in Figure 4.2 will be used to illustrate the interplay of excitation, emission, and oxygen concentration.

The chapter is split up in four parts: first, the activation process is addressed, also referred to as *printing*, *writing*, or *programming* (Section 4.1). Second, the preservation of the imprint is illustrated (4.2). Then, the deactivation or *erasing* techniques are presented (Section 4.3), and in Section 4.4, the multiple repetition of this cycle is addressed. For all PLTs, the oxygen barrier material was Exceval and, if not stated differently, the emission layer consisted of PMMA550k as host, with the RTP emitter N,N'-di(naphtha-1-yl)-N,N'-diphenyl-benzidine (NPB) doped at 2 wt% as guest material. This host-guest system showed fluorescence and, in the absence of oxygen, additional phosphorescence. For details on further photophysical properties, see Section 5.1.1 in the next chapter.

4.1. Activation - Removing of Molecular Oxygen

4.1.1. Dynamics of Activation

Measurements showed that a freshly prepared PLT containing NPB did not show phosphorescence, but only intense fluorescence at around $\lambda_f = 420$ nm when excited at $\lambda_{ex} = 365$ nm (Figure 4.3 a). Through ongoing excitation, at some point phosphorescence at around $\lambda_p = 540$ nm began to appear (Figure 4.3 b). This increase was overlaid by the intense fluorescence, but could be seen with the naked eye using pulsed excitation (Figure 4.3 c, right). Due to the long lifetime of the triplet states, the PLT showed green phosphorescence after turning off the illumination, which will be denoted as delayed emission. A sample without an oxygen barrier layer did not show phosphorescence at any time (Figure 4.3 c, left), but only blue fluorescence in cw emission.

These results suggest the involvement of molecular oxygen, which originally is present in both samples with and without oxygen barrier. At that time, virtually all excited

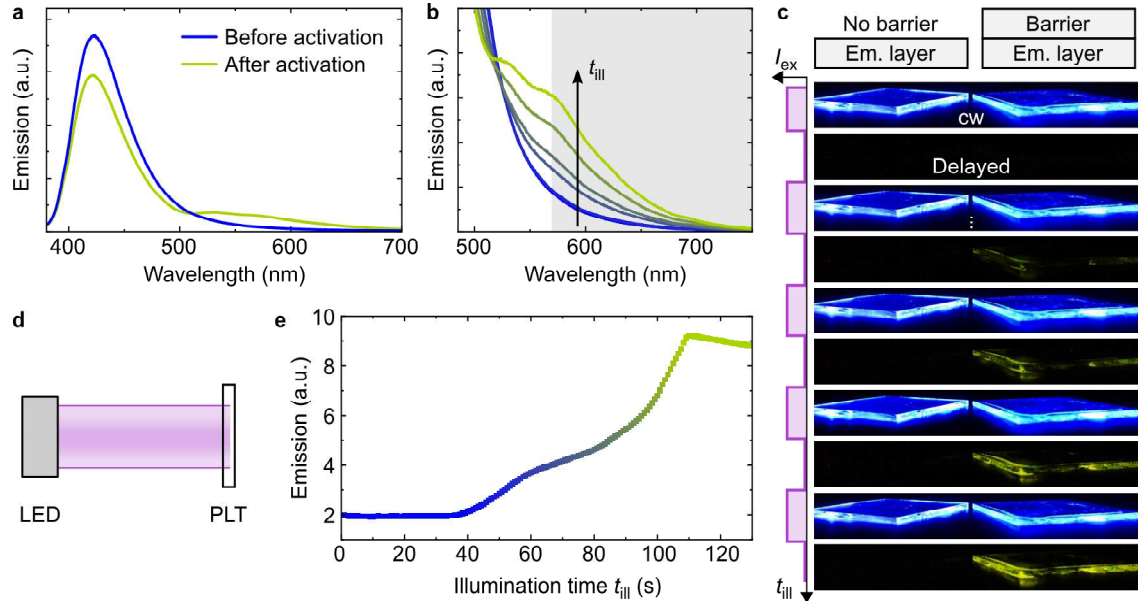


Figure 4.3.: **a** Prompt cw emission of a PLT before and after activation. **b** Intermediate cw spectra showing the increase of phosphorescence with illumination time t_{III} . The shaded region was integrated to obtain Figure e. **c** Images of prompt and delayed emission of an uncoated and a barrier-coated emission layer evolving over t_{III} . **d** Illustration of the large-area illumination of the PLT as used here. **e** Integrated prompt emission in the range of $\lambda = 570$ nm to $\lambda = 750$ nm against t_{III} .

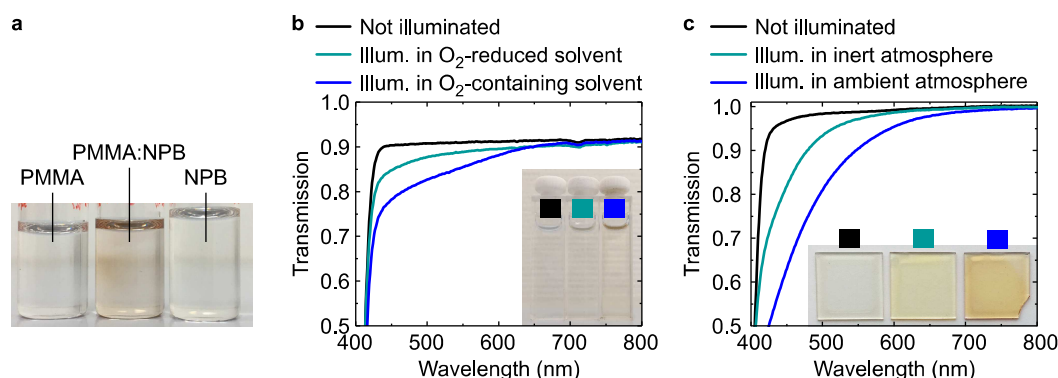


Figure 4.4.: **a** Solvents containing PMMA, NPB, and both. Only the mixture shows yellowing after UV-illumination. **b** Transmission data for UV-illuminated solvents with normal and reduced oxygen concentration. In the presence of oxygen the UV-induced yellowing is more pronounced. **c** Transmission data for solid-state samples illuminated in inert and ambient atmosphere. Again, in the presence of oxygen the UV-induced yellowing is more pronounced. UV degradation of the thin films was performed by Dr. Heidi Thomas.

triplet states of NPB are quenched by triplet-triplet interaction with the triplet ground state of O₂, leading to the generation of excited singlet oxygen ¹O₂ (cf. Section 2.3.2). The subsequent appearance of emission from the NPB's triplet state in the protected sample indicates that the ¹O₂ undergoes photoconsumption (cf. Section 2.3.3) and forms chemical bonds to neighboring host or guest materials. Therefore, the concentration of molecular oxygen in the emission layer decreases, at some point the quenching term $k_{qT}[\text{O}_2]$ in Equation 2.64 becomes negligible and phosphorescence emerges. The same processes also take place in the non-coated sample, but with one difference: due to the high oxygen permeability of PMMA (cf. Section 2.1.11) and the absence of a barrier layer, the photoconsumed O₂ is permanently compensated by fresh ambient oxygen flowing into the sample.

In order to further prove the oxygen uptake mechanism, several solutions and thin films were prepared. First, PMMA only, NPB only, and PMMA:NPB (2 wt%), diluted in anisole, were illuminated with intense UV radiation for several minutes. As a result, the mixture of both host and guest showed yellowing, while the solutions containing the individual materials remained fully transparent (Figure 4.4 a). In a next step, PMMA:NPB (2 wt%) in dry anisole with a reduced amount of oxygen was introduced. In this sample, the UV-induced yellowing was reduced compared to the mixture in ordinary anisole (Figure 4.4 b). This could be quantified via the comparison of the transmission spectra. Both illuminated solutions showed a decrease

of transmission in the short-wavelength regime of the visible spectrum, but the effect was more pronounced in the oxygen-containing solvent.

These two datasets suggest that the yellowing is induced by the interplay of four participants: UV radiation, PMMA, NPB, and oxygen. The absence of only one of these factors significantly reduces the effect. This is in agreement with photooxidation, where excited singlet oxygen is formed by chemical quenching of an excited triplet state and then oxidizes a polymer¹⁶¹. Indeed, PMMA is known for turning yellowish through oxidation²²².

The same effect was observed in solid-state samples when illuminated in ambient and inert atmosphere (Figure 4.4 c). Here, the yellowing was significantly increased in the presence of oxygen^a. In total, the O₂-removal under UV illumination can be attributed to the photooxidation of the host polymer PMMA. In addition, it cannot be foreclosed that complementary oxidation of the guest emitter NPB may also play a role.

Returning to the activation of the PLTs as shown above, the increase of the phosphorescence over time was obtained through integration of the cw spectra in the range of $\lambda = 570 \text{ nm}$ to $\lambda = 750 \text{ nm}$ during activation (Figure 4.3 e). The selection of this spectral window was necessary, since in the full spectral range the triplet-induced decrease of the fluorescence would have overlaid the phosphorescent rise (cf. Section 5.1.1 for details). The uneven slope of the increase may be caused by inhomogeneities of the excitation light or the sample. Therefore, additional data with a narrowed illumination aperture were collected (Figure 4.5 a). Similarly as before, the data were obtained from the cw emission spectra, but now showed a more smooth increase (Figure 4.5 b). The fluorescent background was removed from the signal by subtracting the emission in ambient atmosphere. Interestingly, the rise of the phosphorescence was far from linear. Instead, the triplets remained fully quenched for a certain amount of illumination time t_{ill} . Subsequently, a gradual increase of detected emission is seen. Due to residual inhomogeneity of the excitation light, the rise consisted of a growing area showing phosphorescence, which overlaid the actual activation curve of the triplet emission of distinct molecules. Nevertheless, this behavior shows a decrease of oxygen concentration [O₂]. In the beginning the quenching factor $k_{\text{qT}}[\text{O}_2]$ is dominating, but at some point it reaches the order of magnitude of k_{p} . At this threshold level ϑ_{O_2} , the radiative share of the T_1 depopulation abruptly

^aNote that the UV intensity here was substantially higher than it was for usual photoluminescent measurements, where no color change of the sample emerges.

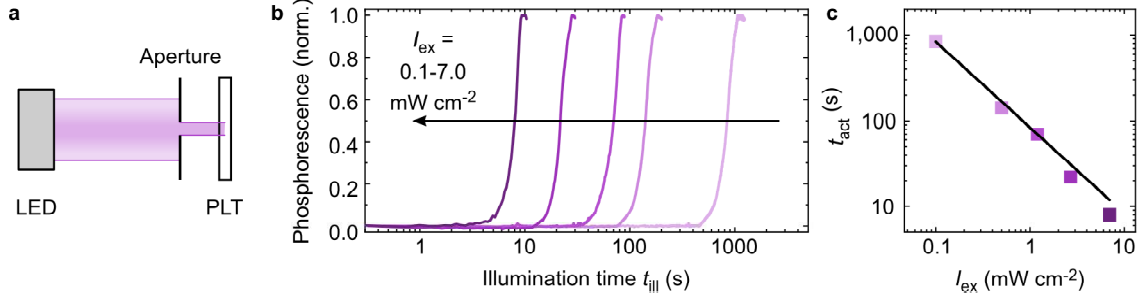


Figure 4.5.: **a** Illustration of the spatially reduced illumination of the PLT as used here. **b** Phosphorescence activation curves for different excitation intensities I_{ex} , extracted from cw spectra. **c** PLT activation time t_{act} for different I_{ex} . The black line is a power-law fit using an exponent of -1 .

slopes upwards and emission appears. Further measurements are planned to check whether the slope of the rise can be tuned to actually resemble the ratio of k_p and $k_{qT}[\text{O}_2]$. Thus, the homogeneity of the illumination beam has to be further increased. The illumination time when half of the maximum phosphorescence was detected, t_{act} , was used as benchmark for the influence of different excitation intensities I_{ex} on the activation. The excitation ranged from $I_{\text{ex}} = 0.1 \text{ mW cm}^{-2}$ to $I_{\text{ex}} = 7.0 \text{ mW cm}^{-2}$. Plotting the respective values of t_{act} reveals a reciprocal dependency on I_{ex} , which can be fitted using a power law function with an exponent of -1 (Figure 4.5 c). This means that doubling the intensity reduces the activation time by a factor of two:

$$t_{\text{act}} \propto \frac{1}{I_{\text{ex}}} \quad (4.1)$$

Since the total excitation dose required for the activation D_{act} is a product of those two values, their proportionality hints to a constant value of D_{act} :

$$D_{\text{act}} = I_{\text{ex}} t_{\text{act}} = \text{const.} \quad (4.2)$$

From the acquired data, $D_{\text{act}} = 70 \pm 12 \text{ mJ cm}^{-2}$ for PMMA:NPB (2 wt%) can be inferred. The rather big standard deviation could be originated both in the measurement and in variations of the samples. Nevertheless, it should be noted, that the similar D_{act} values result from intensity data spanning almost two orders of magnitude.

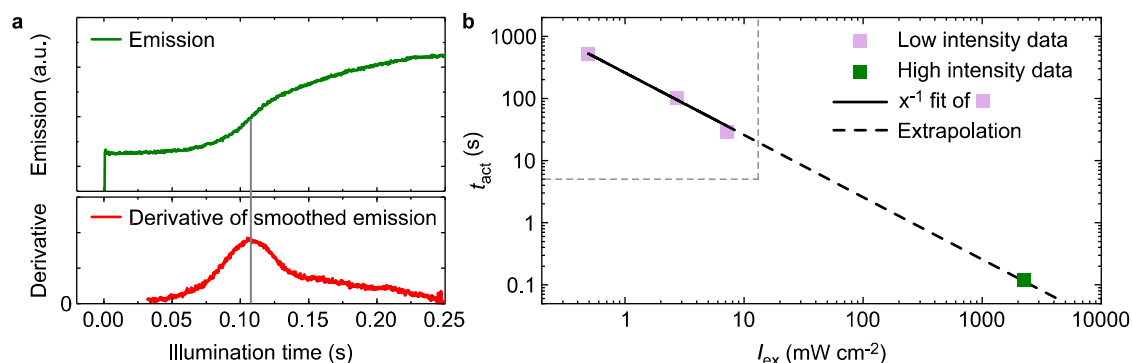


Figure 4.6.: **a** Top: Rise of the emission of a PLT with PMMA:BP-2TA (5 wt%) after turning on the highly focused LED. Bottom: Derivative of the smoothed emission. The indicated inflection point was used as value for t_{act} . **b** PLT activation time t_{act} for low (violet) and high (green) I_{ex} . The black line is a fit of the low-intensity data, which is extrapolated (dashed).

Since the measurements for the activation curve of NPB required spectrally resolved detection, the maximum time resolution was limited to the speed of the spectrometer. In order to address ultrafast rise times, the emitter material of the PLTs was changed to BP-2TA, which shows almost pure phosphorescent emission (cf. Section 5.17). Thus, the emission change could be logged with a single photodiode at high temporal resolution.

But first, low intensity measurements at $I_{ex} = 0.5 \text{ mW cm}^{-2}$ to $I_{ex} = 7.2 \text{ mW cm}^{-2}$ were conducted on PLTs with BP-2TA similar to as before^b. They resulted in t_{act} values, which again could be fitted with a power law function with an exponent of -1 (Figure 4.6 b, upper left). The average activation dose here was $D_{act} = 250 \pm 40 \text{ mJ cm}^{-2}$.

Then, with the use of a sharply focused UV LED, a fresh PLT was illuminated through a pinhole with a diameter of 1 mm. Right behind the pinhole, the excitation intensity was $I_{ex} = 2.3 \text{ W cm}^{-2}$. This was up to four orders of magnitude more compared to the previous intensities. The detected emission showed an increase already 0.1 to 0.2 seconds after turning on the LED (Figure 4.6 a). Due to scattered light, the sample was additionally partly illuminated in the area around the pinhole with lower intensity. Therefore, the measured rise of the emission did not stop sharply after

^bThis accounts to the setup and the measurement, but not to the evaluation method. In order to ensure data consistency, t_{act} was determined as it was in the high intensity measurement, using the inflection-point method. The difference in both methods, however, is low, with $D_{act} = 260 \pm 70 \text{ mJ cm}^{-2}$ when using the NPB method.

activation of the area right behind the pinhole, leading to a smeared-out plateau of the emission. Thus, the inflection point of the activation curve instead of the time-stamp of 50% emission was used as t_{act} in this case. Five identical measurements resulted in an average activation time of $t_{\text{act}} = 110 \pm 20$ ms, and therefore in an average activation dose of $D_{\text{act}} = 270 \pm 30$ mJ cm⁻².

The great similarity to the low-intensity value calculated above further strengthens the hypothesis of a constant D_{act} , here shown for intensities spanning four orders of magnitude. Consequently, the pair of $I_{\text{ex}} = 2.3$ W cm⁻² and $t_{\text{act}} = 120 \pm 20$ ms perfectly fits into the extrapolated reciprocal power law curve for low intensity measurements on PLTs with BP-2TA (Figure 4.6 b). This also indicates that even faster activation times should be achievable with a further increase of I_{ex} .

4.1.2. Writing Patterns

The previously described activation process was used to write spatially resolved patterns of reduced oxygen concentration into the emission layer of the PLTs. Therefore, the illumination light had to resemble the desired pattern. As soon as the required activation dose D_{act} was reached, phosphorescence emerged at that position. The easiest way to create luminescent patterns was moving a focused LED over the PLT (Figure 4.7).

A more sophisticated technique was the printing via mask illumination (Figure 4.8). For activation with near UV of $\lambda_{\text{ex}} = 365$ nm, common overhead transparencies were suitable as masks due to their transparency in this spectral region. With the help of a standard laser printer, any chosen pattern was inversely printed onto the foil, yielding black blocking layers and a transparent cutout in the shape of the desired image

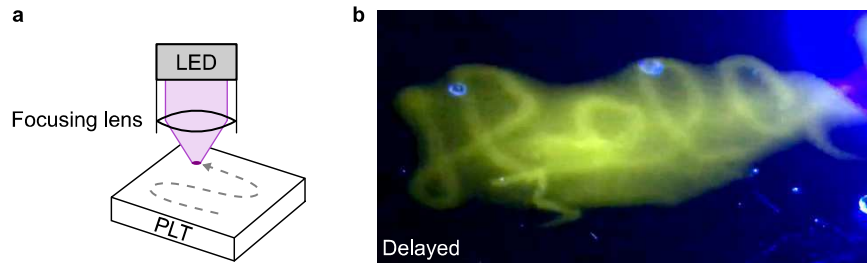


Figure 4.7.: Writing patterns by moving a focused intense spot over the PLT. **a** Principle. **b** Resulting PLT imprint in delayed emission.

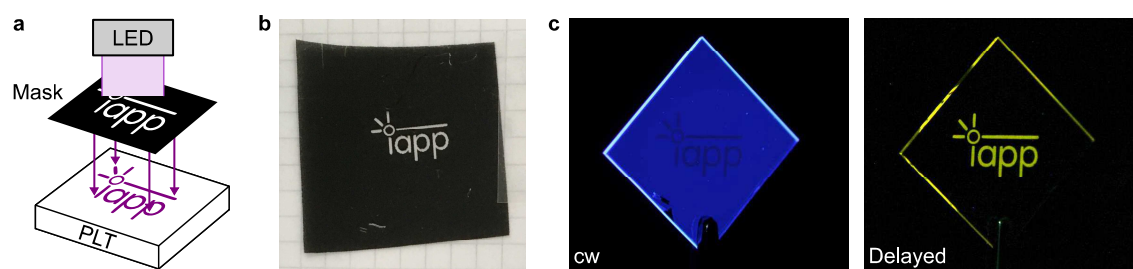


Figure 4.8.: Writing patterns by mask illuminating the PLT. **a** Principle. **b** Photograph of a mask used to program PLTs. **c** cw fluorescence (left) and resulting imprint in delayed emission (right) after removal of the mask.

(Figure 4.8 b). Via this mask, the PLT then was illuminated (Figure 4.8 a). After removing the mask, the full sample showed fluorescence, but in delayed emission only the programmed imprint was visible as phosphorescence for a few seconds. (Figure 4.8 c). This shows the basic potential of invisible data storage or security labeling.

Further, fully digital PLT writing, without the need of printing masks before, was tested using a maskless lithography system SF-100 XTREME from scoTech. Via a micro-mirror array, a monochrome bitmap was projected onto the PLT (Figure 4.9 a). This illumination activated the phosphorescence of the PLT (Figure 4.9 b).

In order to quantify the resolution of the printed patterns, a PLT was monitored using a self-assembled microscope. As activation mask, a 1951 USAF test chart by Thorlabs was used, which is a standard measuring tool for the microscopic optical resolution of a device (Figure 4.10 a). Here the spatial resolvability of differently sized lines correlates to a certain image resolution. One element consists of three transparent lines, which are separated by black blocking layers. After removing the mask, images of the delayed emission of the PLT were recorded (Figure 4.10 b). The smallest

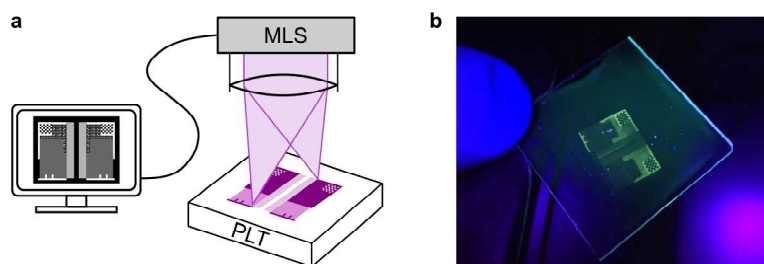


Figure 4.9.: Writing patterns using a maskless lithography system (MLS). **a** Principle. **b** Resulting phosphorescent imprint.

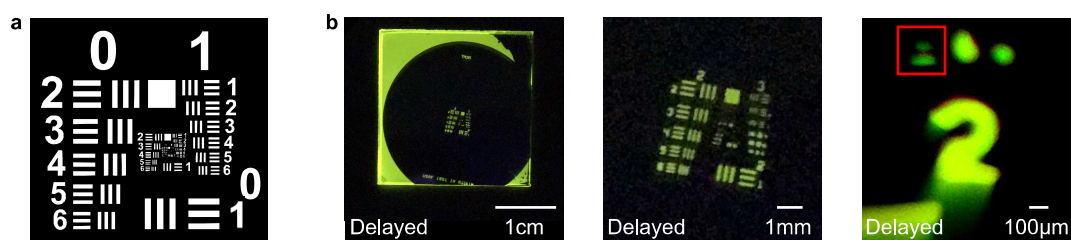


Figure 4.10.: **a** 1951 USAF test chart. **b** PLT with an imprint created with the test chart on different scales. The separated lines on the top of the right image (red box) correspond to a resolution of 724 dpi.

pattern with clearly separated lines was element 6 of group 3. This corresponds to a resolution of 724 dpi, which is in the range of the quality of common office printers. From a physical point of view, the actual resolution of the PLTs, however, may be much higher than that, since the intramolecular distance between single emitters is in the range of nanometers. The critical point here may be the sharpness of the masked excitation light.

In Figure 4.11 a, a microscopic delayed image of a PLT is shown, where the activation was not completely finished yet. Further, the USAF mask was still on the sample here and phosphorescence from three distinct lines was visible. Removing the mask (Figure 4.11 b) revealed additional activated areas below the blocking layers, which ideally should not have been exposed to excitation light. Hence, only at first glance the test-chart mask allows spatially narrow activation (Figure 4.11 c). But in the actual printing process, the illumination is not perfectly collimated. In consequence, back reflection from the PLT's interfaces may activate regions, which are not part of the mask's pattern (Figure 4.11 d). As a result, the maximum possible resolution is always connected to the quality of the light source used for writing.

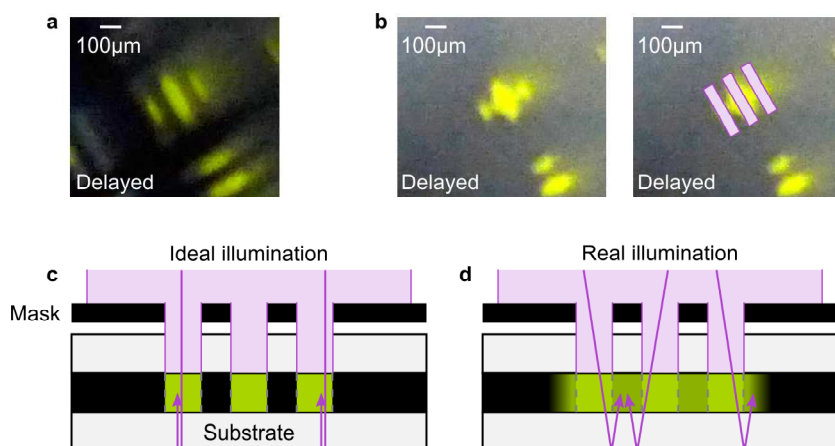


Figure 4.11.: **a** Partly activated phosphorescence of a PLT with the mask still applied. **b** Partly activated phosphorescence of the PLT without the mask, showing activation of undesired areas. On the right, the ideally illuminated regions are sketched as overlay. **c** Theoretical ideal programming of a PLT with a perfectly collimated light source. **d** Real printing process with light containing a non-parallel portion. The latter is back-reflected on the interfaces into adjacent areas and leads to unwanted activation.

4.2. Preservation - Keeping the Disequilibrium Stable

The activation of highly resolved phosphorescent imprints was reliably shown. However, the luminescent contrast in the PLT, which results from the oxygen disequilibrium and forms the detectable pattern, may unintentionally be corrupted by several processes. This will be discussed in this section.

4.2.1. Unintended Activation

During the measurement process, it emerged that after a prolonged readout time-frame, at some point phosphorescence appeared in the previously non-activated regions. In consequence, the imprinted pattern got superimposed by homogeneous emission of the full PLT (Figure 4.12 b). This drawback is a very general issue in PLTs. Basically, the writing and the readout processes have the identical photophysical background. In both procedures, excited triplet states are generated via illumination, and they either decay radiatively (reading) or form $^1\text{O}_2$ (writing). Thus, in our experiments every readout process was accompanied by an unwanted reduction of the oxygen concentration in the regions which had not been activated yet (Fig-

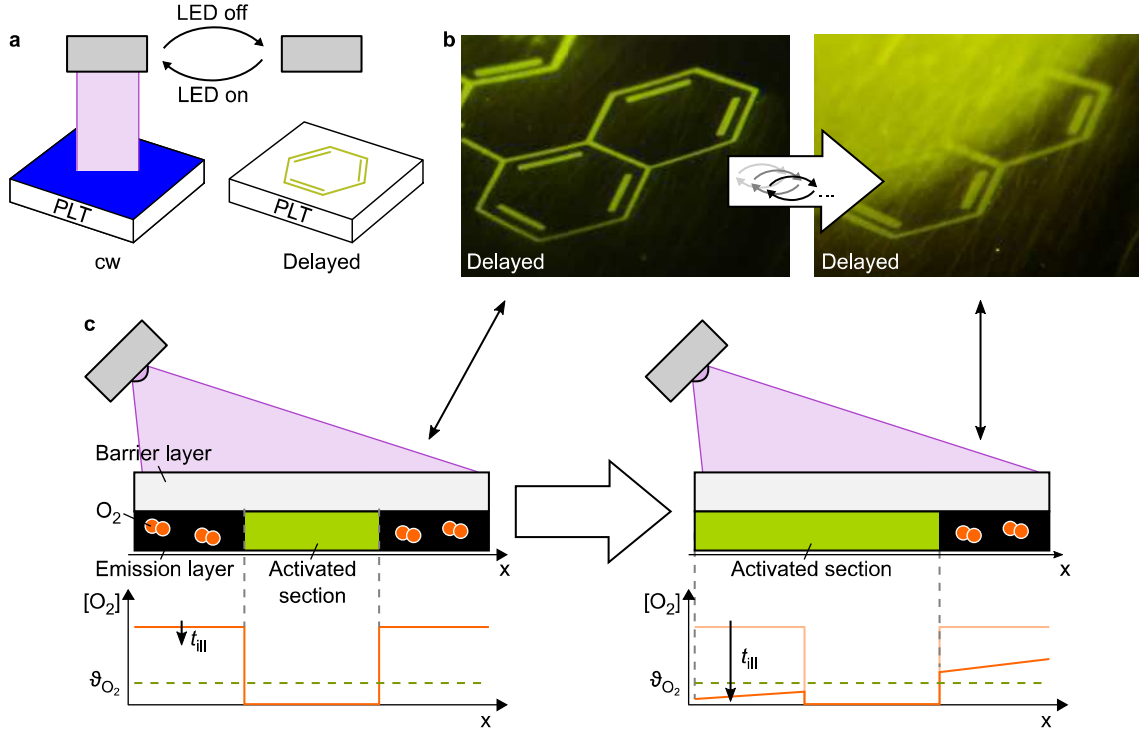


Figure 4.12.: **a** Multiple reading of PLTs by repeatedly switching the LED on and off. The imprinted patterns are visible in delayed emission. **b** Images of PLTs, which show that prolonged excitation resulting from multiple readouts leads to unintended activation of the pattern's background. **c** Sketch of the readout of a programmed PLT via excitation of the phosphorescence, which is inevitably connected to a reduction of the oxygen concentration $[O_2]$. Therefore, at some point, when $[O_2]$ drops below ϑ_{O_2} , unintended activation occurs.

ure 4.12 c). Therefore, after ongoing read out at some point their O_2 concentrations dropped below the threshold ϑ_{O_2} . In consequence, they also showed phosphorescence and the pattern vanished. Thus, the number of possible readouts was limited.

4.2.2. Storage Stability

Another important aspect that may have detrimental impact on the quality of PLTs is the stability of the triplet emission over storage time. In order to investigate this dependency, PLTs were fully activated and then put into darkness at ambient conditions. The change of phosphorescence was monitored at different times by illuminating the samples for a very short time at very low intensity. This was necessary to avoid unintended photoconsumption of oxygen as well as possible, which influences the oxygen concentration and therefore the measurement outcome. As a result a deactivation of

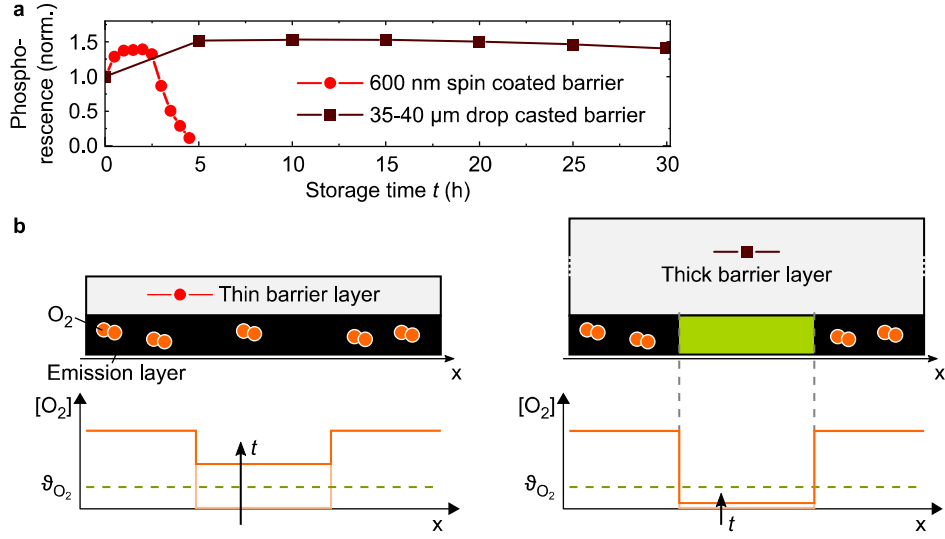


Figure 4.13.: **a** Normalized phosphorescence as a function of storage time for two different film thicknesses, $d = 600\text{ nm}$ (light red circles) and $d = 35\text{ }\mu\text{m}$ to $d = 40\text{ }\mu\text{m}$ (dark red squares), stored and measured under ambient conditions. **b** Illustration of the two PLTs and their oxygen concentration after a storage time of 10 hours.

the phosphorescence was observed. A sample having a spin-coated barrier layer with a thickness of $d = 600\text{ nm}$ showed phosphorescence up to five hours of storage time (Figure 4.13 a). Thicker drop-casted barriers with $d = 35\text{ }\mu\text{m}$ to $d = 40\text{ }\mu\text{m}$ enabled stable phosphorescence of more than 30 hours.

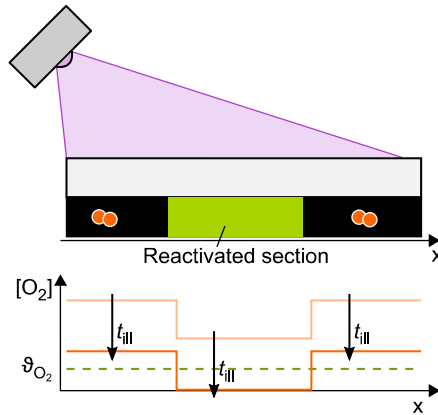


Figure 4.14.: Illustration of the reactivation of a vanished pattern. Through illumination, the former luminescent structure reappears, because the oxygen concentration concentration $[\text{O}_2]$ there drops below ϑ_{O_2} faster than the one of the previously non-illuminated areas.

The dependency of emission stability on the coating's thickness shows that a small amount of O_2 still passes through the barrier layer and penetrates the emission layer. Therefore, in the absence of photoconsumption, the oxygen concentration $[O_2]$ slowly increases again, which leads to a deactivation of the PLT at some stage. Note that the point where phosphorescence has completely vanished does not resemble a full restoration of the initial oxygen concentration, but only a value above ϑ_{O_2} which is sufficient for quenching the emitters' triplets (Figure 4.13 b). In consequence, previously vanished patterns can be reconstructed to a certain extent by carefully illuminating the whole sample. Doing so reduces the overall oxygen concentration, but the areas where the pattern had been before reach the emissive state more quickly than the previously non-activated parts (Figure 4.14).

In addition to the oxygen penetration through the barrier layer, lateral oxygen diffusion from activated to non-activated sections may also corrupt the quality of patterns in PLTs. A freshly printed pattern showed an image, which resembled the mask very

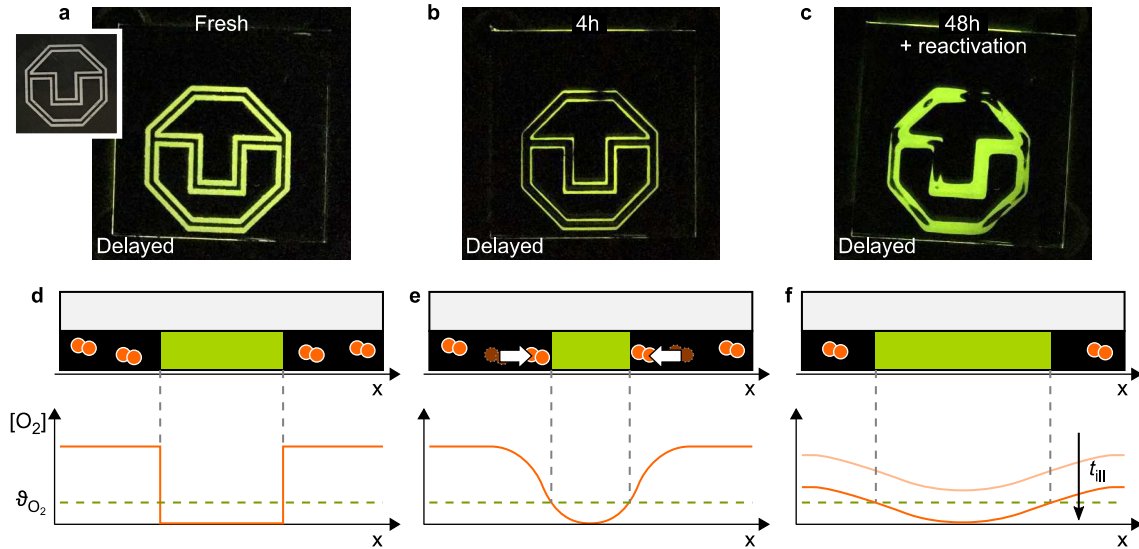


Figure 4.15.: The influence of lateral diffusion on the patterns in PLTs, displayed in images of the PLTs and the schematic oxygen distributions. **a** A freshly programmed pattern, identical to the mask (inset). **b** The same sample after four hours of storage, showing a constricted pattern. **c** The PLT after 48 hours of storage, reactivated through illumination and showing a smeared-out pattern. **d** Oxygen distribution $[O_2]$ in the freshly programmed PLT. **e** Diffused oxygen distribution after four hours, narrowing the activated area. **f** Flattened oxygen distribution after 48 hours. The PLT had to be reactivated for a certain time t_{ill} in order to locally drop $[O_2]$ below the phosphorescence threshold ϑ_{O_2} .

nicely (Figure 4.15 a). However, after storing it for 4 hours, the lines of the pattern had been significantly narrowed (Figure 4.15 b). 48 hours after printing, the pattern had fully vanished. A blurred image could be restored via illumination, which roughly resembled the initial pattern (Figure 4.15 c).

These observations are in accordance with the picture of lateral oxygen diffusion. The narrowing of the lines after four hours results from the penetration of the activated regions with oxygen originating from the adjacent non-activated sections (Figure 4.15 e). Due to the local increase of molecular oxygen at the edges of the pattern, the threshold value ϑ_{O_2} is exceeded and phosphorescence disappears, causing the narrowing. After storing for two days, the oxygen concentration $[O_2]$ in the whole PLT is high enough to prevent triplet emission. Still, the distribution of O_2 is not homogeneous when comparing the programmed to the non-activated areas (Figure 4.15 f). Under excitation, ϑ_{O_2} for phosphorescence therefore is first reached in the regions of the printed patterns. Due to the lateral diffusion, however, its sharpness is drastically reduced.

4.2.3. Moisture Protection

A further interesting observation regarding potential issues was made when a PLT was activated and then cooled down to $T = 3^\circ\text{C}$. As can be seen in Figure 4.16 a, under this condition the phosphorescence disappeared completely. This was unexpected, since RTP generally increases when reducing the temperature, resulting from

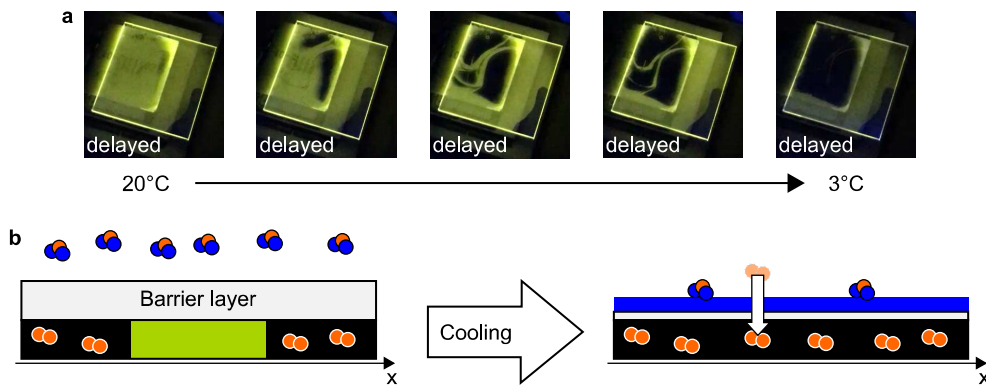


Figure 4.16.: **a** Delayed emission from a PLT, which is partly cooled on the upper left area starting from 20°C down to 3°C . **b** Proposed influence of condensation, leading to a weakening of the barrier layer.

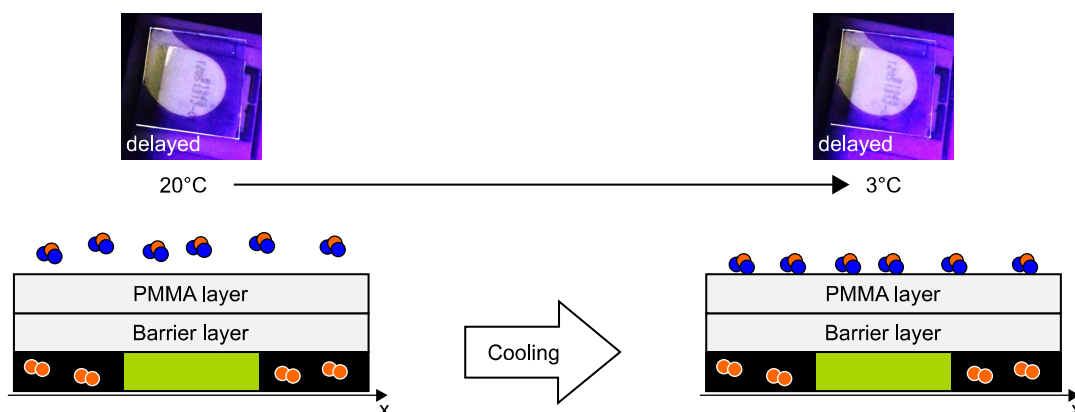


Figure 4.17.: Delayed emission of a PLT with an additional PMMA layer on top at different temperatures 20°C and 3°C. Due to the PMMA, ambient moisture cannot attack the barrier layer.

suppressed nonradiative channels¹² (cf. Appendix C). Notably, heating the sample back to room temperature did not restore the triplet emission. After a second activation via illumination, the phosphorescence emerged again. This indicates that the quality of the oxygen barrier decreases when cooling down the PLT. Indeed, at 3°C, the film had been wet due to atmospheric humidity and the subsequent condensation of water on the cool surface. By that, the barrier layer was solvated and its oxygen permeability increased, which deactivated the PLT.

A modified PLT with an additional PMMA layer on top did not show the loss of phosphorescence when cooled down to 3°C (Figure 4.17). This can be attributed to the fact that the PMMA, which is not water-soluble, protects the oxygen barrier from moisture. For a reliable performance in humid environment, this additional layer therefore should be applied.

4.3. Deactivation - Refilling with Molecular Oxygen

In the last section, unintended loss of phosphorescence was introduced. Now the deliberate vanishing of the PLT's imprints is discussed. Two identical fully activated PLTs with a spin-coated barrier layer were put onto a hotplate at $T = 50^\circ\text{C}$ for 10 and 20 seconds, respectively. Then they were cooled down to RT and put into the measurement setup. Both samples exhibited a decrease of phosphorescent emission, and for the sample with $t = 20\text{ s}$ the triplet emission had disappeared almost completely

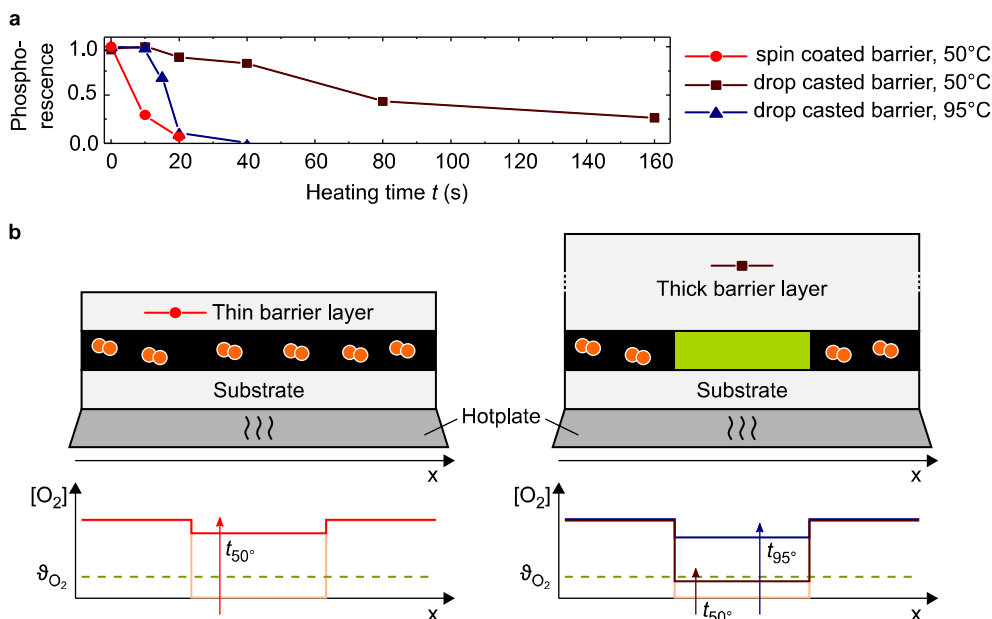


Figure 4.18.: **a** Normalized phosphorescence as a function of heating time for two different film thicknesses, at $T = 50^\circ\text{C}$ and $T = 95^\circ\text{C}$. **b** Illustration of the PLTs and their oxygen distribution after heating for 40 seconds.

(Figure 4.18 a). Subsequently, PLTs with a thick drop-casted layer were heated in the same conditions. Their phosphorescence, measured at RT, remained almost at the initial value. Measurements on further PLTs of the same kind revealed that it took more than $t = 160\text{ s}$ to erase the phosphorescence by heating at 50°C . At an increased temperature of $T = 95^\circ\text{C}$, the triplet emission vanished after heating for 20 to 40 seconds.

As already described in the last section, oxygen diffusion through the barrier layer results in a repopulation of the emission layer with molecular O_2 . The data here indicate that this process is accelerated when heating the sample (Figure 4.18 b). Therefore, the PLTs with thin Exceval layers are deactivated within several seconds. An increase of their thickness slows down the process, but can be compensated by elevating the temperature. EVOH, a barrier material similar to Exceval, shows an exponential dependence of the oxygen permeability on the temperature²²³. Our results indicate that the behavior of Exceval is similar. Additionally, fresh non-activated PLTs were put into inert atmosphere. First, they did not show phosphorescence, while samples without barrier layer did from the beginning. After heating at $T = 60^\circ\text{C}$ for ten minutes in darkness and subsequent cooling to RT, triplet emission became visible after

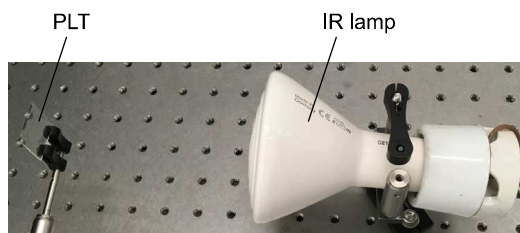


Figure 4.19.: Deactivating the PLTs via illumination with IR radiation.

excitation of the PLTs as well. That shows that molecular oxygen, which first was present in the emitting layer, had been successfully removed at elevated temperature. This is a further indication of the heat-induced increase of the barrier permeability of Exceval.

Besides the hotplate, an infrared light source IOT-90 from Elstein-Werk M. Steinmetz GmbH and Co. KG was used to heat up the PLTs (Figure 4.19). Its radiation of $\lambda \approx 4\mu\text{m}$ is well absorbed by PMMA²²⁴, so it caused a heat-up of the PLT. As will be shown in the next section, this enabled the contact-less deactivation of the PLTs.

4.4. Reactivation - Restarting the Cycle

After deactivation via IR illumination, a PLT was successfully and repeatedly re-programmed with new patterns (Figure 4.20 a). The erasing time was roughly one minute each. Shorter values resulted in an incomplete deactivation. This led to a superposition of the new pattern with the previous one (Figure 4.20 b). However, sufficient IR-induced heating together with subsequent UV-printing enabled convenient contact-less repeatable writing, reading, and erasing using light only (Figure 4.20 c). The time span for three writing and two erasing steps, as shown in Figure 4.20 a, was around five minutes. These experiments show that PLTs offer the possibility of fast multiple printing cycles and may act as programmable optical information storages.

As a next step, a higher number of cycle repetitions was investigated by repetitively fully activating a PLT and then erasing it with intense IR illumination for 30 seconds. In total, 40 repetitions were performed. It was shown that the total triplet emission decreased continuously, down to 40% of its original value in the last measurement (Figure 4.21). At the same time, the fluorescence dropped to 80%. An additional measurement series with 15 cycles showed that a decrease of the phosphorescence

— 4.4. Reactivation - Restarting the Cycle —

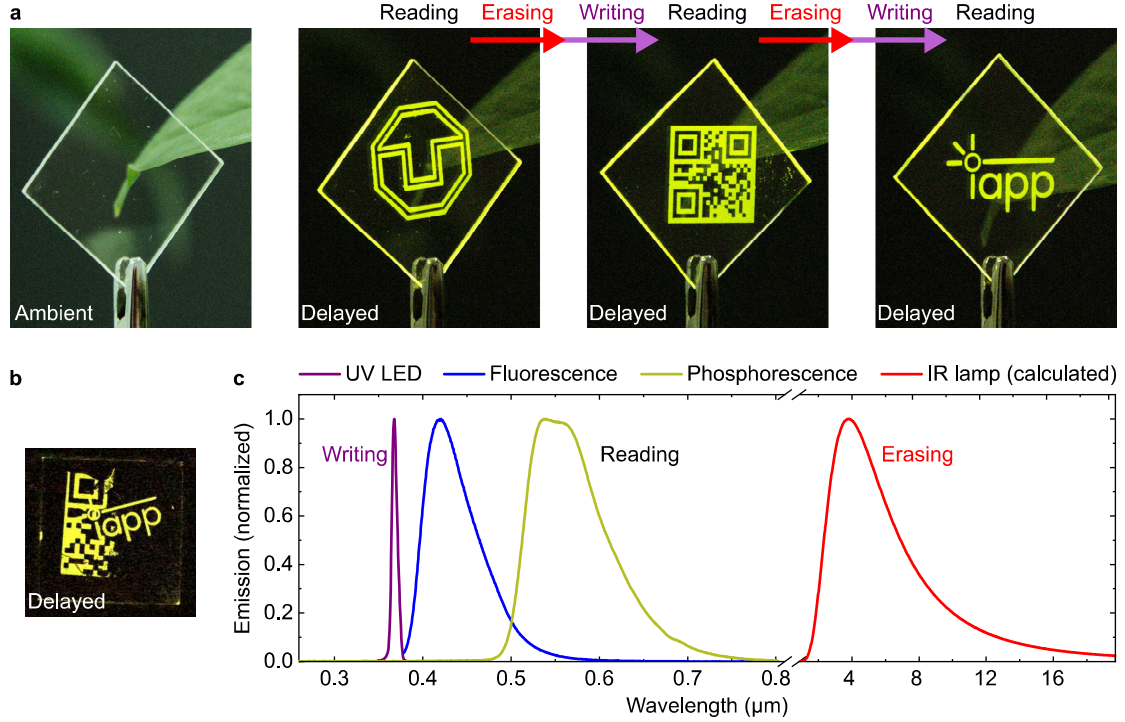


Figure 4.20.: **a** A PLT in ambient light (left) and showing different phosphorescent patterns, successively printed and erased using UV and IR light. **b** Corruption of a pattern by a previous image, which had not been erased completely. **c** Emission spectra of the excitation LED, NPB’s fluorescence and phosphorescence and the IR lamp.

down to 75% was accompanied by a reduction of its lifetime from $\tau_p = 418$ ms to $\tau_p = 393$ ms.

The results show that the intensity of both fluorescence and phosphorescence decrease with ongoing writing and erasing. That may be partly attributed to photobleaching, i.e. the destruction of the emitter materials caused by ongoing excitation. However, this effect should affect both singlet and triplet emission to a similar extent. The reduction of the phosphorescent lifetime τ_p indicates an additional increase of non-radiative decay channels of the triplet states. This could be attributed to a reduced rigidity of the PMMA next to the emitting molecules, which may be caused by its photooxidation in the activation step, as described in Section 4.1. Since this still does not fully explain the decrease of phosphorescence, the degradation of this system currently is subject to further investigation in the scope of another thesis (see also Appendix C).

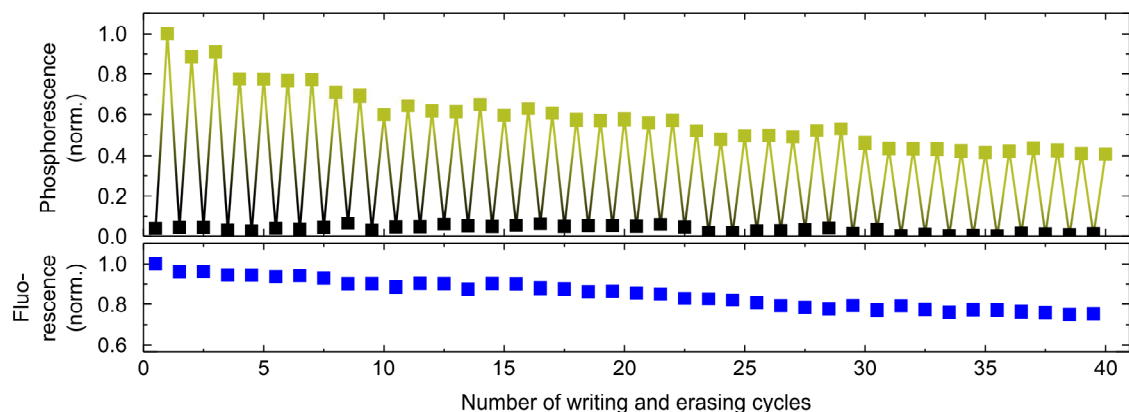


Figure 4.21.: Phosphorescence in the on and off state (top) and fluorescence (bottom) of a PLT for 40 writing and erasing cycles.

4.5. Discussion

Taken together, the operating principle of PLTs is based on photophysical and photochemical effects. By carefully manipulating the concentration of molecular oxygen in the emission layer, switchable phosphorescence (SwiP) is realized and a luminescent contrast can be created. The functional layers with a thickness in the range of micrometers are very thin and transparent in the visible. The small amount of material needed in combination with the high availability of the host polymers enables the fabrication of PLTs at very low cost. The barrier material Exceval is extensively used in food packaging and therefore highly available as well. As an order of magnitude, the material expense for an NPB-containing film of 1 m^2 is below 2€. Further, no expensive processing techniques like vacuum deposition are required, which may further facilitate large scale production of these devices.

With the capability of multiple writing, reading and erasing using light only, PLTs show a novel technology using SwiP for data storage. They could enable on-demand readout of information like QR codes or tracking numbers in logistics or manufacturing facilities at very low cost. When not read out, the programmed patterns are fully invisible, which shows their application potential in document and banknote security.

Intentional and Unintentional Activation

In short, the activation of triplet emission in PLTs by illumination is realized via a sequence of energy transfer processes. Incident radiation generates excited singlet

states S_1 in the emitters in the illuminated regions. Via ISC, triplet states T_1 are populated. The presence of molecular oxygen, which has a triplet ground state, leads to a quenching of the emitter’s phosphorescence and no triplet emission is visible. Instead, the exciton’s energy is transferred to the oxygen, generating an excited singlet state 1O_2 . Via photoconsumption, this highly reactive species oxidizes the host material. Therefore, at some point molecular oxygen is completely consumed in the illuminated regions. At this stage, the triplet states T_1 are not quenched anymore and become emissive. In the non-activated areas, however, the phosphorescence is still quenched. Therefore, luminescent patterns can be read by illuminating the whole sample. At some point, this read-out process leads to an unintended activation of the non-activated areas, and the patterns disappear.

The illumination dose necessary for the activation is dependent on the material composition. The D_{act} value of the BP-2TA samples is 3.5 times higher as it is for the NPB sample. The origin of this difference may be found in a multitude of parameters. It is likely, that D_{act} depends on the triplet generation yield Φ_{isc} (cf. Section 2.2.5), with higher Φ_{isc} leading to lower D_{act} . Another decisive value might be the extinction coefficient ε of the respective molecule (cf. Section 2.2.3), as a higher absorption rate increases the absolute number of excited states and therefore accelerates the photoconsumption. Measurements on these values are in preparation.

For one and the same sample, the activation dose was not dependent on the illumination intensity I_{ex} . This constant D_{act} can be used to address the drawback of unintended activation in the readout step. Lowering I_{ex} in the reading process prolongs the total illumination time until D_{act} is reached in the non-activated areas. Due to the power-law dependency (cf. Equation 4.1), a reduction of I_{ex} by one magnitude increases the possible readout time by a factor of ten. Thereby, the decrease of oxygen in the film during the readout is not prevented, but it is slowed down.

The lowering of I_{ex} goes along with a weakening of the emission, so there is always a trade-off between image brightness and stability. In order to ensure sufficiently high values for both parameters, a high intrinsic D_{act} is advantageous. Thereby, prolonged readout at adequately bright emission is feasible. However, to still ensure a fast writing process, very high I_{ex} is needed. In Section 6.1.4, material systems with different D_{act} will be introduced.

High-Speed Writing

Using an illumination mask, any pattern can be reversibly printed into the tag. Since for industrial application, the fabrication of individual masks is not suitable, maskless programming was successfully realized using a UV lithography system as a proof of concept. A further promising technique would be writing with a highly collimated laser beam. This would also reduce unwanted activation caused by non-parallel light rays. Therefore, the maximum resolution should be further increased. So far, a resolution of up to 724 dpi was realized, which equals the range of common office printers.

The writing speed is proportional to the excitation intensity. During the experiments, the activation time was pushed down to $t_{\text{act}} = 120 \pm 20$ ms. The reciprocal dependency of t_{act} from I_{ex} shown for over four orders of magnitude in both values indicates, that even faster writing may be possible with higher I_{ex} . The theoretical lower limit of the activation time is given by three factors. The first one is the time it takes to chemically quench an oxygen molecule after excitation of an emitter molecule. This value is a combination of the emitters singlet state lifetime τ_{f} , its triplet state lifetime in the presence of oxygen $\tau_{\text{p},\text{O}_2}$, and the lifetime of singlet oxygen. The second one is the singlet oxygen formation rate S_{Δ} , and the third one is the number of oxygen molecules, which have to be quenched by one excited emitter. However, addressing all of these numbers quantitatively was beyond the scope of this thesis. Still, a rational approach would be of great interest.

Oxygen Diffusion and Refilling

Our experiments showed that both vertical oxygen motion through the barrier layer and lateral diffusion within the emission layer influence the storage stability of patterns in PLTs. The first leads to an O_2 refilling and a deactivation of the emission after several hours to days, dependent on the layer thickness. This may be counteracted by adjusting the oxygen permeability of the barrier. The second one induces an equilibration of the lateral oxygen concentration and therefore reduces the spatial resolution of the patterns after a few hours. Here, improved host materials with reduced oxygen diffusion are desired. In order to further address the oxygen dynamics in PLTs, theoretical calculations are required. For an in-depth understanding, it would be helpful to fully reconstruct the observed diffusion behavior (cf. Figure 4.15 d to f) in numerical simulations. It was further shown that heating the PLTs results in a

refilling of the emission layer with oxygen, caused by an increased permeability of the barrier layer. A further mechanism of the heat-induced increase of molecular oxygen concentration may be reverse photoconsumption (cf. Section 2.3.3 and Figure 2.39), where the chemically quenched O_2 is released again¹⁷⁶. This effect was not specifically addressed here, but based on the presented data, the permeability change of Exceval seems to be the dominating process in deactivation via heating.

What is Next

The description of the basic properties of PLTs is completed at this point. Therefore, the basis is set to pursue the investigation of further SwiP material systems. These include various emitters and additives as well as different host materials, substrates and processing techniques, which will be covered in the next chapters.

5. Characterization of Guest Materials

In this chapter, a multitude of different guest materials is examined. Every system is characterized in high detail, including absorption and emission, phosphorescent lifetimes, yields and P2F data. First, single emitter materials are investigated, including NPB (Section 5.1.1) and BP-2TA (Section 5.1.7), which have already been introduced in the last chapter. NPB is the material which, until now, had been the main focus of our group. As will be seen, BP-2TA shows a very high P2F value, rendering it to be most suitable for the realization of PLTs (cf. Section 6.1.1). In addition to that, further single-guest and multi-guest systems with different objectives are presented.

5.1. Single-Guest Systems

Almost all of the presented RTP emitters here are already known in literature. However, the main focus of this thesis was not to design new materials, but to find possible candidates out of the vast number of RTP publications for the rational application in photoluminescent SwiP devices like PLTs. Besides, many of the important material parameters like PLQY or P2F had not been depicted in detail yet. Therefore, interesting candidates were identified and purchased or synthesized. They were dispersed into PMMA550k and spin-coated or drop-casted onto quartz glass. The resulting thin-film host-guest systems (Figure 5.1) were investigated regarding their photophysical properties.

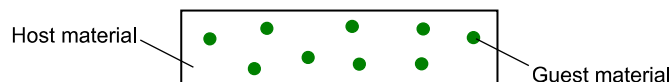


Figure 5.1.: A host-guest sample. The guest molecules (green) are equally distributed in the rigid host material.

5.1.1. NPB - The Starting Material

It is well known that NPB shows RTP when dispersed into a rigid host matrix^{28;225}. The reason for its sufficient ISC, as we have shown²²⁶, may lay in the biphenyl core and its twisted nature (cf. Section 2.2.5). In our measurements, its absorption reached up to 400 nm (Figure 5.2 a). Embedded in PMMA at 5 wt%, it showed intense blue fluorescence at $\lambda_f = 420$ nm with a lifetime of $\tau_f = 3.2$ ns in ambient atmosphere. When oxygen was removed, the fluorescence dropped to 50% of its original value (Figure 5.2 b). At the same time, phosphorescence emerged at $\lambda_p = 540$ nm and $\lambda_p = 570$ nm with a lifetime of $\tau_p = 406$ ms for a 2 wt% sample (Figure 5.2 d). With $\Phi_f = 23\%$ and $\Phi_p = 3\%$ (Figure 5.2 c), measured for a low concentration of 0.5 wt%, PMMA:NPB showed a phosphorescence to fluorescence ratio of P2F = 0.13. PLTs could only be realized using the delayed emission (Figure 5.2 g). The PLT pattern in cw illumination was barely visible (Figure 5.2 f). Further, its contrast was not a result of phosphorescence, but of the triplet-state-induced reduction of the fluorescence.

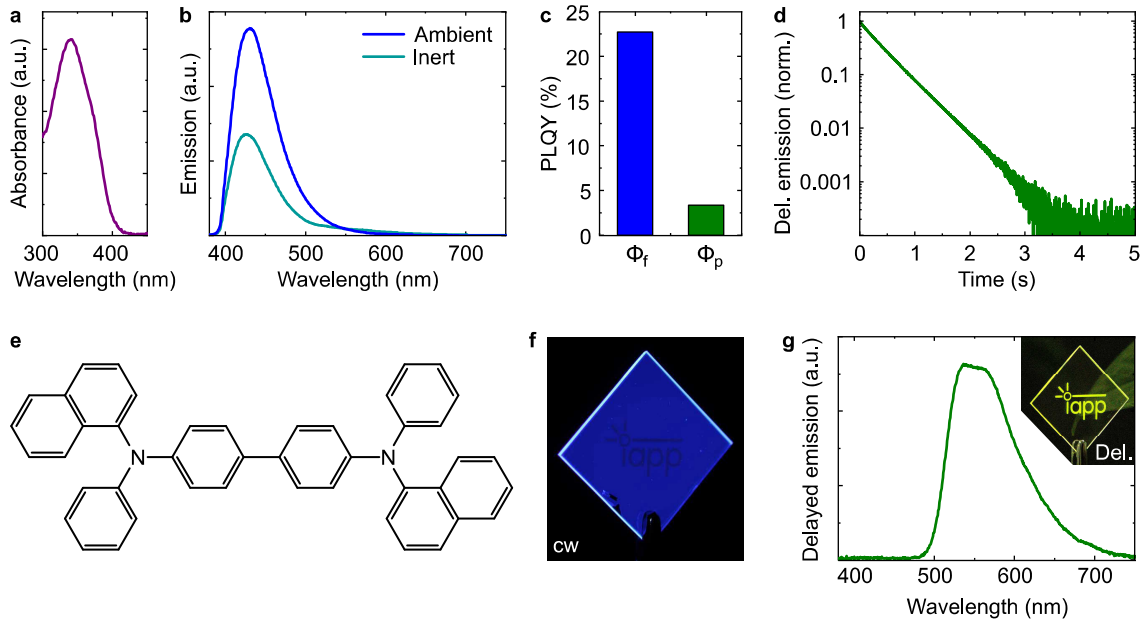


Figure 5.2.: PMMA:NPB, $\lambda_{\text{ex}} = 365$ nm and 340 nm (PLQY). **a** Absorbance. **b** Emission spectra of a 5 wt% sample in ambient and inert conditions. **c** Φ_f and Φ_p of a 0.5 wt% sample. **d** Phosphorescent decay of a 2 wt% sample after turning off the excitation LED. **e** Molecular structure of NPB. **f** PLT made of PMMA:NPB in cw emission. **g** Delayed emission. Inset: PLT using delayed emission.

5.1. Single-Guest Systems

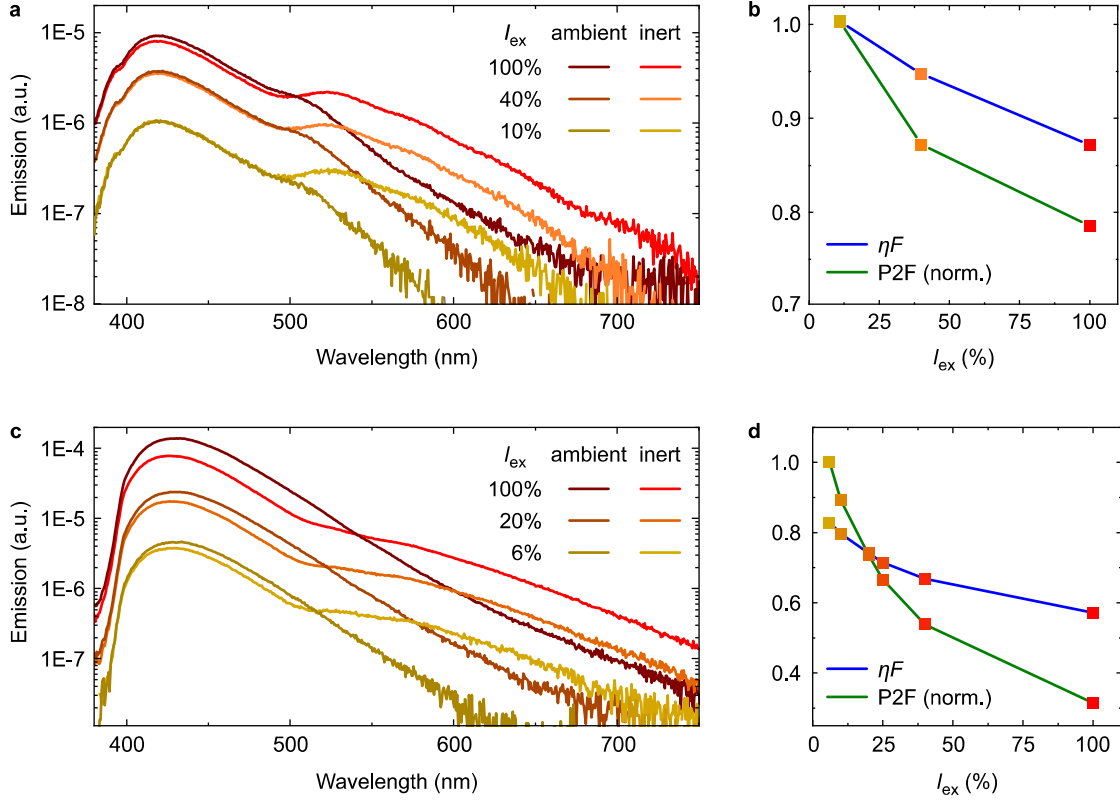


Figure 5.3.: Emission data for different excitation intensities I_{ex} . **a** cw emission spectra of PMMA:NPB 2 wt% in ambient and inert atmosphere. **b** Respective relative change of fluorescence ηF and P2F. **c** cw emission spectra of PMMA:NPB 5 wt% in ambient and inert atmosphere. **d** Relative change of fluorescence ηF and P2F.

This fluorescence decrease was shown to be induced by STA and saturation (cf. Section 2.2.9), as described in Martin Kroll's master thesis¹²⁶. A measure for these influences is the fluorescence ratio ηF , defined as

$$\eta F = \frac{I_{\text{f},\text{N}_2}}{I_{\text{f},\text{O}_2}}, \quad (5.1)$$

where I_{f,N_2} and I_{f,O_2} resemble the integrated emission for $\lambda = 410, \text{ nm}$ to $440, \text{ nm}$ in inert and ambient conditions, respectively. In a PMMA:NPB 2 wt% sample, this ratio was $\eta F = 1$ for low excitation intensity (Figure 5.3 a and b). This hints to the absence of STA and saturation. For higher excitation intensity or higher emitter concentration (Figure 5.3 c and d), the ratio was reduced down to $\eta F = 0.6$.

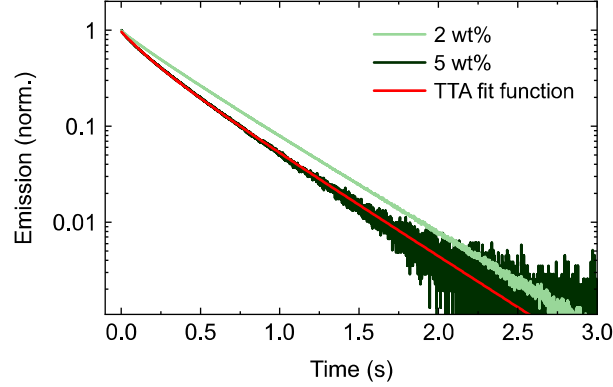


Figure 5.4.: Phosphorescence decays of a 2 wt% and 5 wt% PMMA:NPB sample. The red line is a fit of the 5 wt% decay using equation 2.54.

Also the P2F value^a decreased when going to high excitation intensity or higher concentration, notably even more than ηF did. This can be attributed to TTA¹²⁶, which again is a quenching effect with a dependency on triplet states. Due to an average nearest-neighbor distance of > 2 nm for both the 2 wt% and 5 wt% sample²²⁷, TTA here has to be FRET-based and does not lead to RISC and delayed fluorescence (cf. Section 2.2.9). This is in agreement with the delayed emission spectrum, where no fluorescence is visible (see also Appendix C).

The phosphorescent decays of the 2 wt% and 5 wt% samples are shown in Figure 5.4. The high concentration sample showed a faster decrease of intensity. The red line is a fit of this dataset using Equation 2.54, which describes the time-dependent intensity in the presence of TTA. It resembles the measurement very well and results in an intrinsic lifetime of $\tau_{p0} = 409$ ms. This agrees with the value obtained for the 2 wt% sample with $\tau_{p0} = 406$ ms. Therefore, TTA is further confirmed.

An additional evidence for the presence of STA may be found on the nanosecond timescale, which had not been investigated so far. From equation 2.52 it is known that STA reduces τ_f by introducing a triplet-dependent decay channel:

$$\tau_{f,STA} = \frac{1}{k_f + k_{nr,f} + k_{isc} + k_{STA}[T_1]}.$$

^aDue to the STA, no reliable absolute values for P2F could be obtained. Therefore, only the relative change of P2F for increasing intensity is described here. The raw data were obtained via spectral integration from $\lambda = 610$ nm to 650 nm and subsequent division by I_{f,O_2} . The results then were normalized to their maximum value.

5.1. Single-Guest Systems

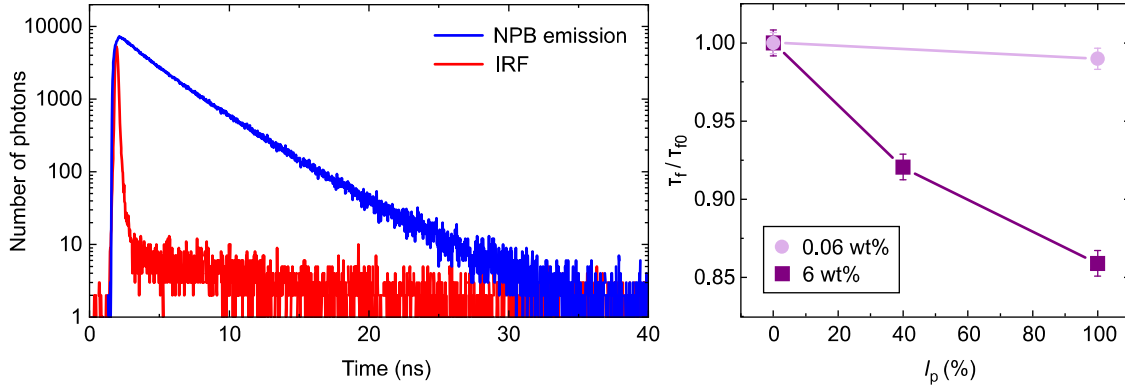


Figure 5.5.: **a** Blue: Nanosecond decay of PMMA:NPB (2 wt%), detected at $\lambda = 420$ nm (blue). Red: Instrument response function (IRF) of the TCSPC setup. **b** Relative change in τ_f for different pump intensities I_p in PMMA:NPB (0.06 wt%) and (6 wt%) samples.

Therefore, due to STA, an increase in $[T_1]$ should lead to a decrease of τ_f . In order to investigate this dependence, samples with different emitter concentrations were put into a modified pump-probe TCSPC setup (cf. Figure 3.3 c). The measurement procedure was the following: the probe laser was operated with low intensity in pulsed mode at 1 MHz, which is a standard setting for TCSPC data acquisition. At the same time, the 365 nm pump LED was turned on and off at 1 Hz. Ten milliseconds after LED turnoff, the shutter between the sample and the detection monochromator was opened for 50 ms. Therefore, no pump-LED-excited fluorescence reached the TCSPC detector, while around 90% to 95% of the excited triplet states were still populated. Thus, the probe-laser-excited singlet states could be affected by singlet-triplet interactions. Their emission was then detected and counted. The resulting decays yielded fluorescence lifetimes.

By changing the intensity of the pump LED from $I_{\text{ex}} = 0\%$ to $I_{\text{ex}} = 100\%$, the excited triplet density $[T_1]$ was manipulated. The respective change in fluorescence lifetimes is plotted in Figure 5.5 b for two samples with 0.06 wt% and 6 wt% of NPB in PMMA. For the very low concentration, the fluorescence lifetime did not change significantly when switching from $I_{\text{ex}} = 0\%$ to $I_{\text{ex}} = 100\%$ pump intensity. In contrast, at high emitter density, it dropped down to $\frac{\tau_f}{\tau_{f0}} = 86\%$. This clearly suggests the presence of STA.

STA, saturation and TTA all correlate with the density of excited triplet states. Since the latter is dependent on the respective lifetime τ_p , RTP emitters with similar or

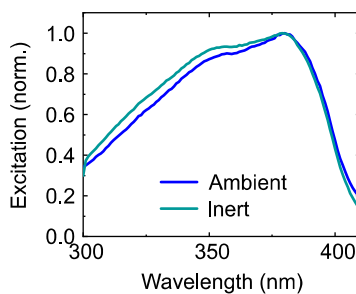


Figure 5.6.: Normalized excitation scans of PMMA:NPB in ambient and inert conditions. The detection wavelength was $\lambda = 570$ nm.

longer lifetime than NPB are likely to show similar behavior. In contrast, shorter τ_p should lead to reduced annihilation and saturation effects.

Figure 5.6 shows excitation scans of PMMA:NPB covered with an Exceval layer. The barrier layer was necessary because it was not possible to flush the sample with nitrogen in the respective setup. The detection wavelength was 570 nm in order to detect mainly phosphorescence in the inert measurement. Due to its long-wavelength tail, fluorescence in ambient conditions could also be acquired at this spectral position. The blue curve shows the measurement before activation of the phosphorescence, so for fluorescent emission only. For the sky blue curve, the sample was fully activated to allow the measurement of both emissive states. As a result, both curves look highly similar for NPB. As it will be shown in Section 5.1.7, this is not a general conclusion as it does not hold true for all investigated emitters.

In total, the implementation of NPB into PLTs shows several drawbacks. Its low phosphorescence yield is further reduced by annihilation effects at high excitation intensities. In addition, the bright fluorescence results in a very low P2F value, so PLTs can only be used in delayed emission. As a last point, UV irradiation is necessary for the activation and the readout process, which limits its application in everyday scenarios.

5.1.2. PhenDpa - Shifting to Visible Absorption

One goal of our group was to shift the absorption of a biluminescent emitter to the visible. The resulting PhenDpa, synthesized by Dr. Marine Louis²²⁸, has a similar molecular structure as NPB (Figure 5.7 e) but showed absorption up to $\lambda = 420$ nm (Figure 5.7 a). It exhibited bright fluorescence at $\lambda_f = 450$ nm, which was reduced

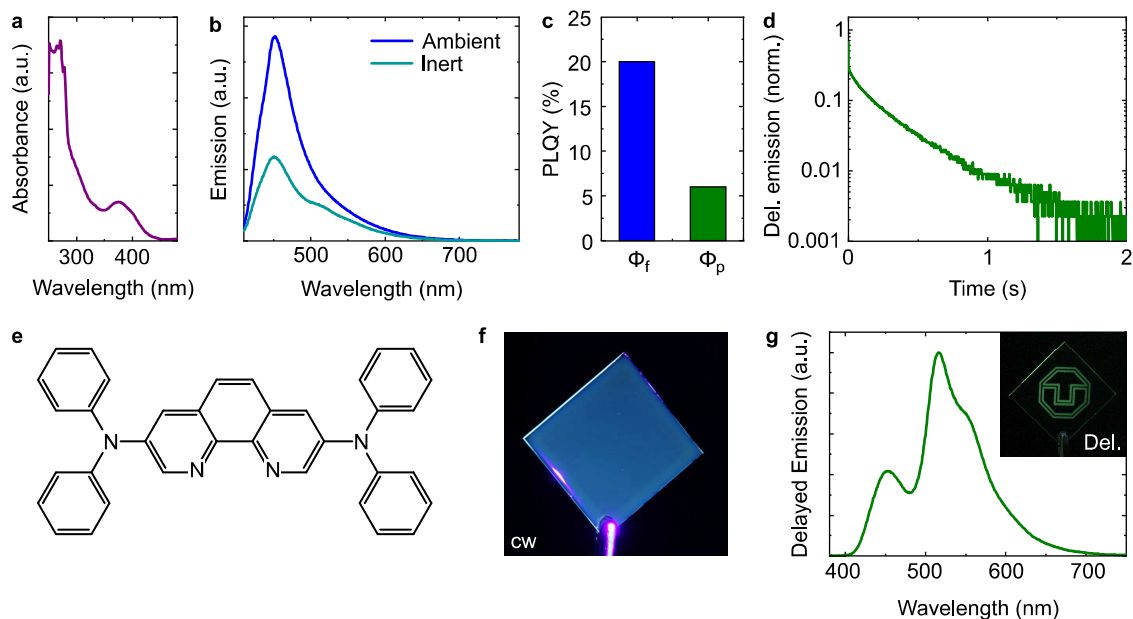


Figure 5.7.: PMMA:PhenDpa (2 wt%), excited at $\lambda_{\text{ex}} = 405$ nm, 420 nm as well as 380 nm (PLQY). Measurements performed by Dr. Heidi Thomas. **a** Absorbance. **b** Emission spectra in ambient and inert conditions. **c** Φ_f and Φ_p . **d** Phosphorescent decay after turning off the excitation LED. **e** Molecular structure of PhenDpa. **f** cw emission of PMMA:PhenDpa. **g** Delayed emission. Inset: PLT using delayed emission.

when going to inert atmosphere. This again may be caused by TTA and saturation, similar to the situation in NPB. Further, in inert conditions notable phosphorescence was present with $\Phi_p = 6\%$ (Figure 5.7 c) at $\lambda_p = 515$ nm and $\lambda_p = 560$ nm and a phosphorescence lifetime of $\tau_p = 330$ ms. In cw illumination, the fluorescence dominated over the phosphorescence (Figure 5.7 f) with P2F = 0.3. PLTs could again only be realized using the delayed emission (Figure 5.7 g), with patterns visible shortly after the excitation was turned off. Here, the phosphorescence was accompanied by a further peak at $\lambda = 450$ nm. Notably, this is at the same position as the cw fluorescence emission peak, rendering it to be either E-type (TADF) or P-type (TTA) fluorescence (cf. Sections 2.2.5 and 2.2.9).

In order to address this question, additional spectral measurements were performed. When proceeding towards liquid nitrogen temperature of 77 K (Figure 5.8 a), the 0-0 transition of the phosphorescence at $\lambda_p = 515$ nm became more prominent. More importantly, the fluorescent peak in delayed emission disappeared completely. This is a strong hint to its TADF based E-type nature, since at 77 K, there is not enough thermal energy to lift the excited triplet excitons in energy to overcome ΔE_{ST} and

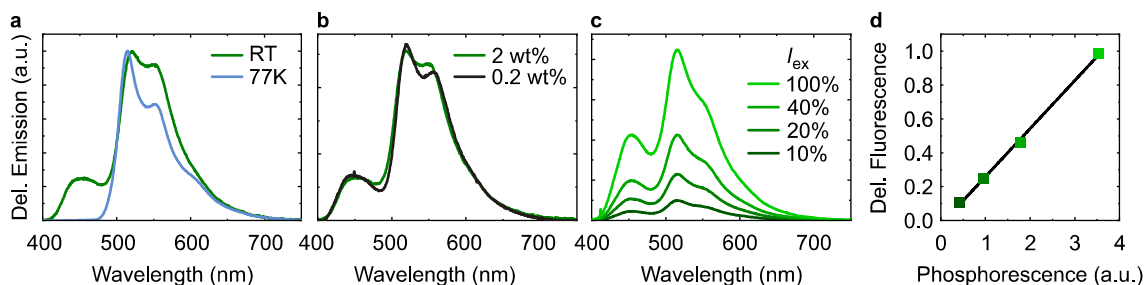


Figure 5.8.: Delayed emission measurements on PMMA:PhenDpa. **a** A 2 wt% sample at room temperature (RT) and at 77 K. **b** Emission of standard (2 wt%) and low concentration (0.2 wt%) samples. **c** A 2 wt% sample at different excitation intensities. **d** Delayed fluorescence intensity versus delayed phosphorescence intensity from Figure c, linear fit (black).

enable RISC. In addition, P-type TTA-based delayed fluorescence would result from the annihilation of two excited triplet states T_1 and would therefore be quadratically dependent on the density of these states (see also Appendix C). In this case, either a reduction of the guest emitter concentration or a variation of the excitation intensity should impact on the delayed fluorescence ratio. Going from the standard 2 wt% concentration to 0.2 wt%, however, this ratio did not change at all (Figure 5.8 b). An excitation-density series (Figure 5.8 c and d) for a 2 wt% sample did also show no bimolecular effects, but a linear correlation of delayed fluorescence and phosphorescence. These results outrule TTA-based P-type fluorescence. Therefore, the blue delayed emission peak can be attributed to pure E-type TADF. In order to obtain the respective values for Figure 5.8 d, the emission was integrated at $\lambda = 430$ nm to 460 nm for the fluorescence and at $\lambda = 520$ nm to 600 nm for the phosphorescence signal. It should be noted that even though Figures 5.8 b (2 wt%) and c (100%) show the emission of two identical samples, they differ in spectral shape. This is due to a spectral distortion occurring at the samples' edge emission, which was detected during this measurement series. For more details, see Section 3.2 and Appendix D.

In conclusion, PhenDpa was successfully proven to emit RTP when excited with visible light at $\lambda_{\text{ex}} = 420$ nm. However, this wavelength still is on the edge to the UV regime, and a more desirable spectral position would be $\lambda_{\text{ex}} = 450$ nm, where common white LEDs show a strong blue emission peak. Further, P2F is far below 1, again resulting in a low phosphorescent contrast.

5.1.3. HPhN and BF₂(HPhN) - A Different Approach

Organic RTP materials bearing absorption of visible light are rarely found in literature. For the purpose of organic oxygen sensing, Lehner et al. introduced difluoroboron-9-hydro-xyphenalenone (BF₂(HPhN)), a fluorine-containing chelate of 9-hydro-xyphenalenone (HPhN)¹¹⁵. They embedded these materials in PS at a concentration of 0.02 wt% and achieved absorption in the visible up to $\lambda = 460$ nm. For the BF₂(HPhN) sample, they showed oxygen-dependent RTP with a yield of up to $\Phi_p = 9\%$. Thus, it is an interesting candidate for the realization of PLTs.

In order to check their suitability and acquire further properties, HPhN as well as BF₂(HPhN) were embedded into a PMMA matrix. Figure 5.9 shows the molecular structure and the photophysical properties of HPhN. This sample shows low $\Phi_f = 2\%$ and no phosphorescence at all. Note that the Φ_f value might have been corrupted due to reabsorption and actually have been higher. In detail, a comparison of the sample's face emission to the spectrum for the PLQY measurement in the integrating sphere showed differences. The high-energetic peak at $\lambda = 447$ nm turned out to be drastically reduced when going from the face measurement to the one in the sphere (Figure 5.10 a). This may have been caused by the sample itself, since in the sphere the emitted light could pass the sample repeatedly before it reached the spectrometer head. If the absorption of the sample overlaps with its emission, as it is the case in HPhN, the emitted light can be absorbed again. This lowers the measured PLQY. The same effect will be seen more clearly for BF₂(HPhN) in the following.

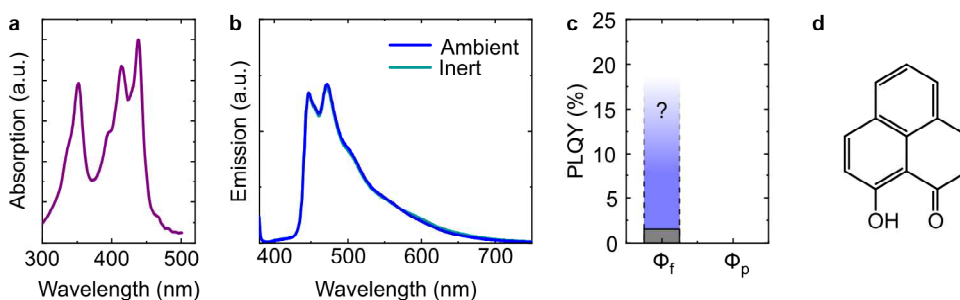


Figure 5.9.: PMMA:HPhN (2 wt%), $\lambda_{\text{ex}} = 365$ nm and 340 nm (PLQY). **a** Excitation scan. **b** Emission spectra in ambient and inert conditions. **c** Measured Φ_f (grey), which may be underestimated. No phosphorescence was visible. **d** Molecular structure of HPhN.

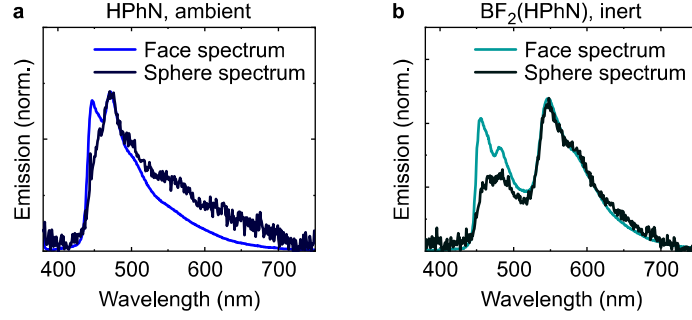


Figure 5.10.: Comparison of spectra in face emission (light) and from the integrating sphere (dark). All spectra are normalized with respect to the maximum. **a** HPhN in ambient conditions. **b** BF₂(HPhN) in inert atmosphere.

While PMMA:HPhN showed no RTP, PMMA:BF₂(HPhN) did (Figure 5.11). In addition to a redshifted absorption reaching up to $\lambda = 470$ nm, its main difference to PMMA:HPhN was a prominent phosphorescent emission peak at $\lambda_p = 550$ nm when switching to inert atmosphere. The respective lifetime was $\tau_p = 220$ ms, and the phosphorescence yield was $\Phi_p = 12\%$. The measured fluorescence yield $\Phi_f < 1\%$ again was very low. This would lead to a P2F value of > 12 . However, the face emission spectrum in Figure 5.11 b indicates, that this high value is not reliable. A comparison of the sphere spectrum with respect to the face emission shows an intensity drop at shorter wavelengths (Figure 5.10 b), similar as seen in HPhN. In order to overcome this corruption, one can calculate the actual fluorescence yield using $\Phi_p = 12\%$ and the face emission spectra. The latter are converted to the number of photons and yield the ratio of fluorescence and phosphorescence of $P2F = 1.5$. With the assumption that the phosphorescent emission was not reabsorbed, the calculated value for the fluorescence is $\Phi_f = 8\%$.

In total, PMMA:BF₂(HPhN) is suitable for PLTs with absorption in the visible (cf. Section 6.1.3). The good contrast in cw emission also enables cw-PLTs, i.e. PLTs which can be read out during illumination (see Section 6.1.1 for details).

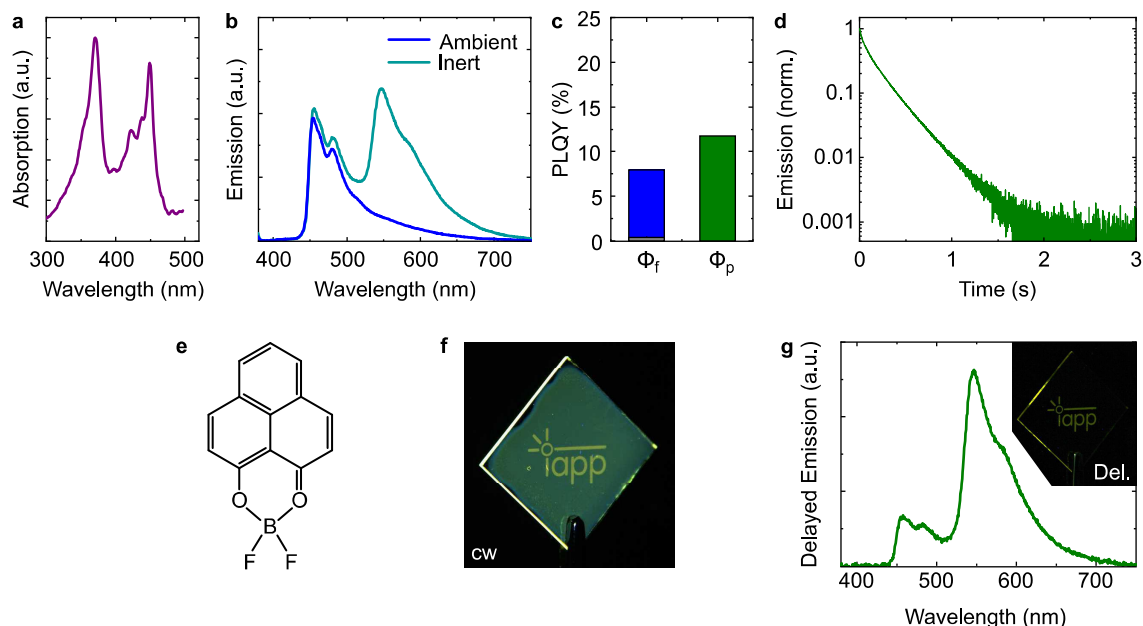


Figure 5.11.: PMMA:BF₂(HPhN) (2 wt%), $\lambda_{\text{ex}} = 365$ nm and 340 nm (PLQY). **a** Excitation scan. **b** Emission spectra in ambient and inert conditions. **c** Measured (grey) and calculated (blue) Φ_f as well as measured Φ_p . **d** Phosphorescent decay after turning off the excitation LED. **e** Molecular structure of BF₂(HPhN). **f** PLT made of PMMA:BF₂(HPhN) in cw emission. **g** Delayed emission. Inset: PLT using delayed emission.

5.1.4. 2-Hydroxycarbazole - Blue Phosphorescence

A turn in the opposite direction is shifting the excitation and emission into the higher energetic regime. Therefore, the fluorescence peak would be located in the UV, while phosphorescence may remain in the visible regime. This should enable high phosphorescent contrast even at low P2F values, since a large portion of fluorescence is not visible to the eye. Wu et al. showed that the commercially available 2-hydroxycarbazole (2HC) embedded into PVA emits both fluorescence in the UV and RTP in the visible²²⁹. Therefore, a PMMA:2HC sample (Figure 5.12) was fabricated to test its capabilities as PLT. When excited at $\lambda = 300$ nm, it showed a dominating fluorescence peak at $\lambda_f = 348$ nm and very little phosphorescence peaking between $\lambda_p = 425$ nm and $\lambda_p = 450$ nm. The phosphorescence lifetime was $\tau_p = 819$ ms.

Since common overhead transparencies are not transparent at the excitation wavelength $\lambda = 300$ nm, they could not be used as masks here. Therefore, a simple square of black aluminum foil was put on top of the sample for the writing step. The resulting cw pattern, recorded after removing the mask, is shown in Figure 5.12 e. The

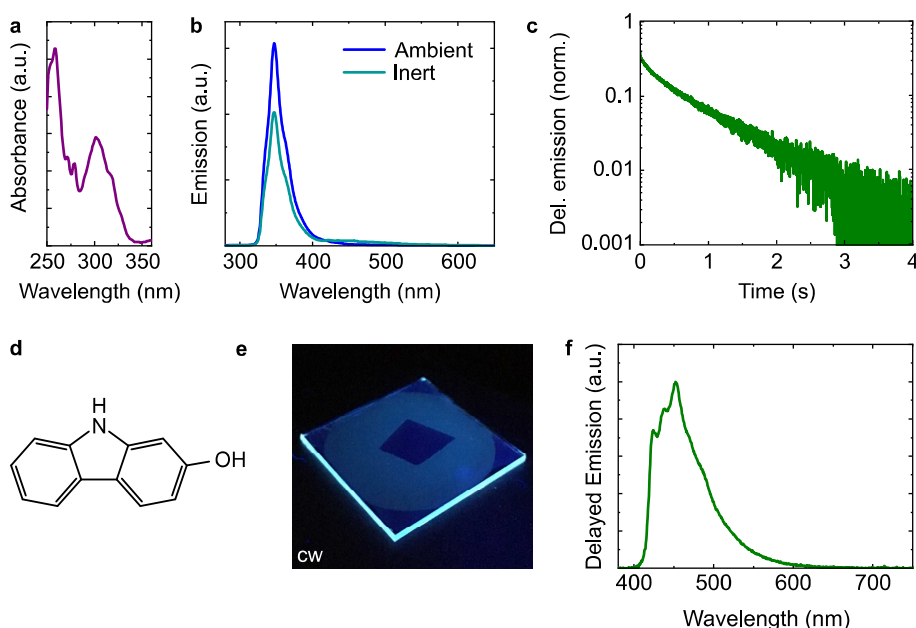


Figure 5.12.: PMMA:2HC (2 wt%), $\lambda_{\text{ex}} = 300 \text{ nm}$. Measurements performed by Dr. Heidi Thomas. **a** Absorbance. **b** Emission spectra in ambient and inert conditions. **c** Phosphorescent decay after turning off the excitation LED. **d** Molecular structure of 2HC. **e** PLT made of PMMA:2HC in cw-emission. **f** Delayed emission.

area of activated RTP was clearly brighter than the square-shaped center, which was covered with the aluminum foil while writing. This verifies the suitability of 2HC as blue phosphorescent emitter material in cw-PLTs.

5.1.5. Ir(MDQ)₂(acac) and PtOEP - The Old Hands

In order to widen the picture, the well known heavy-metal-containing phosphorescent OLED emitters⁹⁵ bis(2-methyldibenzo[f,h]quinoxaline)-(acetylacetonate)iridium(III) (Ir(MDQ)₂(acac)) and platinum octaethylporphyrin (PtOEP) were investigated. Both materials possess very high ISC due to the heavy atom effect (cf. Section 2.2.5) and therefore emit phosphorescence only, with a high radiative rate k_p .

PMMA:Ir(MDQ)₂(acac) (Figure 5.13) showed emission peaking at $\lambda_p = 610 \text{ nm}$ with a yield of $\Phi_p = 41\%$ and a lifetime of $\tau_p = 1.5 \mu\text{s}$. These values were identical both for ambient and inert atmosphere. Thus, no contrast could be generated through photoconsumption of ¹O₂ and PLTs could not be realized using Ir(MDQ)₂(acac) (Figure 5.13 f). These results indicate that the high radiative triplet rate k_p fully outcompetes the oxygen quenching rate k_{qT} even at ambient conditions.

5.1. Single-Guest Systems

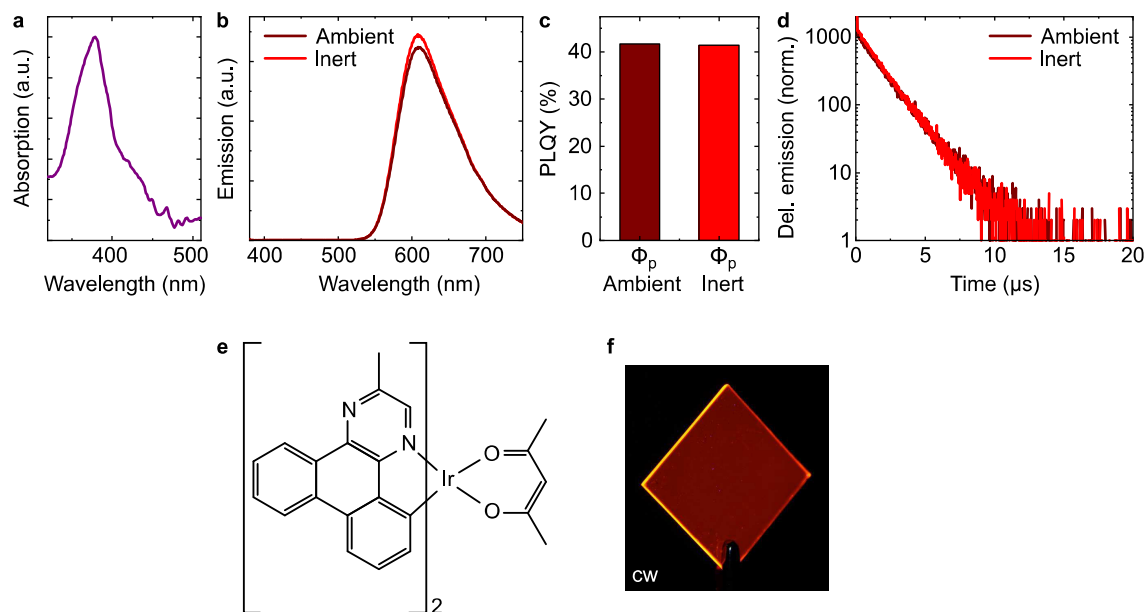


Figure 5.13.: PMMA:Ir(MDQ)₂(acac) (6 wt%), $\lambda_{\text{ex}} = 365$ nm and 340 nm (PLQY), measured in ambient and inert conditions. **a** Excitation scan. **b** Emission spectra. **c** Φ_p . **d** Phosphorescent decay measured using TCSPC. **e** Molecular structure of Ir(MDQ)₂(acac). **f** Non-functional PLT made of PMMA:Ir(MDQ)₂(acac).

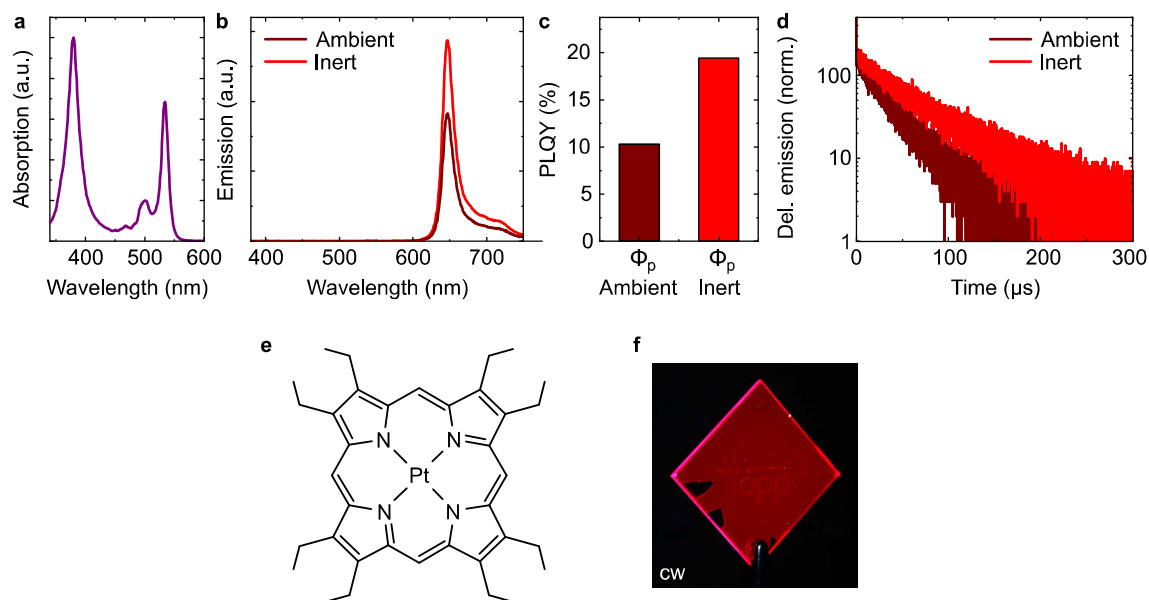


Figure 5.14.: PMMA:PtOEP (6 wt%), $\lambda_{\text{ex}} = 365$ nm and 340 nm (PLQY), measured in ambient and inert atmosphere. **a** Excitation scan. **b** Emission spectra. **c** Φ_p . **d** Phosphorescent decay measured using TCSPC. **e** Molecular structure of PtOEP. **f** PLT made of PMMA:PtOEP.

For PMMA:PtOEP (Figure 5.14), in contrast, a dependence on the oxygen concentration $[O_2]$ was visible. Here, the yield of the phosphorescent emission at $\lambda_p = 645$ nm increased from $\Phi_{p,O_2} = 10\%$ to $\Phi_{p,N_2} = 19\%$ when changing from ambient to inert atmosphere. At the same time, the lifetime increased from $\tau_{p,O_2} = 31$ μ s to $\tau_{p,N_2} = 53$ μ s. Due to the absence of fluorescence, defining a P2F value is not meaningful here. Instead, the ratio of the Φ_p increase when removing the oxygen gives information on the PLT contrast and is calculated to a rather low value of 0.9. A PLT in cw emission showed a pattern with low contrast (Figure 5.14 f).

A detailed evaluation of these results is presented in Section 6.1.2, where the influence of the phosphorescence lifetime on the performance of PLTs is discussed.

5.1.6. BP and TA - The Components

As entry point to the investigation of BP-2TA, its underlying compounds benzophenone (BP) and thianthrene (TA) are introduced first.

PMMA:BP (5 wt%) showed absorption up to $\lambda = 385$ nm with two peaks located at $\lambda = 290$ nm and $\lambda = 345$ nm (Figure 5.15 a). The emission peaks (Figure 5.15 b), located at $\lambda_p = 420$ nm, $\lambda_p = 450$ nm, and $\lambda_p = 480$ nm, can be attributed to phosphorescence¹⁵. The absence of fluorescence and the short triplet lifetime of $\tau_p < 1$ ms (Figure 5.15 d) hint to a very high SOC. Indeed, an ISC yield of unity is reported for

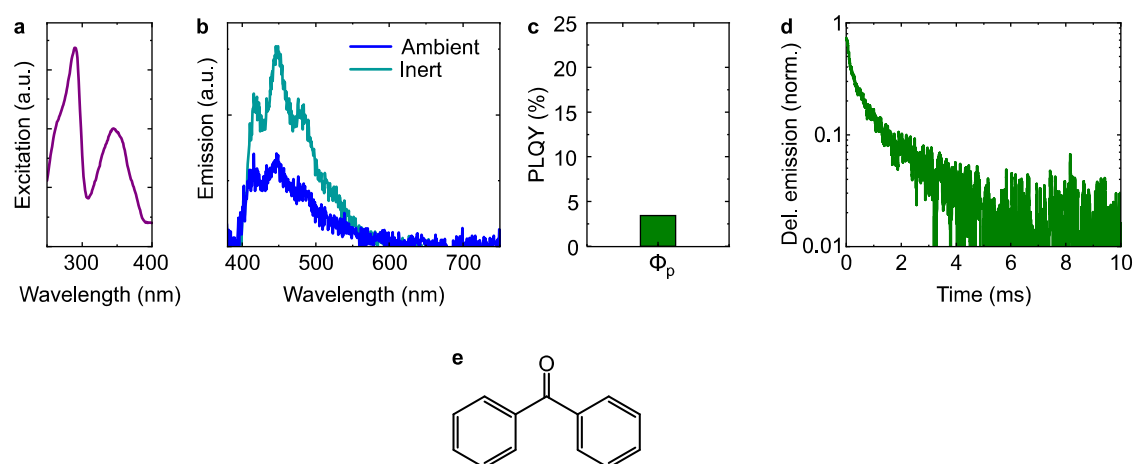


Figure 5.15.: PMMA:BP (5 wt%), $\lambda_{ex} = 365$ nm and 340 nm (PLQY). **a** Excitation scan. **b** Emission spectra in ambient and inert conditions. **c** Φ_p . The Φ_f measurement did not yield a meaningful result. **d** Phosphorescent decay after turning off the excitation LED. **e** Molecular structure of BP.

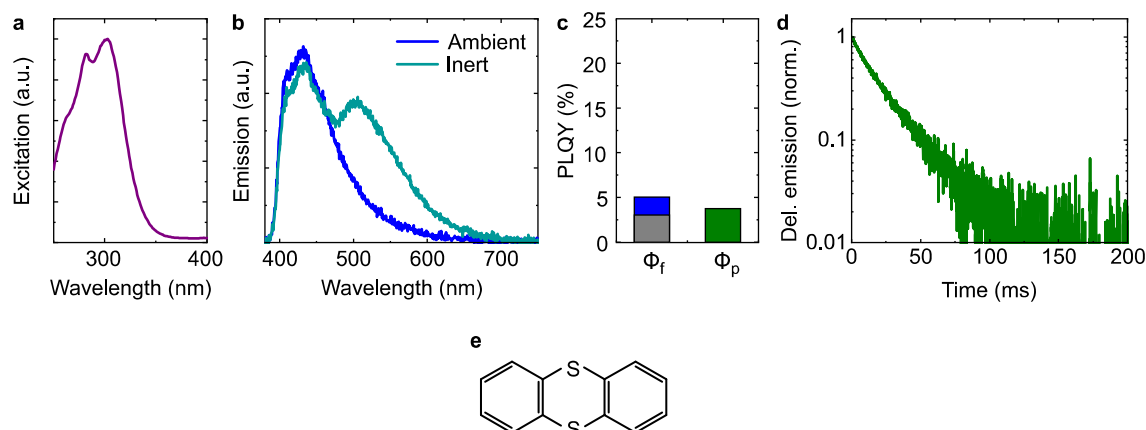


Figure 5.16.: PMMA:TA (2 wt%), $\lambda_{\text{ex}} = 365$ nm and 340 nm (PLQY). **a** Excitation scan. **b** Emission spectra in ambient and inert conditions. **c** Φ_f from an ambient measurement (gray) and from spectral analysis of an inert measurement (blue), and Φ_p . **d** Phosphorescent decay after turning off the excitation LED. **e** Molecular structure of TA.

BP²³⁰. This is in accordance to El Sayed’s rules as described in Section 2.2.5. The PLQY $\Phi_p = 3\%$ in inert conditions was rather low (Figure 5.15 c).

The absorption of PMMA:TA (2 wt%) reached up to $\lambda = 350$ nm with two peaks at $\lambda = 280$ nm and $\lambda = 300$ nm (Figure 5.16 a). In ambient atmosphere, it showed fluorescence at $\lambda_f = 430$ nm (Figure 5.16 b). When switching to nitrogen atmosphere, a phosphorescent peak at $\lambda_p = 515$ nm with a lifetime $\tau_p = 25$ ms emerged. A PLQY measurement in inert conditions and a spectral analysis of the face emission resulted in $\Phi_p = 4\%$. The fluorescent yield was determined to $\Phi_f = 3\%$ to $\Phi_f = 5\%$.^b

5.1.7. BP-2TA - The Workhorse

The chemical linking of the acceptor material BP and the electron donating TA results in BP-2TA, which shows enhanced RTP emission properties compared to its constituents when embedded into Zeonex⁷¹. A more detailed look into its photophysical properties for different emitter concentrations or excitation wavelengths will be given in the following. In a PMMA:BP-2TA (2 wt%) sample, the emitter showed fluorescence at $\lambda_f = 475$ nm with $\Phi_f = 1\%$. In inert atmosphere, the phosphorescence peaked at $\lambda_p = 515$ nm, showing $\Phi_p = 20\%$, P2F = 20, and $\tau_p = 30$ ms. A

^bThe two values result from measurements in ambient conditions ($\Phi_f = 3\%$) and from a spectral analysis of the data in inert atmosphere ($\Phi_f = 5\%$).

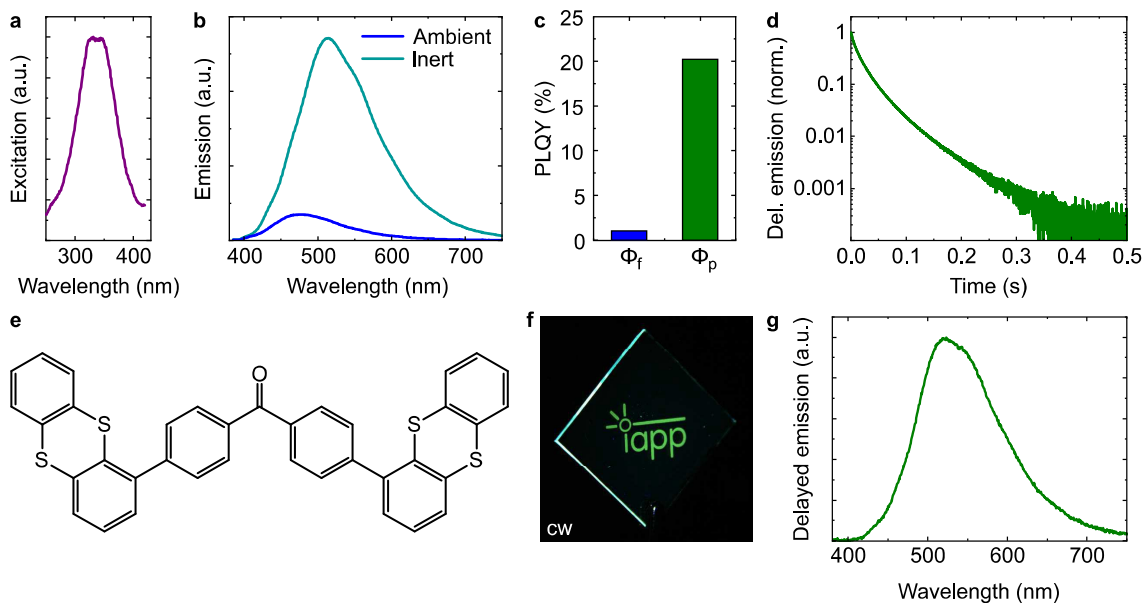


Figure 5.17.: PMMA:BP-2TA (2 wt%), $\lambda_{\text{ex}} = 340$ nm. **a** Excitation scan in ambient conditions. **b** Emission spectra in ambient and inert conditions. **c** Φ_f and Φ_p . **d** Phosphorescent decay after turning off the excitation LED. **e** Molecular structure of BP-2TA. **f** cw-PLT made of PMMA:BP-2TA in cw-emission. **g** Delayed emission.

cw-PLT showed a high-contrast image of the imprinted pattern (Figure 5.17 f). The intensity-averaged fluorescence lifetime was $\tau_f = 3.3$ ns (Figure 5.18).

In comparison to the prompt emission of its constituents BP and TA, BP-2TA revealed a red-shifted fluorescence (Figure 5.19 a). In contrast to that, its phosphorescence closely resembled the triplet emission of TA both in spectral position and shape (Figure 5.19 b). This indicates a local emissive triplet state ^3LE , located in the TA-moiety of BP-2TA. At the same time, the red-shifted fluorescence is a clear sign

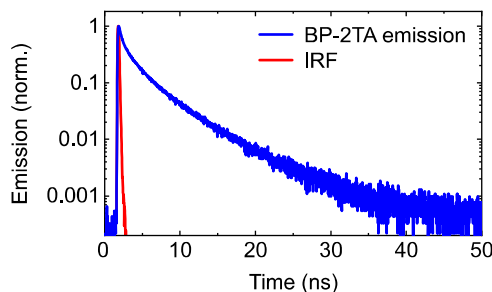


Figure 5.18.: Blue: Nanosecond decay of PMMA:BP-2TA (5 wt%), detected at $\lambda = 500$ nm (blue). Red: Instrument response function (IRF).

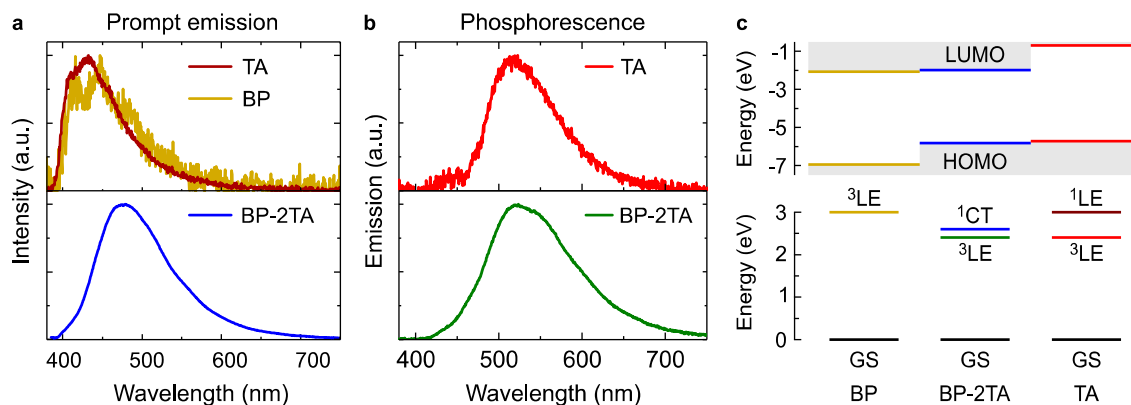


Figure 5.19.: **a** Prompt emission of TA, BP and BP-2TA. **b** Phosphorescence spectra of TA and BP-2TA. **c** Top: Calculated HOMO and LUMO energies of BP, BP-2TA and TA, with values taken from different publications^{44;71;231}. Bottom: Excited state diagram, calculated from emission peak energies, showing the BP triplet ^3LE , TA singlet ^1LE and triplet ^3LE , as well as BP-2TA ^1CT and ^3LE state, referring to the respective ground state GS.

for the presence of a ^1CT state, which is formed between the HOMO of the donor TA and the LUMO of the acceptor BP (cf. Section 2.2.7). Further confirmation is found in the comparison of the theoretically calculated energies of the involved orbitals (Figure 5.19 c). These energy values were taken from three independent publications^{44;71;231}. The LUMO of BP-2TA ($E_{\text{LUMO}} = -1.98 \text{ eV}$) is in good agreement with the LUMO of BP ($E_{\text{LUMO}} = -2.07 \text{ eV}$). The same accounts for the HOMO of BP-2TA ($E_{\text{HOMO}} = -5.82 \text{ eV}$) and TA ($E_{\text{HOMO}} = -5.72 \text{ eV}$). In total, the CT-state-induced RTP of BP-2TA showed impressively high Φ_p and P2F values when compared to its basic components and also to other RTP materials.

Varying the Emitter Concentration

In order to further optimize the intensity as well as the P2F ratio of the samples containing PMMA:BP-2TA, an emitter-concentration series was prepared, ranging from 0.5 wt% to 20 wt% of BP-2TA in PMMA550k. All further data were obtained using drop-casted samples, since the spin-coated low-concentration ones did not provide enough signal for reliable results (Figure 5.20 a). For thicker drop-casted layers, the phosphorescence yield $\Phi_p = 20\%$ was constant up to 2 wt% and then dropped down to $\Phi_p = 7\%$ at 20 wt% (Figure 5.20 b). At the same time, $\Phi_f \approx 1$ remained nearly unchanged.

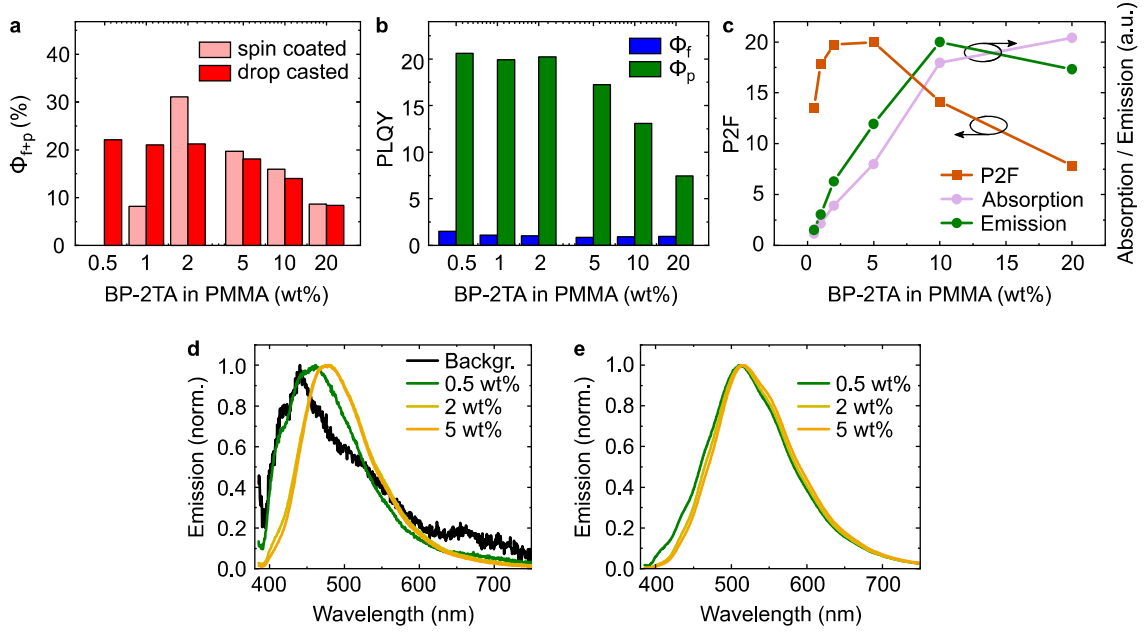


Figure 5.20.: For all data, the excitation wavelength was $\lambda_{\text{ex}} = 340$ nm. **a** Overall yield Φ_{f+p} measured in inert atmosphere of spin-coated and drop-casted PMMA:BP-2TA. **b** Φ_f and Φ_p of drop-casted PMMA:BP-2TA. **c** P2F (orange), total phosphorescence (green) and absorption (violet) of drop-casted PMMA:BP-2TA. **d** Normalized emission of drop-casted PMMA:BP-2TA in ambient conditions in comparison to a measurement of an empty sample box. **e** Normalized emission of drop-casted PMMA:BP-2TA in inert conditions.

The emission spectra in ambient and inert conditions are plotted in Figure 5.20 d and e. In the presence of oxygen, the emission should consist of fluorescence only. For very low concentration, the normalized spectrum differed compared to the other samples and showed increased relative emission at low wavelengths. Therefore, an additional spectral measurement of the empty sample box was obtained and revealed a background signal, which most probable originates in a long-wavelength tail of the excitation LED. This influence fits to the deviation of the 0.5 wt% sample. Since for higher emitter concentrations it was outshined by the brighter sample emission, the respective data did not show this artifact.

In Figure 5.20 c, the calculated P2F values are shown in orange. Apart from the two lowest concentration samples, the P2F showed the same trend as Φ_p and dropped from $\text{P2F} = 20$ for 2 wt% to $\text{P2F} = 8$ for 20 wt%. For 0.5 wt% and 1 wt%, the background signal of the LED again corrupted the data. The total phosphorescent emission increased with the concentration up to 10 wt%, but then decreased again

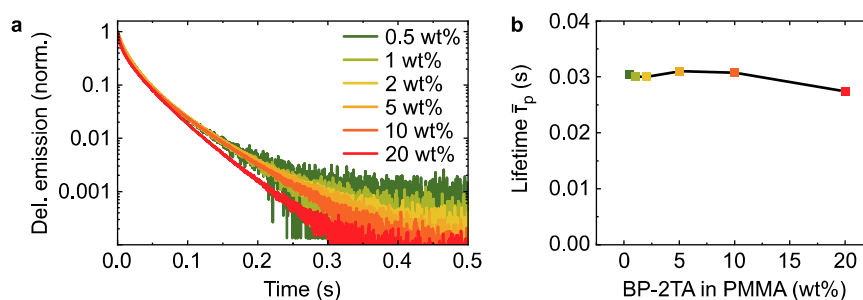


Figure 5.21.: Decay dynamics of PMMA:BP-2TA for different concentrations. **a** Phosphorescent decays after turning off the excitation LED. **b** Intensity averaged phosphorescent lifetimes.

going to 20 wt%. This reduction originated on the one hand from the drop of Φ_p . On the other hand, the absorption of the 20 wt% sample was only 1.14 times higher than it was for 20 wt%. For samples with lower emitter density, it scaled nearly linear to the concentration. At 20 wt%, the validity of Beer's law might have been lost (cf. Section 2.2.3).

The phosphorescent decays of PMMA:BP-2TA with different concentrations and their respective lifetimes are depicted in Figure 5.21. While for low to medium concentrations $\tau_p = 30$ ms remained constant, it dropped to 0.90 of its value for 20 wt%. That decrease could be assigned to TTA. This is in contrast to PMMA:NPB, where TTA already occurred at 2 wt%. Still this conclusion is reasonable, since TTA and its underlying triplet density $[T_1]$ are strongly dependent on τ_p , which is one order of magnitude larger for NPB compared to BP-2TA.

At the first glance, the small decrease of the measured lifetime τ_p does not explain the drastic reduction of Φ_p at 20 wt% (cf. Figure 5.20 b). As seen in equation 2.41, both values should be closely related. However, with increasing concentration the guest emitters may tend to form aggregates instead of dispersing homogeneously. These aggregates often form nonradiative triplet states, which are energetically below T_1 of the single emitters¹². Therefore, an excited triplet state in an aggregate quickly relaxes thermally and does not contribute to the overall T_1 emission. In consequence, these pathways are not visible in photoluminescent measurements and the acquired decay results from non-aggregated emitters only. The formation of aggregates may also contribute to the reduced absorption at 20 wt%.

Varying the Excitation Wavelength

Further measurements revealed, that the P2F value of PMMA:BP-2TA was not only dependent on the guest concentration, but also on the excitation wavelength. Figure 5.22 a shows emission from a PMMA:BP-2TA (5 wt%) sample both in ambient and inert atmosphere when excited with different excitation sources ranging from $\lambda_{\text{ex}} = 275 \text{ nm}$ to $\lambda_{\text{ex}} = 360 \text{ nm}$. All data were normalized to the peak intensity in inert atmosphere. The resulting P2F values are plotted in Figure 5.22 b. The general trend was a reduction of P2F when going to higher excitation wavelength, namely from P2F = 28 at $\lambda_{\text{ex}} = 275 \text{ nm}$ to P2F = 6 at $\lambda_{\text{ex}} = 360 \text{ nm}$. At the same time, the shapes of both fluorescence and phosphorescence did not change.

In order to further investigate this dependency, excitation scans were performed. These were taken once in ambient conditions and once using an Exceval-covered fully activated sample resembling inert atmosphere. Apart from the Exceval layer, both PMMA:BP-2TA (5 wt%) samples were identical. The detection wavelength was $\lambda_{\text{ex}} = 470 \text{ nm}$ for both measurements, because at this spectral position fluorescence and phosphorescence show sufficient emission. The resulting raw data are shown in Figure 5.23 a, and are presented as normalized data in Figure 5.23 b. The big difference in intensity between ambient and inert raw data represents a high P2F value. The more interesting result is the change of the spectral shape. In ambient conditions, a broad plateau from $\lambda_{\text{ex}} = 320 \text{ nm}$ to $\lambda_{\text{ex}} = 350 \text{ nm}$ dominated the excitation scan. In the absence of oxygen, one single peak at $\lambda_{\text{ex}} = 320 \text{ nm}$ was present. That difference resembles a dependency of P2F on λ_{ex} , similar to as seen

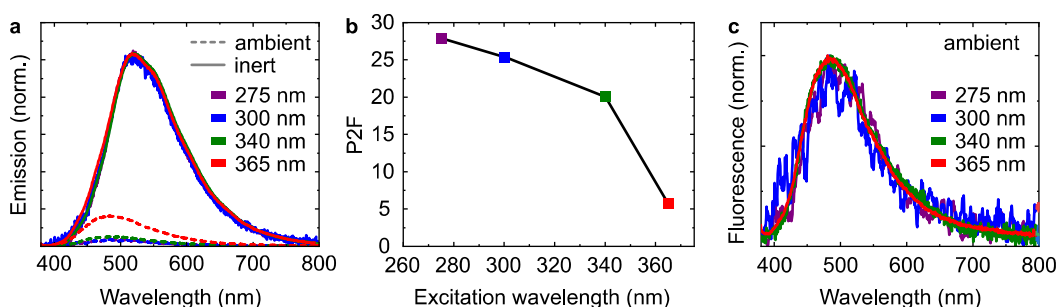


Figure 5.22.: Emission of PMMA:BP-2TA (5 wt%). **a** Ambient and inert spectra for different excitation wavelengths λ_{ex} , normalized to the peak intensity of the inert one. **b** P2F values for different λ_{ex} . **c** Normalized fluorescence spectra for different excitation wavelengths λ_{ex} .

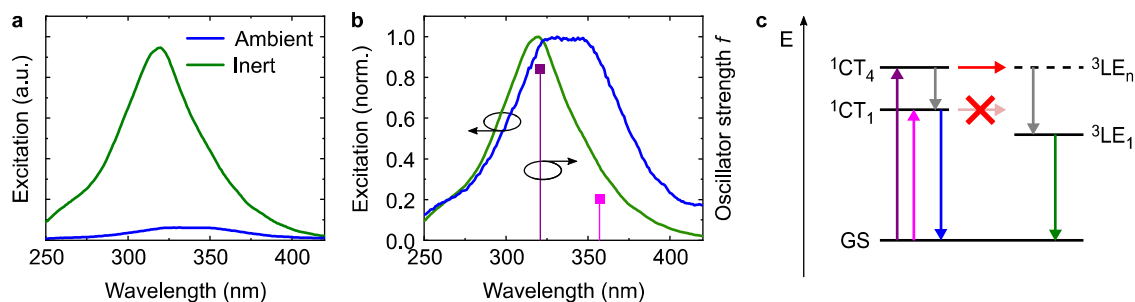


Figure 5.23.: Excitation scans of PMMA:BP-2TA (5 wt%) in ambient (blue) and inert (green) conditions. The detection wavelength was $\lambda = 470$ nm. **a** Raw data. **b** Normalized data. The violet dots refer to the computed oscillator strengths f for the dominant excitation transitions at $\lambda_{\text{ex}} = 321$ nm (dark) and $\lambda_{\text{ex}} = 357$ nm (light). **c** Proposed pathways of the excitons for the two given λ_{ex} . Note that the position of the intermediate ${}^3\text{LE}_n$ state is an assumption.

before (cf. Figure 5.22 b). For higher wavelengths, the relative amount of fluorescence in respect to phosphorescence increased.

This behavior is in contrast to other RTP emitters like NPB (cf. Figure 5.6) and will be discussed in the following. In Figure 5.23 b, theoretically calculated oscillator strengths for the two dominating absorption transitions of BP-2TA are added. These values were computed by Tomkeviciene et al.⁷¹ and resemble the CT transitions from the ground state to ${}^1\text{CT}_4$ and ${}^1\text{CT}_1$.^c A possible explanation for the deviation of both excitation scans is a difference in the ISC efficiency from ${}^1\text{CT}_4$ and ${}^1\text{CT}_1$. It is conceivable that a higher lying triplet state ${}^3\text{LE}_n$ energetically fits to ${}^1\text{CT}_4$, which could increase the ISC probability due to a reduced ΔE_{STn} ⁴⁸ (cf. Section 2.2.5). This intermediate state then relaxes to ${}^3\text{LE}_1$, from where phosphorescence originates. Excitation to ${}^1\text{CT}_1$ at the same time mainly decays as fluorescence, as no efficient ISC is possible. On the other hand, the internal conversion from a higher lying state of the same multiplicity is on a timescale of 10^{-12} s, at least for locally excited states⁷⁵. Therefore, the ISC rate should be sufficiently high to ensure a high population rate of the triplet state. In order to fully address this question, further theoretical and experimental insights into the ISC processes of CT states are necessary.

^cThe notation ${}^1\text{CT}_4$ and ${}^1\text{CT}_1$ is analogous to S_4 and S_1 in ${}^1\text{LE}$ states.

5.2. Multi-Guest Systems

In a short summary, several multi-guest systems are addressed in this Section. As will be shown, the addition of a further guest material can be used to change the emission color or the P2F value.

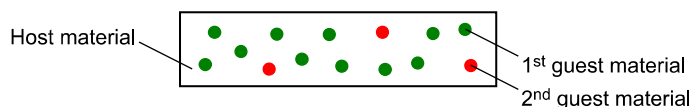


Figure 5.24.: A multi-guest sample. The guests (green and red) are equally distributed in the rigid host material in their respective concentrations.

5.2.1. NPB:DCJTB and BP-2TA:DBP - Towards Red PLTs

Recently we showed efficient FRET from the triplet state of NPB to the singlet state of the red fluorescent emitter 4-(dicyano-methylene)-2-tert-butyl-6-(1,1,7,7-tetramethyl-julolidyl-9-enyl)-4H-pyran (DCJTB)²³². Via this, oxygen-dependent emission in the orange color regime was realized. In order to use this color shift in PLTs, we dispersed both NPB and DCJTB into PMMA. The NPB concentration was 2 wt%, and different samples with varying DCJTB concentration were manufactured. Via experimental and theoretical validation, an efficient nonradiative energy transfer from the triplet state of NPB to the singlet state of DCJTB with a Förster radius $R_F = 2.5$ nm was proven (Figure 5.25). In addition, singlet-singlet (S-S) FRET was observed, but is not of interest here. The triplet-singlet (T-S) pathway not only reduced the phosphorescence lifetime (Figure 5.26 c), but also shifted the overall emission to the red, both in cw (Figure 5.26 b) and delayed emission (Figure 5.26 f).

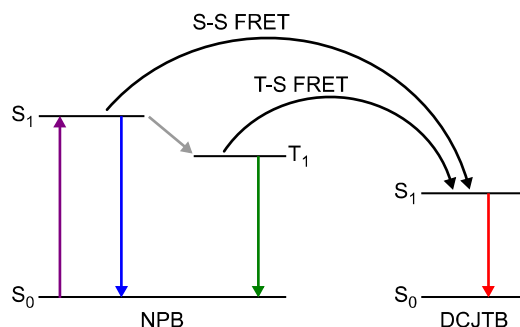


Figure 5.25.: Singlet-singlet (S-S) and Triplet-Singlet (T-S) FRET from the donor NPB to the red fluorescing acceptor DCJTB.

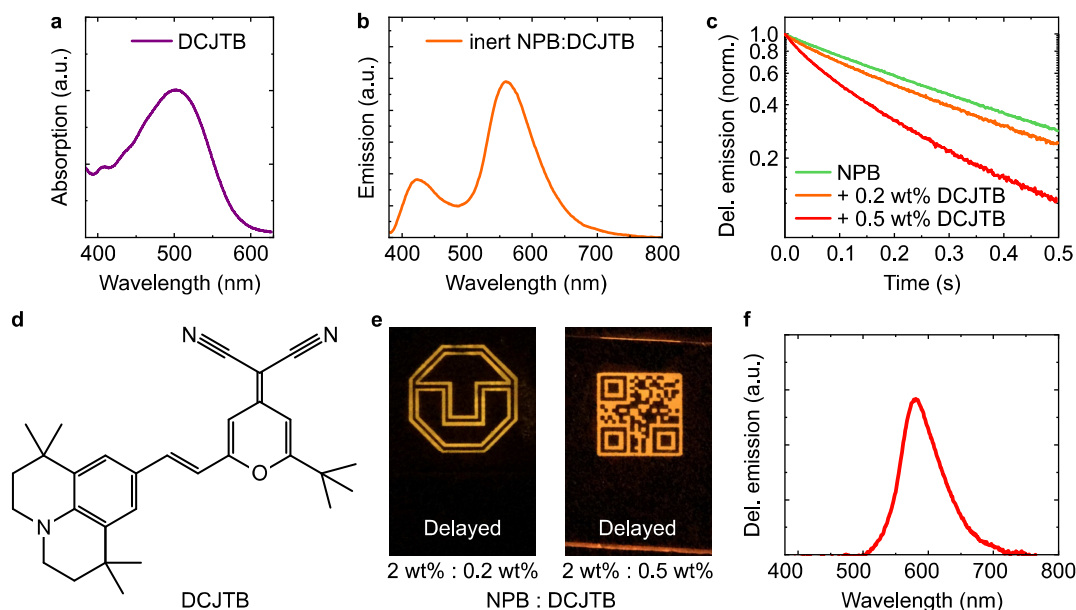


Figure 5.26.: PMMA:NPB(2 wt%):DCJTB(0.2 and 0.5 wt%), $\lambda_{\text{ex}} = 365$ nm. Measurements performed by Anton Kirch. **a** Absorbance of PMMA:DCJTB. **b** Emission spectrum of a PMMA:NPB:DCJTB(0.2 wt%) sample in inert conditions. **c** Phosphorescent decays of PMMA:NPB(2 wt%):DCJTB(0.2 and 0.5 wt%) in comparison to PMMA:NPB. **d** Molecular structure of DCJTB. **e** PLTs in delayed emission made of PMMA:NPB:DCJTB. **f** Delayed emission of PMMA:NPB:DCJTB(0.5 wt%).

This concept could successfully be applied in the realization of PLTs with redshifted emission (cf. Figure 5.2 g for pure NPB PLTs as comparison). In delayed emission, the PMMA:NPB:DCJTB sample showed orange and reddish emission (Figure 5.26 e). In cw emission, no pattern was visible due to the dominating prompt emission of both NPB and DCJTB.

In order to overcome the low P2F value in cw excitation, NPB was replaced by BP-2TA, and dibenzo[(f,f')-4,4',7,7'-tetraphenyl]diindeno[1,2,3-cd:1',2',3'-lm]perylene (DBP) was used as a red acceptor. The latter showed highest absorption at $\lambda = 500$ nm to $\lambda = 600$ nm (Figure 5.27 a). This overlaps nicely with the triplet emission of BP-2TA, indicating the possibility of T-S-FRET. Indeed, the phosphorescence lifetime of PMMA:BP-2TA (5 wt%) decreased from 30 ms to 18 ms when adding 0.5 wt% of DBP (Figure 5.27 c). Further, an intense red peak was visible in the delayed emission (Figure 5.27 f). The cw emission slightly increased when going from ambient to inert atmosphere (Figure 5.27 b). Thus, orange cw-PLTs were feasible, but the contrast

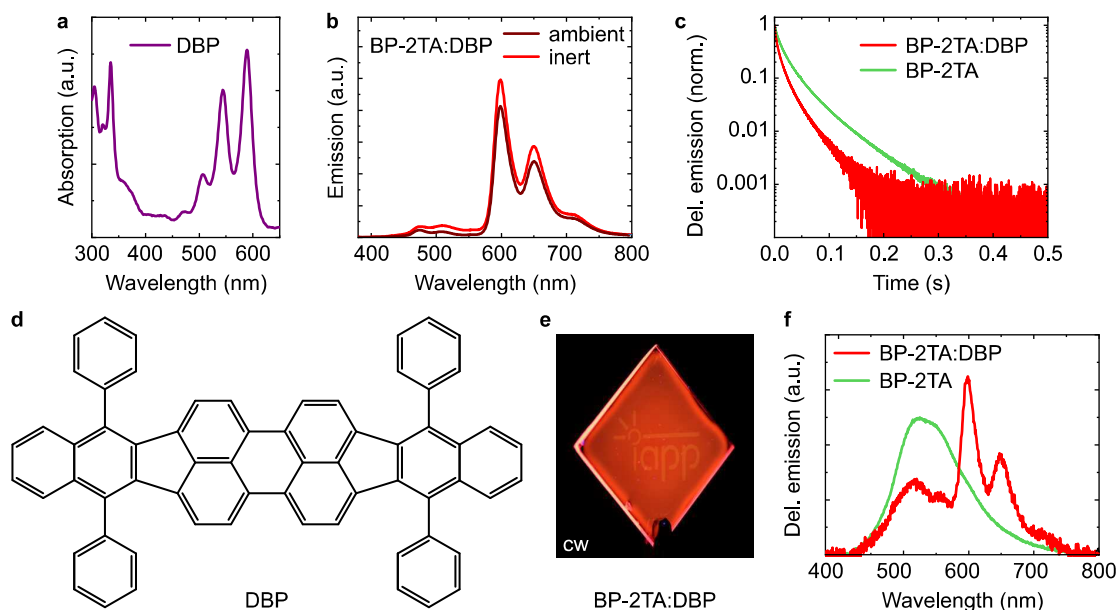


Figure 5.27.: PMMA:BP-2TA(5 wt%):DBP(0.5 wt%), $\lambda_{\text{ex}} = 365 \text{ nm}$. **a** Absorbance of PMMA:DBP. **b** Emission spectra of a PMMA:BP-2TA:DBP sample in ambient and inert conditions. **c** Phosphorescent decay of a PMMA:BP-2TA:DBP sample in comparison to PMMA:BP-2TA. **d** Molecular structure of DBP. **e** cw-PLT made of PMMA:BP-2TA:DBP. **f** Delayed emission of PMMA:BP-2TA:DBP in comparison to PMMA:BP-2TA.

of the pattern was low (Figure 5.27 e). This may be mainly due to the intense red emission also in the presence of oxygen, which resulted from direct excitation of DBP.

5.2.2. PhenDpa:DBP - Delayed Emission Spanning the Full Visible Range

In Section 5.1.2, PhenDpa was introduced. Due to TADF, which accompanied RTP in delayed emission, a broad range of the visible spectrum from $\lambda = 400 \text{ nm}$ to $\lambda = 650 \text{ nm}$ is covered. In order to complete this to the full visible range, DBP was introduced into the system. The resulting PMMA:PhenDpa(2 wt%):DBP(0.2 wt%) showed delayed emission up to $\lambda = 720 \text{ nm}$ with CIE color coordinates (0.44, 0.43), close to warm white emission (Figure 5.28). The corresponding lifetime $\tau = 290 \text{ ms}$ was shorter than for PhenDpa only, indicating T-S-FRET from PhenDpa to DBP.

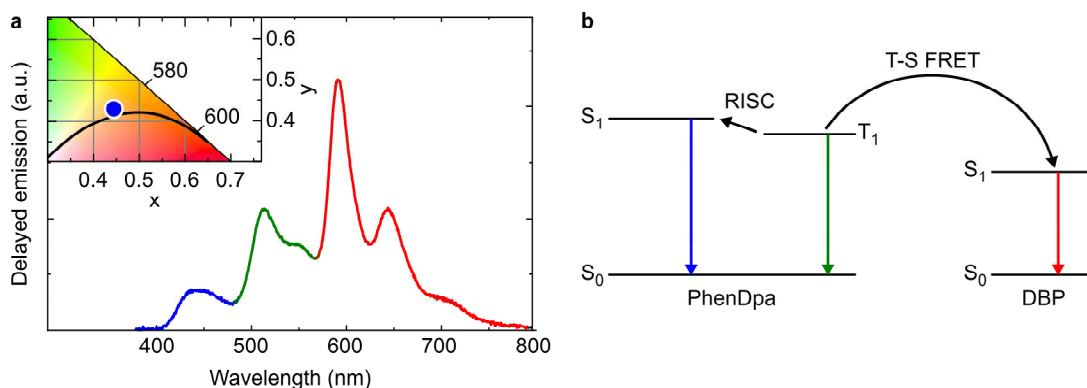


Figure 5.28.: **a** Delayed emission from PMMA:PhenDpa:DBP, consisting of TADF (blue) and Phosphorescence (green) from PhenDpa and FRET-induced fluorescence from DBP (red). Inset: CIE Color coordinates of the emission (blue dot). The black line is the Planckian locus.

5.2.3. NPB:DBBP - Improving P2F with Additives

As shown in Section 5.1.1, the phosphorescence contrast of PMMA:NPB with P2F = 0.13 is very low. The adding of polymers containing bromine ($Z = 35$) into the environment of NPB is known to increase the share of phosphorescence²⁸ due to the external heavy atom effect (cf. Section 2.2.5). Therefore, we introduced 4,4'-dibromobenzophenone (DBBP), a brominated derivative of BP, as additive into a PMMA:NPB (0.5 wt%) sample. With increasing concentration of DBBP from 0 wt% to 40 wt%, the cw emission both in ambient and inert atmosphere changed (Figure 5.29 a). The fluorescence dropped and almost disappeared at high shares of additive. At the same time, the phosphorescence showed a slight increase. Further, we observed an increased depopulation of both the singlet and triplet state of NPB (Figure 5.29 b and e), the latter owning a lifetime of $\tau_p = 125$ ms at 40 wt% of DBBP (Figure 5.29 f). However, the shape of the delayed spectrum did barely change for increasing concentration, only a weak shoulder at $\lambda = 490$ nm arose (Figure 5.29 d). The results indicate both an increased ISC, which depopulates the singlet state of NPB, and an enhanced k_p , which leads to reduced τ_p . Both may be explained by the influence of the external heavy atoms, which increase the spin-orbit coupling of the excitons.

The PLQY values of the singlet and triplet states of NPB matched these results. With increasing concentration of DBBP, the fluorescence yield of samples consisting of PMMA:NPB(0.5 wt%):DBBP decreased from $\Phi_f = 23\%$ at 0 wt% DBBP to $\Phi_f < 1\%$

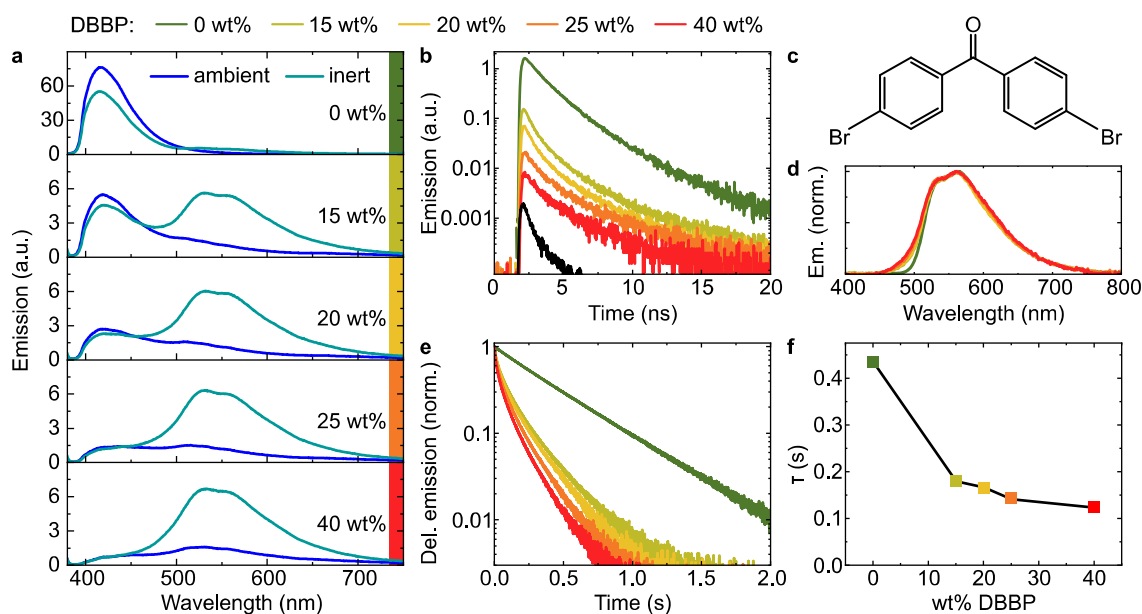


Figure 5.29.: Emission properties of PMMA:NPB(0.5 wt%):DBBP for different concentrations of DBBP. **a** cw emission in ambient and inert conditions for 0 wt% to 40 wt% of DBBP. **b** TCSPC decays of the prompt emission at $\lambda = 410$ nm. The black curve shows the emission of a pure PMMA:DBBP (40 wt%) sample. **c** Molecular structure of DBBP. **d** Delayed emission. **e** Phosphorescence decays. **f** Average phosphorescence lifetimes.

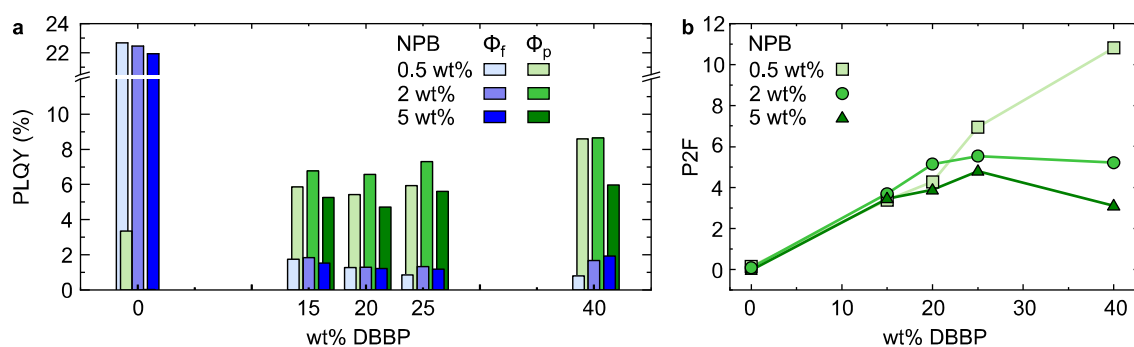


Figure 5.30.: PLQY and P2F data of PMMA:NPB:DBBP for different concentrations of both guests. **a** Fluorescence and phosphorescence PLQY. **b** P2F values.

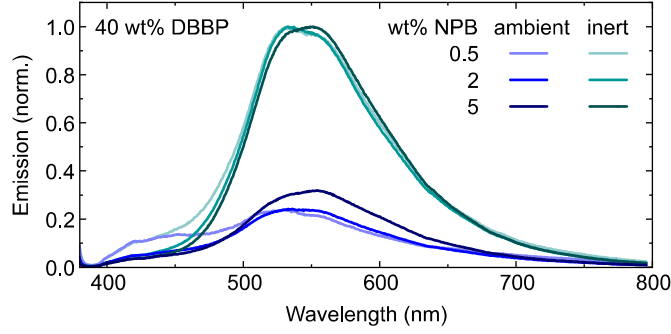


Figure 5.31.: PMMA:NPB:DBBP(40 wt%) cw-emission spectra with different concentrations of NPB for ambient and inert atmosphere. The spectra are normalized to the samples' emission peaks in inert atmosphere.

at 40 wt%. In contrast to that, the phosphorescence showed an increase from $\Phi_p = 3\%$ without DBBP to $\Phi_p = 9\%$ at 40 wt% (Figure 5.30 a). The P2F value showed a gradual increase with the DBBP concentration up to $P2F = 11$ for 40 wt% DBBP. This resembles an increase of a factor of 70 compared to the sample without DBBP. For higher NPB concentration (2 wt% and 5 wt%) the results were similar, but P2F only rose up to $P2F = 5$ and $P2F = 3$, respectively. These values correlate with Φ_f , which showed an increase with the NPB concentration from $\Phi_f < 1\%$ (0.5 wt% of NPB) to $\Phi_f = 2\%$ (5 wt% of NPB), both at 40 wt% DBBP. A closer look at the cw spectra (Figure 5.31) shows that the dominating emission in ambient conditions not only consisted of fluorescence, but with increasing NPB concentration, a further peak at $\lambda = 530$ nm to $\lambda = 570$ nm evolved. Its spectral position and shape hint to a phosphorescent nature^d, which apparently was not quenched by oxygen. This could be explained by a very high radiative rate k_p , outcompeting the oxygen quenching k_{qT} .

Using TCSPC, the lifetime of this new peak was determined to be $\tau = 160$ μ s in a PMMA:NPB(2 wt%):DBBP(25 wt%) sample (Figure 5.32 a). This is almost in the same order of magnitude as the lifetime of PtOEP ($\tau_{p,O_2} = 31$ μ s, cf. Section 5.1.5), which shows phosphorescence in air. In a next step, the emission on the microsecond timescale at different TCSPC detection wavelengths was integrated in the range of $t = 1$ μ s to $t = 2000$ μ s. These results pretty much resemble the delayed emission in the millisecond range $t = 5$ ms to $t = 455$ ms (Figure 5.32 b). Therefore, this

^dIn this case, the notations Φ_f , Φ_p and P2F may be inaccurate, since there is an amount of triplet emission in Φ_f in ambient conditions. Still this notation is kept up, since for PLTs the ratio of emission in inert and ambient conditions is decisive.

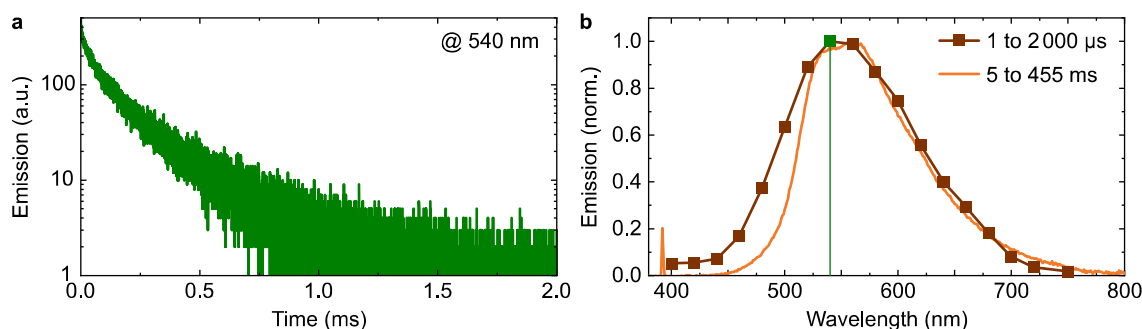


Figure 5.32.: Emission from PMMA:NPB(2 wt%):DBBP(25 wt%). **a** Microsecond decay, detected at $\lambda = 540$ nm. **b** Integrated μ s decays for different detection wavelengths, compared to the delayed emission in the millisecond timescale. The green dot represents the integrated decay of figure a.

additional peak indeed can be attributed to very fast phosphorescence, which may be induced by high SOC resulting from DBBP molecules in very close position to NPB. Still, further investigation is needed to fully understand the spectral shapes and the emission dynamics and therefore the exciton pathways. A detailed study of similar additives including bromobenzophenone (BrBP), difluorobenzophenone (DFBP) and diiodobenzophenone (DIBP) is currently in preparation.

To sum up, a strong increase of the P2F value of NPB was achieved using DBBP as an additive. This enabled dominating phosphorescence in cw emission (Figure 5.33 c) and therefore the realization of cw-PLTs (Figure 5.33 d).

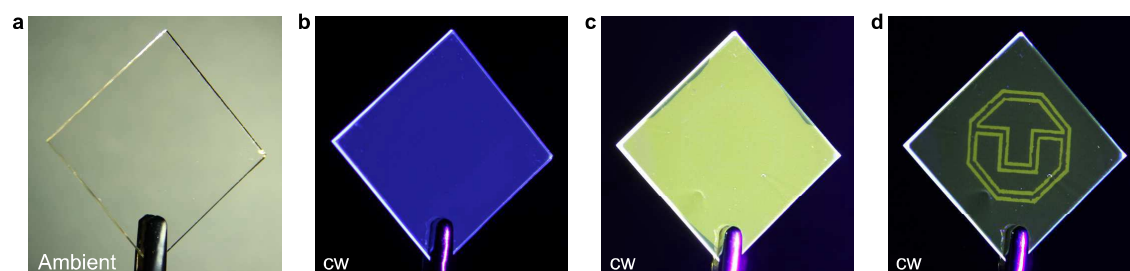


Figure 5.33.: **a** Exemplary sample in ambient light **b** cw emission of PMMA:NPB(2 wt%) in the absence of oxygen. **c** cw emission of PMMA:NPB(2 wt%):DBBP(25 wt%) in the absence of oxygen. **d** cw-PLT realized with PMMA:NPB(2 wt%):DBBP(25 wt%).

5.3. Overview and Summary

Table 5.1 shows all relevant parameters of the investigated materials. Most emitters show green to yellow phosphorescence in the range of $\lambda = 500$ nm to $\lambda = 600$ nm. With 2HC, an RTP emitter with blue phosphorescence is introduced. Its fluorescence peaks in the UV, which is why it is barely visible in cw emission (cf. Figure 5.12 e). Therefore, the phosphorescent contrast is better than the $P2F < 1$ at first glance suggests. Further, the introduction of an additional red-emitting guest to NPB or BP-2TA as FRET acceptor enabled oxygen-dependent emission in the orange and red color regime. Thus, combining different emitter systems in multiple stacked layers may open up the possibility of multi-color PLTs. With 2HC as blue, BP-2TA as green, and BP-2TA:DBP as red emitters, a full RGB color coding is thinkable. However, the biggest challenge here is fine tuning the absorption spectra in order to avoid a spectral overlap. This would be necessary for selective activation of each layer separately.

The emission yield of the emitters ranged up to $\Phi_p = 20\%$ for BP-2TA, which is comparably high for purely organic phosphorescence at room temperature¹². In combination with the high $P2F = 20$ for $\lambda_{ex} = 340$ nm, this value renders BP-2TA as the most suitable material for the use in PLTs up to now. A closer look into the dependence of the PLT emission on the $P2F$ value will be given in the next chapter. Absorption is mostly found in the UV range, but some materials like PhenDpa and $BF_2(HPhN)$ can be excited in the visible as well. The addition of DBBP to PMMA:NPB was shown to enable the enhancement of $P2F$ as well as Φ_p via increasing SOC. The generalization of this effect to further emitter materials was not part of this thesis, but may allow the possibility to fine-tune the $P2F$ of any RTP emitter.

Table 5.1.: The important photophysical properties of the investigated guest materials.

| Guest material | λ_{abs} | λ_p | Φ_p | τ_p | P2F |
|----------------|-----------------|------------------|------------------|---------------------|--------------------------------------|
| NPB | up to 400 nm | 530 nm, 570 nm | 3% ^{iv} | 406 ms ^v | 0.13 ^{iv} |
| PhenDpa | up to 420 nm | 515 nm, 560 nm | 6% | 330 ms | 0.3 |
| $BF_2(HPhN)$ | up to 470 nm | 550 nm | 12% | 220 ms | 1.5 |
| 2HC | up to 330 nm | 425 nm, 450 nm | - | 819 ms | < 1 |
| BP | up to 385 nm | 420 nm to 480 nm | 3% | < 1 ms | - |
| TA | up to 350 nm | 515 nm | 4% | 25 ms | ≈ 1 |
| BP-2TA | up to 400 nm | 515 nm | 20% | 30 ms | 20 ^{vi} , 28 ^{vii} |

^{iv} for 0.5 wt%. ^v for 2 wt%. ^{vi} for $\lambda_{ex} = 340$ nm. ^{vii} for $\lambda_{ex} = 275$ nm.

—— 5. Characterization of Guest Materials ——

This is planned to be realized in a follow-up study. With the elaborate collection of the diverse photophysical properties of the different guests, the optimization of PLTs now can be addressed in the following chapter.

6. Optimization via Diversification: PLTs with Various Material Systems

This last experimental chapter addresses the optimization of PLTs with respect to different aspects. Therefore, the most promising SwiP emitters identified and described in Chapter 5 are used to build PLTs with different properties. Hereby, the focus is set on several important parameters, namely the P2F value, the phosphorescent lifetime τ_p , the excitation wavelength λ_{ex} , and the activation dose D_{act} . In order to address the last one, new host polymers are introduced. Additionally, a variety of possible substrates beyond common quartz glass as well as multiple PLT processing techniques are presented in order to increase the variety of possible applications.

6.1. Tuning the Important Parameters

6.1.1. P2F: Simplifying the Readout Process

Almost all images of printed PLT-patterns shown so far were recorded in delayed emission shortly after turning off the excitation source (Figure 6.1 a). That timing procedure was necessary, since in cw emission, the fluorescence of NPB dominated over the phosphorescence, and only in the latter the imprint was visible (cf. Figure 4.9 c). This originated from the low phosphorescence yield $\Phi_p = 3\%$ of PMMA:NPB compared to its fluorescence $\Phi_f = 23\%$ (cf. Section 5.1.1 for details). The resulting $P2F = 0.13$ indicates the poor visibility of the imprint in cw emission. An increase of that value would enable reading the imprints in cw emission, leading to cw-PLTs. As a result, a drastically simplified readout process without the need of any timing routine could be realized (Figure 6.1 b).

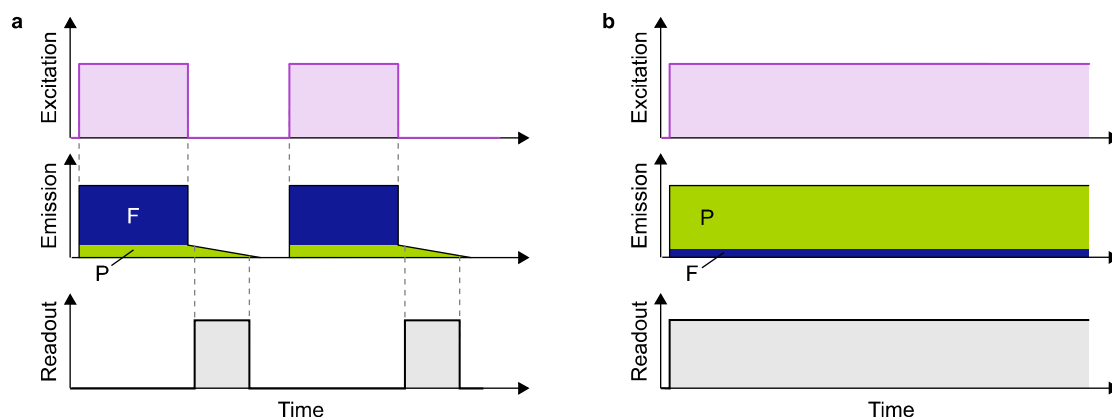


Figure 6.1.: Timing schemes of the readout of PLTs with different P2F values. **a** At low P2F, excitation and readout have to be separated in time in order to eliminate the fluorescent emission. **b** High P2F ratios enable continuous readout at ongoing excitation.

In Figure 6.2, a simulated emission pattern is sketched for an increasing P2F ratio. It consists of blue fluorescence and green phosphorescence. A $P2F = 0$ is shown on the left, where no contrast is visible at all. The right end shows $P2F = \infty$. This value corresponds to the delayed emission of NPB, since in this case no fluorescence is emitted.

The P2F values, the yield Φ_p , as well as PLT images of different material systems from Chapter 5 are put together in Figure 6.3. They show that even $BF_2(HPhN)$ with $P2F = 1.5$ already shows enough contrast for cw readout. BP-2TA with $P2F = 20$ closely resembles the quality of the delayed NPB emission (Figure 6.3 c). In addition, its high phosphorescence yield $\Phi_p = 18\%$ at 5wt% renders it as the most suitable emitter for the use in PLTs (cf. Section 5.1.7 for all data on BP-2TA).



Figure 6.2.: Simulated increasing of P2F and the resulting contrast between activated and non-activated areas on the PLT.

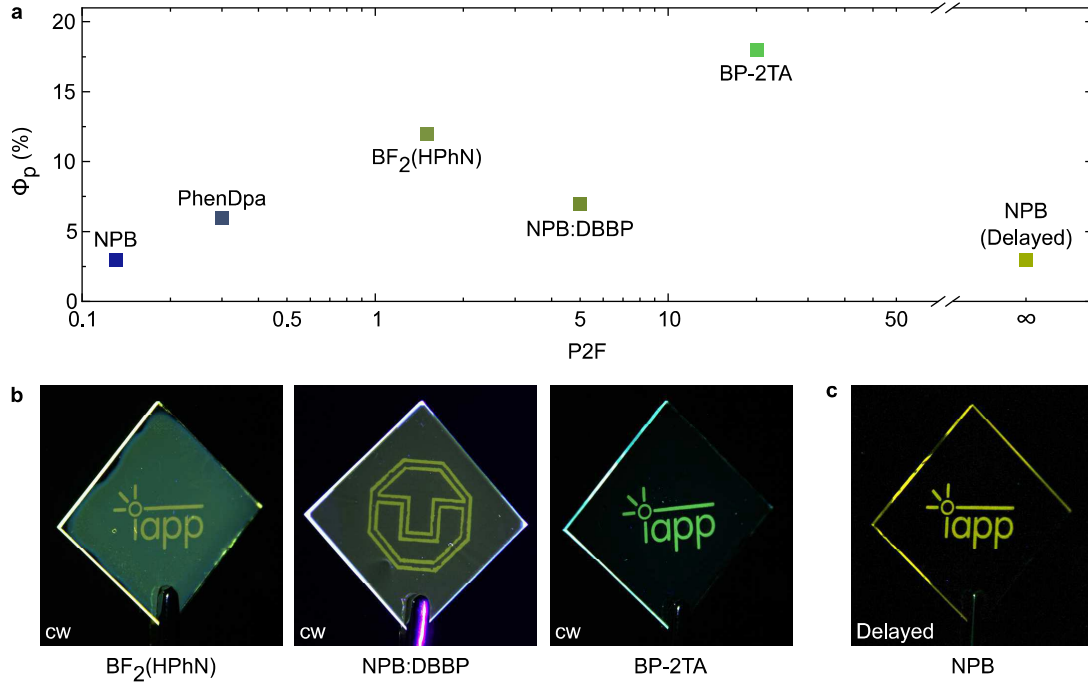


Figure 6.3.: **a** P2F and Φ_p of different emitters in cw and delayed emission. **b** Images of PLTs with different emitters in cw emission. **c** Image of a PLT using NPB in delayed emission.

Therefore, a PLT made of PMMA:BP-2TA (5 wt%) could be used to realize high-contrast rewritable phosphorescent patterns in cw emission (Figure 6.4). Experiments showed, that again it was possible to erase the patterns by heating as well as to rewrite new patterns multiple times. The excitation here was $\lambda_{\text{ex}} = 365 \text{ nm}$, thus the contrast was $\text{P2F} = 6$ (cf. Section 5.1.7).

The high pattern contrast in cw emission of PLTs containing BP-2TA is a key feature for the successful practical implementation in any application, since it drastically simplifies the readout process. The P2F value can be used as a benchmark for this contrast. As lower level for readout in cw excitation, the conducted experiments suggest $\text{P2F} = 1.5$. For $\text{P2F} \geq 6$, the undesired background is reduced to a level that competes with PLTs in delayed emission, which only show phosphorescence. In order to realize high P2F, very high phosphorescent yield Φ_p in combination with low fluorescence Φ_f is essential.

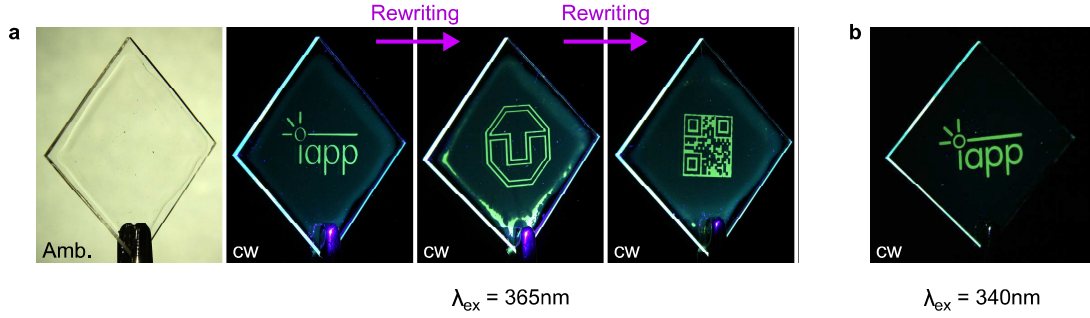


Figure 6.4.: PLTs consisting of PMMA:BP-2TA (5 wt%). **a** A PLT in ambient light and under excitation with $\lambda_{\text{ex}} = 365 \text{ nm}$. In the rewriting steps, the patterns were erased by heating and reprinted using masks. **b** A PLT under excitation at $\lambda_{\text{ex}} = 340 \text{ nm}$.

6.1.2. τ_p : Ensuring Oxygen Quenching

In addition to a high P2F, in cw-PLTs the excited triplet states have to be fully quenched in the presence of oxygen. Otherwise, they may contribute to the reduction of the contrast, as seen for NPB:DBBP (cf. Section 5.2.3).

The data of $\text{Ir}(\text{MDQ})_2(\text{acac})$ show that triplet lifetimes in the range of several microseconds lead to efficient phosphorescence in the presence of oxygen due to a very high k_p (cf. Section 5.1.5). In consequence, the removal of oxygen cannot increase the emission any further and no pattern is visible in the PLT. In contrast, PtOEP, owning a slightly higher lifetime, shows dependence on the presence of O_2 with $\tau_{p,\text{O}_2} = 31 \mu\text{s}$ and $\tau_{p,\text{N}_2} = 53 \mu\text{s}$ for 5 wt% in PMMA. Assuming that this difference is purely caused by oxygen quenching, one can deduce the quenching term $k_{qT}[\text{O}_2]$:

$$\tau_{p,\text{O}_2} = \frac{1}{k_p + k_{\text{nr}} + k_{qT} \cdot [\text{O}_2]} \quad (6.1)$$

$$\tau_{p,\text{N}_2} = \frac{1}{k_p + k_{\text{nr}} + k_{qT} \cdot 0} = \frac{1}{k_p + k_{\text{nr}}} \quad (6.2)$$

$$\frac{1}{\tau_{p,\text{O}_2}} - \frac{1}{\tau_{p,\text{N}_2}} = k_{qT}[\text{O}_2]. \quad (6.3)$$

This results in

$$k_{qT}[\text{O}_2] = 1.3 \times 10^4 \text{ s}^{-1}. \quad (6.4)$$

—— 6.1. Tuning the Important Parameters ——

Note that this is a value for the product of k_{qT} and the oxygen concentration in the film $[O_2]$. The individual numbers could not be addressed here. For the following steps, it is assumed that this number is a rough generalized value for oxygen quenching of any emitter embedded in PMMA with 5 wt%. In order to achieve high contrast, the phosphorescence yield should drop at least two orders of magnitude when changing from inert to ambient conditions:

$$\Phi_{p,O_2} \stackrel{!}{<} 10^{-2} \times \Phi_{p,N_2}. \quad (6.5)$$

Using Equation 2.41, this leads to

$$\Phi_{isc} \times \frac{k_p}{k_p + k_{nr} + k_{qT} \cdot [O_2]} \stackrel{!}{<} 10^{-2} \times \Phi_{isc} \times \frac{k_p}{k_p + k_{nr}} \quad (6.6)$$

$$k_p + k_{nr} + k_{qT} \cdot [O_2] \stackrel{!}{>} 10^2 \times (k_p + k_{nr}) \quad (6.7)$$

$$k_{qT} \cdot [O_2] \stackrel{!}{\gtrsim} 10^2 \times (k_p + k_{nr}) \quad (6.8)$$

$$k_{qT} \cdot [O_2] \stackrel{!}{\gtrsim} 10^2 \times \frac{1}{\tau_p} \quad (6.9)$$

The lower limit of the phosphorescent lifetime in the absence of oxygen, which corresponds to this yield decrease, therefore can be deduced to

$$\tau_p \stackrel{!}{\gtrsim} 10^2 \frac{1}{k_{qT}[O_2]} \quad (6.10)$$

$$\tau_p \stackrel{!}{\gtrsim} 10^{-2} \text{ s} = 10 \text{ ms}. \quad (6.11)$$

This approximate value proves to be reasonable, since the PMMA:BP-2TA sample with $\tau_p = 30 \text{ ms}$ shows no phosphorescence in ambient conditions and the best contrast, while the fast triplet emission of PMMA:NPB:DBBP with $\tau_p = 160 \mu\text{s}$ is visible in air, reducing the contrast of the PLT.

At the same time, the measurements on the guest material NPB show that long triplet lifetimes of several hundred milliseconds on the one hand enable long-lasting afterglow emission, but on the other hand promote different quenching channels (cf. Section 5.1.1). Particularly at high excitation intensities, STA, TTA, and saturation are present. While all three pathways reduce the overall emission yield, TTA and

saturation additionally lower the P2F value. Therefore, long phosphorescent lifetimes should be avoided when designing material systems for cw-PLTs.

In conclusion, for the design of new material systems, a phosphorescence lifetime of several tens of milliseconds should be set as ideal. A very interesting, but complex measurement for future experiments would be the detection of the change of τ_p while activating a PLT. Due to the constantly decreasing $[O_2]$, the lifetime should rise accordingly.

6.1.3. λ_{ex} : Extension of the Excitation Window

Excitation of PLTs in the visible regime, ideally using a common white LED, is highly desirable. In Chapter 4, the PLTs were excited with $\lambda_{ex} = 365$ nm. This results from their respective absorption spectra. Visible absorption is provided by the emitter materials PhenDpa (cf. Section 5.1.2) and $BF_2(HPhN)$ (cf. Section 5.1.3).

The phosphorescence of a PLT containing PhenDpa could successfully be activated via illumination at $\lambda_{ex} = 420$ nm (Figure 6.5 a). Measurements with different excita-

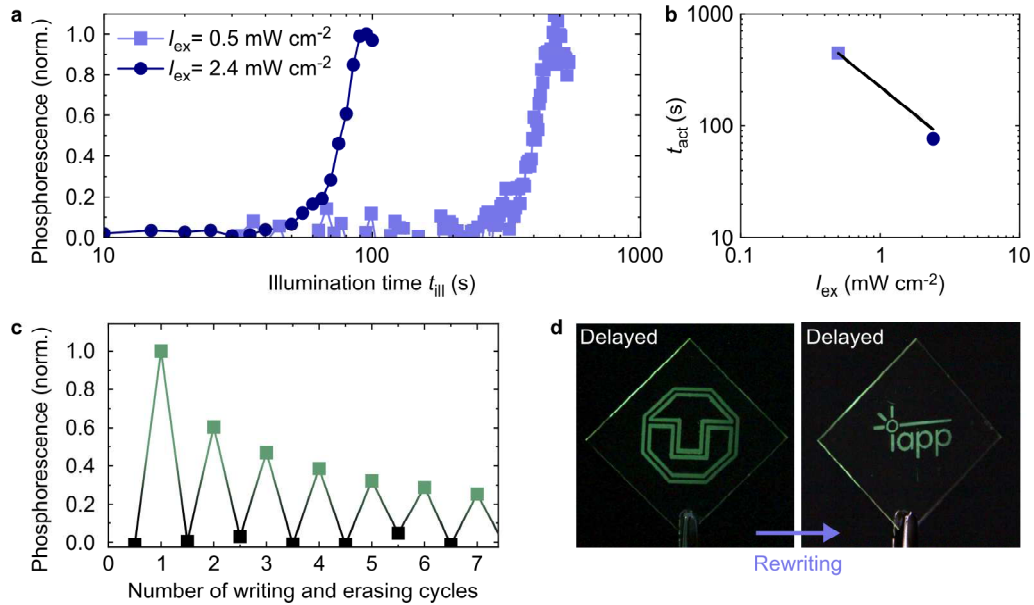


Figure 6.5.: A PLT based on PMMA:PhenDpa (2 wt%). **a** Activation curves of the phosphorescence for different excitation intensities and $\lambda_{ex} = 420$ nm. **b** Corresponding activation times t_{act} . The black line is a power-law fit using an exponent of -1 . **c** Phosphorescence in the on and off state for seven activation and deactivation cycles. **d** Images of a PLT with two subsequently printed patterns.

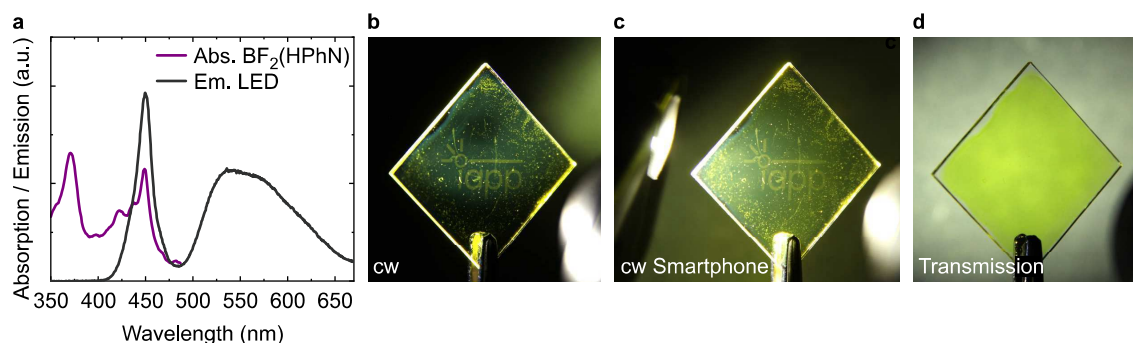


Figure 6.6.: A PLT based on PMMA:BF₂(HPhN) (5 wt%NPB). **a** Absorption of BF₂(HPhN) and emission of a common smartphone LED. **b** Reading the imprint using a flashlight as excitation. **c** Reading the imprint using a common smartphone LED as excitation. **d** Yellowish transmission of the sample.

tion intensities again reveal a power-law dependency of the activation time t_{act} with an exponent of -1 (Figure 6.5 b). Once again, cyclic full activation and subsequent deactivation by heating was feasible (Figure 6.5). After seven cycles, the phosphorescent emission was degraded to 30% of its original value. The capability of writing multiple patterns into a PhenDpa-PLT is depicted in Figure 6.5 d. Note that due to the low $\text{P2F} = 0.3$ of PhenDpa, the monitoring of delayed emission is necessary for sufficient PLT contrast.

As introduced in Section 5.1.3, BF₂(HPhN) shows $\text{P2F} = 1.5$. In addition, its absorption up to $\lambda = 470$ nm (cf. Section 5.1.3) overlaps with the emission of a common white LED (Figure 6.6 a and b). In consequence, the readout of PLTs using BF₂(HPhN) was possible with a simple smartphone LED in cw emission (Figure 6.6 c). This obsoletes the use of UV light sources and significantly improves the value of PLTs in end-user applications. At the same time, the sample's transparency is reduced and it appears yellowish in transmission (Figure 6.6 d).

In order to increase the image quality of PLTs with visible absorption in further development steps, the heavy-atom-containing additive DBBP could be mixed into the system. As shown for PMMA:NPB:DBBP in Section 5.2.3, this can increase the P2F value by a factor of seventy. Another approach would be the use of emitters, which already contain heavy atoms in their structure. A promising material could be the RTP polymer BF₂dnm(I)PLA¹⁹⁹, which also shows absorption up to $\lambda = 460$ nm, in combination with intense phosphorescence due to the presence of iodine ($Z = 53$). A very recent heavy-atom-free compound is BF₂dk (cf. Figure 2.46 e). It shows $\text{P2F} >$

2 and absorbs up to $\lambda = 440 \text{ nm}$.²⁰⁵ Both materials would be interesting candidates for the realization of cw-PLTs with visible absorption and enhanced contrast.

It should be noted, that a general drawback of the sensitivity in the visible regime is the risk of unintended activation. This occurs if the radiation dose D_{act} necessary to activate the PLT is reached by sunlight or artificial light sources.

6.1.4. D_{act} : Extending the Readout Timeframe

Up to now, only PMMA550k was used as host material. For a test of further hosts, BP-2TA was dispersed in various polymers at 5 wt%. The activation curve of a PLT consisting of PMMA46k shows a faster rise of the phosphorescence than a PLT with PMMA550k (Figure 6.7). At identical excitation wavelength and intensity, the activation time was reduced by a factor of three when going from an average molecular weight $M_W = 5.5 \times 10^5 \text{ u}$ to $M_W = 4.6 \times 10^4 \text{ u}$.

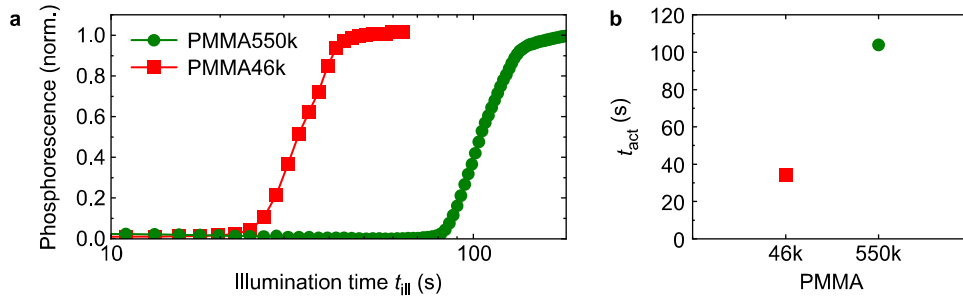


Figure 6.7.: **a** Activation curves of PLTs using PMMA550k:BP-2TA (5 wt%) and PMMA46k:BP-2TA (5 wt%). **b** Respective activation times t_{act} .

A sample containing polystyrene with $M_W = 3.5 \times 10^4 \text{ u}$ (PS35k) showed a phosphorescent rise corresponding to an activation dose of $D_{\text{act}} = 460 \text{ mJ cm}^{-2}$ at $\lambda_{\text{ex}} = 365 \text{ nm}$, which is almost double the value of PMMA550k (cf Section 4.1). Again, a reciprocal dependency of the activation time t_{act} on the excitation intensity was observed (Figure 6.8). A PLT consisting of PS280k with high molecular weight $M_W = 2.8 \times 10^5 \text{ u}$ showed a very high activation dose of $D_{\text{act}} = 4.6 \text{ J cm}^{-2}$. This means that at fixed excitation intensity, the illumination time had to be increased by a factor of ten to activate the phosphorescence of a PLT with PS280 instead of PS35.

Measurements on different blends of PS35k and PS280k revealed that by changing the ratio of those two polymers, D_{act} could be tuned within this range (Figure 6.9 a and b). The emission properties of the PS:BP-2TA samples closely resembled the

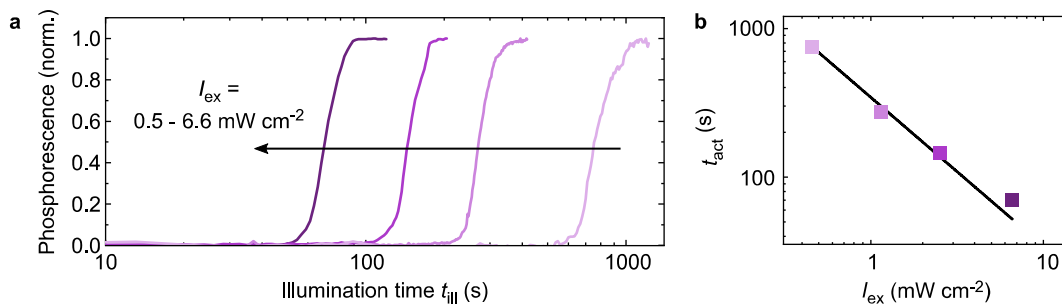


Figure 6.8.: **a** Activation curves of PLTs using PS35k:BP-2TA (5 wt%) and $\lambda_{\text{ex}} = 365$ nm at different excitation intensities. **b** Respective activation times. The black line is a power-law fit using an exponent of -1 .

PMMA:BP-2TA data (cf. Section 5.1.7). The phosphorescence peaked at $\lambda_{\text{p}} = 515$ nm (Figure 6.9 c) and showed a lifetime of $\tau_{\text{p}} = 32$ ms (Figure 6.9 e), both independent of the molecular weight of the PS. Interestingly, the P2F ratio did vary from $\text{P2F} = 9$ to $\text{P2F} = 14$ for different M_{W} (Figure 6.9 d), when excited at $\lambda_{\text{ex}} = 365$ nm. The fluorescence peak at $\lambda_{\text{f}} = 460$ nm is shifted to the blue for all PS samples, when compared to the emission of PMMA:BP-2TA. This can be explained by the lower polarity of PS, which leads to an increase of the energy of the ^1CT state of BP-2TA (cf. Section 2.2.7).

As described in Section 2.3.3, PMMA shows higher sensitivity to photooxidation than PS does. It is reported that methyl groups, which are part of the PMMA's side chains, may be subject to photooxidation¹⁶¹. This is in accordance with the data presented here, where the required activation dose D_{act} for PMMA samples is lower than the one for PS without methyl groups. The underlying mechanism of the activation in PS samples remains unclear. Its dependence on the molecular weight M_{W} may hint to an involvement of the end groups of the polymers, since due to the higher average chain length, the number of end groups in PS280 is much smaller than in the same amount of PS35. Still, this correlation has to be investigated in more detail. Measurements on PS with narrow molecular weight distribution in multiple orders of magnitude may clarify the presence of an influence of the end groups.

At the same time, further open questions remain to be answered. The increase of the phosphorescence and the P2F value at higher PS280 ratio may result from a more rigid environment, which may reduce the nonradiative decay channels. This assumption, however, is in contrast to the constant phosphorescence lifetime, which then should be increased as well. Furthermore, the calculated lifetimes of singlet oxygen in various

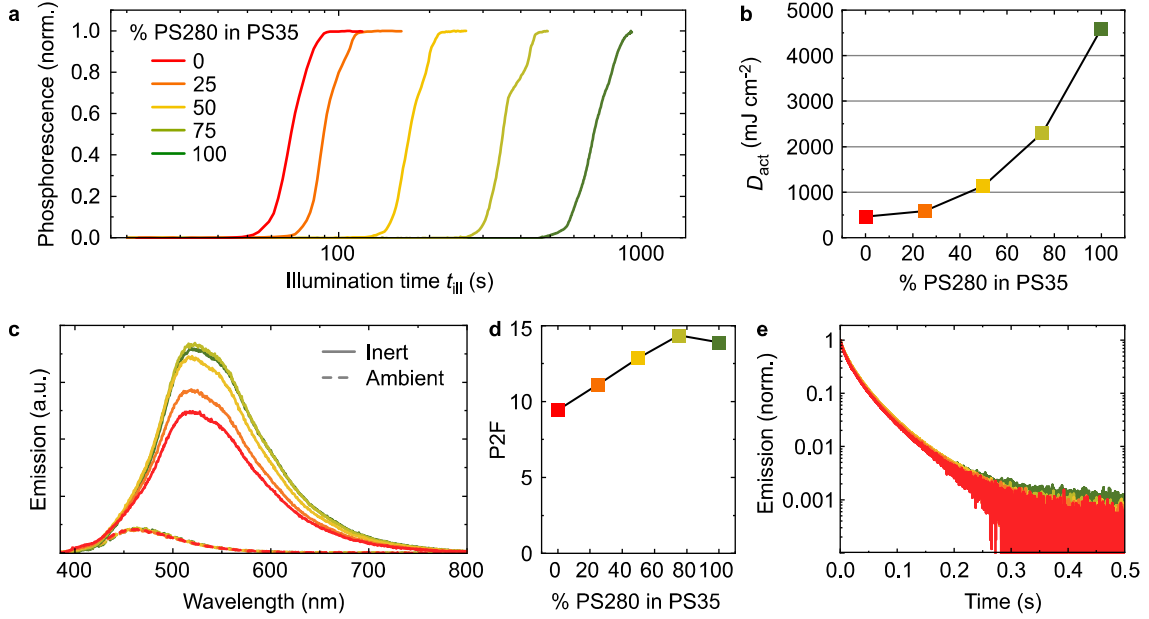


Figure 6.9.: Measurement data for PS:BP-2TA (5 wt%) with different blends of PS35k and PS280k. **a** Activation curves of PLTs using different PS blends at $I_{\text{ex}} = 6.6 \text{ mW cm}^{-2}$. **b** Activation dose D_{act} , plotted against the PS ratio. **c** Emission of PS:BP-2TA layers in ambient and inert atmosphere for different PS ratio when excited at $\lambda_{\text{ex}} = 365 \text{ nm}$. **d** Respective P2F values. **e** Respective phosphorescent decays.

polymers (cf. Table 2.4) have to be implemented into the picture. An experimental approach to these lifetimes may be realized by monitoring the infrared emission of $^1\text{O}_2$ at $\lambda = 1270 \text{ nm}$ in future experiments.

In total, the large increase of the activation dose from $D_{\text{act}} = 250 \text{ mJ cm}^{-2}$ for PMMA550k:BP-2TA to $D_{\text{act}} = 4.6 \text{ J cm}^{-2}$ for PS280k:BP-2TA enables PLTs with a prolonged readout timeframe. This results from the slowdown of unintended activation caused by illumination of the whole sample while reading. At the same time, the intensity of the illumination used for writing has to be set to a very high level to ensure a fast programming of the pattern.

In order to fully overcome the drawback of unintended activation, an additional material system would be necessary, which shows oxygen-dependent emission, but at the same time does not generate excited state singlet oxygen. In other words, this emitter's singlet- or triplet-state quenching-rates k_{qS} or k_{qT} should be high, while the singlet-oxygen generation rate S_{Δ} ideally should be zero (cf. Section 2.3.2). Further, this system should possess an absorption spectrum orthogonal to a common RTP emitter. Then, both materials may be mixed into the emission layer, and the writing

process could be realized as previously shown, using the RTP emitter. For subsequent reading, only the additive is excited, which then shows a contrast in emission due to the inhomogeneous oxygen concentration in the layer. Since no $^1\text{O}_2$ is generated, the oxygen concentration is stable and the readout time is not limited. There is indication in literature that S_Δ may drop for emitters with high triplet energy $E_T > 2.49\text{ eV}$ ($< 500\text{ nm}$)¹⁴⁵. Further, oxygen-induced quenching of singlet states is reported with $S_\Delta^S \approx 0$ for phenanthrene, anthracene or triphenylene in solution¹⁵⁸. In order to assess the suitability of these materials in PLTs, further investigation is necessary.

Another approach would be the use of a PLT with high intrinsic D_{act} in combination with a chemical quencher like HOPEMP as additive¹⁶¹ (cf. Figure 2.38). The chemical quencher may decrease the activation time and enable ultrafast writing. Before starting the readout, this additive could be removed by specific photodegradation. As a consequence, unintended activation may be drastically reduced due to the high intrinsic D_{act} . Again, this technique requires orthogonal absorption of the materials. Besides, the reusability of the PLTs would be lost in this case. Nevertheless, this pathway should be investigated in future experiments.

6.2. Substrates and Processing Techniques

6.2.1. Substrate Diversity

In addition to the quartz glass platelets with 25 mm edge length, further substrates were used to spin-coat and drop-cast PLTs on top to realize proof-of-concept samples. Figure 6.10 b shows PLTs consisting of PMMA:NPB and Exceval using flexible adhesive films. In order to spin-coat the layers, the substrate films were temporarily attached to glass platelets. The emission layer was sandwiched between two Exceval layers in three spin-coating steps (Figure 6.10 a). This ensured protection against ambient oxygen from both sides and at the same time it shielded the flexible substrate from anisole during the application of the emission layer. The resulting PLTs could be programmed and then applied to various surfaces like curved glass or a plastic box, where they were used as invisible on-demand labels (Figure 6.11 a). Large-scale PLTs were manufactured by drop casting PMMA:NPB and Exceval onto overhead transparencies. Again, two Exceval layers and one emission layer in between were applied. The resulting PLTs were fully functional (Figure 6.11 b).

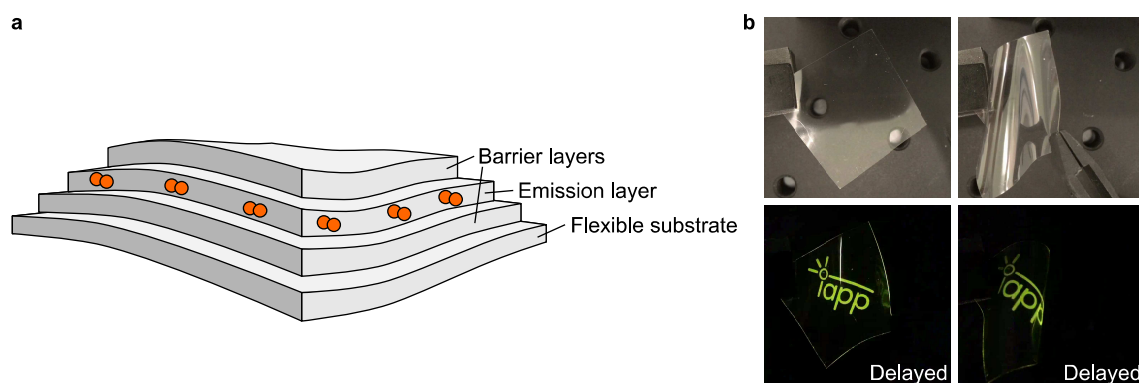


Figure 6.10.: **a** A PLT comprising a flexible substrate and an additional barrier layer below the emission layer. Note that the layer thicknesses are not in scale. **b** A flexible PLT containing PMMA:NPB in ambient light and an imprinted pattern in delayed emission.

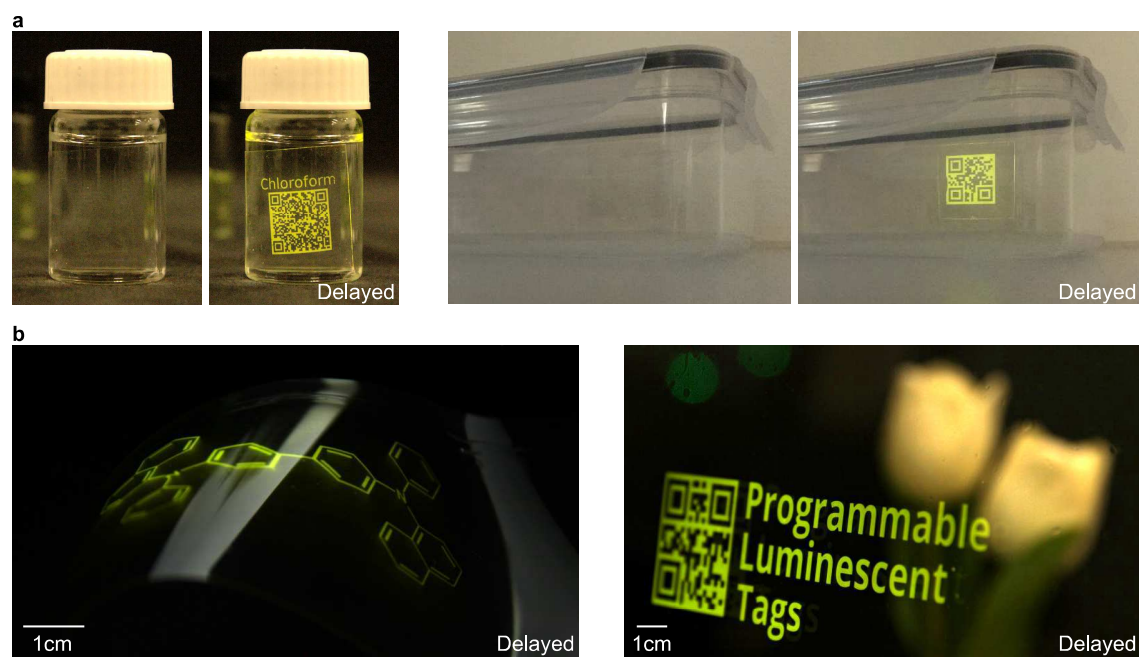


Figure 6.11.: Flexible PLTs made of PMMA:NPB on transparent substrates. **a** Small spin-coated PLTs used as on-demand labels. **b** Large-scale drop-casted PLTs.

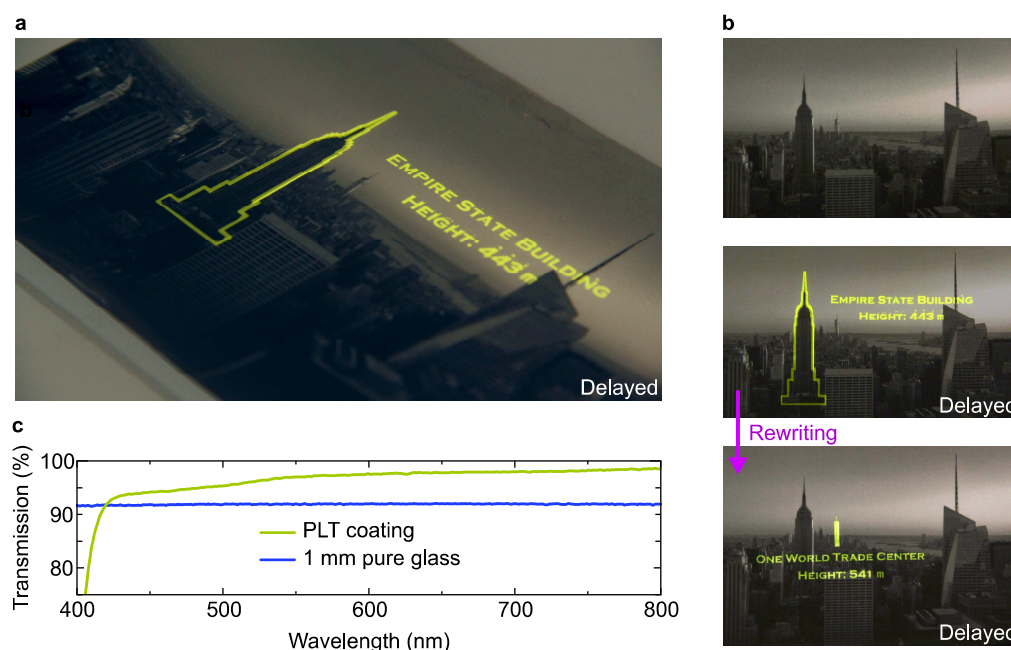


Figure 6.12.: **a** A PMMA:NPB PLT coated on top of a common photograph, showing an imprint in delayed emission. **b** The same PLT when not read out (top), and with a second pattern programmed into the emission layer (bottom). **c** Transmission curve of the PLT coating, compared to the values of pure borosilicate glass with a thickness of 1 mm.

In a next step, a common photograph was coated with three layers as described above by drop casting. As a result, the photograph could be tagged with a rewriteable caption with the help of a mask (Figure 6.12 a and b). By heating and reactivating, a second imprint was realized. With an identically coated glass substrate, the transmission of this PLT coating could be determined. To do so, the data of an uncoated glass substrate were subtracted by the data of the coated one. As a result, it was revealed that the PLTs transmission did not drop below 90% (Figure 6.12 c) in almost the complete visible range. These transmission values were higher than for pure borosilicate glass with a thickness of 1 mm, demonstrating the suitability of PLT coatings as fully transparent captioning layers.

6.2.2. Additional Processing Techniques

Alongside to drop casting and spin coating (Figure 6.13 a), PMMA:NPB was applied to multiple substrates by spray coating (Figure 6.13 b) or dip coating (Figure 6.13 c). Further, PLA:NPB was extruded and 3D-printed (Figure 6.13 d), and powdery

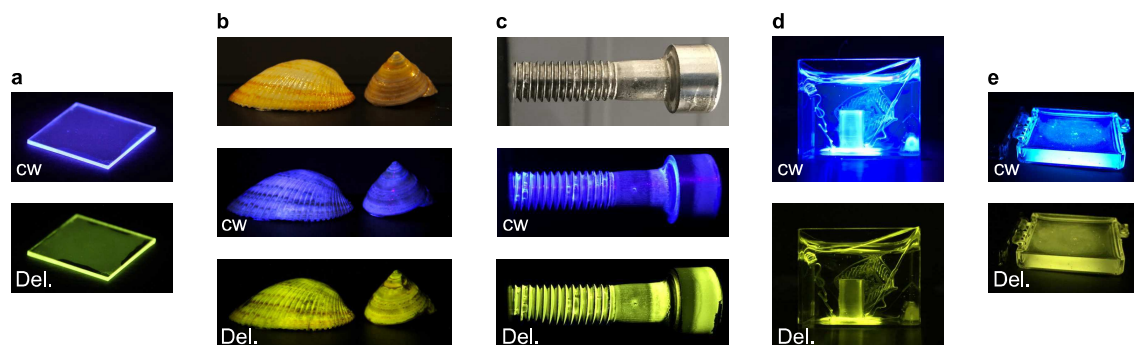


Figure 6.13.: Different processing techniques realized for NPB. **a** Fluorescence (top) and phosphorescence (bottom) of spin-coated PMMA:NPB, with an Exceval barrier on top. **b** Fluorescence (middle) and phosphorescence (bottom) of PMMA:NPB spray-coated onto shells. An additional Exceval layer was spray-coated on top. **c** Fluorescence and phosphorescence of PMMA:NPB dip-coated onto a metal screw. An Exceval layer was dip-coated on top. **d** Fluorescence and phosphorescence of 3D printed PLA:NPB embedded in epoxy. **e** Fluorescence and phosphorescence of NPB dispersed in epoxy.

NPB was dispersed in common epoxy at low concentration (Figure 6.13 e). In order to protect the emission layer against oxygen quenching, an Exceval layer was coated on top of some of the samples (Figure 6.13 a, b and c). The 3D-printed samples were fabricated using a Renkforce RF2000 3D printer. The printing filament consisted of a blend of the powdery emitter material and pellet-shaped PVA, PLA, or Exceval, which was extruded using the Notztek Pro Filament Extruder. This work was mainly done by Jakob Lindenthal as part of his bachelor thesis. Notably, all of these straightforward preparation techniques lead to samples showing RTP emission. However, each sample had to be activated via illumination before phosphorescence was visible. Thus, it can be resumed that all processing techniques are suitable for the preparation of PLTs, and basically any material can serve as substrate. This flexibility in processing is one of the great advantages of simple host-guest systems compared to crystalline or aggregation-induced RTP materials, which are highly dependent on the emitter's morphology.

7. Conclusions and Outlook

7.1. Conclusion

As previously described, organic RTP is a growing field of interest, but most publications so far have focused on new materials and barely on relevant applications. Thus, the aim of this thesis was to introduce an implementation of stimuli-responsive RTP by using the newly discovered switchable phosphorescence (SwiP) effect in thin polymeric films. The resulting programmable luminescent tags (PLTs) enable the printing of phosphorescent patterns into transparent layers. When illuminated with light of appropriate wavelength, the interplay of excited states and molecular oxygen leads to a depletion of the latter resulting from its chemical uptake by the host polymer. Since the inflow of ambient oxygen is prevented by a barrier layer, at some point all molecular oxygen is removed at the illuminated areas and phosphorescence is activated. Via illumination with infrared light, the temperature, and therefore the permeability of the barrier layer is increased, and the emission layer is refilled with oxygen, leading to a deactivation of phosphorescence. In consequence, the PLTs can be programmed and erased multiple times (Figure 7.1), and may be used as low-cost data storage devices for QR codes, labels, or other captions. Since the imprint is fully invisible when not read out, a further area of application could be found in document and banknote security. In comparison to similar application proposals^{40;53–55;219}, our technology is characterized by easier processing and handling as well as improved image quality. The processes of the SwiP cycle as well as the PLT's structure itself both are subject of current patent applications. The potential relevance of this development is reflected in the fact that the initial publication about the PLTs was subject of great interest by a multitude of national and international news agencies^{233–235}.

In more detail, the programming was shown to work using an intense focused beam, via mask illumination, as well as using a maskless lithography system, and resulted in imprints with a resolution in the range of common office printers. Depending on

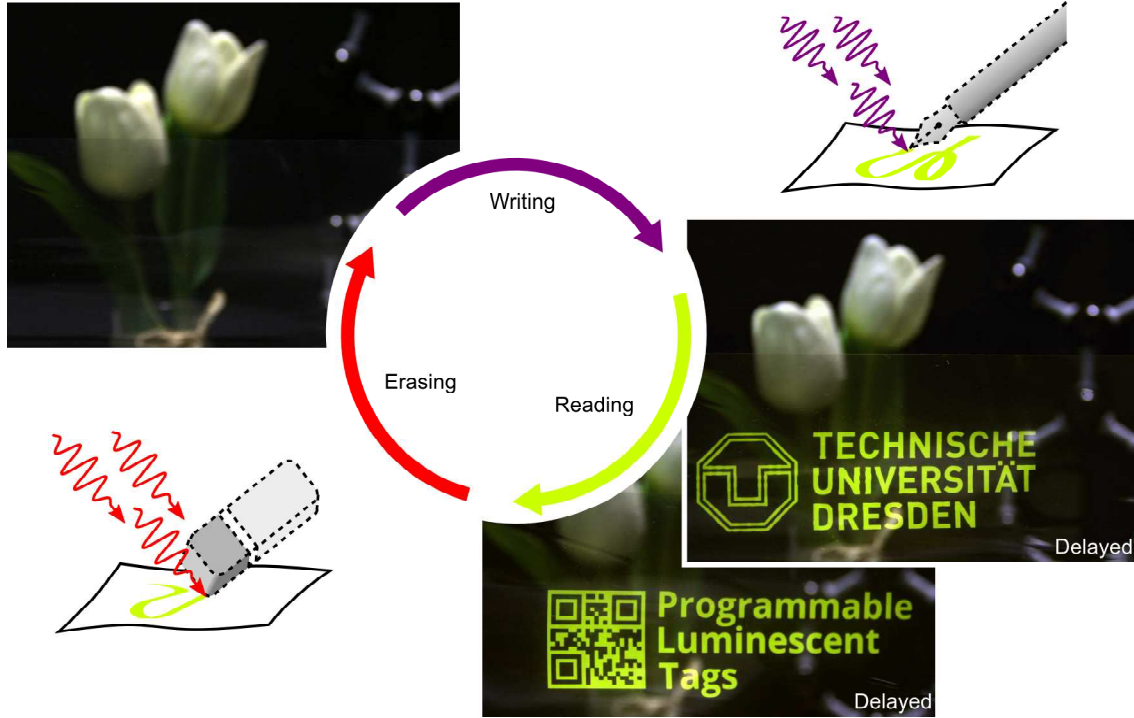


Figure 7.1.: Multiple writing, reading and erasing of a flexible large-scale PLT consisting of PMMA:NPB.

the thickness of the respective barrier layer, these patterns are stable for a few hours up to several days. Due to lateral diffusion of oxygen, however, the pattern quality decreases over time.

In further steps, via the careful adjustment of several parameters, the design of PLTs could be optimized. In total, several decisive parameters were identified. Since the pattern's emission consists of phosphorescence, a high yield Φ_p of the emitter material significantly contributes to good readability. Therefore, nonradiative decay channels like vibronic transitions or quenching interactions like TTA should be suppressed as well as possible. At the same time, for the realization of cw-PLTs, the fluorescence yield Φ_f should be very low, since this emission usually is independent of the presence of oxygen. Therefore, it does not contribute to the PLT pattern, but reduces the images' contrast by generating an ubiquitous background glow. A measure for the material system's suitability for cw-PLTs is the P2F value, where $P2F = 1.5$ is set as the bottom limit, and $P2F \geq 6$ as sufficient for high-quality images. In addition, using the delayed afterglow of the tags, the fluorescence is removed and PLTs can be realized with material systems with lower P2F as well. However, this complicates

the readout process. Similarly, it has to be ensured that phosphorescence is fully quenched in the presence of molecular oxygen. Therefore, it was shown that the emitter material should possess a phosphorescence lifetime $\tau_p > 10$ ms.

One of the most important demands on the host material is sensitivity to oxidation. This property, which can be evaluated by determining the D_{act} value, is crucial for the writing step in the PLT cycle. It was shown that D_{act} is independent of the excitation intensity and can be tuned within one order of magnitude by changing the average molecular weight of the host polymer. On a last note, the material should be transparent and amorphous, facilitating invisible, flexible, large-scale and easy-to-process PLT devices.

The broad variety of compounds investigated in this thesis shows that the SwiP effect and the working principles of the PLTs are, within the parameters listed above, very general and not dependent on specific material systems only. This becomes manifest in PLTs with diverse spectral excitation ranges, spanning from deep UV to the visible regime, as well as multiple emission colors including blue, green, yellow, and orange.

7.2. Outlook

With the requirements mentioned above, a basis for the future development of tailored RTP systems is given. This may be a starting point for a more application-oriented synthesis of new materials, possibly increasing the practical outcome of the vast amount of RTP publications that will be published in the upcoming years.

7.2.1. SwiP and PLTs

Since this work deals with the completely new effect of SwiP, it also gives rise to numerous questions that should be addressed in future research. First, the dynamics of the PLT activation and deactivation should be investigated in more detail. In this regard, a numerical simulation could approach the correlation of phosphorescence with the respective concentration of molecular oxygen in the emission layer. Especially the observed lateral diffusion of oxygen from non-activated areas to activated ones, which to date reduces the resolution of the imprints, should be addressed quantitatively. At the same time, the observed timescale of the inter-layer diffusion process through the oxygen barrier material may be addressed by theoretical calculations.

—— 7. Conclusions and Outlook ——

In this thesis, the appearance of phosphorescence in the activation step resulting from photoconsumption of oxygen was theoretically described using an oxygen-concentration threshold value. Here, no triplet emission is visible above this value and full phosphorescence is emitted below. However, the exact behavior is rather an interplay between the radiative rate and the rate of oxygen-induced quenching. The continuous decrease of the latter permanently leads to a change of the ratio of both rates, and theoretical calculations may actually resemble the observed activation curves. By that, it could be possible to quantify the actual photoconsumption rate of oxygen. Further, the quenching rate may be experimentally determined by monitoring the phosphorescence lifetime while activating the PLT. This measurement may be performed using a fast RTP emitter like PtOEP, which shows different triplet lifetimes in ambient and inert atmosphere, respectively.

In addition, the theoretical limitation of the speed of activation is of interest. The current lower limit of the activation time, $t_{\text{act}} = 120 \pm 20$ ms, was governed by restrictions of the setup. Approaching faster times is of high relevance for high-speed labeling such as employed in production chains. Therefore, the theoretical lower limits of t_{act} should be addressed. They may be correlated with the average time, which is needed for the photoconsumption of one oxygen molecule after excitation of the emitter material. Here, the excited state lifetimes of the emitters as well as the formation rate of singlet oxygen may play a role. The lifetime of the latter could be determined by monitoring its emission in the infrared regime.

Concerning further research on materials, the oxygen uptake rate may be adjusted in a wider range spanning several orders of magnitude. This requires experiments regarding its dependence on emitter properties as well as on host material features. In addition, an implementation of antioxidant additives may accelerate or slow down the oxygen uptake process^{137;161}. Via that, a fine tuning of the radiation dose D_{act} needed for activation could be achieved.

Via the implementation of phosphorescent emitters with visible absorption and high P2F values, the readout process using common white LEDs could be further improved. One promising material may be BF₂dk, which was published recently²⁰⁵. Another essential item concerning the materials is the improvement of emission stability and the reduction of degradation over the activation and deactivation cycles. The readout stability may be enhanced by a new kind of emitter system, which shows oxygen-dependent emission, but does not generate singlet oxygen when quenched. Therefore,

a singlet generation rate of $S_{\Delta} = 0$ would be necessary. In addition, by using PLA as host polymer and NFC as oxygen barrier material^{210;211}, a biodegradable PLT could be realized.

Beyond the realization of PLTs, further fields of RTP application were identified within this work, which will be shortly listed in the following. To date, each of them is in a very early stage and subject to ongoing investigation.

7.2.2. Further Application Pathways

Optical Batteries

As part of this work, another application field of RTP beyond PLTs was assayed. A straightforward utilization of RTP in ambient conditions is its use as optical battery. Here, the phosphorescent emitters serve as short-time reservoir for the absorbed energy. By that, a luminescent system with temporal separation of excitation and emission can be realized. Implemented into bicycle tires as luminescent strips, this can serve as nighttime safety illumination (Figure 7.2 a). In order to realize a prototype, PMMA:NPB and two surrounding Exceval layers were blade-coated onto a transparent plastic ring. After activation, the ring showed bright green phosphorescence (Figure 7.2 b). This system was successfully patented. In order to overcome the multi-layer structure, RTP emitters are embedded directly into the barrier layer in ongoing experiments.

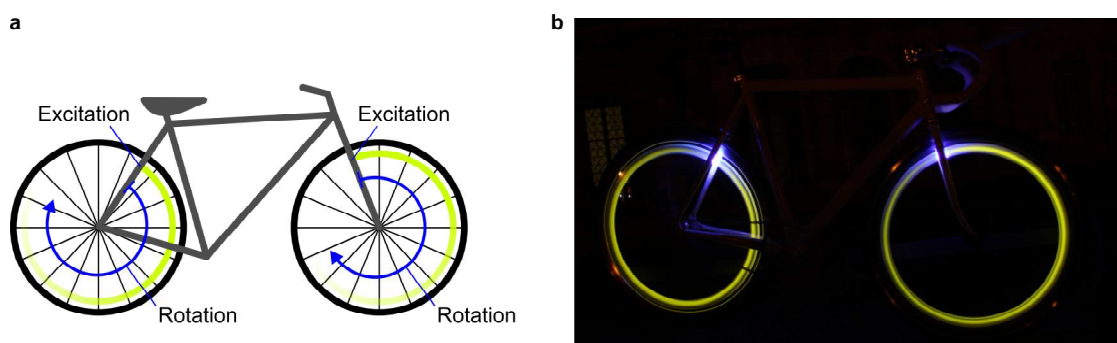


Figure 7.2.: **a** Schematic of RTP used in afterglow bicycle illumination. **b** Photograph of a working prototype using PMMA:NPB with an Exceval barrier layer.

UV sensing

The dynamics of activation of phosphorescence can further be used as indicator for properties of the excitation radiation. Since D_{act} is an intrinsic material property, the excitation intensity I_{ex} can be monitored by measuring the time until phosphorescence emerges, according to Equation 4.1. This technique is the basis of a successive research project with granted funding by the Federal Ministry of Education and Research of Germany^a. Here, two measurement techniques are proposed. The first one is a threshold detection, which indicates the areas where a certain illumination dose was exceeded (Figure 7.3 a). The second one uses a material system owning a gradient of D_{act} , which shows gradual activation over illumination time and therefore is suitable for the detection of absolute I_{ex} data (Figure 7.3 b). In first measurements, a gradient UV light-source illuminated a large-scale cw-PLT made of PMMA:BP-2TA. The results nicely show a step-by-step activation of phosphorescence (Figure 7.3 c). Both methods are part of an international patent application.

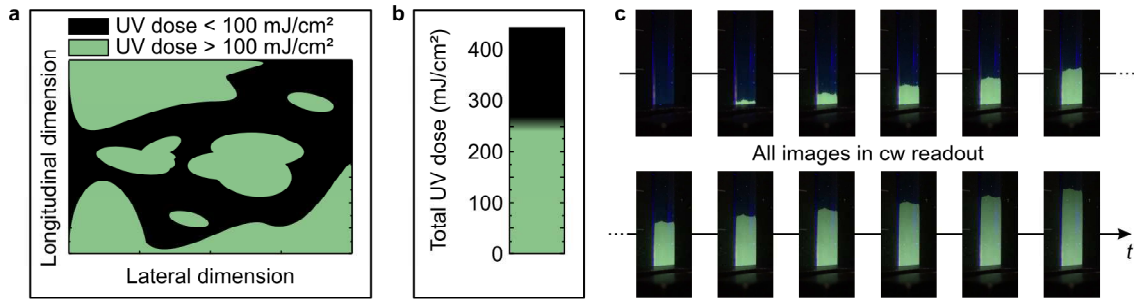


Figure 7.3.: **a** Proposed device for a threshold measurement. Activated areas are depicted in green. **b** Proposed device for absolute measurements. **c** Consecutive photographs of PMMA:BP-2TA, covered with Exceval, under UV illumination, whose intensity spatially decreases from bottom to top.

7.2.3. Widening the Scope

In the end, the multiple dependencies of the PLT system on environmental parameters like oxygen, radiation, temperature, or additives may enable a plethora of sensing applications. In order to address these additional exploitation directions, a project proposal was submitted to the European Research Council, which focuses on the investigation of the potential economical impact of every single one of them. This

^aProject 'Großflächige, elektronikfreie und flexible UV-Dosismessfolien (UV-Sens)', Funding initiative 'Wissenschaftliche Vorprojekte'

—— 7.2. Outlook ——

again benefits from the versatility of the SwiP introduced in this work, as well as from the elaborate characterization of its multiple parameters. At the same time, many scientific and technological questions regarding this RTP technology remain to be answered. While the basis is set within the scope of this thesis, it will take time and effort to identify the most promising research directions and the most exciting application pathways for future developments.

The journey has only just begun.

A. List of Abbreviations and Symbols

For the sake of clarity, only abbreviations that have been mentioned more frequently in the text are listed below.

| | |
|-------------------------------|--|
| A | Electron or Energy Acceptor Compound |
| cf. | confer |
| CT | Charge Transfer |
| ^1CT | CT Singlet State |
| ^3CT | CT Triplet State |
| $^1\text{CT}_n$ | n -th CT Singlet State |
| cw | Continuous Wave |
| cw-PLT ... | PLT with cw-Readout Capability |
| D | Electron or Energy Donor Compound |
| D_{act} | Phosphorescence Activation Dose |
| $^1\Delta$ | First Excited Singlet State of Oxygen |
| ΔE_{ST} | Singlet-Triplet Splitting Energy |
| $\Delta E_{\text{ST}n}$ | Energy Gap between a Singlet and Triplet State T_n |
| E_{A} | Electron Affinity |
| E_{B} | Coulomb Binding Energy |
| E_{HOMO} | HOMO Energy |
| E_{LUMO} | LUMO Energy |
| E_{S} | S_1 Energy |
| E_{T} | T_1 Energy |
| ηF | Fluorescence Ratio |
| f | Oscillator Strength |
| FRET | Förster Resonance Energy Transfer |
| HOMO | Highest Occupied Molecular Orbital |

—— A. List of Abbreviations and Symbols ——

| | |
|-----------------------------|--|
| I_{ex} | Excitation Intensity |
| ICT | Intramolecular Charge Transfer |
| IR | Infrared |
| IRF | Instrument Response Function |
| ISC | Intersystem Crossing |
| k_{qT} | Oxygen-Induced Triplet-Quenching Rate |
| λ_{ex} | Excitation Wavelength |
| λ_{f} | Emission Wavelength of Fluorescence |
| λ_{p} | Emission Wavelength of Phosphorescence |
| LE | Local Excited |
| ^1LE | LE Singlet State |
| ^3LE | LE Triplet State |
| LED | Light Emitting Diode |
| LUMO | Lowest Unoccupied Molecular Orbital |
| M | Spin Multiplicity |
| M_{W} | Molecular Weight |
| NFC | Nanofibrillated Cellulose |
| O_2 | Molecular Oxygen |
| $^1\text{O}_2$ | Excited Singlet Oxygen |
| $^3\text{O}_2$ | Ground State Triplet Oxygen |
| $[\text{O}_2]$ | Oxygen Concentration |
| OD | Optical Density |
| OLED | Organic Light Emitting Diode |
| OTR | Oxygen Transmission Rate |
| P2F | Phosphorescence to Fluorescence Ratio |
| PAN | Polyacrylonitrile |
| Φ_{f} | Fluorescence Yield |
| Φ_{FRET} | FRET Yield |
| Φ_{isc} | ISC Yield |
| Φ_{p} | Phosphorescence Yield |
| PLA | Poly(lactic Acid) |
| PLQY | Photoluminescent Quantum Yield |
| PLT | Programmable Luminescent Tag |
| PMMA | Poly(methyl methacrylate) |

| | |
|--------------------------------|--|
| PS | Polystyrene |
| ψ | Electronic Wave Function |
| ψ_{M} | Molecular Wave Function |
| PVA | Poly(vinyl alcohol) |
| QR | Quick Response |
| R_{F} | Förster Radius |
| RISC | Reverse ISC |
| RT | Room Temperature |
| RTP | Room Temperature Phosphorescence |
| S | Total Spin |
| S_0 | Singlet Ground State |
| S_{Δ} | Singlet Oxygen Generation Rate |
| S_n | n -th Excited Singlet State |
| $^1\Sigma$ | Second Excited Singlet State of Oxygen |
| $^3\Sigma$ | Ground State Triplet Oxygen |
| SOC | Spin-Orbit Coupling |
| STA | Singlet-Triplet Annihilation |
| SwiP | Switchable Phosphorescence |
| t_{act} | Phosphorescence Activation Time |
| t_{ill} | Illumination Time |
| T_n | n -th Excited Triplet State |
| ϑ_{O_2} | Upper $[\text{O}_2]$ Threshold for Phosphorescence |
| TADF | Thermally Activated Delayed Fluorescence |
| τ_{f} | Fluorescence Lifetime |
| τ_{p} | Phosphorescence Lifetime |
| TCSPC | Time-Correlated Single-Photon Counting |
| TICT | Twisted Intramolecular Charge Transfer |
| TTA | Triplet-Triplet Annihilation |
| UV | Ultraviolet |
| ε | Extinction Coefficient |
| ε_{r} | Dielectric Constant |
| VB | Valence Bond |

B. Beyond Science

The first publication on SwiP and PLTs was chosen to be pictured on the cover of the February 2019 Issue of Science Advances (Figure B.1 a). Additionally to the scientific part of this work, further projects were realized during the course of this thesis.



Figure B.1.: **a** Cover of Science Advances of Feb. 2019, showing PLTs. **b** Cover of the textbook written as part of this work. **c** Welcome screen of the digital training seminar created as part of this work.

In 2019, the textbook 'Durchblick in Optik - Mit Phänomenen, Formeln und Fragen zum Verständnis' was published by Springer Spektrum Berlin (Figure B.1 b). It is a book for college students and contains all relevant aspects of optics, which are part of the studies of physics on a bachelor level. From mid 2017 to the end of 2018, it was written by the author of this thesis. Sebastian Reineke was the responsible senior author, providing the framework and addressing corrections in terms of content. Another project was the 'Online-Vorbereitungskurs Physik' by TU Dresden (Figure B.1 c), where the author was responsible for the creation of scientific and teaching content for a digital training seminar, which can be consulted by first-year students of the university.

C. Additional Data

Low-T-Emission of PMMA:NPB

To reveal emission of PMMA:NPB at reduced temperature, a sample was put into a liquid nitrogen bath. Subsequently, emission spectra in prompt and delayed measurements were recorded (Figure C.1). The phosphorescence lifetime at 77 K was $\tau_p = 590$ ms.

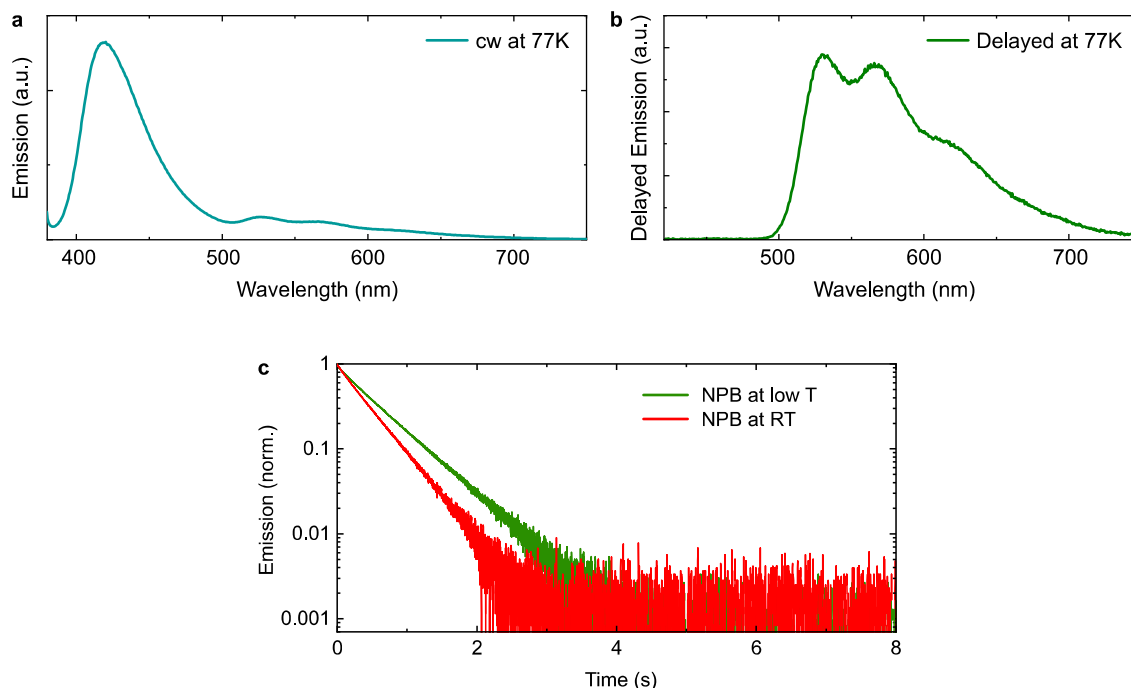


Figure C.1.: **a** cw emission of PMMA:NPB at $T = 77$ K, showing an increased ratio of phosphorescence compared to emission at room temperature. **b** Delayed emission of PMMA:NPB at $T = 77$ K. **c** Phosphorescent decay of PMMA:NPB at low and room-temperature phosphorescence.

Degradation of PMMA:NPB

Additional measurements on degradation of PMMA:NPB, performed by Toni Bär-schneider, confirmed the reduction of P2F due to degradation. He further observed that a new emission peak emerged during ongoing degradation. As part of this work, this new peak was investigated using TCSPC data. Therefore, a PMMA:NPB sample, which was degraded by UV illumination in ambient atmosphere, was compared to a fresh one.

The nanosecond lifetime of the emission at the peak of NPB's fluorescence was drastically reduced after degradation, while at emission wavelengths further in the red, the decay showed an additional longer component (Figure C.2). In the fresh sample, an integration of the wavelength-resolved nanosecond decays below 1 ns pretty nicely resembled the cw emission spectrum, peaking at $\lambda = 430$ nm.

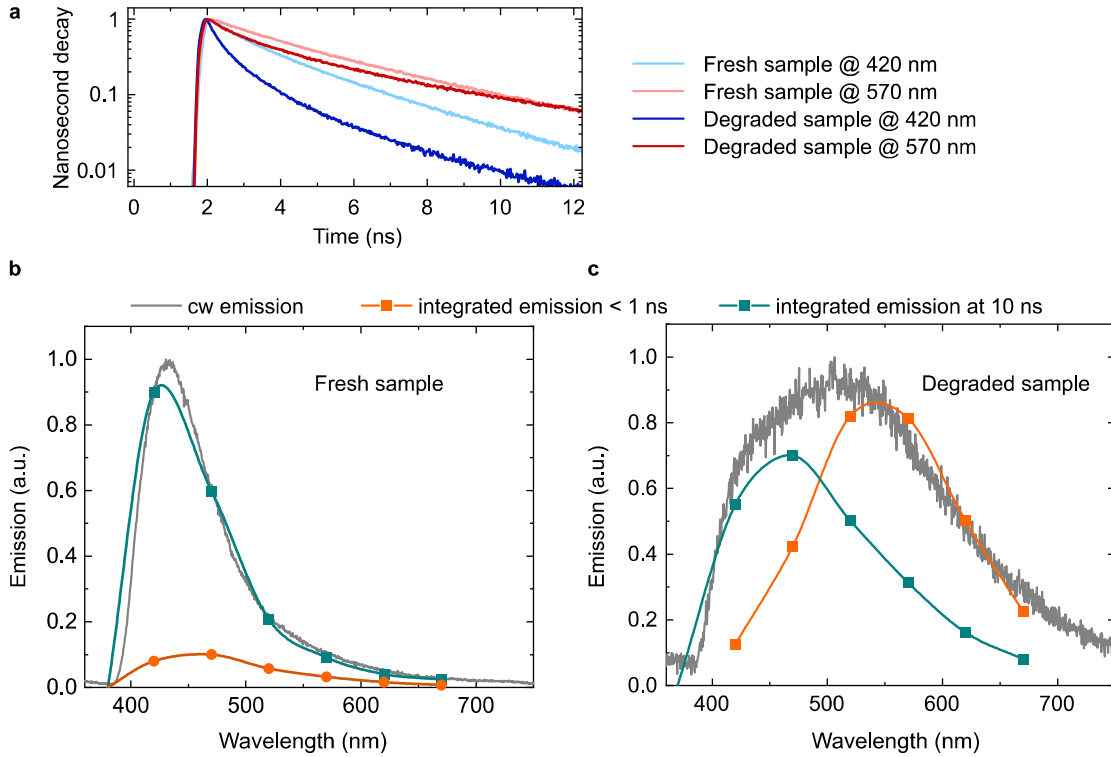


Figure C.2.: **a** Nanosecond decays of PMMA:NPB samples at different detection wavelengths. **b** Integrated nanosecond decays at different times, compared to the cw emission of a fresh PMMA:NPB sample. The connection lines are modified Bézier curves. **c** Integrated nanosecond decays at different times, compared to the cw emission of a degraded PMMA:NPB sample. The connection lines are modified Bézier curves.

At longer timescales around 10 ns, the emission showed a small redshift, with a peak at around $\lambda = 470$ nm (Figure C.2 b). The degraded sample shows a greater change when going from < 1 ns to 10 ns. Here a redshift of around $\Delta\lambda \approx 100$ nm is visible (Figure C.2 c). In addition, the comparison of the cw spectra reveals an overall redshifted spectrum compared to the non-degraded sample. The results can be concluded by the appearance of an additional radiative state, which may be populated via direct excitation and FRET energy transfer from the NPB's singlet state. The latter would explain the very fast component in the decay of the degraded sample at $\lambda = 420$ nm. In total, this could explain the reduced P2F ratio in degraded samples, since this new state may contribute to the fluorescence emission, but not to the phosphorescence. However, more experiments on this effect are already running.

P-Type (TTA) Delayed Fluorescence in TCTA:NPB

In addition to the use of polymeric hosts, it is also possible to embed RTP emitters into a small molecule host. In this work, NPB was dispersed into a layer consisting of the small molecule tris(4-carbazoyl-9-ylphenyl)amine (TCTA). As a result, RTP from NPB was visible in inert conditions (Figure C.3 a). In addition to the phosphorescence, a second prominent emission peak was visible in delayed emission, which fully resembled the fluorescent emission in cw excitation. By changing the excitation intensity it was shown that this peak scales quadratically to the intensity of the

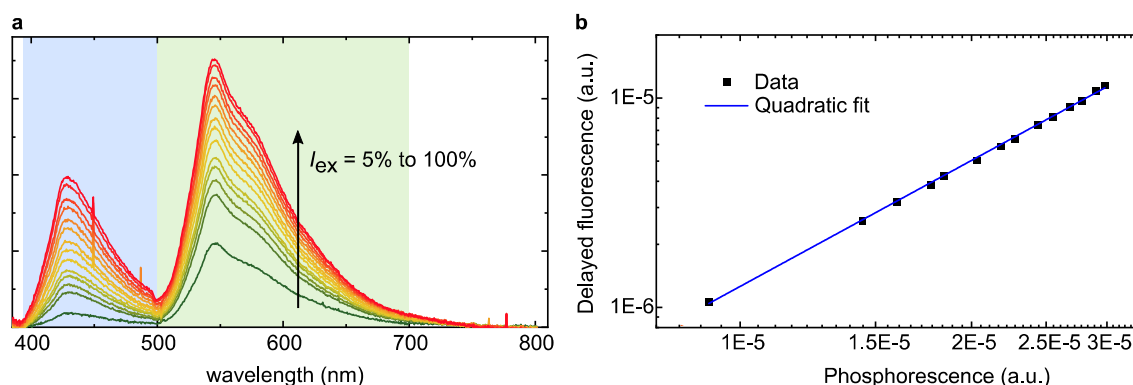


Figure C.3.: **a** Delayed emission of TCTA:NPB at different excitation intensities, showing phosphorescence (light green background) and delayed fluorescence (light blue background). **b** Relation of integrated values of phosphorescence and delayed fluorescence, fitted by a quadratic function.

phosphorescence (Figure C.3 b). This is a clear hint to P-type fluorescence caused by TTA. However, the exact photophysical processes behind this effect still need to be clarified.

Degradation of PMMA:BP-2TA

BP2-TA, embedded into PMMA, showed a new increasing peak during illumination in inert atmosphere. This is centered around $\lambda = 490$ nm (Figure C.4 a) and gradually increases under prolonged illumination (Figure C.4 b). The excitation scan of the degraded sample shows a new shoulder redshifted to the data of the fresh sample (Figure C.4 c). This again hints to the presence of a new absorbing state. Interestingly, PS:BP-2TA did not show the emerging of a new peak when degrading (Figure C.4 d). Further, illumination in ambient conditions did not trigger the new peak, either.

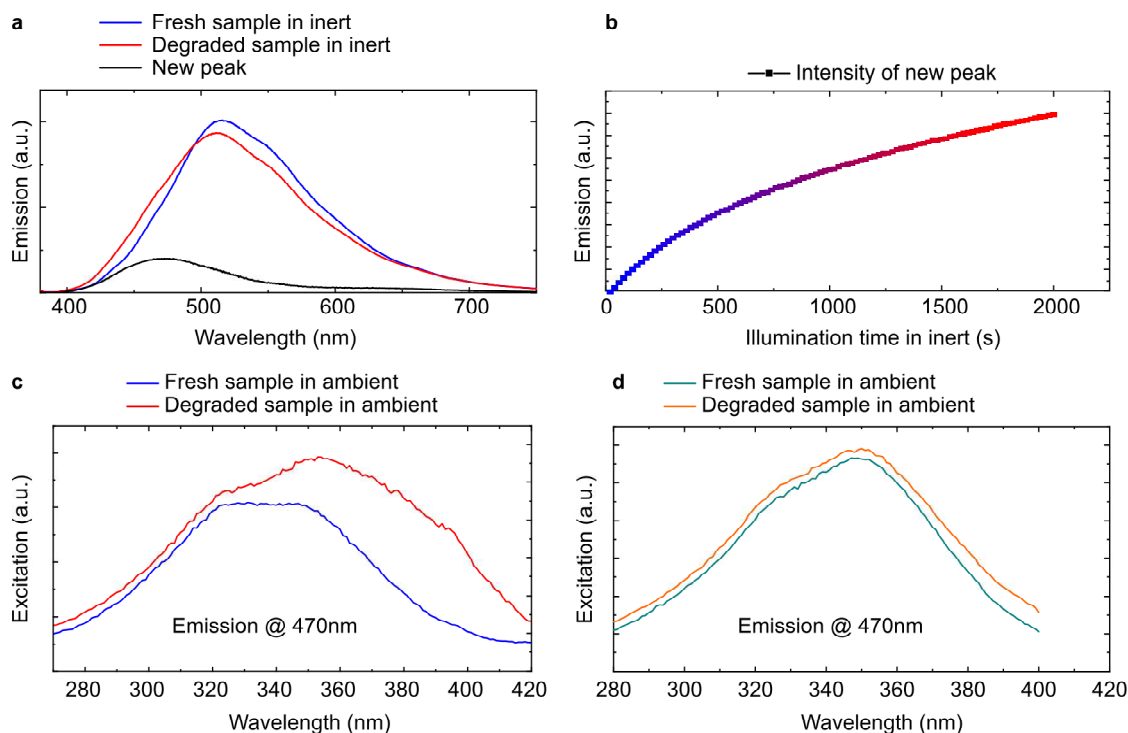


Figure C.4.: **a** Emission of fresh and degraded PMMA:BP-2TA in ambient conditions. The new peak is calculated using the difference of both scaled spectra. **b** Rise of the new peak during illumination. **c** Excitation scans of a fresh and degraded PMMA:BP-2TA sample. **d** Excitation scans of a fresh and degraded PS:BP-2TA sample.

D. Details on Setups

Edge-Emission and Face-Emission

The detection of the photoluminescent spectrum of a thin film sample is not independent from the angle of emission. As can be seen in Figure D.1, the rotation angle of the sample inside of the sample box drastically influences the resulting data. Especially measurements at 90° , namely in edge emission, strongly change the resulting curves (Figure D.1 b). This can also be seen by eye, where edge emission clearly appears orange to red, while the actual emission of the reference sample is white (Figure D.1 c). This effect may be caused by reabsorption as well as waveguide ef-

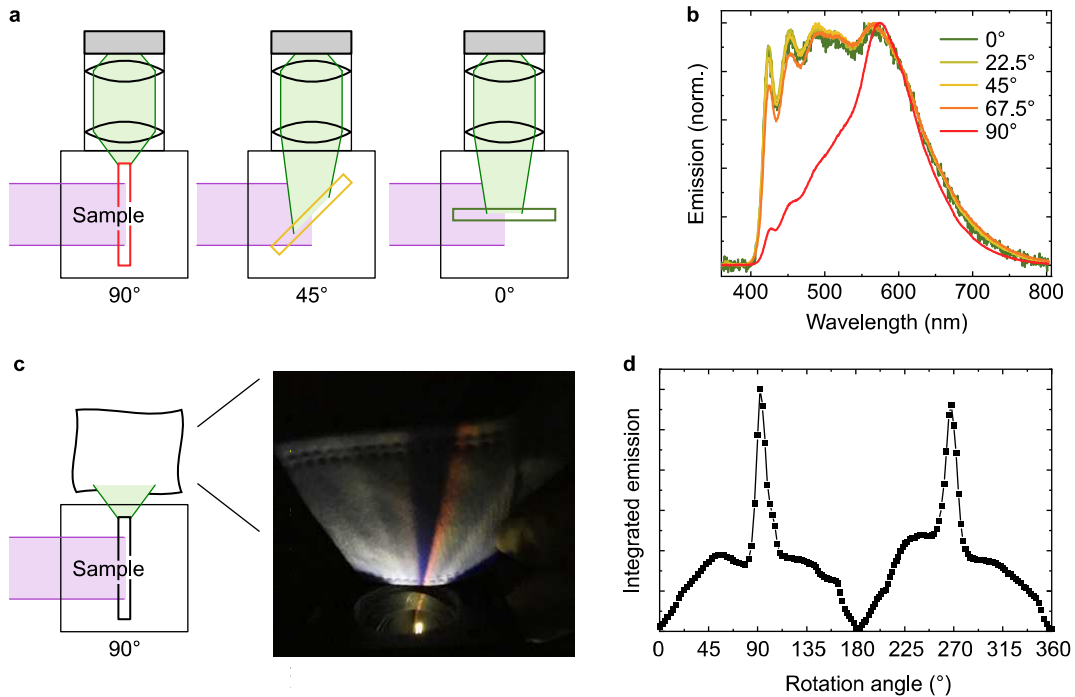


Figure D.1.: **a** Sketches of the setup with different sample position angles. **b** Emission spectra at different angles. **c** Verification by eye. **d** Angle-dependent intensity.

fects. Therefore, to ensure reliable and reproducible spectral results, measurements should always be performed in face emission configuration. Only experiments with a focus on intensity only may be performed using edge emission, since typically the absolute intensity here is much higher than it is in face emission (Figure D.1 d).

TCSPC Settings

During the work on this thesis, a major error in the TCSPC measurement setup was discovered. In detail, the electronic parameter 'Input Level' of the detector was set to the wrong values of -110 mV and -150 mV . This caused both a reduction of detection sensitivity and a virtual decrease of resulting nanosecond lifetimes of acquired decays (Figure D.2 a). When setting the value to -40 mV , literature values were reproduced. Luckily, different samples showed the same dependency on this value (Figure D.2 b and c), so within one measurement run, the results should be comparable.

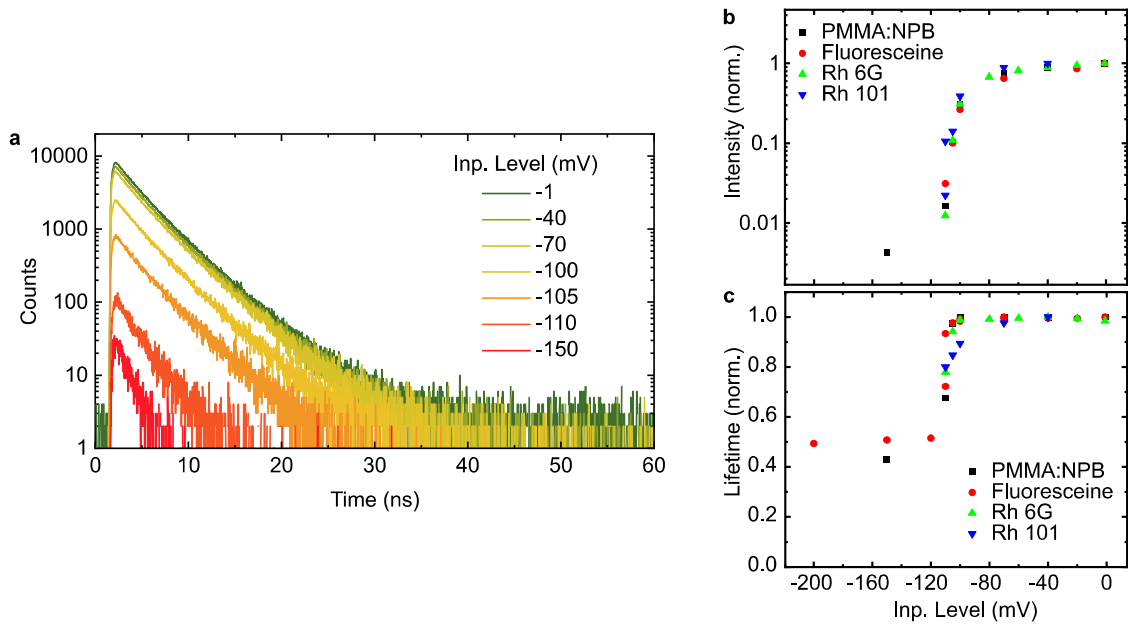


Figure D.2.: **a** Nanosecond decays of PMMA:NPB with identical setup parameters except the Input Level. **b** Integrated decay intensities and **c** resulting lifetimes for different emitters and Input Levels, normalized to the maximum.

Bibliography

- [1] Hans Peter Latscha, Uli Kazmaier, Helmut A. Klein, and Hans Peter Latscha. *Organische Chemie*. Chemie-Basiswissen 2. Springer Spektrum, Berlin Heidelberg, 7. auflage edition, 2016. ISBN 978-3-662-46179-2 978-3-662-46180-8.
- [2] Takatoshi Tsujimura. *OLED Display Fundamentals and Applications*. Wiley Series in Display Technology. Wiley, Hoboken, NJ, second edition edition, 2017. ISBN 978-1-119-18731-8.
- [3] Wallace C. H. Choy, editor. *Organic Solar Cells: Materials and Device Physics*. Green Energy and Technology. Springer, London ; New York, 2013. ISBN 978-1-4471-4822-7 978-1-4471-4823-4.
- [4] Giorgio Mattana, Piero Cosseddu, Beatrice Fraboni, George G. Malliaras, Juan P. Hinestroza, and Annalisa Bonfiglio. Organic electronics on natural cotton fibres. *Organic Electronics*, 12(12):2033–2039, December 2011. ISSN 15661199. doi: 10.1016/j.orgel.2011.09.001.
- [5] Mahiar Hamedi, Robert Forchheimer, and Olle Inganäs. Towards woven logic from organic electronic fibres. *Nature Materials*, 6(5):357–362, May 2007. ISSN 1476-1122, 1476-4660. doi: 10.1038/nmat1884.
- [6] Sergey Lamansky, Peter Djurovich, Drew Murphy, Feras Abdel-Razzaq, Raymond Kwong, Irina Tsyba, Manfred Bortz, Becky Mui, Robert Bau, and Mark E. Thompson. Synthesis and Characterization of Phosphorescent Cyclometalated Iridium Complexes. *Inorganic Chemistry*, 40(7):1704–1711, March 2001. ISSN 0020-1669, 1520-510X. doi: 10.1021/ic0008969.
- [7] F. Clabau, X. Rocquefelte, S. Jobic, P. Deniard, M.-H. Whangbo, A. Garcia, and T. Le Mercier. Mechanism of Phosphorescence Appropriate for the Long-Lasting Phosphors Eu^{2+} -Doped SrAl_2O_4 with Codopants Dy^{3+} and B^{3+} .

- Chemistry of Materials*, 17(15):3904–3912, July 2005. ISSN 0897-4756, 1520-5002. doi: 10.1021/cm050763r.
- [8] T. Matsuzawa. A New Long Phosphorescent Phosphor with High Brightness, $\text{SrAl}_2\text{O}_4:\text{Eu}^{2+}, \text{Dy}^{3+}$. *Journal of The Electrochemical Society*, 143(8):2670, 1996. ISSN 00134651. doi: 10.1149/1.1837067.
- [9] Google Scholar. <https://scholar.google.de/scholar?q=%22room+temperature+phosphorescence%22+OR+%22room+temperature+phosphorescent%22>.
- [10] Gilbert N. Lewis and M. Kasha. Phosphorescence and the Triplet State. *Journal of the American Chemical Society*, 66(12):2100–2116, December 1944. ISSN 0002-7863, 1520-5126. doi: 10.1021/ja01240a030.
- [11] Jacobus Kuijt, Freek Ariese, Udo A.Th. Brinkman, and Cees Gooijer. Room temperature phosphorescence in the liquid state as a tool in analytical chemistry. *Analytica Chimica Acta*, 488(2):135–171, July 2003. ISSN 00032670. doi: 10.1016/S0003-2670(03)00675-5.
- [12] Shuzo Hirata. Recent Advances in Materials with Room-Temperature Phosphorescence: Photophysics for Triplet Exciton Stabilization. *Advanced Optical Materials*, 5(17):1700116, September 2017. ISSN 21951071. doi: 10.1002/adom.201700116.
- [13] Yuichiro Kawamura, Kenichi Goushi, Jason Brooks, Julie J. Brown, Hiroyuki Sasabe, and Chihaya Adachi. 100% phosphorescence quantum efficiency of Ir(III) complexes in organic semiconductor films. *Applied Physics Letters*, 86(7):071104, 2005. ISSN 00036951. doi: 10.1063/1.1862777.
- [14] Huili Ma, Anqi Lv, Lishun Fu, Shan Wang, Zhongfu An, Huifang Shi, and Wei Huang. Room-Temperature Phosphorescence in Metal-Free Organic Materials. *Annalen der Physik*, 531(7):1800482, July 2019. ISSN 0003-3804, 1521-3889. doi: 10.1002/andp.201800482.
- [15] Wang Zhang Yuan, Xiao Yuan Shen, Hui Zhao, Jacky W. Y. Lam, Li Tang, Ping Lu, Chunlei Wang, Yang Liu, Zhiming Wang, Qiang Zheng, Jing Zhi Sun, Yuguang Ma, and Ben Zhong Tang. Crystallization-Induced Phosphorescence of Pure Organic Luminogens at Room Temperature. *The Journal of Physical*

- Chemistry C*, 114(13):6090–6099, April 2010. ISSN 1932-7447, 1932-7455. doi: 10.1021/jp909388y.
- [16] Yongyang Gong, Lifang Zhao, Qian Peng, Di Fan, Wang Zhang Yuan, Yongming Zhang, and Ben Zhong Tang. Crystallization-induced dual emission from metal- and heavy atom-free aromatic acids and esters. *Chemical Science*, 6(8):4438–4444, 2015. ISSN 2041-6520, 2041-6539. doi: 10.1039/C5SC00253B.
- [17] Chenyu Li, Xi Tang, Liuqing Zhang, Cuihong Li, Zhengping Liu, Zhishan Bo, Yong Qiang Dong, Yong-Hui Tian, Yuping Dong, and Ben Zhong Tang. Reversible Luminescence Switching of an Organic Solid: Controllable On-Off Persistent Room Temperature Phosphorescence and Stimulated Multiple Fluorescence Conversion. *Advanced Optical Materials*, 3(9):1184–1190, September 2015. ISSN 21951071. doi: 10.1002/adom.201500115.
- [18] Andrea Fermi, Giacomo Bergamini, Romain Peresutti, Enrico Marchi, Myriam Roy, Paola Ceroni, and Marc Gingras. Molecular asterisks with a persulfurated benzene core are among the strongest organic phosphorescent emitters in the solid state. *Dyes and Pigments*, 110:113–122, November 2014. ISSN 01437208. doi: 10.1016/j.dyepig.2014.04.036.
- [19] Andrea Fermi, Giacomo Bergamini, Myriam Roy, Marc Gingras, and Paola Ceroni. Turn-on Phosphorescence by Metal Coordination to a Multivalent Terpyridine Ligand: A New Paradigm for Luminescent Sensors. *Journal of the American Chemical Society*, 136(17):6395–6400, April 2014. ISSN 0002-7863, 1520-5126. doi: 10.1021/ja501458s.
- [20] Hong Wang, Hao Wang, Xiaoqiong Yang, Qin Wang, and Yajiang Yang. Ion-Unquenchable and Thermally “On-Off” Reversible Room Temperature Phosphorescence of 3-Bromoquinoline Induced by Supramolecular Gels. *Langmuir*, 31(1):486–491, January 2015. ISSN 0743-7463, 1520-5827. doi: 10.1021/la5040323.
- [21] Elena Lucenti, Alessandra Forni, Chiara Botta, Lucia Carlucci, Clelia Gianini, Daniele Marinotto, Andrea Previtali, Stefania Righetto, and Elena Cariati. H-Aggregates Granting Crystallization-Induced Emissive Behavior and Ultra-long Phosphorescence from a Pure Organic Molecule. *The Journal of Phys-*

- ical Chemistry Letters*, 8(8):1894–1898, April 2017. ISSN 1948-7185. doi: 10.1021/acs.jpcllett.7b00503.
- [22] Suzhi Cai, Huifang Shi, Jiewei Li, Long Gu, Yun Ni, Zhichao Cheng, Shan Wang, Wei-wei Xiong, Lin Li, Zhongfu An, and Wei Huang. Visible-Light-Excited Ultralong Organic Phosphorescence by Manipulating Intermolecular Interactions. *Advanced Materials*, 29(35):1701244, September 2017. ISSN 09359648. doi: 10.1002/adma.201701244.
- [23] Zhongfu An, Chao Zheng, Ye Tao, Runfeng Chen, Huifang Shi, Ting Chen, Zhixiang Wang, Huanhuan Li, Renren Deng, Xiaogang Liu, and Wei Huang. Stabilizing triplet excited states for ultralong organic phosphorescence. *Nature Materials*, 14(7):685–690, July 2015. ISSN 1476-1122, 1476-4660. doi: 10.1038/nmat4259.
- [24] Chan Wang, Yueyue Chen, Yalan Xu, Guoxia Ran, Yimin He, and Qijun Song. Aggregation-Induced Room-Temperature Phosphorescence Obtained from Water-Dispersible Carbon Dot-Based Composite Materials. *ACS Applied Materials & Interfaces*, 12(9):10791–10800, March 2020. ISSN 1944-8244, 1944-8252. doi: 10.1021/acsami.9b20500.
- [25] Jinxiao Zhang, Edward Sharman, Li Yang, Jun Jiang, and Guozhen Zhang. Aggregation-Induced Enhancement of Molecular Phosphorescence Lifetime: A First-Principle Study. *The Journal of Physical Chemistry C*, 122(45):25796–25803, November 2018. ISSN 1932-7447, 1932-7455. doi: 10.1021/acs.jpcc.8b07087.
- [26] Nan Gan, Huifang Shi, Zhongfu An, and Wei Huang. Recent Advances in Polymer-Based Metal-Free Room-Temperature Phosphorescent Materials. *Advanced Functional Materials*, 28(51):1802657, December 2018. ISSN 1616301X. doi: 10.1002/adfm.201802657.
- [27] Xiang Ma, Jie Wang, and He Tian. Assembling-Induced Emission: An Efficient Approach for Amorphous Metal-Free Organic Emitting Materials with Room-Temperature Phosphorescence. *Accounts of Chemical Research*, 52(3):738–748, March 2019. ISSN 0001-4842, 1520-4898. doi: 10.1021/acs.accounts.8b00620.

- [28] Sebastian Reineke and Marc A. Baldo. Room temperature triplet state spectroscopy of organic semiconductors. *Scientific Reports*, 4(1), May 2015. ISSN 2045-2322. doi: 10.1038/srep03797.
- [29] Sebastian Reineke, Nico Seidler, Shane R. Yost, Ferry Prins, William A. Tisdale, and Marc A. Baldo. Highly efficient, dual state emission from an organic semiconductor. *Applied Physics Letters*, 103(9):093302, August 2013. ISSN 0003-6951, 1077-3118. doi: 10.1063/1.4819444.
- [30] Hiroyuki Mieno, Ryota Kabe, Naoto Notsuka, Mark D. Allendorf, and Chihaya Adachi. Long-Lived Room-Temperature Phosphorescence of Coronene in Zeolitic Imidazolate Framework ZIF-8. *Advanced Optical Materials*, 4(7):1015–1021, July 2016. ISSN 2195-1071, 2195-1071. doi: 10.1002/adom.201600103.
- [31] Lu Xiao, Yishi Wu, Jianwei Chen, Zhenyi Yu, Yanping Liu, Jiannian Yao, and Hongbing Fu. Highly Efficient Room-Temperature Phosphorescence from Halogen-Bonding-Assisted Doped Organic Crystals. *The Journal of Physical Chemistry A*, 121(45):8652–8658, November 2017. ISSN 1089-5639, 1520-5215. doi: 10.1021/acs.jpca.7b10160.
- [32] Michael Koch, Karthikeyan Perumal, Olivier Blacque, Jai Anand Garg, Ramanathan Saiganesh, Senthamarakannan Kabilan, Kallupattu Kuppusamy Balasubramanian, and Koushik Venkatesan. Metal-Free Triplet Phosphors with High Emission Efficiency and High Tunability. *Angewandte Chemie International Edition*, 53(25):6378–6382, June 2014. ISSN 14337851. doi: 10.1002/anie.201402199.
- [33] Ritika Joshi, Oinam Romesh Meitei, Manojkumar Jadhao, Himank Kumar, and Sujit Kumar Ghosh. Conformation controlled turn on–turn off phosphorescence in a metal-free biluminophore: Thriving the paradox that exists for organic compounds. *Physical Chemistry Chemical Physics*, 18(40):27910–27920, 2016. ISSN 1463-9076, 1463-9084. doi: 10.1039/C6CP04336D.
- [34] Xiaofeng Chen, Cheng Xu, Tao Wang, Cao Zhou, Jiajun Du, Zhongping Wang, Hangxun Xu, Tongqing Xie, Guoqiang Bi, Jun Jiang, Xuepeng Zhang, James N. Demas, Carl O. Trindle, Yi Luo, and Guoqing Zhang. Versatile Room-Temperature-Phosphorescent Materials Prepared from N-Substituted Naphthalimides: Emission Enhancement and Chemical Conjugation. *Angewandte*

- Chemie International Edition*, 55(34):9872–9876, August 2016. ISSN 14337851. doi: 10.1002/anie.201601252.
- [35] Dongwook Lee, Onas Bolton, Byoung Choul Kim, Ji Ho Youk, Shuichi Takayama, and Jinsang Kim. Room Temperature Phosphorescence of Metal-Free Organic Materials in Amorphous Polymer Matrices. *Journal of the American Chemical Society*, 135(16):6325–6329, April 2013. ISSN 0002-7863, 1520-5126. doi: 10.1021/ja401769g.
- [36] Xuepeng Zhang, Tongqing Xie, Minxin Cui, Li Yang, Xingxing Sun, Jun Jiang, and Guoqing Zhang. General Design Strategy for Aromatic Ketone-Based Single-Component Dual-Emissive Materials. *ACS Applied Materials & Interfaces*, 6(4):2279–2284, February 2014. ISSN 1944-8244, 1944-8252. doi: 10.1021/am405209w.
- [37] Songpan Xu, Ruffin E. Evans, Tiandong Liu, Guoqing Zhang, J. N. Demas, Carl O. Trindle, and Cassandra L. Fraser. Aromatic Difluoroboron β -Diketonate Complexes: Effects of π -Conjugation and Media on Optical Properties. *Inorganic Chemistry*, 52(7):3597–3610, April 2013. ISSN 0020-1669, 1520-510X. doi: 10.1021/ic300077g.
- [38] Margaret L. Daly, Caroline Kerr, Christopher A. DeRosa, and Cassandra L. Fraser. *Meta* -Alkoxy-Substituted Difluoroboron Dibenzoylmethane Complexes as Environment-Sensitive Materials. *ACS Applied Materials & Interfaces*, 9(37):32008–32017, September 2017. ISSN 1944-8244, 1944-8252. doi: 10.1021/acsami.7b06910.
- [39] Tiandong Liu, Guoqing Zhang, Ruffin E. Evans, Carl O. Trindle, Zikri Altun, Christopher A. DeRosa, Fang Wang, Meng Zhuang, and Cassandra L. Fraser. Phosphorescence Tuning through Heavy Atom Placement in Unsymmetrical Difluoroboron β -Diketonate Materials. *Chemistry - A European Journal*, 24(8):1859–1869, February 2018. ISSN 09476539. doi: 10.1002/chem.201703513.
- [40] Yan Su, Soo Zeng Fiona Phua, Youbing Li, Xianju Zhou, Deblin Jana, Guofeng Liu, Wei Qi Lim, Wee Kong Ong, Chaolong Yang, and Yanli Zhao. Ultralong room temperature phosphorescence from amorphous organic materials toward confidential information encryption and decryption. *Science Advances*, 4(5):eaas9732, May 2018. ISSN 2375-2548. doi: 10.1126/sciadv.aas9732.

- [41] Hameed A. Al-Attar and Andrew P. Monkman. Room-Temperature Phosphorescence From Films of Isolated Water-Soluble Conjugated Polymers in Hydrogen-Bonded Matrices. *Advanced Functional Materials*, 22(18):3824–3832, September 2012. ISSN 1616301X. doi: 10.1002/adfm.201200814.
- [42] Min Sang Kwon, Dongwook Lee, Sungbaek Seo, Jaehun Jung, and Jinsang Kim. Tailoring Intermolecular Interactions for Efficient Room-Temperature Phosphorescence from Purely Organic Materials in Amorphous Polymer Matrices. *Angewandte Chemie International Edition*, 53(42):11177–11181, October 2014. ISSN 14337851. doi: 10.1002/anie.201404490.
- [43] Richa Gahlaut, Hem C. Joshi, Neeraj K. Joshi, Neetu Pandey, Priyanka Arora, Ranjana Rautela, Kanchan Suyal, and Sanjay Pant. Luminescence characteristics and room temperature phosphorescence of naphthoic acids in polymers. *Journal of Luminescence*, 138:122–128, June 2013. ISSN 00222313. doi: 10.1016/j.jlumin.2013.01.031.
- [44] Piotr Pander, Agnieszka Swist, Jadwiga Soloduch, and Fernando B. Dias. Room temperature phosphorescence lifetime and spectrum tuning of substituted thianthrenes. *Dyes and Pigments*, 142:315–322, July 2017. ISSN 01437208. doi: 10.1016/j.dyepig.2017.03.049.
- [45] Rongjuan Huang, João Avó, Thomas Northey, E. Channing-Pearce, Paloma L. dos Santos, Jonathan S. Ward, Przemyslaw Data, Marc K. Etherington, Mark A. Fox, Thomas J. Penfold, Mário N. Berberan-Santos, João C. Lima, Martin R. Bryce, and Fernando B. Dias. The contributions of molecular vibrations and higher triplet levels to the intersystem crossing mechanism in metal-free organic emitters. *Journal of Materials Chemistry C*, 5(25):6269–6280, 2017. ISSN 2050-7526, 2050-7534. doi: 10.1039/C7TC01958K.
- [46] Haichao Liu, Yu Gao, Jungang Cao, Tingxuan Li, Yating Wen, Yunpeng Ge, Lili Zhang, Guocui Pan, Tong Zhou, and Bing Yang. Efficient room-temperature phosphorescence based on a pure organic sulfur-containing heterocycle: Folding-induced spin-orbit coupling enhancement. *Materials Chemistry Frontiers*, 2(10):1853–1858, 2018. ISSN 2052-1537. doi: 10.1039/C8QM00320C.
- [47] Tomoki Ogoshi, Hiromu Tsuchida, Takahiro Kakuta, Tada-aki Yamagishi, Ai Taema, Toshikazu Ono, Manabu Sugimoto, and Motohiro Mizuno. Ultralong

- Room-Temperature Phosphorescence from Amorphous Polymer Poly(Styrene Sulfonic Acid) in Air in the Dry Solid State. *Advanced Functional Materials*, 28(16):1707369, April 2018. ISSN 1616301X. doi: 10.1002/adfm.201707369.
- [48] Kenry, Chengjian Chen, and Bin Liu. Enhancing the performance of pure organic room-temperature phosphorescent luminophores. *Nature Communications*, 10(1):2111, December 2019. ISSN 2041-1723. doi: 10.1038/s41467-019-10033-2.
- [49] Alexander Nicol, Ryan T. K. Kwok, Congping Chen, Weijun Zhao, Ming Chen, Jianan Qu, and Ben Zhong Tang. Ultrafast Delivery of Aggregation-Induced Emission Nanoparticles and Pure Organic Phosphorescent Nanocrystals by Saponin Encapsulation. *Journal of the American Chemical Society*, 139(41):14792–14799, October 2017. ISSN 0002-7863, 1520-5126. doi: 10.1021/jacs.7b08710.
- [50] Xu Zhen, Ye Tao, Zhongfu An, Peng Chen, Chenjie Xu, Runfeng Chen, Wei Huang, and Kanyi Pu. Ultralong Phosphorescence of Water-Soluble Organic Nanoparticles for In Vivo Afterglow Imaging. *Advanced Materials*, 29(33):1606665, September 2017. ISSN 09359648. doi: 10.1002/adma.201606665.
- [51] Jie Yang, Xu Zhen, Bin Wang, Xuming Gao, Zichun Ren, Jiaqiang Wang, Yujun Xie, Jianrong Li, Qian Peng, Kanyi Pu, and Zhen Li. The influence of the molecular packing on the room temperature phosphorescence of purely organic luminogens. *Nature Communications*, 9(1), December 2018. ISSN 2041-1723. doi: 10.1038/s41467-018-03236-6.
- [52] Youngchang Yu, Min Sang Kwon, Jaehun Jung, Yingying Zeng, Mounggon Kim, Kyeongwoon Chung, Johannes Gierschner, Ji Ho Youk, Sergey M. Borisov, and Jinsang Kim. Room-Temperature-Phosphorescence-Based Dissolved Oxygen Detection by Core-Shell Polymer Nanoparticles Containing Metal-Free Organic Phosphors. *Angewandte Chemie International Edition*, 56(51):16207–16211, December 2017. ISSN 14337851. doi: 10.1002/anie.201708606.
- [53] Kai Jiang, Yuhui Wang, Congzhong Cai, and Hengwei Lin. Conversion of Carbon Dots from Fluorescence to Ultralong Room-Temperature Phosphorescence by Heating for Security Applications. *Advanced Materials*, 30(26):1800783, June 2018. ISSN 09359648. doi: 10.1002/adma.201800783.

- [54] Shuzo Hirata, Kenro Totani, Hironori Kaji, Martin Vacha, Toshiyuki Watanabe, and Chihaya Adachi. Reversible Thermal Recording Media Using Time-Dependent Persistent Room Temperature Phosphorescence. *Advanced Optical Materials*, 1(6):438–442, June 2013. ISSN 21951071. doi: 10.1002/adom.201300136.
- [55] Shigang Wan and Wei Lu. Reversible Photoactivated Phosphorescence of Gold(I) Arylethynyl Complexes in Aerated DMSO Solutions and Gels. *Angewandte Chemie International Edition*, 56(7):1784–1788, February 2017. ISSN 14337851. doi: 10.1002/anie.201610762.
- [56] Wilhelm Schlenk. *Organische Chemie*. De Gruyter, Berlin, Boston, December 1954. ISBN 978-3-11-168034-7. doi: 10.1515/9783111680347.
- [57] A. F. Holleman, Friedrich Richter, and Egon Wiberg. *Lehrbuch der Chemie, Teil 2, Organische Chemie*. 2019. ISBN 978-3-11-168401-7.
- [58] M. Dreizler and Cora S. Lüdde. *Theoretische Physik*. Springer Berlin Heidelberg, Berlin, Heidelberg, 2008. ISBN 978-3-540-48801-9. doi: 10.1007/978-3-540-48802-6.
- [59] Markus Schworer, Hans Christoph Wolf, and William D. Brewer. *Organic Molecular Solids*. Physics Textbook. Wiley-VCH, Weinheim, 2007. ISBN 978-3-527-40540-4.
- [60] Mark Thompson. The Evolution of Organometallic Complexes in Organic Light-Emitting Devices. *MRS Bulletin*, 32(9):694–701, September 2007. ISSN 0883-7694, 1938-1425. doi: 10.1557/mrs2007.144.
- [61] Bureau International des Poids et Mesures, editor. *Le système international d’unités (SI) =: The international system of units (SI)*. BIPM, Sèvres, 8. édition, 2006. ISBN 978-92-822-2213-3.
- [62] Nicholas J. Turro, V. Ramamurthy, and J. C. Scaiano. *Modern Molecular Photochemistry of Organic Molecules*. University Science Books, Sausalito, Calif, 2010. ISBN 978-1-891389-25-2.

- [63] Ian Fleming and Joachim Podlech. *Molekülorbitale und Reaktionen organischer Verbindungen*. Wiley-VCH, Weinheim, 1. Aufl. edition, 2012. ISBN 978-3-527-33069-0.
- [64] Kazumi Nakao, Masayuki Nishimura, Tomoya Tamachi, Yoshiyuki Kuwatani, Hitoshi Miyasaka, Tohru Nishinaga, and Masahiko Iyoda. Giant Macrocycles Composed of Thiophene, Acetylene, and Ethylene Building Blocks. *Journal of the American Chemical Society*, 128(51):16740–16747, December 2006. ISSN 0002-7863, 1520-5126. doi: 10.1021/ja067077t.
- [65] M. Knupfer. Exciton binding energies in organic semiconductors. *Applied Physics A*, 77(5):623–626, October 2003. ISSN 0947-8396, 1432-0630. doi: 10.1007/s00339-003-2182-9.
- [66] Wolfgang Brütting, editor. *Physics of Organic Semiconductors*. Wiley-VCH-Verl, Weinheim, 1. ed., 2. reprint edition, 2008. ISBN 978-3-527-40550-3.
- [67] Wolfgang Demtröder. *Atome, Moleküle und Festkörper*. Number Wolfgang Demtröder ; 3 in Experimentalphysik. Springer Spektrum, Berlin Heidelberg, fifth edition, 2016. ISBN 978-3-662-49094-5 978-3-662-49093-8.
- [68] Jörg Zimmermann, Andre Zeug, and Beate Röder. A generalization of the Jablonski diagram to account for polarization and anisotropy effects in time-resolved experiments. *Phys. Chem. Chem. Phys.*, 5(14):2964–2969, 2003. ISSN 1463-9076, 1463-9084. doi: 10.1039/B303138A.
- [69] Electron Affinity, Eea. In Miloslav Nič, Jiří Jiráť, Bedřich Košata, Aubrey Jenkins, and Alan McNaught, editors, *IUPAC Compendium of Chemical Terminology*. IUPAC, Research Triangle Park, NC, 2.1.0 edition, June 2009. ISBN 978-0-9678550-9-7. doi: 10.1351/goldbook.E01977.
- [70] Yuchao Liu, Chensen Li, Zhongjie Ren, Shouke Yan, and Martin R. Bryce. All-organic thermally activated delayed fluorescence materials for organic light-emitting diodes. *Nature Reviews Materials*, 3(4):18020, April 2018. ISSN 2058-8437. doi: 10.1038/natrevmats.2018.20.
- [71] Ausra Tomkeviciene, Asta Dabulienė, Tomas Matulaitis, Matas Guzauskas, Viktorija Andruleviciene, Juozas Vidas Grazulevicius, Yuri Yamanaka, Yoshio

- Yano, and Toshikazu Ono. Bipolar thianthrene derivatives exhibiting room temperature phosphorescence for oxygen sensing. *Dyes and Pigments*, 170:107605, November 2019. ISSN 01437208. doi: 10.1016/j.dyepig.2019.107605.
- [72] Zbigniew R. Grabowski, Krystyna Rotkiewicz, and Wolfgang Rettig. Structural Changes Accompanying Intramolecular Electron Transfer: Focus on Twisted Intramolecular Charge-Transfer States and Structures. *Chemical Reviews*, 103(10):3899–4032, October 2003. ISSN 0009-2665, 1520-6890. doi: 10.1021/cr940745l.
- [73] Z. R. Grabowski and Jacek Dobkowski. Twisted intramolecular charge transfer (TICT) excited states: Energy and molecular structure. *Pure and Applied Chemistry*, 55(2):245–252, January 1983. ISSN 1365-3075, 0033-4545. doi: 10.1351/pac198855020245.
- [74] Shunsuke Sasaki, Gregor P. C. Drummen, and Gen-ichi Konishi. Recent advances in twisted intramolecular charge transfer (TICT) fluorescence and related phenomena in materials chemistry. *Journal of Materials Chemistry C*, 4(14):2731–2743, 2016. ISSN 2050-7526, 2050-7534. doi: 10.1039/C5TC03933A.
- [75] Joseph R. Lakowicz. *Principles of Fluorescence Spectroscopy*. Springer, New York, NY, third edition, corrected at 4. printing edition, 2010. ISBN 978-0-387-46312-4 978-0-387-31278-1.
- [76] Tarsilla Gerthsen. *Chemie für den Maschinenbau. 2: Organische Chemie für Kraft- und Schmierstoffe: Polymerchemie für Polymerwerkstoffe*. Univ.-Verl, Karlsruhe, 2008. ISBN 978-3-86644-080-7.
- [77] SigmaAldrich - Poly(methyl methacrylate) product comparison page. [sigmaaldrich.com/catalog/substance/polymethylmethacrylate12345901114711](https://www.sigmaaldrich.com/catalog/substance/polymethylmethacrylate12345901114711), March 2020.
- [78] SigmaAldrich - analytical standard, for GPC, 4,000 - Poly(methyl methacrylate). <https://www.sigmaaldrich.com/catalog/product/sial/94131>, March 2020.
- [79] W. Schnabel. *Polymers and Light: Fundamentals and Technical Applications*. Wiley, first edition, February 2007. ISBN 978-3-527-31866-7 978-3-527-61102-7. doi: 10.1002/9783527611027.

- [80] N. Sultanova, S. Kasarova, and I. Nikolov. Dispersion Properties of Optical Polymers. *Acta Physica Polonica A*, 116(4):585–587, October 2009. ISSN 0587-4246, 1898-794X. doi: 10.12693/APhysPolA.116.585.
- [81] Max J. Schnepf, Martin Mayer, Christian Kuttner, Moritz Tebbe, Daniel Wolf, Martin Dulle, Thomas Altantzis, Petr Formanek, Stephan Förster, Sara Bals, Tobias A. F. König, and Andreas Fery. Nanorattles with tailored electric field enhancement. *Nanoscale*, 9(27):9376–9385, 2017. ISSN 2040-3364, 2040-3372. doi: 10.1039/C7NR02952G.
- [82] Kuraray - Gas Barrier Units. <http://www.evalevoh.com/us/eval-properties/barrier-to-oxygen/gas-barrier-units.aspx>, March 2020.
- [83] Nivedita S. Sangaj and V.C. Malshe. Permeability of polymers in protective organic coatings. *Progress in Organic Coatings*, 50(1):28–39, June 2004. ISSN 03009440. doi: 10.1016/j.porgcoat.2003.09.015.
- [84] Marjoleine Drieskens, Roos Peeters, Jules Mullens, Dirk Franco, Pieter J. Lemstra, and Denka G. Hristova-Bogaerds. Structure versus properties relationship of poly(lactic acid). I. Effect of crystallinity on barrier properties. *Journal of Polymer Science Part B: Polymer Physics*, 47(22):2247–2258, November 2009. ISSN 08876266, 10990488. doi: 10.1002/polb.21822.
- [85] Physical properties of polymers. <http://photos.labwrench.com/equipmentManuals/15174-5924.pdf>.
- [86] I. Siró, D. Plackett, and P. Sommer-Larsen. A comparative study of oxygen transmission rates through polymer films based on fluorescence quenching. *Packaging Technology and Science*, 23(6):301–315, October 2010. ISSN 08943214. doi: 10.1002/pts.895.
- [87] A. Ammala. Nylon-MXD6 resins for food packaging. In *Multifunctional and Nanoreinforced Polymers for Food Packaging*, pages 243–260. Elsevier, 2011. ISBN 978-1-84569-738-9. doi: 10.1533/9780857092786.1.243.
- [88] Samuel Michel. Exceval – The PVOH barrier specialist. <https://www.linkedin.com/pulse/exceval-pvoh-barrier-specialist-dr-samuel-michel>, December 2015.

- [89] Max Gmelch and Sebastian Reineke. *Durchblick in Optik: Mit Phänomenen, Formeln und Fragen Zum Verständnis*. Springer Berlin / Heidelberg, Berlin, Heidelberg, 2019. ISBN 978-3-662-58939-7.
- [90] Ian Carmichael and Gordon L. Hug. Triplet–Triplet Absorption Spectra of Organic Molecules in Condensed Phases. *Journal of Physical and Chemical Reference Data*, 15(1):1–250, January 1986. ISSN 0047-2689, 1529-7845. doi: 10.1063/1.555770.
- [91] Ye Tao, Kai Yuan, Ting Chen, Peng Xu, Huanhuan Li, Runfeng Chen, Chao Zheng, Lei Zhang, and Wei Huang. Thermally Activated Delayed Fluorescence Materials Towards the Breakthrough of Organoelectronics. *Advanced Materials*, 26(47):7931–7958, December 2014. ISSN 09359648. doi: 10.1002/adma.201402532.
- [92] Karla Roszeitis. A rate model for organic luminophores - Simulations and calculations on organic light-emitting systems, Bachelor Thesis, May 2017.
- [93] Christel M. Marian. Spin-orbit coupling and intersystem crossing in molecules: Spin-orbit coupling. *Wiley Interdisciplinary Reviews: Computational Molecular Science*, 2(2):187–203, March 2012. ISSN 17590876. doi: 10.1002/wcms.83.
- [94] M. A. Baldo, D. F. O’Brien, Y. You, A. Shoustikov, S. Sibley, M. E. Thompson, and S. R. Forrest. Highly efficient phosphorescent emission from organic electroluminescent devices. *Nature*, 395(6698):151–154, September 1998. ISSN 0028-0836, 1476-4687. doi: 10.1038/25954.
- [95] Hartmut Yersin, editor. *Highly Efficient OLEDs with Phosphorescent Materials*. WILEY-VCH, Weinheim, 2008. ISBN 978-3-527-40594-7.
- [96] Sebastian Reineke, Michael Thomschke, Björn Lüssem, and Karl Leo. White organic light-emitting diodes: Status and perspective. *Reviews of Modern Physics*, 85(3):1245–1293, July 2013. ISSN 0034-6861, 1539-0756. doi: 10.1103/RevModPhys.85.1245.
- [97] Weijun Zhao, Zikai He, Jacky W.Y. Lam, Qian Peng, Huili Ma, Zhigang Shuai, Gongxun Bai, Jianhua Hao, and Ben Zhong Tang. Rational Molecular Design for Achieving Persistent and Efficient Pure Organic Room-Temperature

- Phosphorescence. *Chem*, 1(4):592–602, October 2016. ISSN 24519294. doi: 10.1016/j.chempr.2016.08.010.
- [98] Zhiyi Yuan, Jie Wang, Lu Chen, Xueqing Gong Zou, and Xiang Ma. Methanol Dynamically Activated Room-Temperature Phosphorescence from a Twisted 4-Bromobiphenyl System. *Chinese Chemical Society Chemistry*, (2):158–167, 2020. doi: 10.31635/ccschem.020.201900121.
- [99] Cristian A. M. Salla, Giliandro Farias, Mathieu Rouzières, Pierre Dechambenoit, Fabien Durola, Harald Bock, Bernardo de Souza, and Ivan H. Bechtold. Persistent Solid-State Phosphorescence and Delayed Fluorescence at Room Temperature by a Twisted Hydrocarbon. *Angewandte Chemie International Edition*, 58(21):6982–6986, May 2019. ISSN 14337851. doi: 10.1002/anie.201901672.
- [100] David Danovich, Christel M. Marian, Thomas Neuheuser, Sigrid D. Peyerimhoff, and Sason Shaik. Spin-Orbit Coupling Patterns Induced by Twist and Pyramidalization Modes in C_2H_4 : A Quantitative Study and a Qualitative Analysis. *The Journal of Physical Chemistry A*, 102(29):5923–5936, July 1998. ISSN 1089-5639, 1520-5215. doi: 10.1021/jp980391s.
- [101] Zhiyong Yang, Zhu Mao, Zongliang Xie, Yi Zhang, Siwei Liu, Juan Zhao, Jiarui Xu, Zhenguo Chi, and Matthew P. Aldred. Recent advances in organic thermally activated delayed fluorescence materials. *Chemical Society Reviews*, 46(3):915–1016, 2017. ISSN 0306-0012, 1460-4744. doi: 10.1039/C6CS00368K.
- [102] Shuzo Hirata, Yumi Sakai, Kensuke Masui, Hiroyuki Tanaka, Sae Youn Lee, Hiroko Nomura, Nozomi Nakamura, Mao Yasumatsu, Hajime Nakanotani, Qisheng Zhang, Katsuyuki Shizu, Hiroshi Miyazaki, and Chihaya Adachi. Highly efficient blue electroluminescence based on thermally activated delayed fluorescence. *Nature Materials*, 14(3):330–336, March 2015. ISSN 1476-1122, 1476-4660. doi: 10.1038/nmat4154.
- [103] Pengchong Xue, Jiabao Sun, Peng Chen, Panpan Wang, Boqi Yao, Peng Gong, Zhenqi Zhang, and Ran Lu. Luminescence switching of a persistent room-temperature phosphorescent pure organic molecule in response to external stimuli. *Chemical Communications*, 51(52):10381–10384, 2015. ISSN 1359-7345, 1364-548X. doi: 10.1039/C5CC03403E.

- [104] Yu Xiong, Zheng Zhao, Weijun Zhao, Huili Ma, Qian Peng, Zikai He, Xuepeng Zhang, Yuncong Chen, Xuewen He, Jacky W. Y. Lam, and Ben Zhong Tang. Designing Efficient and Ultralong Pure Organic Room-Temperature Phosphorescent Materials by Structural Isomerism. *Angewandte Chemie International Edition*, 57(27):7997–8001, July 2018. ISSN 14337851. doi: 10.1002/anie.201800834.
- [105] Qisheng Zhang, Bo Li, Shuping Huang, Hiroko Nomura, Hiroyuki Tanaka, and Chihaya Adachi. Efficient blue organic light-emitting diodes employing thermally activated delayed fluorescence. *Nature Photonics*, 8(4):326–332, April 2014. ISSN 1749-4885, 1749-4893. doi: 10.1038/nphoton.2014.12.
- [106] Hiroki Uoyama, Kenichi Goushi, Katsuyuki Shizu, Hiroko Nomura, and Chihaya Adachi. Highly efficient organic light-emitting diodes from delayed fluorescence. *Nature*, 492(7428):234–238, December 2012. ISSN 0028-0836, 1476-4687. doi: 10.1038/nature11687.
- [107] Dong Ryun Lee, Mounggon Kim, Sang Kyu Jeon, Seok-Ho Hwang, Chil Won Lee, and Jun Yeob Lee. Design Strategy for 25% External Quantum Efficiency in Green and Blue Thermally Activated Delayed Fluorescent Devices. *Advanced Materials*, 27(39):5861–5867, October 2015. ISSN 09359648. doi: 10.1002/adma.201502053.
- [108] Ting-An Lin, Tanmay Chatterjee, Wei-Lung Tsai, Wei-Kai Lee, Meng-Jung Wu, Min Jiao, Kuan-Chung Pan, Chih-Lung Yi, Chin-Lung Chung, Ken-Tsung Wong, and Chung-Chih Wu. Sky-Blue Organic Light Emitting Diode with 37% External Quantum Efficiency Using Thermally Activated Delayed Fluorescence from Spiroacridine-Triazine Hybrid. *Advanced Materials*, 28(32):6976–6983, August 2016. ISSN 09359648. doi: 10.1002/adma.201601675.
- [109] Chihaya Adachi, Marc A. Baldo, Mark E. Thompson, and Stephen R. Forrest. Nearly 100% internal phosphorescence efficiency in an organic light-emitting device. *Journal of Applied Physics*, 90(10):5048–5051, November 2001. ISSN 0021-8979, 1089-7550. doi: 10.1063/1.1409582.
- [110] Jaesang Lee, Hsiao-Fan Chen, Thilini Batagoda, Caleb Coburn, Peter I. Djurovich, Mark E. Thompson, and Stephen R. Forrest. Deep blue phosphorescent organic light-emitting diodes with very high brightness and efficiency.

- Nature Materials*, 15(1):92–98, January 2016. ISSN 1476-1122, 1476-4660. doi: 10.1038/nmat4446.
- [111] Shuzo Hirata. Ultralong-lived room temperature triplet excitons: Molecular persistent room temperature phosphorescence and nonlinear optical characteristics with continuous irradiation. *Journal of Materials Chemistry C*, 6(44): 11785–11794, 2018. ISSN 2050-7526, 2050-7534. doi: 10.1039/C8TC01417E.
- [112] W. Rumsey, J. Vanderkooi, and D. Wilson. Imaging of phosphorescence: A novel method for measuring oxygen distribution in perfused tissue. *Science*, 241(4873):1649–1651, September 1988. ISSN 0036-8075, 1095-9203. doi: 10.1126/science.3420417.
- [113] Hazel A. Collins, Mamta Khurana, Eduardo H. Moriyama, Adrian Mariampillai, Emma Dahlstedt, Milan Balaz, Marina K. Kuimova, Mikhail Drobizhev, Victor X. D. Yang, David Phillips, Aleksander Rebane, Brian C. Wilson, and Harry L. Anderson. Blood-vessel closure using photosensitizers engineered for two-photon excitation. *Nature Photonics*, 2(7):420–424, July 2008. ISSN 1749-4885, 1749-4893. doi: 10.1038/nphoton.2008.100.
- [114] S. M. Ali Fateminia, Zhu Mao, Shidang Xu, Zhiyong Yang, Zhenguo Chi, and Bin Liu. Organic Nanocrystals with Bright Red Persistent Room-Temperature Phosphorescence for Biological Applications. *Angewandte Chemie International Edition*, 56(40):12160–12164, September 2017. ISSN 14337851. doi: 10.1002/anie.201705945.
- [115] Philipp Lehner, Christoph Staudinger, Sergey M. Borisov, and Ingo Klimant. Ultra-sensitive optical oxygen sensors for characterization of nearly anoxic systems. *Nature Communications*, 5(1):4460, December 2014. ISSN 2041-1723. doi: 10.1038/ncomms5460.
- [116] Theodor Förster. Experimentelle und theoretische Untersuchung des zwischenmolekularen Übergangs von Elektronenanregungsenergie. *Zeitschrift für Naturforschung A*, 4(5):321–327, January 1949. doi: 10.1515/zna-1949-0501.
- [117] I Z Steinberg. Long-Range Nonradiative Transfer of Electronic Excitation Energy in Proteins and Polypeptides. *Annual Review of Biochemistry*, 40(1):83–

- 114, June 1971. ISSN 0066-4154, 1545-4509. doi: 10.1146/annurev.bi.40.070171.000503.
- [118] R. G. Bennett, R. P. Schwenker, and R. E. Kellogg. Radiationless Intermolecular Energy Transfer. II. Triplet to Singlet Transfer. *The Journal of Chemical Physics*, 41(10):3040–3041, November 1964. ISSN 0021-9606, 1089-7690. doi: 10.1063/1.1725671.
- [119] D. L. Dexter. A Theory of Sensitized Luminescence in Solids. *The Journal of Chemical Physics*, 21(5):836–850, May 1953. ISSN 0021-9606, 1089-7690. doi: 10.1063/1.1699044.
- [120] Guozhong Cao and C. Jeffrey Brinker. *Annual Review of Nano Research. Volume 2 Volume 2*. World Scientific, Hackensack, NJ, 2008. ISBN 978-981-279-023-1 978-981-279-022-4.
- [121] Zhimin Li, Chao Liu, Hadi Abroshan, Douglas R. Kauffman, and Gao Li. Au₃₈ S₂ (SAdm)₂₀ Photocatalyst for One-Step Selective Aerobic Oxidations. *ACS Catalysis*, 7(5):3368–3374, May 2017. ISSN 2155-5435, 2155-5435. doi: 10.1021/acscatal.7b00239.
- [122] Taro Furukawa, Hajime Nakanotani, Munetomo Inoue, and Chihaya Adachi. Dual enhancement of electroluminescence efficiency and operational stability by rapid upconversion of triplet excitons in OLEDs. *Scientific Reports*, 5(1): 8429, July 2015. ISSN 2045-2322. doi: 10.1038/srep08429.
- [123] Kensuke Masui, Hajime Nakanotani, and Chihaya Adachi. Analysis of exciton annihilation in high-efficiency sky-blue organic light-emitting diodes with thermally activated delayed fluorescence. *Organic Electronics*, 14(11):2721–2726, November 2013. ISSN 15661199. doi: 10.1016/j.orgel.2013.07.010.
- [124] Chen Li, Lian Duan, Dongdong Zhang, and Yong Qiu. Thermally Activated Delayed Fluorescence Sensitized Phosphorescence: A Strategy To Break the Trade-Off between Efficiency and Efficiency Roll-Off. *ACS Applied Materials & Interfaces*, 7(28):15154–15159, July 2015. ISSN 1944-8244, 1944-8252. doi: 10.1021/acsami.5b04090.
- [125] Alastair Buckley. *Organic Light-Emitting Diodes (OLEDs): Materials, Devices and Applications*. 2013. ISBN 978-0-85709-894-8.

- [126] Martin Kroll. Investigation of biluminescent emitter systems in dependence of the excitation density, Master Thesis, December 2017.
- [127] H. van Eersel, P. A. Bobbert, and R. Coehoorn. Kinetic Monte Carlo study of triplet-triplet annihilation in organic phosphorescent emitters. *Journal of Applied Physics*, 117(11):115502, March 2015. ISSN 0021-8979, 1089-7550. doi: 10.1063/1.4914460.
- [128] L. Zhang, H. van Eersel, P.A. Bobbert, and R. Coehoorn. Clarifying the mechanism of triplet–triplet annihilation in phosphorescent organic host–guest systems: A combined experimental and simulation study. *Chemical Physics Letters*, 652:142–147, May 2016. ISSN 00092614. doi: 10.1016/j.cplett.2016.04.043.
- [129] M. A. Baldo, C. Adachi, and S. R. Forrest. Transient analysis of organic electrophosphorescence. II. Transient analysis of triplet-triplet annihilation. *Physical Review B*, 62(16):10967–10977, October 2000. ISSN 0163-1829, 1095-3795. doi: 10.1103/PhysRevB.62.10967.
- [130] Ebinazar B. Namdas, Arvydas Ruseckas, Ifor D. W. Samuel, Shih-Chun Lo, and Paul L. Burn. Triplet exciton diffusion in *fac* -tris(2-phenylpyridine) iridium(III)-cored electroluminescent dendrimers. *Applied Physics Letters*, 86(9):091104, February 2005. ISSN 0003-6951, 1077-3118. doi: 10.1063/1.1867571.
- [131] J. C. Ribierre, A. Ruseckas, K. Knights, S. V. Staton, N. Cumpstey, P. L. Burn, and I. D. W. Samuel. Triplet Exciton Diffusion and Phosphorescence Quenching in Iridium(III)-Centered Dendrimers. *Physical Review Letters*, 100(1):017402, January 2008. ISSN 0031-9007, 1079-7114. doi: 10.1103/PhysRevLett.100.017402.
- [132] Yifan Zhang and Stephen R. Forrest. Triplet diffusion leads to triplet–triplet annihilation in organic phosphorescent emitters. *Chemical Physics Letters*, 590: 106–110, December 2013. ISSN 00092614. doi: 10.1016/j.cplett.2013.10.048.
- [133] W. Staroske, M. Pfeiffer, K. Leo, and M. Hoffmann. Single-Step Triplet-Triplet Annihilation: An Intrinsic Limit for the High Brightness Efficiency of Phosphorescent Organic Light Emitting Diodes. *Physical Review Letters*, 98(19), May 2007. ISSN 0031-9007, 1079-7114. doi: 10.1103/PhysRevLett.98.197402.

- [134] Sebastian Reineke, Karsten Walzer, and Karl Leo. Triplet-exciton quenching in organic phosphorescent light-emitting diodes with Ir-based emitters. *Physical Review B*, 75(12):125328, March 2007. ISSN 1098-0121, 1550-235X. doi: 10.1103/PhysRevB.75.125328.
- [135] Alessandra Forni, Elena Lucenti, Chiara Botta, and Elena Cariati. Metal free room temperature phosphorescence from molecular self-interactions in the solid state. *Journal of Materials Chemistry C*, 6(17):4603–4626, 2018. ISSN 2050-7526, 2050-7534. doi: 10.1039/C8TC01007B.
- [136] Raymond Y. N. Ho, Joel F. Liebman, and Joan Selverstone Valentine. Overview of the Energetics and Reactivity of Oxygen. In Christopher S. Foote, Joan Selverstone Valentine, Arthur Greenberg, and Joel F. Liebman, editors, *Active Oxygen in Chemistry*, pages 1–23. Springer Netherlands, Dordrecht, 1995. ISBN 978-0-7514-0371-8 978-94-007-0874-7. doi: 10.1007/978-94-007-0874-7_1.
- [137] Steven P. Stratton, William H. Schaefer, and Daniel C. Liebler. Isolation and identification of singlet oxygen oxidation products of .beta.-carotene. *Chemical Research in Toxicology*, 6(4):542–547, July 1993. ISSN 0893-228X, 1520-5010. doi: 10.1021/tx00034a024.
- [138] Christian Triantaphylidès, Markus Krischke, Frank Alfons Hoeberichts, Brigitte Ksas, Gabriele Gresser, Michel Havaux, Frank Van Breusegem, and Martin Johannes Mueller. Singlet Oxygen Is the Major Reactive Oxygen Species Involved in Photooxidative Damage to Plants. *Plant Physiology*, 148(2):960–968, October 2008. ISSN 0032-0889, 1532-2548. doi: 10.1104/pp.108.125690.
- [139] Lucymara F. Agnez-Lima, Julliane T.A. Melo, Acarízia E. Silva, Ana Helena S. Oliveira, Ana Rafaela S. Timoteo, Keronninn M. Lima-Bessa, Glaucia R. Martinez, Marisa H.G. Medeiros, Paolo Di Mascio, Rodrigo S. Galhardo, and Carlos F.M. Menck. DNA damage by singlet oxygen and cellular protective mechanisms. *Mutation Research/Reviews in Mutation Research*, 751(1):15–28, July 2012. ISSN 13835742. doi: 10.1016/j.mrrev.2011.12.005.
- [140] T. J. Dougherty, C. J. Gomer, B. W. Henderson, G. Jori, D. Kessel, M. Korbelik, J. Moan, and Q. Peng. Photodynamic Therapy. *JNCI Journal of the National*

- Cancer Institute*, 90(12):889–905, June 1998. ISSN 0027-8874, 1460-2105. doi: 10.1093/jnci/90.12.889.
- [141] Dennis E.J.G.J. Dolmans, Dai Fukumura, and Rakesh K. Jain. Photodynamic therapy for cancer. *Nature Reviews Cancer*, 3(5):380–387, May 2003. ISSN 1474-175X, 1474-1768. doi: 10.1038/nrc1071.
- [142] Brian H. Cumpston and Klavs F. Jensen. Photo-oxidation of polymers used in electroluminescent devices. *Synthetic Metals*, 73(3):195–199, August 1995. ISSN 03796779. doi: 10.1016/0379-6779(95)80015-8.
- [143] Santi Nonell and Cristina Flors, editors. *Singlet Oxygen: Applications in Biosciences and Nanosciences*. Number volume 13-14 in Comprehensive Series in Photochemistry and Photobiology. Royal Society of Chemistry, Cambridge, 2016. ISBN 978-1-78262-038-9 978-1-78262-697-8.
- [144] Heinrich Gobrecht, Hans Bucka, Ludwig Bergmann, Clemens Schaefer, and Klaus Becker, editors. *Aufbau Der Materie*. De Gruyter, Berlin, Boston, December 1981. ISBN 978-3-11-157969-6. doi: 10.1515/9783111579696.
- [145] M. Bodesheim, M. Schütz, and R. Schmidt. Triplet state energy dependence of the competitive formation of $O_2(1\Sigma+g)$, $O_2(1\Delta g)$ and $O_2(3\Sigma-g)$ in the sensitization of O_2 by triplet states. *Chemical Physics Letters*, 221(1-2):7–14, April 1994. ISSN 00092614. doi: 10.1016/0009-2614(94)87008-X.
- [146] Kurt Schiller and Franz Werner Müller. Singlet oxygen lifetime in polymer films. *Polymer International*, 25(1):19–22, 1991. ISSN 09598103, 10970126. doi: 10.1002/pi.4990250105.
- [147] Roger L. Clough, Maria P. Dillon, Kai Kong Iu, and Peter R. Ogilby. Behavior of singlet molecular oxygen ($1.DELTA.gO_2$) in a polymer matrix: Effects of temperature, matrix rigidity, and molecular composition. *Macromolecules*, 22(9):3620–3628, September 1989. ISSN 0024-9297, 1520-5835. doi: 10.1021/ma00199a020.
- [148] Francis Wilkinson, W. Phillip Helman, and Alberta B. Ross. Quantum Yields for the Photosensitized Formation of the Lowest Electronically Excited Singlet

- State of Molecular Oxygen in Solution. *Journal of Physical and Chemical Reference Data*, 22(1):113–262, January 1993. ISSN 0047-2689, 1529-7845. doi: 10.1063/1.555934.
- [149] Robert W. Redmond and Janet N. Gamlin. A Compilation of Singlet Oxygen Yields from Biologically Relevant Molecules. *Photochemistry and Photobiology*, 70(4):391–475, October 1999. ISSN 0031-8655, 1751-1097. doi: 10.1111/j.1751-1097.1999.tb08240.x.
- [150] Reinhard Schmidt. Photosensitized Generation of Singlet Oxygen. *Photochemistry and Photobiology*, 82(5):1161, 2006. ISSN 0031-8655. doi: 10.1562/2006-03-03-IR-833.
- [151] Peter R. Ogilby, Maria P. Dillon, Marianne Kristiansen, and Roger L. Clough. Quenching of singlet oxygen in solid organic polymers. *Macromolecules*, 25(13):3399–3405, June 1992. ISSN 0024-9297, 1520-5835. doi: 10.1021/ma00039a014.
- [152] Peter R. Ogilby, Kai Kong Iu, and Roger L. Clough. The photosensitized production of singlet molecular oxygen ($^1\text{DELTA.gO}_2$) in a solid organic polymer glass: A direct time-resolved study. *Journal of the American Chemical Society*, 109(15):4746–4747, July 1987. ISSN 0002-7863. doi: 10.1021/ja00249a062.
- [153] Claude Schweitzer and Reinhard Schmidt. Physical Mechanisms of Generation and Deactivation of Singlet Oxygen. *Chemical Reviews*, 103(5):1685–1758, May 2003. ISSN 0009-2665, 1520-6890. doi: 10.1021/cr010371d.
- [154] Zahra Mehrdad, Claude Schweitzer, and Reinhard Schmidt. Formation of $\text{O}_2(1\Sigma\text{g}^+)$, $\text{O}_2(1\Delta\text{g})$, and $\text{O}_2(3\Sigma\text{g}^-)$ during Oxygen Quenching of $n\pi^*$ Triplet Phenyl Ketones: The Role of Charge Transfer and Sensitizer-Oxygen Complex Structure. *The Journal of Physical Chemistry A*, 106(2):228–235, December 2001. doi: 10.1021/jp013363+.
- [155] Claude Schweitzer, Zahra Mehrdad, Astrid Noll, Erich-Walter Grabner, and Reinhard Schmidt. Oxygen Quenching of $n\pi^*$ Triplet Phenyl Ketones: Local Excitation and Local Deactivation. *Helvetica Chimica Acta*, (84):2493–2507, October 2001. doi: doi:10.1002/1522-2675(20010919)84:9<2493::AID-HLCA2493>3.0.CO;2-F.

- [156] Peter R. Ogilby. Singlet oxygen: There is indeed something new under the sun. *Chemical Society Reviews*, 39(8):3181, 2010. ISSN 0306-0012, 1460-4744. doi: 10.1039/b926014p.
- [157] Ivana Pibiri, Silvestre Buscemi, Antonio Palumbo Piccionello, and Andrea Pace. Photochemically Produced Singlet Oxygen: Applications and Perspectives. *ChemPhotoChem*, 2(7):535–547, July 2018. ISSN 23670932. doi: 10.1002/cptc.201800076.
- [158] Ayman A. Abdel-Shafi and Francis Wilkinson. Charge Transfer Effects on the Efficiency of Singlet Oxygen Production Following Oxygen Quenching of Excited Singlet and Triplet States of Aromatic Hydrocarbons in Acetonitrile. *The Journal of Physical Chemistry A*, 104(24):5747–5757, June 2000. ISSN 1089-5639, 1520-5215. doi: 10.1021/jp0000432.
- [159] Chris Lambert and Robert W. Redmond. Triplet energy level of β -carotene. *Chemical Physics Letters*, 228(4-5):495–498, October 1994. ISSN 00092614. doi: 10.1016/0009-2614(94)00942-2.
- [160] Pauline F. Conn, Wolfgang Schalch, and T.George Truscott. The singlet oxygen and carotenoid interaction. *Journal of Photochemistry and Photobiology B: Biology*, 11(1):41–47, October 1991. ISSN 10111344. doi: 10.1016/1011-1344(91)80266-K.
- [161] Barbara Enko, Sergey M. Borisov, Johannes Regensburger, Wolfgang Bäuml, Georg Gescheidt, and Ingo Klimant. Singlet Oxygen-Induced Photodegradation of the Polymers and Dyes in Optical Sensing Materials and the Effect of Stabilizers on These Processes. *The Journal of Physical Chemistry A*, 117(36):8873–8882, September 2013. ISSN 1089-5639, 1520-5215. doi: 10.1021/jp4046462.
- [162] D. B. Min and J. M. Boff. Chemistry and Reaction of Singlet Oxygen in Foods. *Comprehensive Reviews in Food Science and Food Safety*, 1(2):58–72, July 2002. ISSN 1541-4337, 1541-4337. doi: 10.1111/j.1541-4337.2002.tb00007.x.
- [163] M DeRosa. Photosensitized singlet oxygen and its applications. *Coordination Chemistry Reviews*, 233-234:351–371, November 2002. ISSN 00108545. doi: 10.1016/S0010-8545(02)00034-6.

- [164] Ariane Felgenträger, Tim Maisch, Andreas Späth, Josef A. Schröder, and Wolfgang Bäumler. Singlet oxygen generation in porphyrin-doped polymeric surface coating enables antimicrobial effects on *Staphylococcus aureus*. *Phys. Chem. Chem. Phys.*, 16(38):20598–20607, 2014. ISSN 1463-9076, 1463-9084. doi: 10.1039/C4CP02439G.
- [165] Philipp Lehner, Christoph Staudinger, Sergey M. Borisov, Johannes Regensburger, and Ingo Klimant. Intrinsic Artefacts in Optical Oxygen Sensors-How Reliable are our Measurements? *Chemistry - A European Journal*, 21(10): 3978–3986, March 2015. ISSN 09476539. doi: 10.1002/chem.201406037.
- [166] J. Peeling and D.T. Clark. An ESCA study of the photo-oxidation of the surface of polystyrene film. *Polymer Degradation and Stability*, 3(2):97–105, February 1981. ISSN 01413910. doi: 10.1016/0141-3910(81)90002-1.
- [167] J. Peeling and D.T. Clark. ESCA study of the surface photo-oxidation of some non-aromatic polymers. *Polymer Degradation and Stability*, 3(3):177–185, May 1981. ISSN 01413910. doi: 10.1016/0141-3910(81)90031-8.
- [168] Michael Schiller and Ralph-Dieter Maier. *Handbuch Kunststoff-Additive*. Hanser, München, 2016. ISBN 978-3-446-43291-8 978-3-446-45216-9.
- [169] Glaucia R. Martinez, Jean-Luc Ravanat, Marisa H. G. Medeiros, Jean Cadet, and Paolo Di Mascio. Synthesis of a Naphthalene Endoperoxide as a Source of ¹⁸O-labeled Singlet Oxygen for Mechanistic Studies. *Journal of the American Chemical Society*, 122(41):10212–10213, October 2000. ISSN 0002-7863, 1520-5126. doi: 10.1021/ja0016452.
- [170] Sebastian Benz, Sarah Nötzli, Jay S. Siegel, Daniel Eberli, and Henning J. Jessen. Controlled Oxygen Release from Pyridone Endoperoxides Promotes Cell Survival under Anoxic Conditions. *Journal of Medicinal Chemistry*, 56(24):10171–10182, December 2013. ISSN 0022-2623, 1520-4804. doi: 10.1021/jm4016137.
- [171] Véronique Nardello and Jean-Marie Aubry. [5] Measurement of photogenerated singlet oxygen in aqueous media. In *Methods in Enzymology*, volume 319, pages 50–58. Elsevier, 2000. ISBN 978-0-12-182220-0. doi: 10.1016/S0076-6879(00)19007-X.

- [172] Susan Callaghan, Mikhail A. Filatov, Elisabeth Sitte, Huguette Savoie, Ross W. Boyle, Keith J. Flanagan, and Mathias O. Senge. Delayed release singlet oxygen sensitizers based on pyridone-appended porphyrins. *Photochemical & Photobiological Sciences*, 16(9):1371–1374, 2017. ISSN 1474-905X, 1474-9092. doi: 10.1039/C7PP00244K.
- [173] N. V. Nazarova, Yu. S. Avlasevich, K. Landfester, and S. Balushev. Stimuli-responsive protection of optically excited triplet ensembles against deactivation by molecular oxygen. *Dalton Transactions*, 47(26):8605–8610, 2018. ISSN 1477-9226, 1477-9234. doi: 10.1039/C7DT03698A.
- [174] Mikhail A. Filatov, Ernesta Heinrich, Dmitry Busko, Iliyana Z. Ilieva, Katharina Landfester, and Stanislav Balushev. Reversible oxygen addition on a triplet sensitizer molecule: Protection from excited state depopulation. *Physical Chemistry Chemical Physics*, 17(9):6501–6510, 2015. ISSN 1463-9076, 1463-9084. doi: 10.1039/C4CP05025H.
- [175] Mikhail A. Filatov and Mathias O. Senge. Molecular devices based on reversible singlet oxygen binding in optical and photomedical applications. *Molecular Systems Design & Engineering*, 1(3):258–272, 2016. ISSN 2058-9689. doi: 10.1039/C6ME00042H.
- [176] Jean-Marie Aubry, Christel Pierlot, Jean Rigaudy, and Reinhard Schmidt. Reversible Binding of Oxygen to Aromatic Compounds. *Accounts of Chemical Research*, 36(9):668–675, September 2003. ISSN 0001-4842, 1520-4898. doi: 10.1021/ar010086g.
- [177] Nerea Epelde-Elezcano, Virginia Martínez-Martínez, Eduardo Peña-Cabrera, César F. A. Gómez-Durán, Iñigo López Arbeloa, and Sylvie Lacombe. Modulation of singlet oxygen generation in halogenated BODIPY dyes by substitution at their meso position: Towards a solvent-independent standard in the vis region. *RSC Advances*, 6(48):41991–41998, 2016. ISSN 2046-2069. doi: 10.1039/C6RA05820E.
- [178] I.M. Byteva, G.P. Gurinovich, O.L. Golomb, and V.V. Kappov. Photosensitized luminescence of singlet oxygen in polymeric films. *Chemical Physics Letters*, 97(2):167–169, May 1983. ISSN 00092614. doi: 10.1016/0009-2614(83)85009-X.

- [179] Hui Li, Huanhuan Li, Wu Wang, Ye Tao, Shuang Wang, Qingqing Yang, Yunbo Jiang, Chao Zheng, Wei Huang, and Runfeng Chen. Stimuli-Responsive Circularly Polarized Organic Ultralong Room Temperature Phosphorescence. *Angewandte Chemie*, 132(12):4786–4792, March 2020. ISSN 0044-8249, 1521-3757. doi: 10.1002/ange.201915164.
- [180] Xianchuang Zheng, Xin Wang, Hui Mao, Wei Wu, Baorui Liu, and Xiqun Jiang. Hypoxia-specific ultrasensitive detection of tumours and cancer cells in vivo. *Nature Communications*, 6(1):5834, May 2015. ISSN 2041-1723. doi: 10.1038/ncomms6834.
- [181] Ryosuke Yoshii, Amane Hirose, Kazuo Tanaka, and Yoshiki Chujo. Functionalization of Boron Diimides with Unique Optical Properties: Multicolor Tuning of Crystallization-Induced Emission and Introduction into the Main Chain of Conjugated Polymers. *Journal of the American Chemical Society*, 136(52):18131–18139, December 2014. ISSN 0002-7863, 1520-5126. doi: 10.1021/ja510985v.
- [182] Zhenyi Yu, Yishi Wu, Lu Xiao, Jianwei Chen, Qing Liao, Jiannian Yao, and Hongbing Fu. Organic Phosphorescence Nanowire Lasers. *Journal of the American Chemical Society*, 139(18):6376–6381, May 2017. ISSN 0002-7863, 1520-5126. doi: 10.1021/jacs.7b01574.
- [183] Yongyang Gong, Gan Chen, Qian Peng, Wang Zhang Yuan, Yujun Xie, Shuhong Li, Yongming Zhang, and Ben Zhong Tang. Achieving Persistent Room Temperature Phosphorescence and Remarkable Mechanochromism from Pure Organic Luminogens. *Advanced Materials*, 27(40):6195–6201, October 2015. ISSN 09359648. doi: 10.1002/adma.201502442.
- [184] Yujun Xie, Yuwei Ge, Qian Peng, Conggang Li, Qianqian Li, and Zhen Li. How the Molecular Packing Affects the Room Temperature Phosphorescence in Pure Organic Compounds: Ingenious Molecular Design, Detailed Crystal Analysis, and Rational Theoretical Calculations. *Advanced Materials*, 29(17):1606829, May 2017. ISSN 09359648. doi: 10.1002/adma.201606829.
- [185] Long Gu, Hongwei Wu, Huili Ma, Wenpeng Ye, Wenyong Jia, He Wang, Hongzhong Chen, Nan Zhang, Dongdong Wang, Cheng Qian, Zhongfu An, Wei

- Huang, and Yanli Zhao. Color-tunable ultralong organic room temperature phosphorescence from a multicomponent copolymer. *Nature Communications*, 11(1):944, December 2020. ISSN 2041-1723. doi: 10.1038/s41467-020-14792-1.
- [186] Zihan He, Heqi Gao, Shitong Zhang, Shuyuan Zheng, Yunzhong Wang, Zihao Zhao, Dan Ding, Bing Yang, Yongming Zhang, and Wang Zhang Yuan. Achieving Persistent, Efficient, and Robust Room-Temperature Phosphorescence from Pure Organics for Versatile Applications. *Advanced Materials*, 31(18):1807222, May 2019. ISSN 0935-9648, 1521-4095. doi: 10.1002/adma.201807222.
- [187] Zikai He, Weijun Zhao, Jacky W. Y. Lam, Qian Peng, Huili Ma, Guodong Liang, Zhigang Shuai, and Ben Zhong Tang. White light emission from a single organic molecule with dual phosphorescence at room temperature. *Nature Communications*, 8(1):416, December 2017. ISSN 2041-1723. doi: 10.1038/s41467-017-00362-5.
- [188] Long Gu, Huifang Shi, Mingxing Gu, Kun Ling, Huili Ma, Suzhi Cai, Lulu Song, Chaoqun Ma, Hai Li, Guichuan Xing, Xiaochun Hang, Jiewei Li, Yaru Gao, Wei Yao, Zhigang Shuai, Zhongfu An, Xiaogang Liu, and Wei Huang. Dynamic Ultralong Organic Phosphorescence by Photoactivation. *Angewandte Chemie International Edition*, 57(28):8425–8431, July 2018. ISSN 14337851. doi: 10.1002/anie.201712381.
- [189] Ying Mu, Jun-Qing Wang, Song-De Han, Jie Pan, Jin-Hua Li, and Guo-Ming Wang. Enhanced Room-Temperature Phosphorescence of an Organic Ligand in 3D Hybrid Materials Assisted by Adjacent Halogen Atom. *Inorganic Chemistry*, 59(2):972–975, January 2020. ISSN 0020-1669, 1520-510X. doi: 10.1021/acs.inorgchem.9b03088.
- [190] Jian-An Li, Jinghong Zhou, Zhu Mao, Zongliang Xie, Zhan Yang, Bingjia Xu, Cong Liu, Xin Chen, Dingyang Ren, Hui Pan, Guang Shi, Yi Zhang, and Zhen-guo Chi. Transient and Persistent Room-Temperature Mechanoluminescence from a White-Light-Emitting AIEgen with Tricolor Emission Switching Triggered by Light. *Angewandte Chemie International Edition*, 57(22):6449–6453, May 2018. ISSN 14337851. doi: 10.1002/anie.201800762.
- [191] Lu Xiao, Yishi Wu, Zhenyi Yu, Zhenzhen Xu, Jinbiao Li, Yanping Liu, Jiannian Yao, and Hongbing Fu. Room-Temperature Phosphorescence in

- Pure Organic Materials: Halogen Bonding Switching Effects. *Chemistry - A European Journal*, 24(8):1801–1805, February 2018. ISSN 09476539. doi: 10.1002/chem.201705391.
- [192] Yajie Li, Tianyu Gai, Yuejin Lin, Wenjing Zhang, Kai Li, Yan Liu, Yanquan Duan, Baojun Li, Jie Ding, and Jinpeng Li. Eight Cd(II) coordination polymers with persistent room-temperature phosphorescence: Intriguing dual emission and time-resolved afterglow modulation. *Inorganic Chemistry Frontiers*, 7(3):777–785, 2020. ISSN 2052-1553. doi: 10.1039/C9QI01273G.
- [193] Bolun Wang, Yue Yu, Hongyue Zhang, Yuzhi Xuan, Guangrui Chen, Wenyan Ma, Jiyang Li, and Jihong Yu. Carbon Dots in a Matrix: Energy-Transfer-Enhanced Room-Temperature Red Phosphorescence. *Angewandte Chemie*, 131(51):18614–18619, December 2019. ISSN 0044-8249, 1521-3757. doi: 10.1002/ange.201911035.
- [194] Peifa Wei, Xuepeng Zhang, Junkai Liu, Guo-Gang Shan, Haoke Zhang, Ji Qi, Weijun Zhao, Herman H.-Y. Sung, Ian D. Williams, Jacky W. Y. Lam, and Ben Zhong Tang. New Wine in Old Bottles: Prolonging Room-Temperature Phosphorescence of Crown Ethers by Supramolecular Interactions. *Angewandte Chemie International Edition*, November 2019. ISSN 14337851. doi: 10.1002/anie.201912155.
- [195] Suzhi Cai, Huifang Shi, Dan Tian, Huili Ma, Zhichao Cheng, Qi Wu, Mingxing Gu, Ling Huang, Zhongfu An, Qian Peng, and Wei Huang. Enhancing Ultralong Organic Phosphorescence by Effective π -Type Halogen Bonding. *Advanced Functional Materials*, 28(9):1705045, February 2018. ISSN 1616301X. doi: 10.1002/adfm.201705045.
- [196] Shuyuan Zheng, Taiping Hu, Xin Bin, Yunzhong Wang, Yuanping Yi, Yongming Zhang, and Wang Zhang Yuan. Clustering-Triggered Efficient Room-Temperature Phosphorescence from Nonconventional Luminophores. *ChemPhysChem*, 21(1):36–42, January 2020. ISSN 1439-4235, 1439-7641. doi: 10.1002/cphc.201901024.
- [197] Guoqing Zhang, Jianbin Chen, Sarah J. Payne, Steven E. Kooi, J. N. Demas, and Cassandra L. Fraser. Multi-Emissive Difluoroboron Dibenzoylmethane Polylactide Exhibiting Intense Fluorescence and Oxygen-Sensitive

- Room-Temperature Phosphorescence. *Journal of the American Chemical Society*, 129(29):8942–8943, July 2007. ISSN 0002-7863, 1520-5126. doi: 10.1021/ja0720255.
- [198] Guoqing Zhang, Gregory M. Palmer, Mark W. Dewhirst, and Cassandra L. Fraser. A dual-emissive-materials design concept enables tumour hypoxia imaging. *Nature Materials*, 8(9):747–751, September 2009. ISSN 1476-1122, 1476-4660. doi: 10.1038/nmat2509.
- [199] Christopher A. DeRosa, Jelena Samonina-Kosicka, Ziyi Fan, Hansford C. Hengdargo, Douglas H. Weitzel, Gregory M. Palmer, and Cassandra L. Fraser. Oxygen Sensing Difluoroboron Dinaphthoylmethane Polylactide. *Macromolecules*, 48(9):2967–2977, May 2015. ISSN 0024-9297, 1520-5835. doi: 10.1021/acs.macromol.5b00394.
- [200] Xiang Ma, Chao Xu, Jie Wang, and He Tian. Amorphous Pure Organic Polymers for Heavy-Atom-Free Efficient Room-Temperature Phosphorescence Emission. *Angewandte Chemie International Edition*, 57(34):10854–10858, August 2018. ISSN 14337851. doi: 10.1002/anie.201803947.
- [201] Qing Zhou, Boyu Cao, Chenxuan Zhu, Si Xu, Yongyang Gong, Wang Zhang Yuan, and Yongming Zhang. Clustering-Triggered Emission of Nonconjugated Polyacrylonitrile. *Small*, 12(47):6586–6592, December 2016. ISSN 16136810. doi: 10.1002/smll.201601545.
- [202] Songyuan Tao, Siyu Lu, Yijia Geng, Shoujun Zhu, Simon A. T. Redfern, Yubin Song, Tanglue Feng, Weiqing Xu, and Bai Yang. Design of Metal-Free Polymer Carbon Dots: A New Class of Room-Temperature Phosphorescent Materials. *Angewandte Chemie International Edition*, 57(9):2393–2398, February 2018. ISSN 14337851. doi: 10.1002/anie.201712662.
- [203] Suzhi Cai, Huili Ma, Huifang Shi, He Wang, Xuan Wang, Leixin Xiao, Wenpeng Ye, Kaiwei Huang, Xudong Cao, Nan Gan, Chaoqun Ma, Mingxing Gu, Lulu Song, Hai Xu, Youtian Tao, Chunfeng Zhang, Wei Yao, Zhongfu An, and Wei Huang. Enabling long-lived organic room temperature phosphorescence in polymers by subunit interlocking. *Nature Communications*, 10(1):4247, December 2019. ISSN 2041-1723. doi: 10.1038/s41467-019-11749-x.

- [204] Piotr Pander, Agnieszka Swist, Roman Turczyn, Stephanie Pouget, David Djurado, Algirdas Lazauskas, Ramin Pashazadeh, Juozas V. Grazulevicius, Radoslaw Motyka, Anastasia Klimash, Peter J. Skabara, Przemyslaw Data, Jadwiga Soloducho, and Fernando B. Dias. Observation of Dual Room Temperature Fluorescence–Phosphorescence in Air, in the Crystal Form of a Thianthrene Derivative. *The Journal of Physical Chemistry C*, 122(43):24958–24966, November 2018. ISSN 1932-7447, 1932-7455. doi: 10.1021/acs.jpcc.8b08329.
- [205] Christopher A. DeRosa, Satoru Hiroto, and Cassandra L. Fraser. Amplified Heavy-Atom Free Phosphorescence from *meta* -Dimethoxy Difluoroboron β -Diketonate Charge-Transfer Materials. *The Journal of Physical Chemistry C*, 123(33):20488–20496, August 2019. ISSN 1932-7447, 1932-7455. doi: 10.1021/acs.jpcc.9b05736.
- [206] Mikhail A. Filatov, Stanislav Balushev, and Katharina Landfester. Protection of densely populated excited triplet state ensembles against deactivation by molecular oxygen. *Chemical Society Reviews*, 45(17):4668–4689, 2016. ISSN 0306-0012, 1460-4744. doi: 10.1039/C6CS00092D.
- [207] Shuzo Hirata, Kenro Totani, Junxiang Zhang, Takashi Yamashita, Hironori Kaji, Seth R. Marder, Toshiyuki Watanabe, and Chihaya Adachi. Efficient Persistent Room Temperature Phosphorescence in Organic Amorphous Materials under Ambient Conditions. *Advanced Functional Materials*, 23(27):3386–3397, July 2013. ISSN 1616301X. doi: 10.1002/adfm.201203706.
- [208] Yoshiaki Shoji, Yasuhiro Iwabata, Qi Wang, Daisuke Nemoto, Atsushi Sakamoto, Naoki Tanaka, Junji Seino, Hiromi Nakai, and Takanori Fukushima. Unveiling a New Aspect of Simple Arylboronic Esters: Long-Lived Room-Temperature Phosphorescence from Heavy-Atom-Free Molecules. *Journal of the American Chemical Society*, 139(7):2728–2733, February 2017. ISSN 0002-7863, 1520-5126. doi: 10.1021/jacs.6b11984.
- [209] G Li. Anti-oxygen-quenching room temperature phosphorescence stabilized by deoxycholate aggregate. *Talanta*, 60(2-3):555–562, June 2003. ISSN 00399140. doi: 10.1016/S0039-9140(03)00185-1.
- [210] Anna J. Svagan, Dmitry Busko, Yuri Avlasevich, Gunnar Glasser, Stanislav Balushev, and Katharina Landfester. Photon Energy Upconverting Nanopa-

- per: A Bioinspired Oxygen Protection Strategy. *ACS Nano*, 8(8):8198–8207, August 2014. ISSN 1936-0851, 1936-086X. doi: 10.1021/nm502496a.
- [211] Hayaka Fukuzumi, Tsuguyuki Saito, Tadahisa Iwata, Yoshiaki Kumamoto, and Akira Isogai. Transparent and High Gas Barrier Films of Cellulose Nanofibers Prepared by TEMPO-Mediated Oxidation. *Biomacromolecules*, 10(1):162–165, January 2009. ISSN 1525-7797, 1526-4602. doi: 10.1021/bm801065u.
- [212] I. Sánchez-Barragán, J.M. Costa-Fernández, A. Sanz-Medel, M. Valledor, and J.C. Campo. Room-temperature phosphorescence (RTP) for optical sensing. *TrAC Trends in Analytical Chemistry*, 25(10):958–967, November 2006. ISSN 01659936. doi: 10.1016/j.trac.2006.07.009.
- [213] Sven Kochmann, Carlos Baleizão, Mário N. Berberan-Santos, and Otto S. Wolfbeis. Sensing and Imaging of Oxygen with Parts per Billion Limits of Detection and Based on the Quenching of the Delayed Fluorescence of $^{13}\text{C}_{70}$ Fullerene in Polymer Hosts. *Analytical Chemistry*, 85(3):1300–1304, February 2013. ISSN 0003-2700, 1520-6882. doi: 10.1021/ac303486f.
- [214] Yusheng Zhou, Wei Qin, Cheng Du, Haiyang Gao, Fangming Zhu, and Guodong Liang. Long-Lived Room-Temperature Phosphorescence for Visual and Quantitative Detection of Oxygen. *Angewandte Chemie International Edition*, 58(35):12102–12106, August 2019. ISSN 1433-7851, 1521-3773. doi: 10.1002/anie.201906312.
- [215] Ya-Chuan Liang, Yuan Shang, Kai-Kai Liu, Zhen Liu, Wen-Jie Wu, Qian Liu, Qi Zhao, Xue-Ying Wu, Lin Dong, and Chong-Xin Shan. Water-induced ultralong room temperature phosphorescence by constructing hydrogen-bonded networks. *Nano Research*, February 2020. ISSN 1998-0124, 1998-0000. doi: 10.1007/s12274-020-2710-3.
- [216] Linkun Huang, Biao Chen, Xuepeng Zhang, Carl O. Trindle, Fan Liao, Yucai Wang, Hui Miao, Yi Luo, and Guoqing Zhang. Proton-Activated “Off-On” Room-Temperature Phosphorescence from Purely Organic Thioethers. *Angewandte Chemie International Edition*, 57(49):16046–16050, December 2018. ISSN 1433-7851, 1521-3773. doi: 10.1002/anie.201808861.

- [217] Zhen Tian, Di Li, Elena V. Ushakova, Vladimir G. Maslov, Ding Zhou, Pengtao Jing, Dezhen Shen, Songnan Qu, and Andrey L. Rogach. Multilevel Data Encryption Using Thermal-Treatment Controlled Room Temperature Phosphorescence of Carbon Dot/Polyvinylalcohol Composites. *Advanced Science*, 5(9):1800795, September 2018. ISSN 21983844. doi: 10.1002/advs.201800795.
- [218] Qi Wu, Huili Ma, Kun Ling, Nan Gan, Zhichao Cheng, Long Gu, Suzhi Cai, Zhongfu An, Huifang Shi, and Wei Huang. Reversible Ultralong Organic Phosphorescence for Visual and Selective Chloroform Detection. *ACS Applied Materials & Interfaces*, 10(39):33730–33736, October 2018. ISSN 1944-8244, 1944-8252. doi: 10.1021/acsami.8b13713.
- [219] Jinxiong Lin, Shigang Wan, Wenfeng Liu, and Wei Lu. Photo-writing self-erasable phosphorescent images using poly(*N* -vinyl-2-pyrrolidone) as a photochemically deoxygenating matrix. *Chemical Communications*, 55(30):4299–4302, 2019. ISSN 1359-7345, 1364-548X. doi: 10.1039/C9CC01388A.
- [220] John C. de Mello, H. Felix Wittmann, and Richard H. Friend. An improved experimental determination of external photoluminescence quantum efficiency. *Advanced Materials*, 9(3):230–232, March 1997. ISSN 0935-9648, 1521-4095. doi: 10.1002/adma.19970090308.
- [221] Felix Fries and Sebastian Reineke. Statistical treatment of Photoluminescence Quantum Yield Measurements. *Scientific Reports*, 9(1):15638, December 2019. ISSN 2045-2322. doi: 10.1038/s41598-019-51718-4.
- [222] Guangjun Lu, W.D. van Driel, Xuejun Fan, M. Yazdan Mehr, Jiajie Fan, Cheng Qian, K.M.B. Jansen, and G.Q. Zhang. Colour shift and mechanism investigation on the PMMA diffuser used in LED-based luminaires. *Optical Materials*, 54:282–287, April 2016. ISSN 09253467. doi: 10.1016/j.optmat.2016.02.023.
- [223] Makoto Muramatsu, Masayuki Okura, Keiichi Kuboyama, Toshiaki Ougizawa, Tomoyuki Yamamoto, Yuko Nishihara, Yoichiro Saito, Kenji Ito, Koichi Hirata, and Yoshinori Kobayashi. Oxygen permeability and free volume hole size in ethylene–vinyl alcohol copolymer film: Temperature and humidity dependence. *Radiation Physics and Chemistry*, 68(3-4):561–564, October 2003. ISSN 0969806X. doi: 10.1016/S0969-806X(03)00231-7.

- [224] R. H. G. Brinkhuis and A. J. Schouten. Thin-film behavior of poly(methyl methacrylates). 2. An FT-IR study of Langmuir-Blodgett films of isotactic PMMA. *Macromolecules*, 24(7):1496–1504, April 1991. ISSN 0024-9297, 1520-5835. doi: 10.1021/ma00007a010.
- [225] Caterin Salas Redondo, Paul Kleine, Karla Roszeitis, Tim Achenbach, Martin Kroll, Michael Thomschke, and Sebastian Reineke. Interplay of Fluorescence and Phosphorescence in Organic Biluminescent Emitters. *The Journal of Physical Chemistry C*, 121(27):14946–14953, July 2017. ISSN 1932-7447, 1932-7455. doi: 10.1021/acs.jpcc.7b04529.
- [226] Felix Fries, Marine Louis, Reinhard Scholz, Max Gmelch, Heidi Thomas, Anna Haft, and Sebastian Reineke. Dissecting Tetra- *N* -phenylbenzidine: Biphenyl as the Origin of Room Temperature Phosphorescence. *The Journal of Physical Chemistry A*, 124(3):479–485, January 2020. ISSN 1089-5639, 1520-5215. doi: 10.1021/acs.jpca.9b09148.
- [227] Anton Kirch. Excitation Wavelength Dependent Response of a Biluminescent-Fluorescent Emitter Blend, Master Thesis, February 2018.
- [228] Marine Louis, Heidi Thomas, Max Gmelch, Anna Haft, Felix Fries, and Sebastian Reineke. Blue-Light-Absorbing Thin Films Showing Ultralong Room-Temperature Phosphorescence. *Advanced Materials*, 31(12):1807887, March 2019. ISSN 0935-9648, 1521-4095. doi: 10.1002/adma.201807887.
- [229] Hongwei Wu, Weijie Chi, Zhao Chen, Guofeng Liu, Long Gu, Anivind Kaur Bindra, Guangbao Yang, Xiaogang Liu, and Yanli Zhao. Achieving Amorphous Ultralong Room Temperature Phosphorescence by Coassembling Planar Small Organic Molecules with Polyvinyl Alcohol. *Advanced Functional Materials*, page 1807243, December 2018. ISSN 1616-301X, 1616-3028. doi: 10.1002/adfm.201807243.
- [230] Angelo A. Lamola and George S. Hammond. Mechanisms of Photochemical Reactions in Solution. XXXIII. Intersystem Crossing Efficiencies. *The Journal of Chemical Physics*, 43(6):2129–2135, September 1965. ISSN 0021-9606, 1089-7690. doi: 10.1063/1.1697084.

- [231] C.U. Ibeji, J. Adegboyega, O.D. Okagu, and B.B. Adeleke. Nature of Ground State of Benzophenone and some of its Substituted Derivatives: Experimental and DFT Study. *Journal of Applied Sciences*, 16(11):504–516, October 2016. ISSN 18125654. doi: 10.3923/jas.2016.504.516.
- [232] Anton Kirch, Max Gmelch, and Sebastian Reineke. Simultaneous Singlet–Singlet and Triplet–Singlet Förster Resonance Energy Transfer from a Single Donor Material. *The Journal of Physical Chemistry Letters*, 10(2):310–315, January 2019. ISSN 1948-7185, 1948-7185. doi: 10.1021/acs.jpclett.8b03668.
- [233] Invisible tags: Physicists write, read and erase using light. <https://www.sciencedaily.com/releases/2019/02/190201142432.htm>, February 2019.
- [234] Programmable transparent tags present a new method of storing information. <https://www.innovationtoronto.com/2019/02/programmable-transparent-tags-present-a-new-method-of-storing-information>, February 2019.
- [235] Dresdner Physiker entwickeln unsichtbare Etiketten. https://www.focus.de/regional/dresden/wissenschaft-dresdner-physiker-entwickeln-unsichtbare-etiketten_id_10266546.html, February 2019.

Danksagung

„Nullum enim officium referenda gratia magis necessarium est“, wusste schon Cicero. All jenen, denen ihr Latinum ähnlich gut in Erinnerung geblieben ist wie mir, möchte ich selbstverständlich auch auf Deutsch meinen Dank verkünden.

- Allen voran möchte ich Prof. Dr. Sebastian Reineke danken, welcher es mir ermöglicht hat, meine Doktorarbeit in seiner Arbeitsgruppe durchzuführen. Ich bedanke mich für die allgegenwärtige Unterstützung, das stets offene Ohr, den kreativen Gedankenaustausch sowie für das in mich gesetzte Vertrauen über die Promotion hinweg und die enorme fachliche Freiheit, mit der ich jeden Tag arbeiten durfte.
- Ich danke Prof. Dr. Tobias Korn, der nicht nur das Zweitgutachten dieser Arbeit übernommen hat, sondern mir auch zu Beginn meiner universitären Laufbahn im Rahmen der Bachelorarbeit die Grundlagen des wissenschaftlichen Arbeitens beigebracht hat.
- Mein herzlicher Dank gilt weiterhin der Mensagruppe, die für mich die Grenzen zwischen Arbeit und Privatleben auf äußerst positive Weise verschwimmen ließ. Besonders die nachmittägliche sportliche Aktivität und die unzähligen fachlichen Diskussionen möchte ich hierbei herausheben.
- Ich bedanke mich bei Ludwig und den Biluminaten, für viele schöne musikalische Stunden, tolle Auftritte und die hoffentlich noch folgende Straßenmusikerkarriere.
- Weiterhin bedanke ich mich bei Anton Kirch, für unzählige Abendessen, hervorragende Zusammenarbeit, und die Erweiterung meines Horizonts weit über das Fachliche hinaus.

—— Bibliography ——

- Ein großes Dankeschön geht an Felix Fries, für die technische Unterstützung beim Schreiben dieser Arbeit, für Korrekturhinweise und nicht zuletzt für die stete Nachsicht bei fragwürdigen Wortspielen.
- Ich bedanke mich bei Dr. Heidi Thomas, für einen erfolgreichen gemeinsamen Start am Institut, für die fruchtbare Zusammenarbeit, für die vielen hergestellten Proben, für das Korrekturlesen und den unterhaltsamen Austausch im Büro.
- Herzlich bedanken möchte ich mich auch bei Tim Achenbach, für die allerersten Einführungen in die Messaufbauten des IAPP, für das Korrekturlesen sowie für die kreative Zusammenarbeit in und außerhalb des Instituts.
- Ein weiteres Dankeschön gilt Toni Bärschneider, für den inspirierenden Austausch, sei es im Büro, im Labor oder in seiner Kellerwerkstatt.
- Ein großer Dank gilt Paul-Anton Will, für sehr erfolgreiche Zusammenarbeit und hilfreiche Hinweise zur Struktur dieser Arbeit.
- Ich danke Martin Kroll für seine Arbeit an den Laboraufbauten und seine Unterstützung.
- Ich bedanke mich bei Karla Roszeitis, Christian Hänisch und Andreas Hofacker, für die vielen musikalischen Stunden im Institutschor.
- Weiterhin danke ich Fanny Uhlig, Johanna Bürger, Carla Schmidt, Dr. Angelika Wolf, Dr. Annette Polte, Kai Schmidt und Peter Leumer für die Unterstützung bei administrativen und IT-bezogenen Fragen, sowie die zahlreichen netten Gespräche.
- Zusätzlich möchte ich allen weiteren Mitarbeitern des IAPP für die stets freundliche Hilfe bei jeglichen Herausforderungen danken, insbesondere Annika Schlögl, Hui-Tzu Chen, Paulius Imbrasas und Dr. Axel Fischer.
- Ein großer Dank gilt meinen Eltern, die mir durch ihre Unterstützung vom ersten Tag meines Studiums an diese Promotion überhaupt erst ermöglicht haben, und noch heute wann immer nötig jederzeit für mich da sind.

—— Bibliography ——

- Abschließend möchte ich mich bei meiner Beinahe-Ehefrau Lena Schindler bedanken, für ihre allgegenwärtige Unterstützung, für das intensive Korrekturlesen dieser Arbeit, für unzählige inspirierende Gespräche sowie für die viele schöne gemeinsame Zeit, vor allem im COVID-19-bedingten Home-Office der letzten Monate.

Versicherung gemäß der Promotionsordnung

Hiermit versichere ich, dass ich die vorliegende Arbeit ohne unzulässige Hilfe Dritter und ohne Benutzung anderer als der angegebenen Hilfsmittel angefertigt habe; die aus fremden Quellen direkt oder indirekt übernommenen Gedanken sind als solche kenntlich gemacht. Die Arbeit wurde bisher weder im Inland noch im Ausland in gleicher oder ähnlicher Form einer anderen Prüfungsbehörde vorgelegt.

Diese Arbeit wurde am Dresden Integrated Center for Applied Physics and Photonic Materials (IAPP) im Bereich Mathematik und Naturwissenschaften der Fakultät Physik an der Technischen Universität Dresden unter wissenschaftlicher Betreuung von Prof. Dr. Sebastian Reineke angefertigt.

Frühere erfolglose Promotionsverfahren haben nicht statt gefunden. Ich erkenne die Promotionsordnung des Bereichs Mathematik und Naturwissenschaften der TU Dresden in der aktuell gültigen Fassung vom 23.02.2011 an.

Datum

Unterschrift